Interaction Application Memos

Memo 15

Surface Field Measurements on Scale Model EC-135 Aircraft

ABSTRACT

The surface currents and charges induced on the EC-135 aircraft when illuminated by a plane electromagnetic wave have been measured over a wide range of (simulated full-scale) frequencies, typically 1 to 35 MHz. The measurements were made using 1/447 to 1/114 scale models over the frequency range 450 to 4000 MHz, and data are presented for aircraft with and without HF wire antennas in configurations simulating (1) free space, topside incidence, (2) near a perfectly conducting ground topside incidence, and (3) near a perfectly conducting ground, oblique incidence.

PREFACE

It is a pleasure to acknowledge the assistance of the many members of the Radiation Laboratory who participated in the collection, reduction and presentation of the data presented in this report. Special thanks are due to Mr. Dan Dusette who carried out most of the free space measurements and data reduction, to Mr. Ted Kowalski who developed the software to digitize the data on a PDP-11/20 system and transfer it to the large computer for processing and replotting, and to Mr. Louis Martins-Camelo who spent long hours reducing the data and overseeing the digital plotting. The unfailing assistance and cooperation of the personnel at AFWL/ELPE, and Mr. William Prather in particular, are also gratefully appreciated.

CONTENTS

SECTION I

INTRODUCTION

In dealing with electromagnetic phenomena there are often cases where information can be obtained using scale models in a laboratory environment that would be difficult, if not impossible, to obtain otherwise. One example of this is the measurement of the skin currents and charges on aircraft to assess their vulnerability to an electromagnetic pulse (EMP), and this report is concerned with measurements carried out on small scale models of the EC-135 aircraft. The models used ranged in scale from 1/447 to 1/114 and the measurements were made from 450 to 4000 MHz to provide coverage from 1 to 35 MHz at full-scale.

Data are presented for the current and charge densities in amplitude and phase at selected stations on the aircraft as functions of frequency. The configurations treated are the aircraft (1) in isolation (free space) with topside incidence, (2) near a perfectly conducting ground with topside incidence, and (3) near the same ground but with oblique incidence. In the first two configurations, data have been obtained for aircraft with and without HF wire antennas joining the top of the fuselage to the vertical stabilizer.

During the course of the contract, there has been continuous development and refinement in the techniques of acquiring, processing and presenting the data. This is particularly true as regards the data reduction and presentation, and the evolution is reflected in the figures presented in Sections II, III and IV. Section II is concerned with the free-space measurements. These data were obtained at the very beginning of the use of swept frequency techniques. As the frequency was swept, typically over a 2:1 band, the sensor output in amplitude and phase was recorded on an analog X-Y plotter. To obtain data at a given station on the aircraft, two measurements are required: one with the sensor mounted appropriately on the model, and the other with the model replaced by a calibrating object, either a sphere or a ground plane, to determine the incident field reference. The ratio of these two is then the current (or charge) relative to the incident field and is the quantity required. In concept at least, such data reduction is easy to perform, but

in practice it can be extremely tedious since it should be carried out at many frequency points within the band. For all the free-space measurements, manual data reduction and plotting was necessary, using sampled values generally at 100 MHz intervals.

Section III is concerned with measurements for topside incidence on the aircraft near to a perfectly conducting ground plane. At the lower frequencies, 1 to 9 MHz full-scale, the data were again reduced and plotted manually, but by the time the higher frequencies, 5 to 35 MHz full-scale, were reached, we had developed the ability to digitize the X-Y recorder plots, and then process and computer-plot the data. This same technique was then used to process the data contained in Section IV for the aircraft near to the ground plane but illuminated at an angle of 18^{o} from the horizontal.

SECTION II

FREE-SPACE MEASUREMENTS

The surface currents and charges have been measured on the EC-135 aircraft in a simulated free-space environment. The measurements were made over the frequency range 1 to 4 GHz which, for the 1/447 to 1/114 scale models used, corresponds to the full-scale frequency range 2.2 to 35 MHz, but the data presented here are only at frequencies up to 20 MHz. The illumination was top-side with the incident field polarized with its electric vector either parallel or perpendicular to the fuselage, representing symmetric or antisymmetric polarization, respectively. Data were obtained for models with and without HF antenna wires connecting the top of the fuselage (near the cockpit) to the vertical stabilizer.

1. Facility and Equipment

The measurements were made in the Radiation Laboratory surface field facility using equipment and procedures similar to those described by Liepa (1975)*. Figure 1 shows a block diagram of the facility whose main elements are:

(1) anechoic chamber,

(2) swept frequency source (sweep generator, power amplifier, isolator and antenna), and

(3) receiving and recording equipment (sensors, preamplifier, phase shifter, network analyzer, analog X-Y recorder, and CRT display).

2. Models

Seven models were used ranging in scale from 1/447 to 1/114. All are either diecast metal or assembled from plastic kits and purport to model some version of the Boeing 707, with the result that they do not have precisely the same scaled dimensions as the EC-135 aircraft. In translating the measurement frequencies to the full-scale ones, a scale factor was used based on the length when the

*Liepa, V.V., (1975), "Sweep Frequency Surface Field Measurements," Sensor and Simulation Note 210.

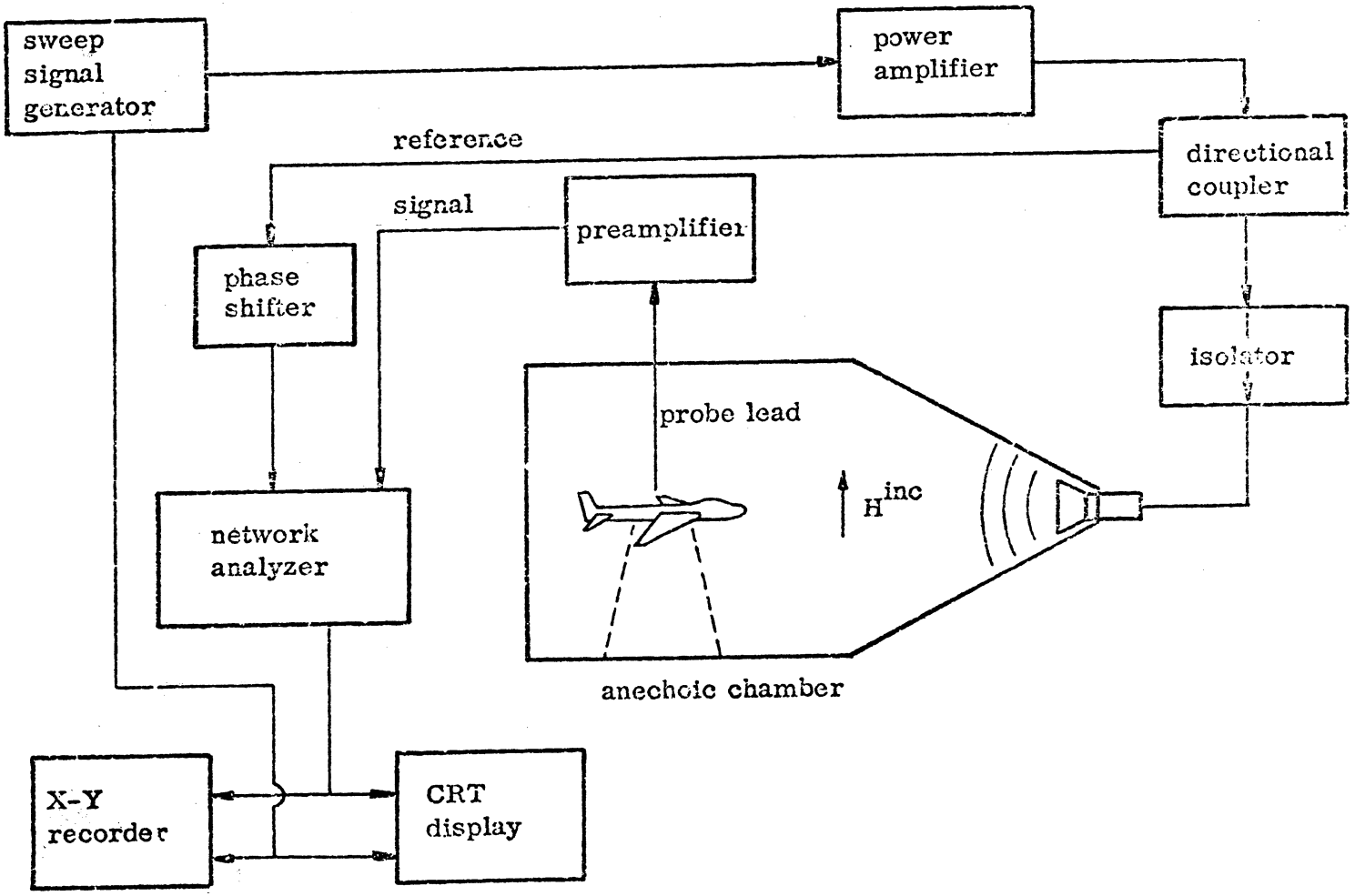

Figure 1. Surface field measurement facility.

excitation was symmetric, but based on the wingspan when the excitation was anti-symmetric. Refueling booms were added to all the models. These were cut out of wood and then spray painted with conducting silver paint. Cockpit and fuselage windows were also painted, and the landing gear doors and fuselage-wing joints (on metal models) were covered with aluminum or copper tape. On some models HF wire antennas were also attached. These were made of No. 30 wire and installed as per the specifications given in figure 2. Both of the wires are electrically shorted at the joint with the fuselage, but at the vertical stabilizer the upper wire is shorted and the lower one open. The open circuit condition was simulated using a section of string approximately 1/16 inch in length. Table 1 lists some of the properties of the various models.

3. Sensors

All of the measurements were made with so-called "hard lead" probes. The surface currents were measured using a bent 3.2 mm diameter shielded loop probe* and the charge measurements were made using an extension of the center conductor of a 0.020 inch diameter coax. This extension or monopole was typically 0.060 inch long and the cable was brought to the surface from within the model. For the charge measurements at the nose of the aircraft, a hole was drilled in the model from the nose (STA:F130)** into the front landing gear cavity. The sensor lead was brought out from there and taped along the belly of the plane up to STA:F800B from which it was taken in a direction normal to the fuselage and parallel to the direction of propagation of the incident wave. In the wingtip charge measurements at STA:W940T, the cable again joined the model at STA:F800B, from which it was taped along the underside of the wing and passed to the top through a 0.025 inch diameter hole drilled through the wing.

---

* Liepa, V.V., (1975), "Sweep Frequency Surface Field Measurements," Sensor and Simulation Note 210, Fig. 18.

** The locations of body station numbers are given in Figure 3. The letter F (or W) in front of the number refers to a fuselage (or wing) location, while the letter T (or B) after the number designates the top (or bottom) of the aircraft.

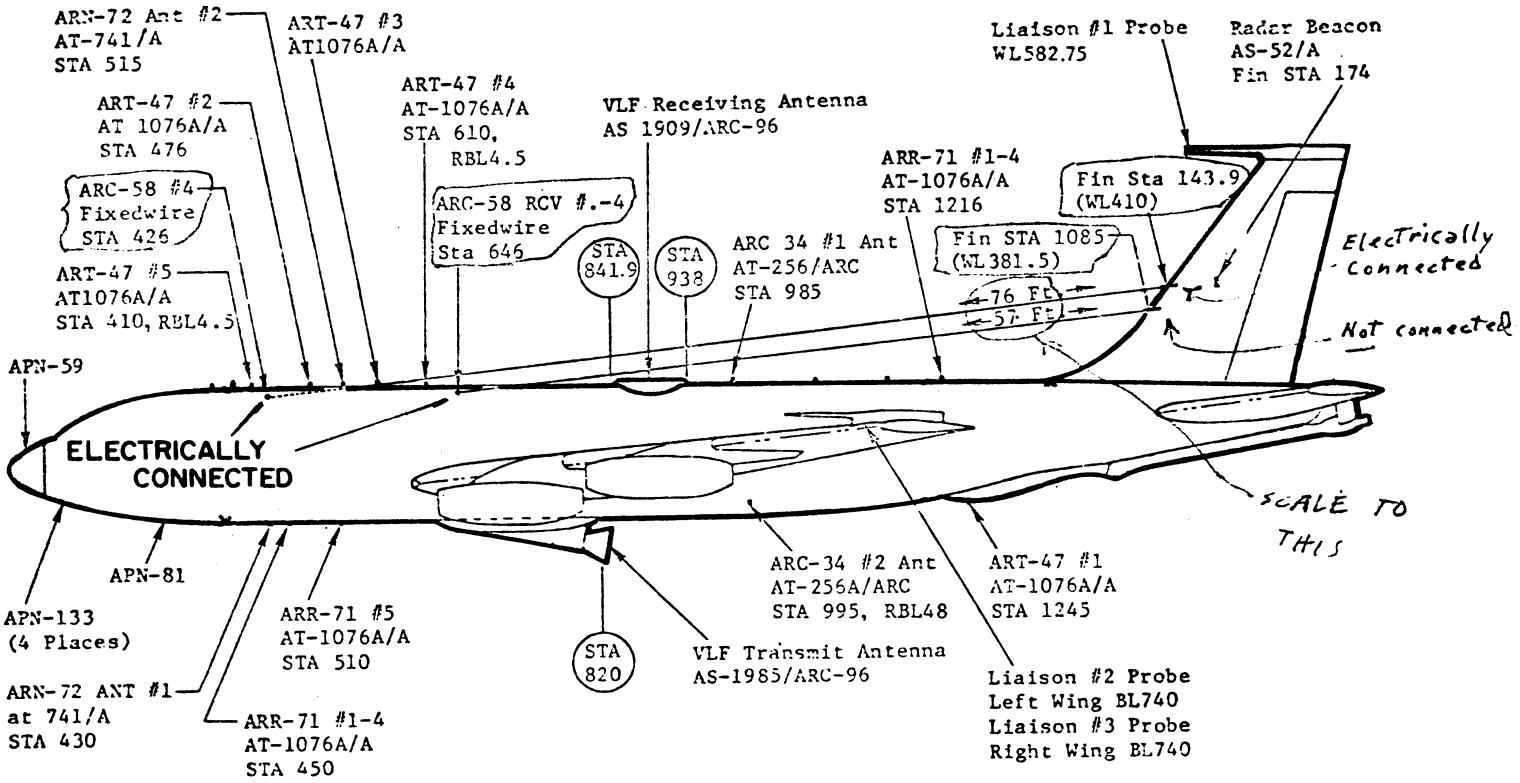

Figure 2. EC-135 HF wire antenna installations.

Table 1

EC-135 MODELS USED

EC-135 Model	Fuselage Scale	Wing Span Scale	Material	Fuselage Diameter at Station			Wing Thickness at W600	With HF Wires	Without HF Wires
				400	800	1200			
447	1/447	1/466	metal	0.93 cm	0.94 cm	0.86 cm	0.17 cm	X	X
325	1/325	1/341	metal	1.15	1.19	1.15	0.23	X	X
224	1/224	1/225	metal	1.80	1.77	1.76	0.28	X	
129	1/129	1/134	plastic	3.01	3.03	3.02	0.59		X
114	1/114	1/117	plastic	3.50	3.44	3.35	0.30	X	

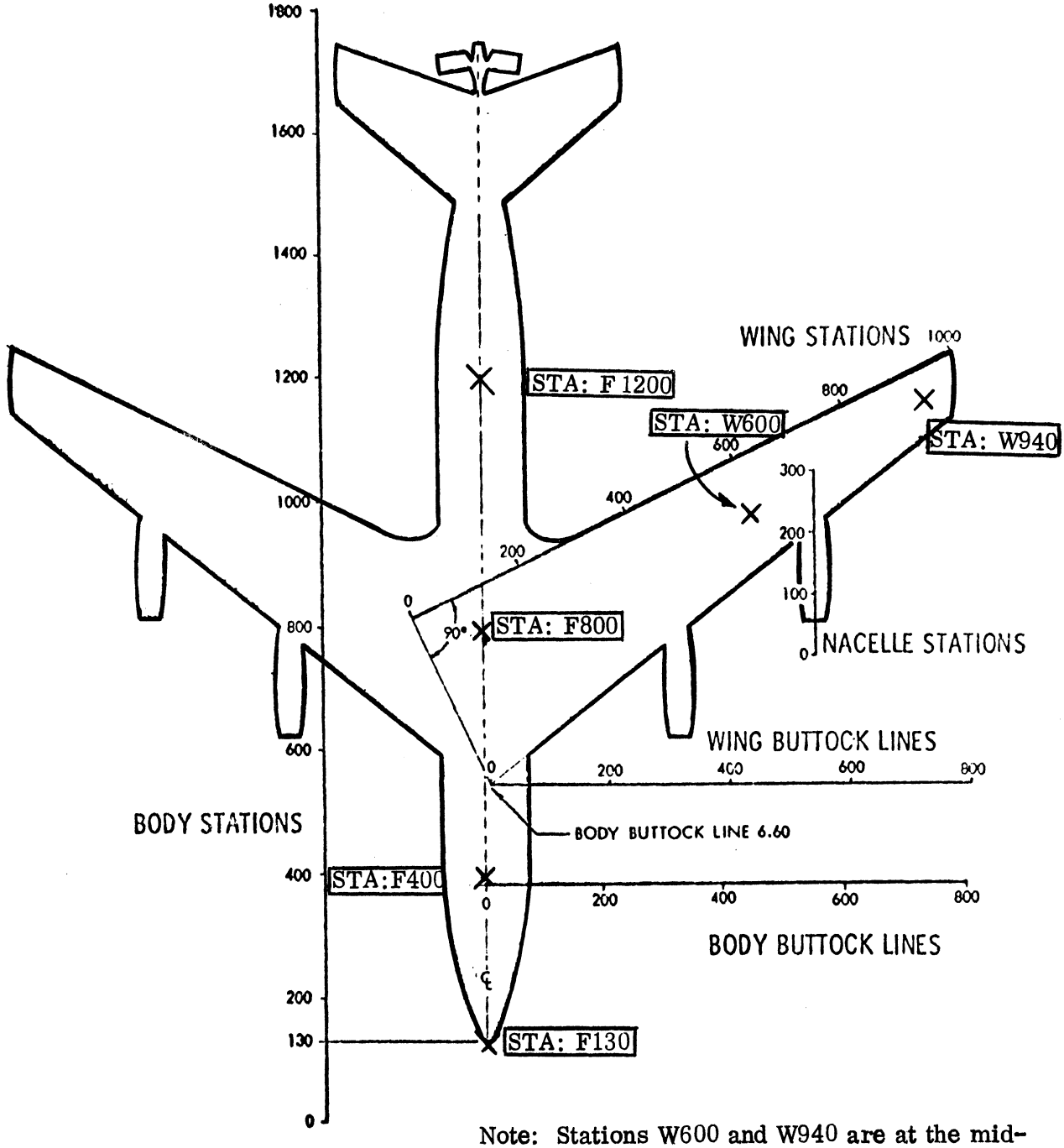

Note: Stations W600 and W940 are at the mid-sections of the wing. Station W940 is located at the center of a circle tangent to the three edges of a wing.

Figure 3. EC-135 aircraft body stations, X designates measurement locations.

Current measurements were made using an external B-dot sensor or current loop probe. This touched the model only at the point of measurement and even there it was separated by a small dielectric epoxy bead. Since the incident field was always horizontally polarized, the incident electric vector was perpendicular to the sensor lead, thus providing minimal interactions with the incident field. Figures 4 through 7 show photographs of the models used and the implementation of current and charge sensors.

4. Data Reduction

For a given frequency scan the plots of current and charge obtained directly from the X-Y recorder show very little resemblance to the behavior that would be expected. This is caused by the nonuniform frequency response of the measuring equipment, and to account for the distortion the model data are normalized to the incident field deduced from data for 3.133 and/or 6.0 inch diameter spheres obtained under the same measurement conditions. To perform the data reduction, values are read off the model and sphere measurement curves, typically at 100 MHz intervals, and the computation is performed using an electronic pocket calculator. When appropriate, corrections for probe integration effects are also applied. These corrections are largest for the smaller models and can adjust the current amplitude by as much as 33 percent and the charge by 60 percent.

5. Data

The surface currents and charges are presented as functions of the full-scale frequency in figures 8 through 31. Corresponding amplitudes and phases are given in figures having the same number but distinguished by the letter a (amplitude) or b (phase). As noted, the amplitudes are normalized to the incident field, and the phase is relative to that of the incident field at the station where the measurement was made. It may also be helpful to note that all figures with even numbers are for aircraft without HF wire antennas, whereas odd numbers are for aircraft with antennas.

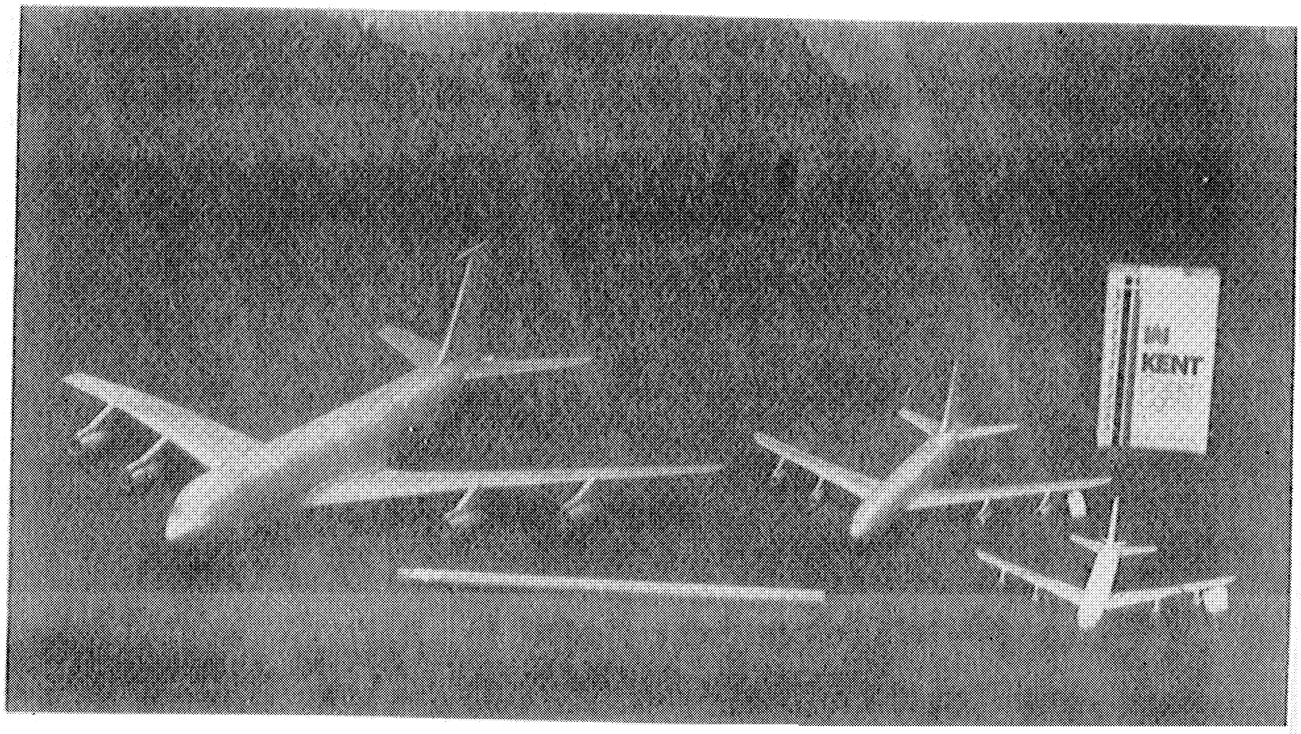

Figure 4. The 1/114, 1/224, 1/325 scale models of the EC-135 aircraft.

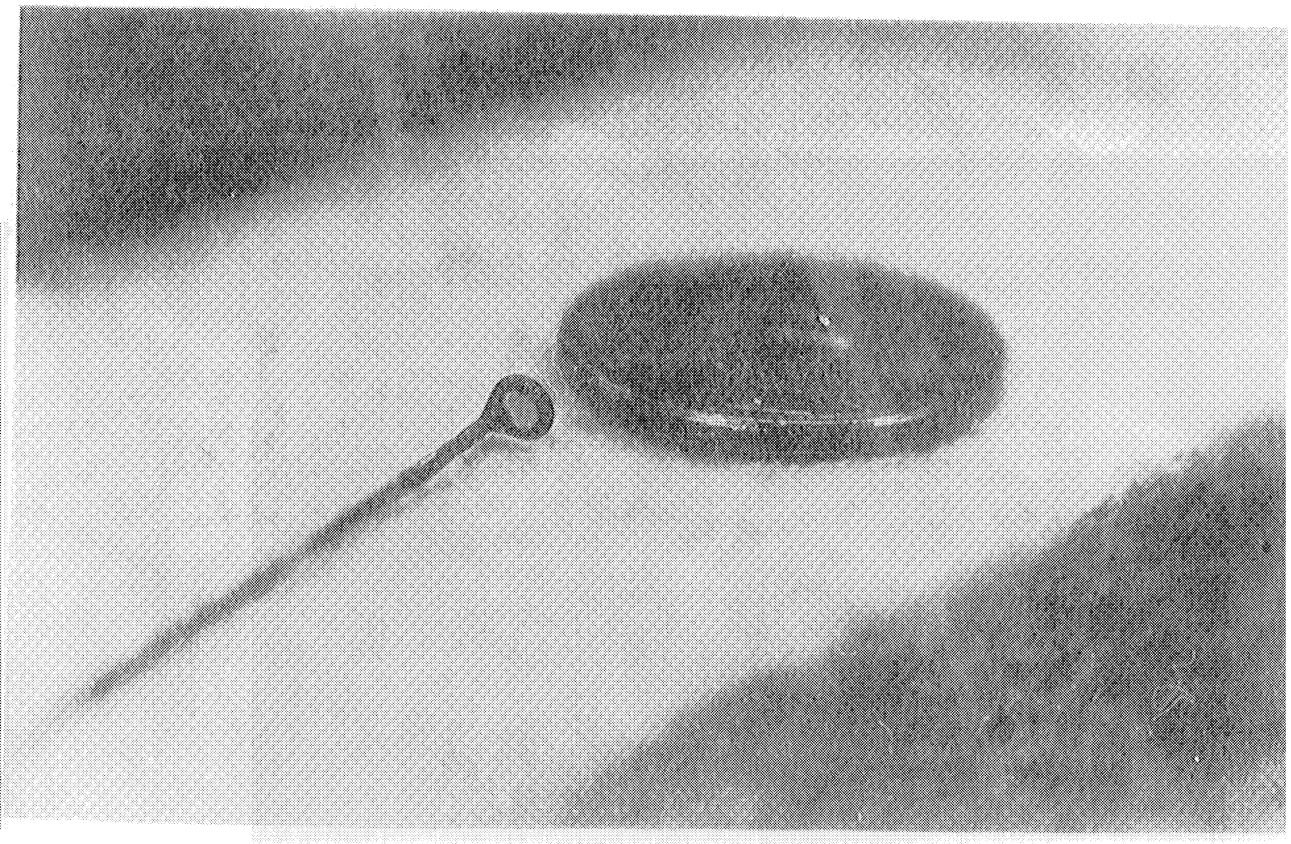

Figure 5. A shielded loop probe in comparison to a 1¢ piece.

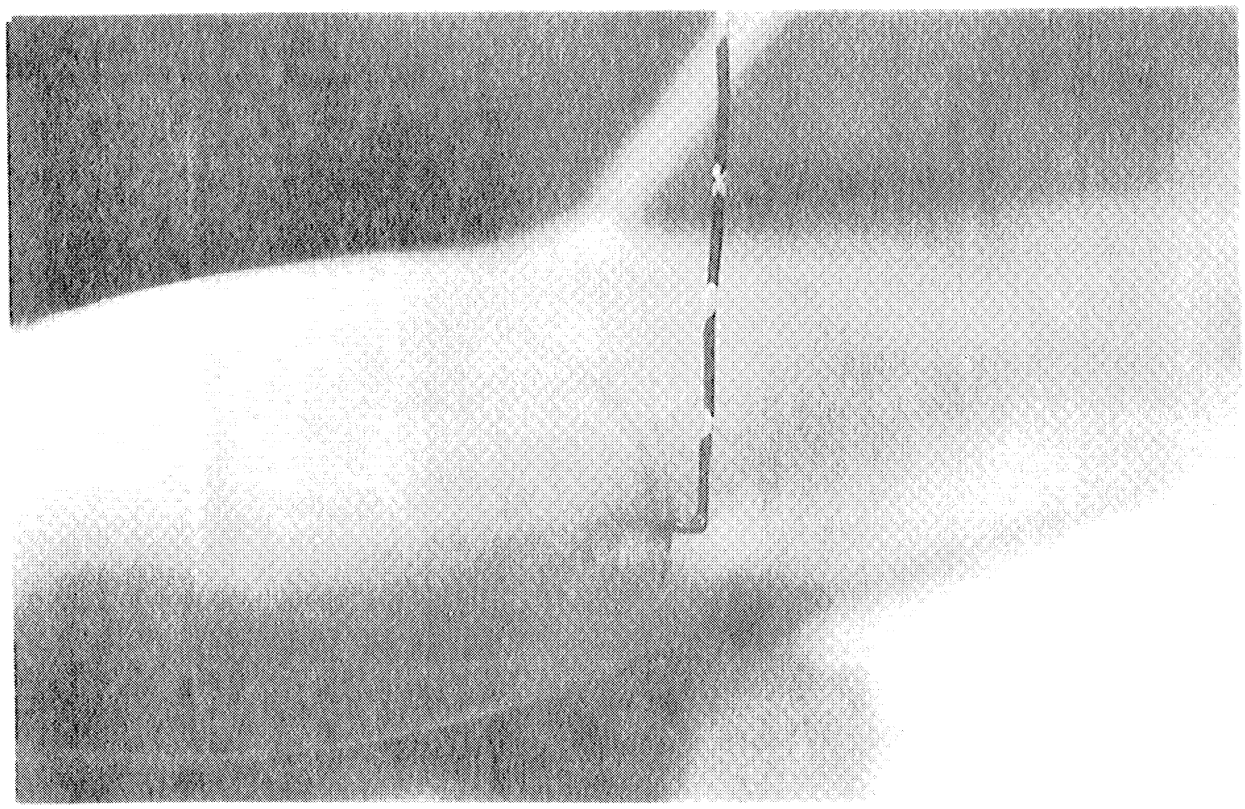

Figure 6. Loop probe at STA:F400T on the 1/114 scale model.

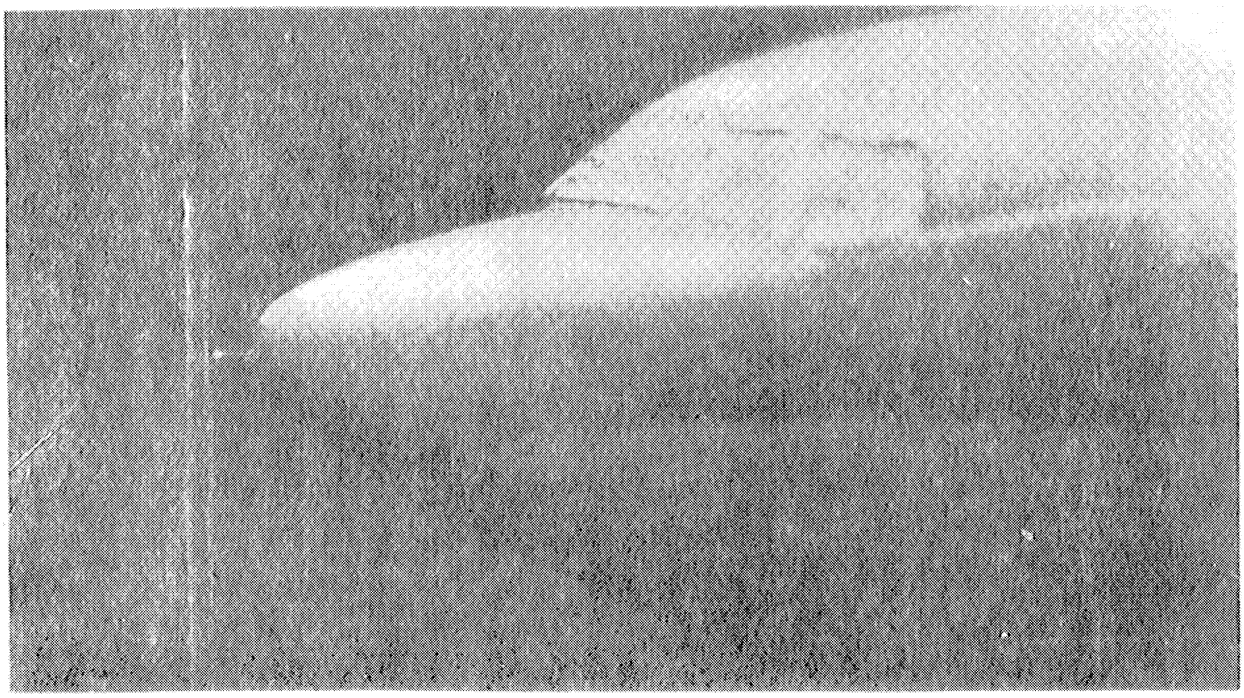

Figure 7. A 2 mm long charge probe at the nose of the 1/144 scale model.

A summary of the data presented is given in Table 2, and this may prove helpful in locating results for a particular measurement condition. Thus, to locate the figure giving the current amplitude on top of the fuselage at station 800 for the aircraft with HF wires, excited antisymmetrically, go to the line designated F800T (Fuselage, 800, Top) and then across the table to find the appropriate entry: figure 27a.

The graphs themselves are self-explanatory. The insert sketch in the upper right-hand corner of each shows the incidence, polarization and measurement location. The vertical scale is always linear. Because of the different scale models used, some figures have two, or even three, curves which partially overlap, and since each represents a different and independent measurement, the degree of fit provides some indication of the measurement accuracy for that particular station and frequency range.

Table 2

DATA SELECTION CHART

Station Number	EC-135 without HF wires				EC-135 with HF wires			
	Symmetric		Antisymmetric		Symmetric		Antisymmetric	
	J	Q	J	Q	J	Q	J	Q
F400T	8a, b				9a, b			
F800T	10a, b		26a, b		11a, b		27a, b	
F1200T	12a, b				13a, b			
F400B	14a				15a			
F800B	16a		28a		17a		29a	
F1200B	18a				19a			
W600T			22a, b				23a, b	
W800B			24a				25a	
F130		20a				21a		
W940T				30a				31a

Note: Figure XXa refers to amplitude data.
Figure XXb refers to phase data.

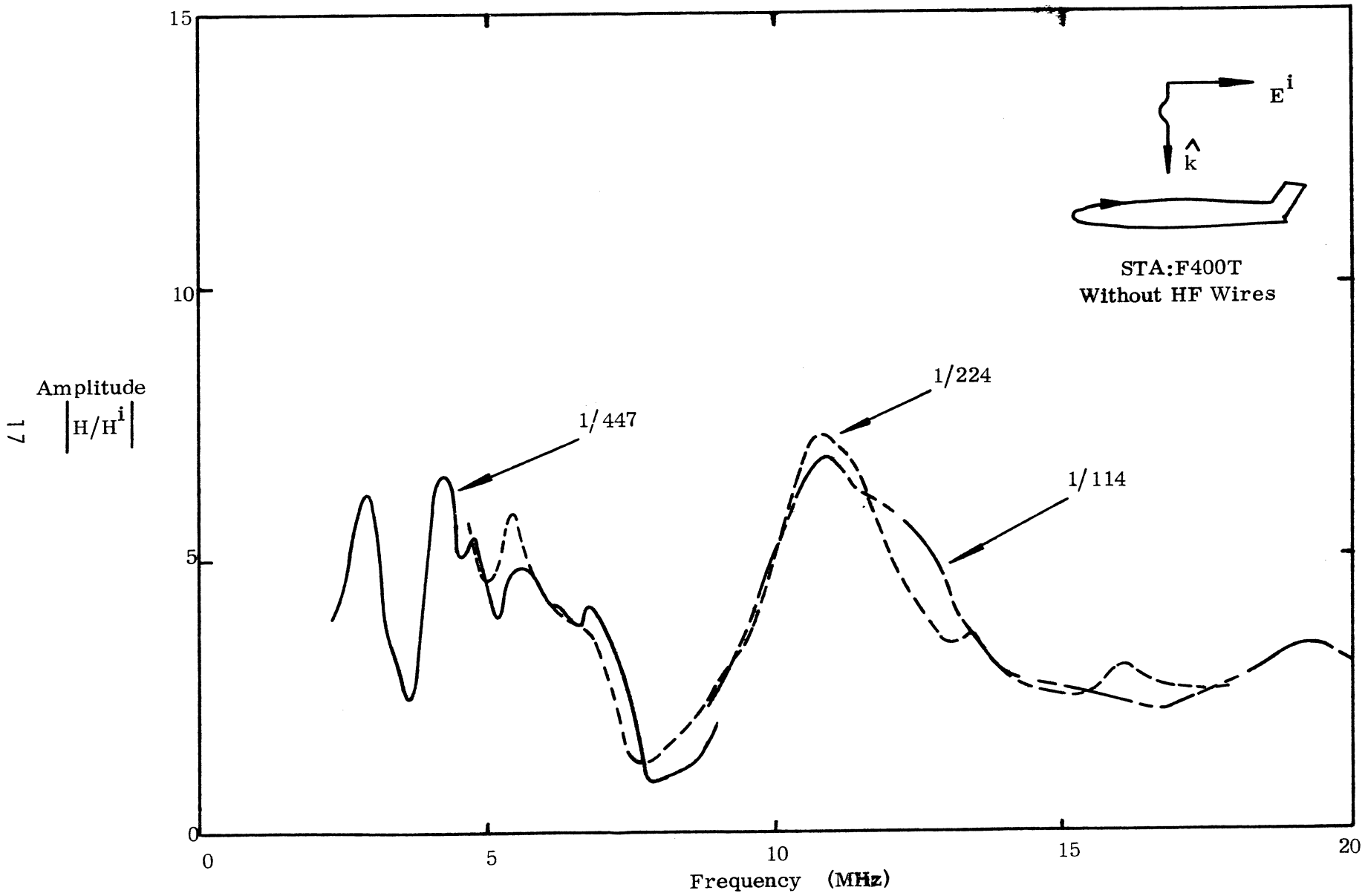

Figure 8a. Current density at STA:F400T, symmetric excitation, without HF wires.

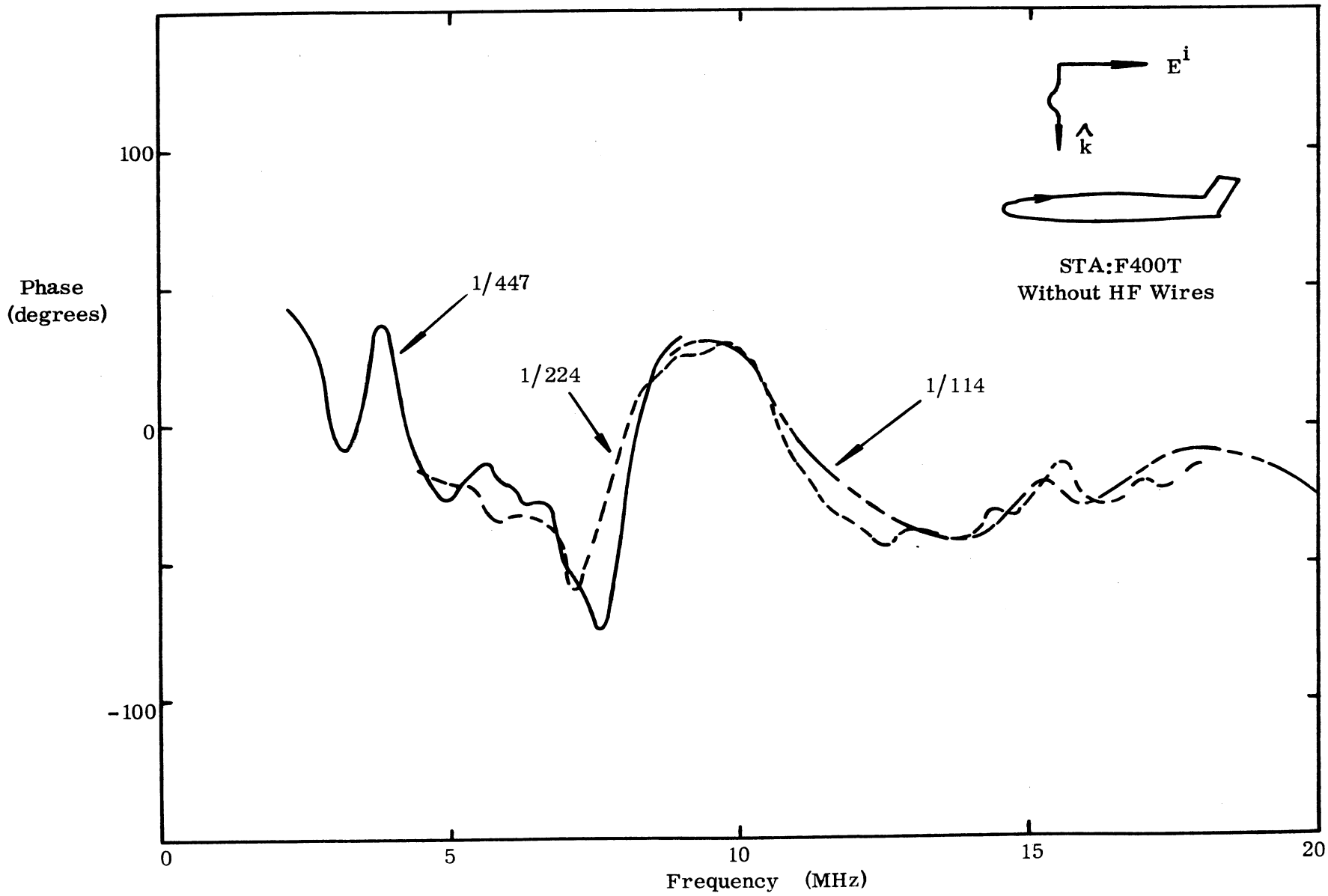

Figure 8b. Current phase at STA:F400T, symmetric excitation, without HF wires.

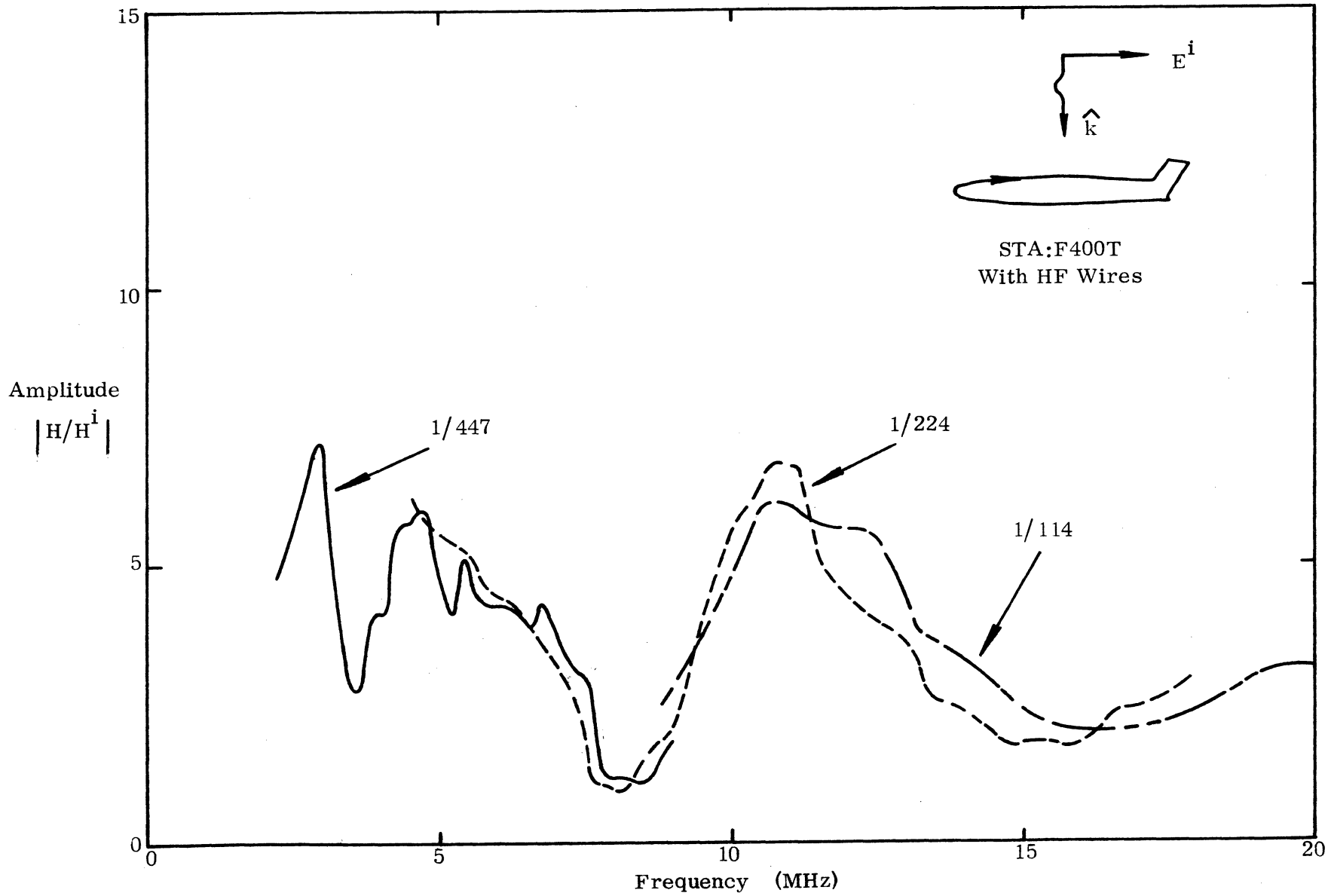

Figure 9a. Current density at STA:F400T, symmetric excitation, with HF wires.

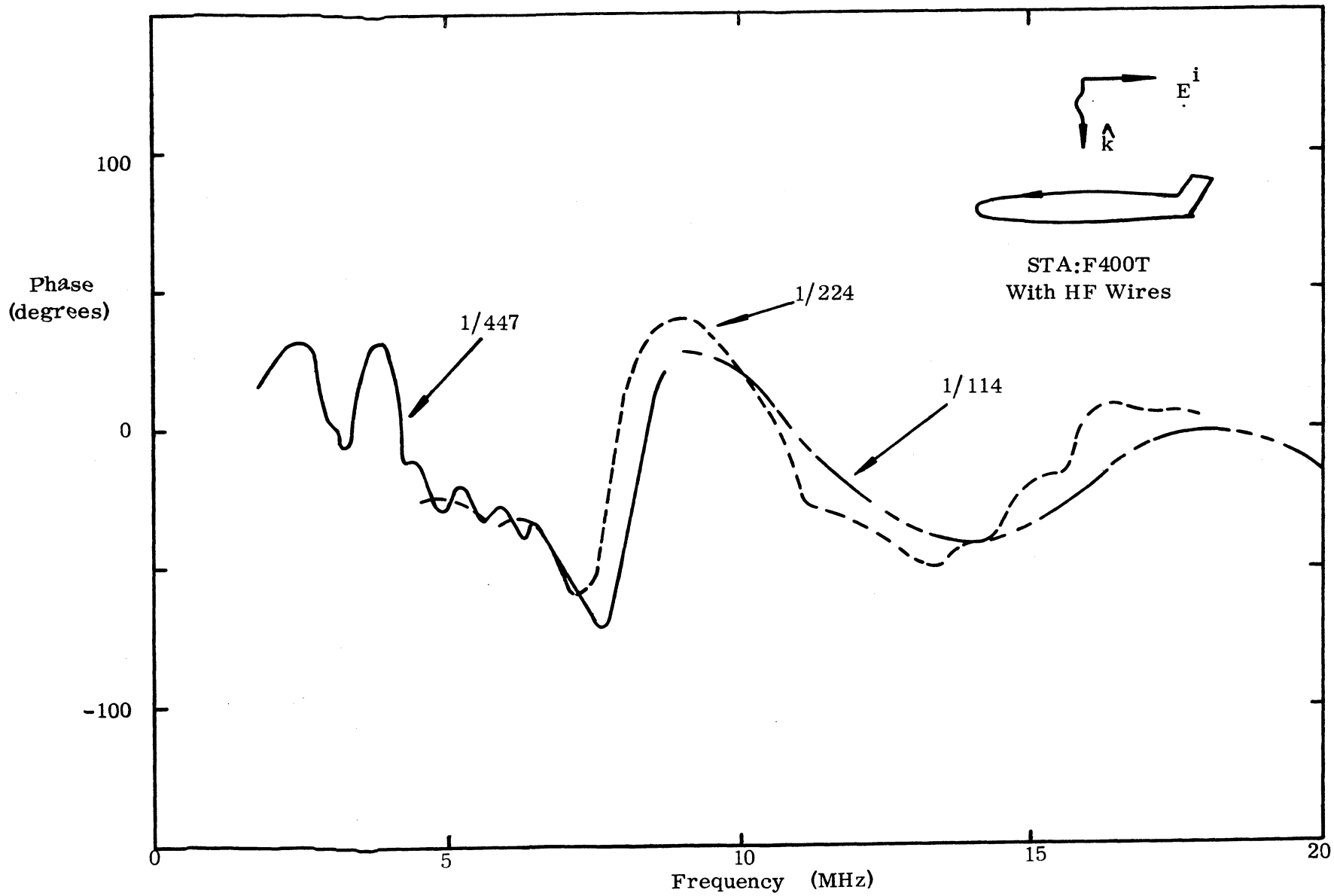

Figure 9b. Current phase at STA:F400T, symmetric excitation, with HF wires.

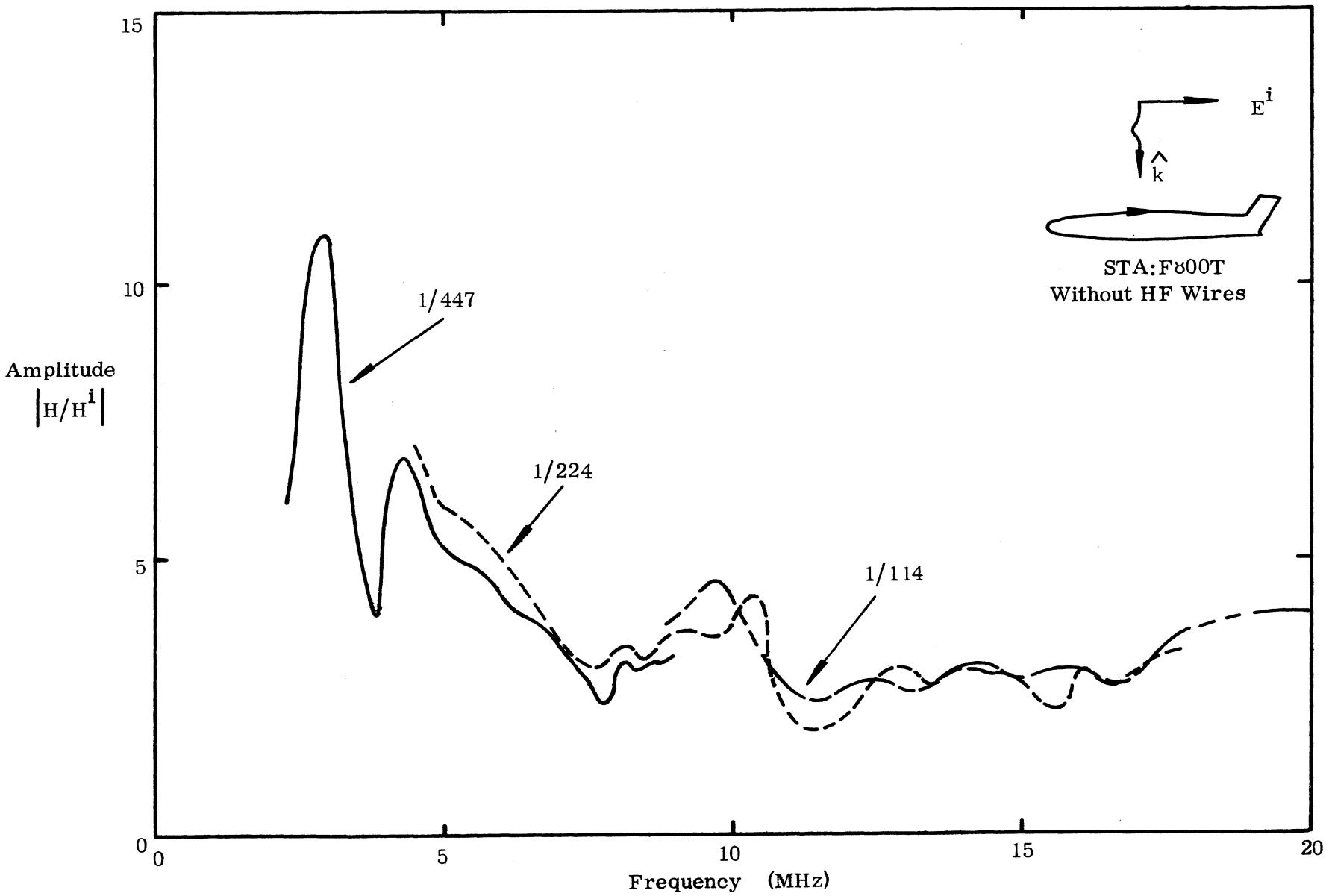

Figure 10a. Current density at STA:F800T, symmetric excitation, without HF wires.

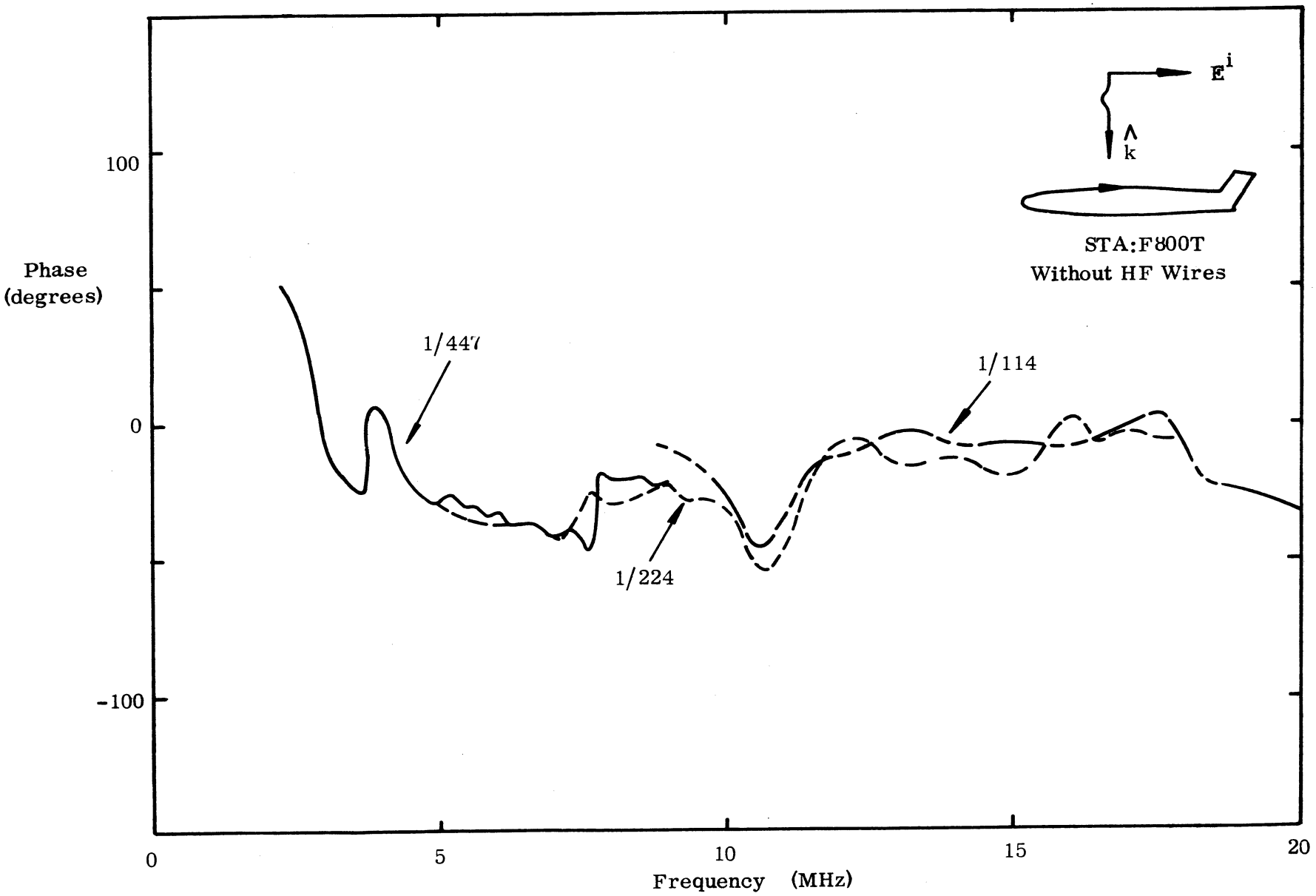

Figure 10b. Current phase at STA:F800T, symmetric excitation, without HF wires.

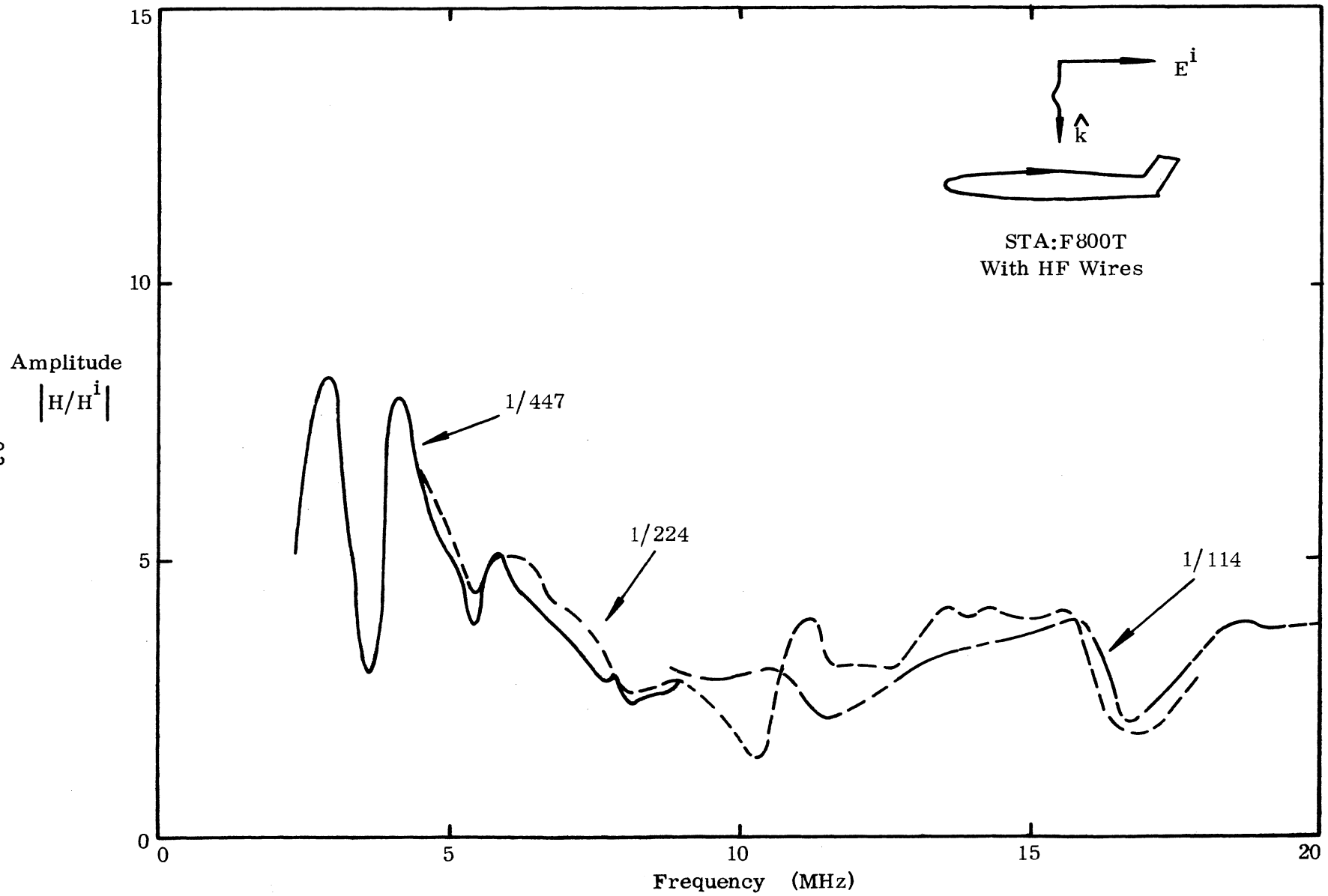

Figure 11a. Current density at STA:F800T, symmetric excitation, with HF wires.

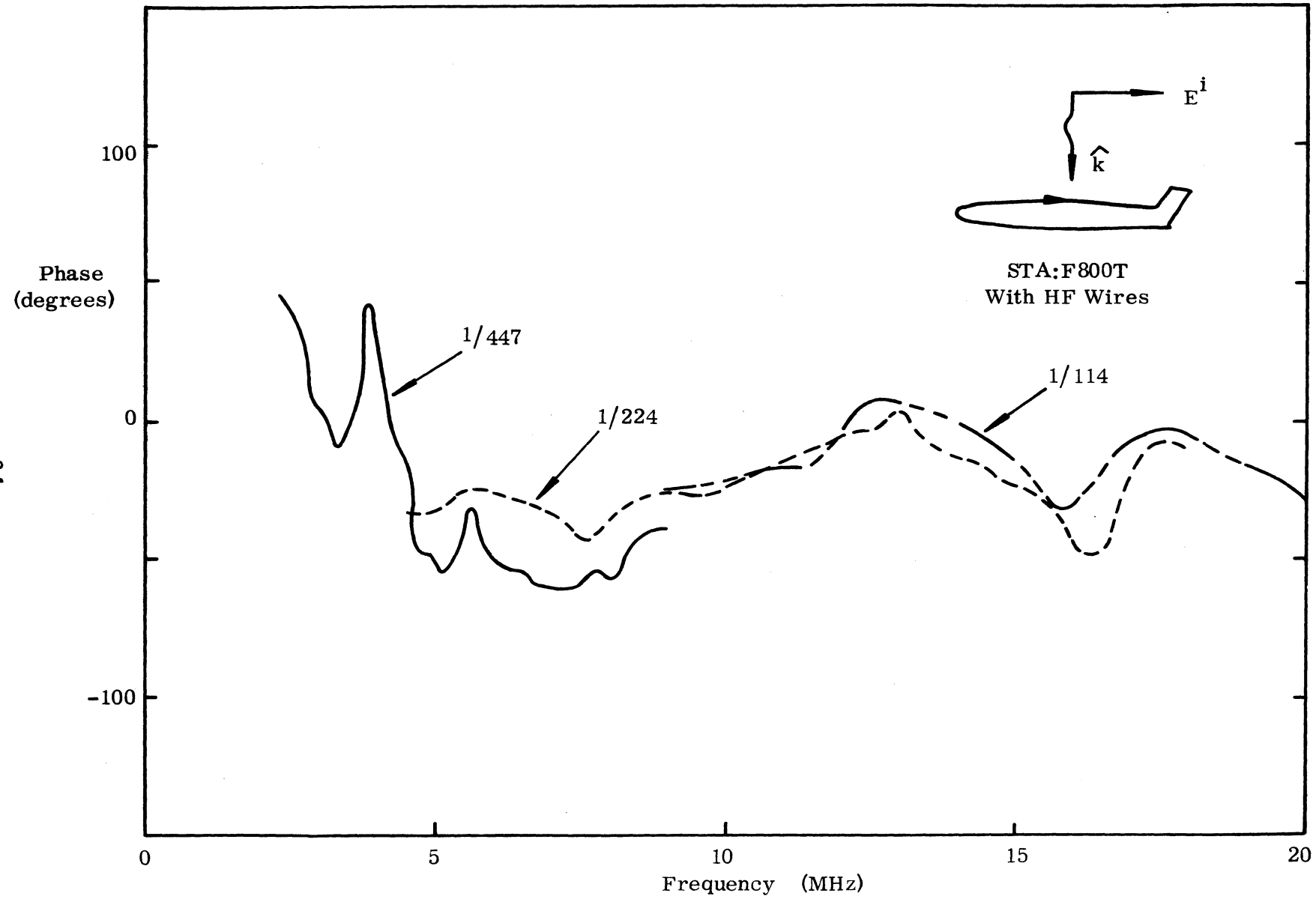

Figure 11b. Current phase at STA:F800T, symmetric excitation, with HF wires.

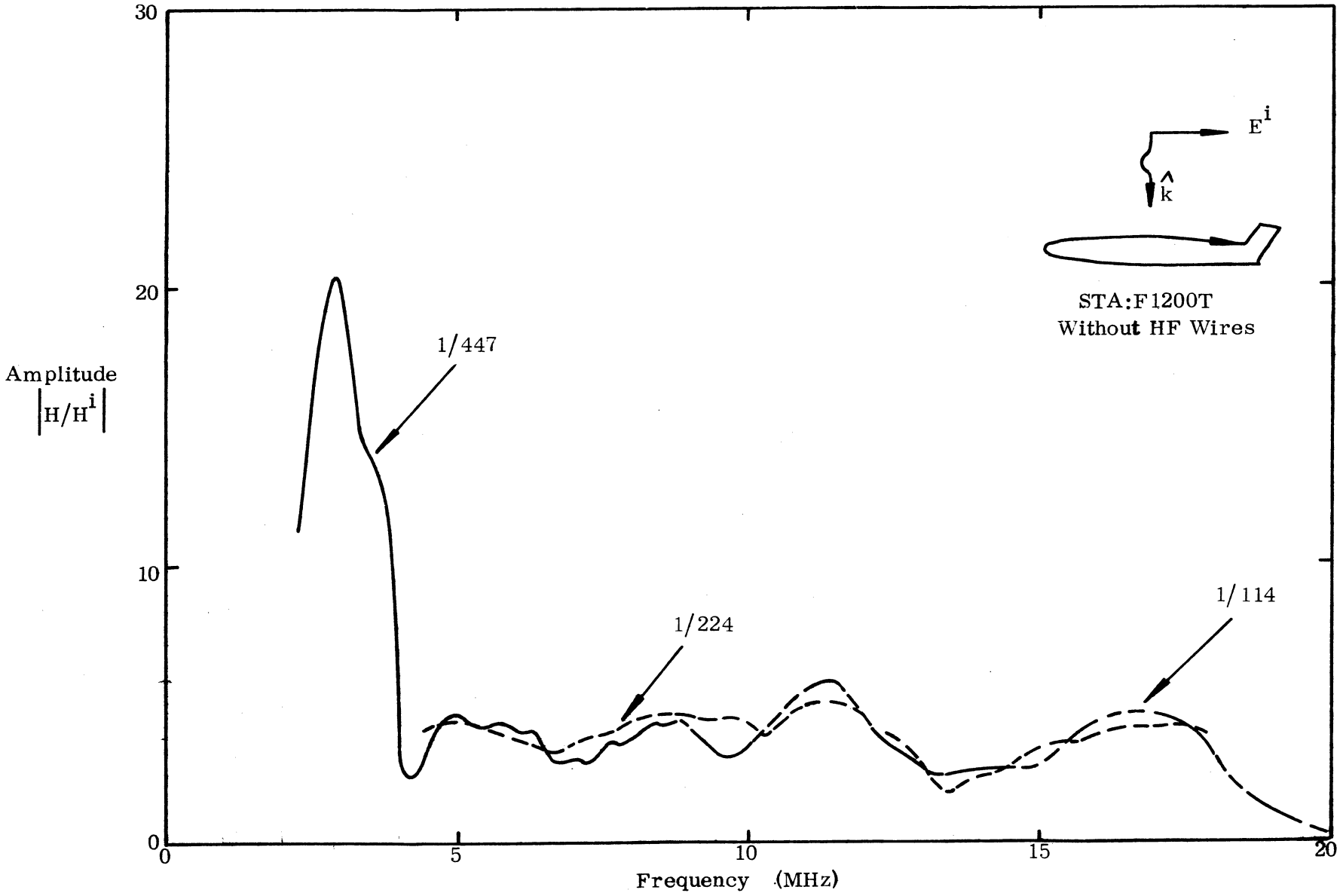

Figure 12a. Current density at STA:F1200T, symmetric excitation, without HF wires.

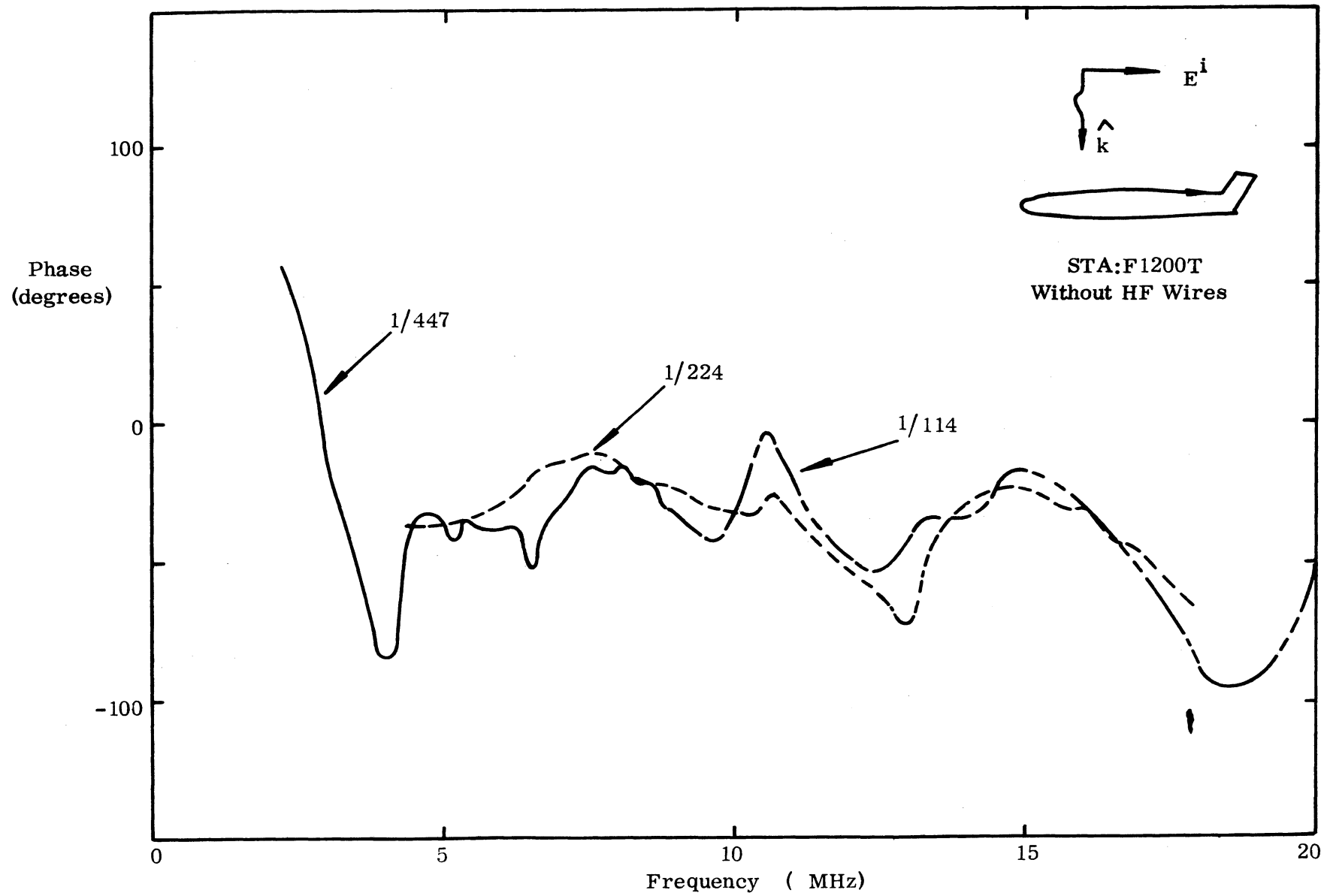

Figure 12b. Current phase at STA:F1200T, symmetric excitation, without HF wires.

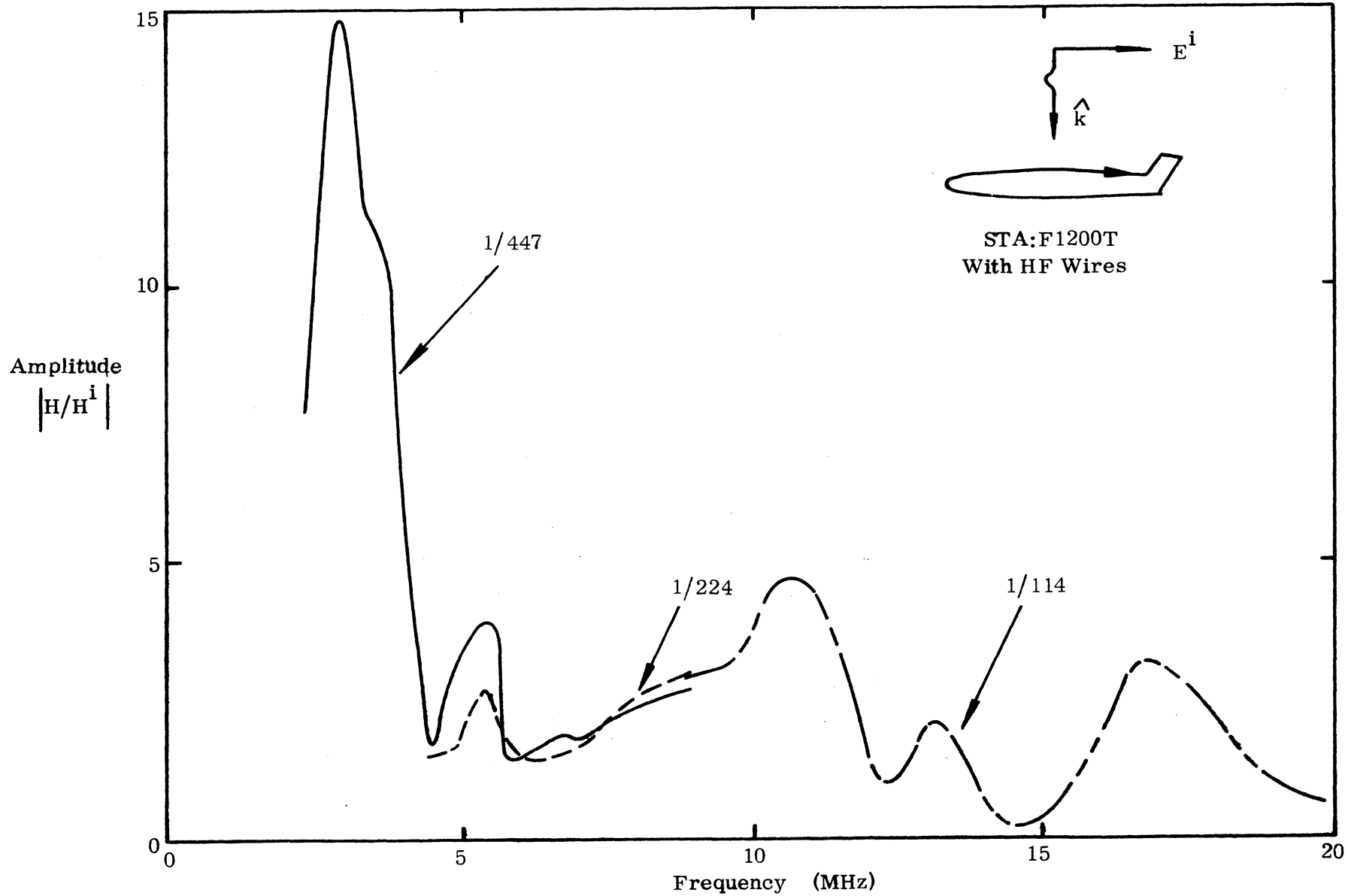

Figure 13a. Current density at STA:F1200T, symmetric excitation, with HF wires.

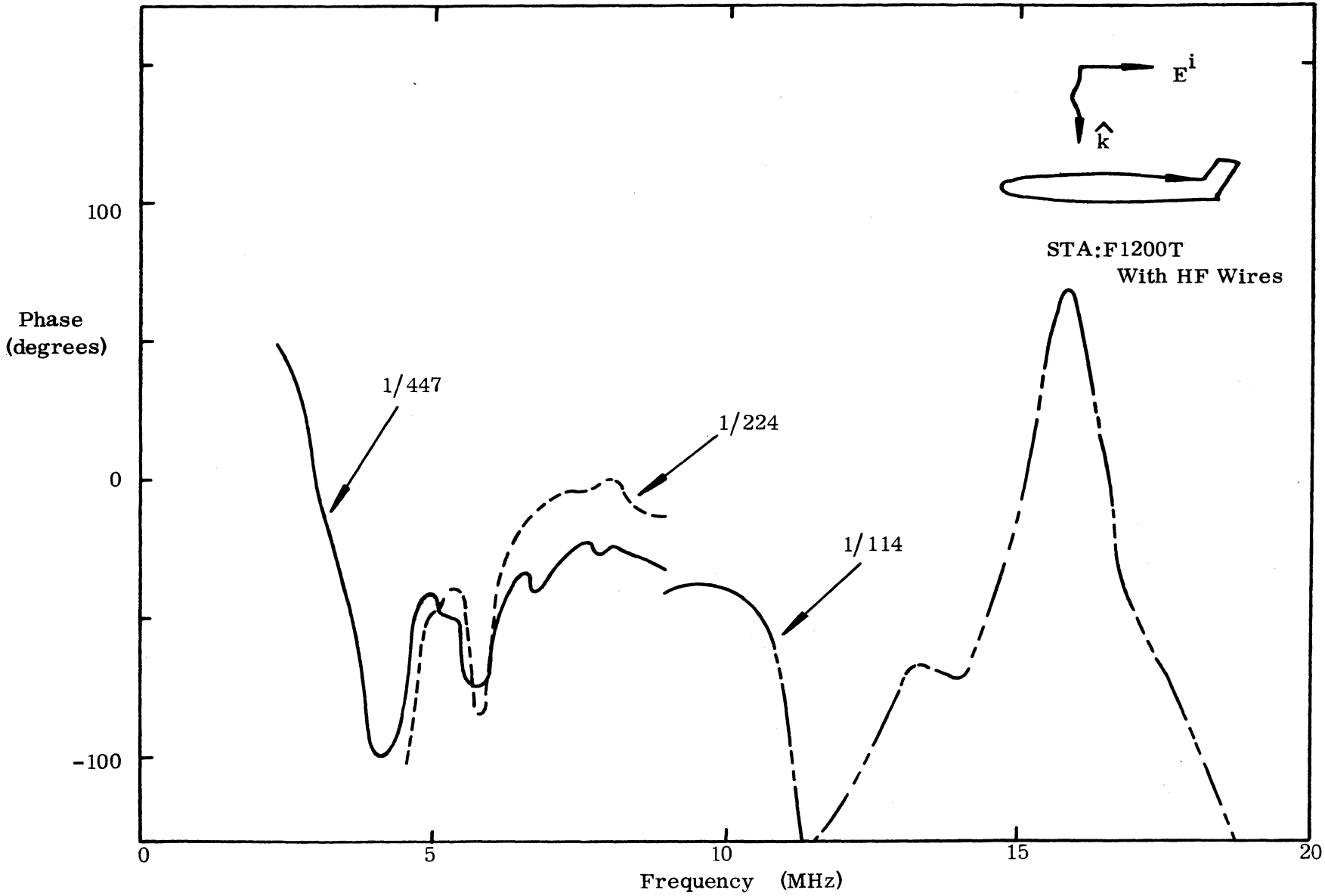

Figure 13b. Current phase at STA:F1200T, symmetric excitation, with HF wires.

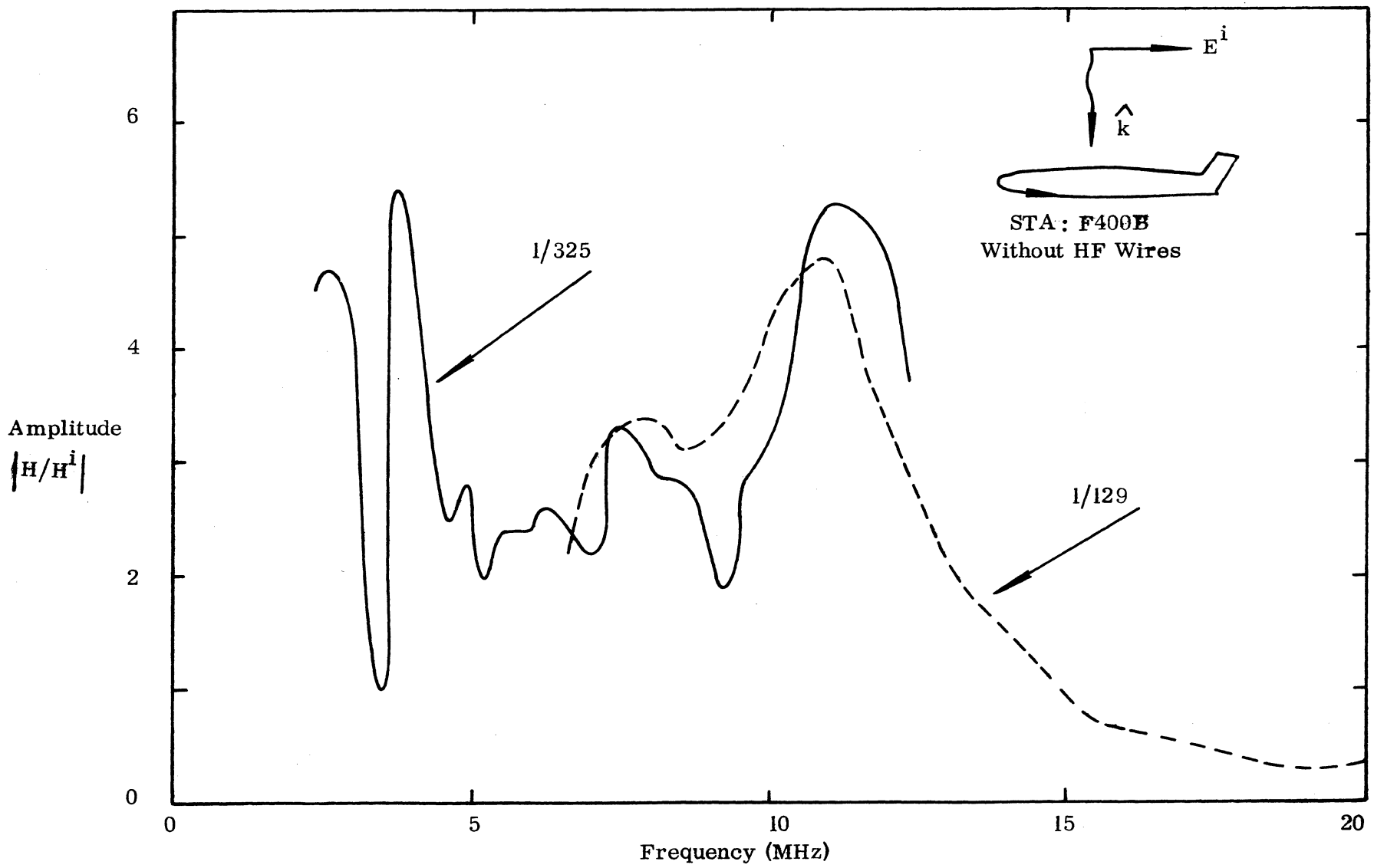

Figure 14a. Current density at STA:F400B, symmetric excitation, without HF wires.

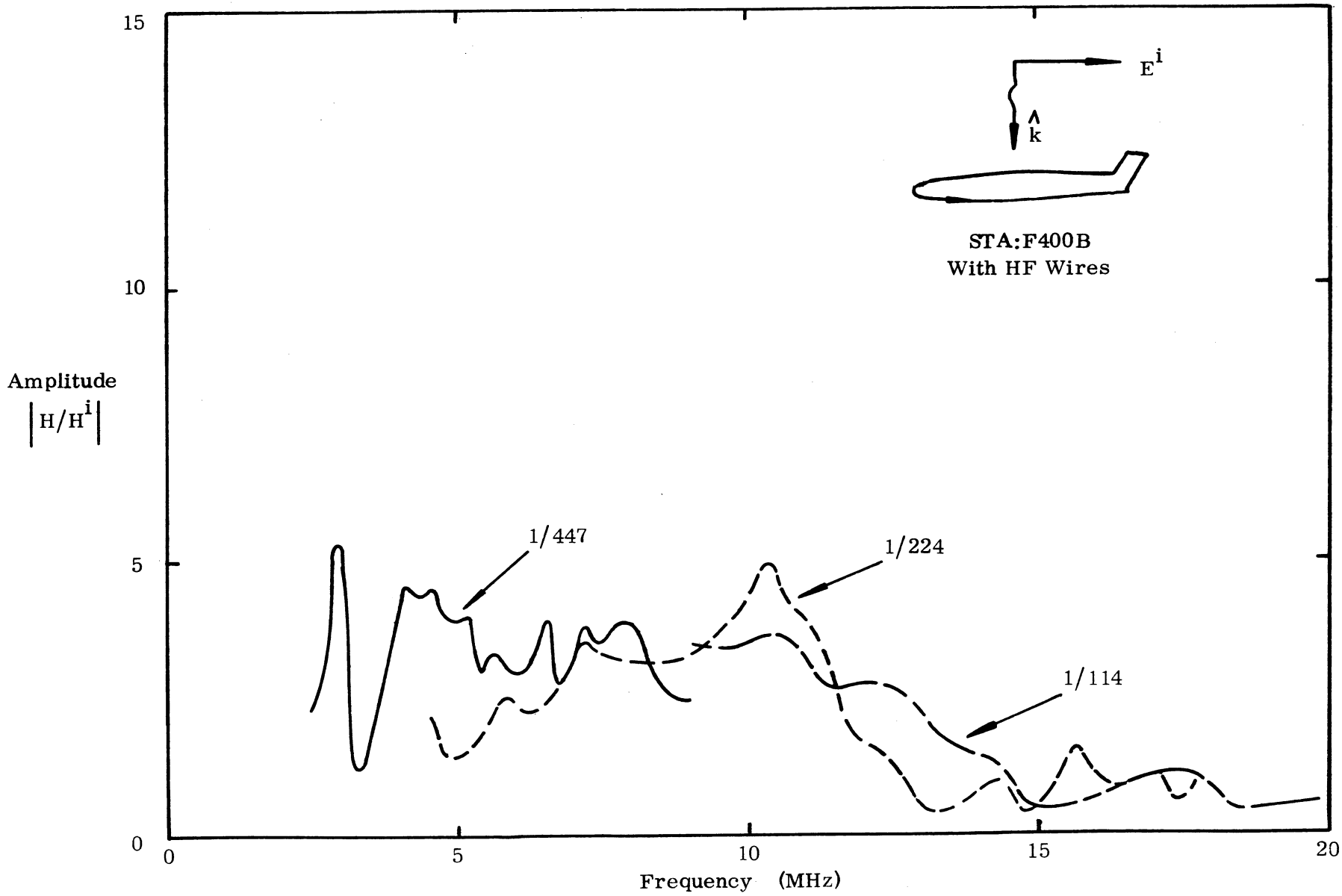

Figure 15a. Current density at STA:F400B, symmetric excitation, with HF wires.

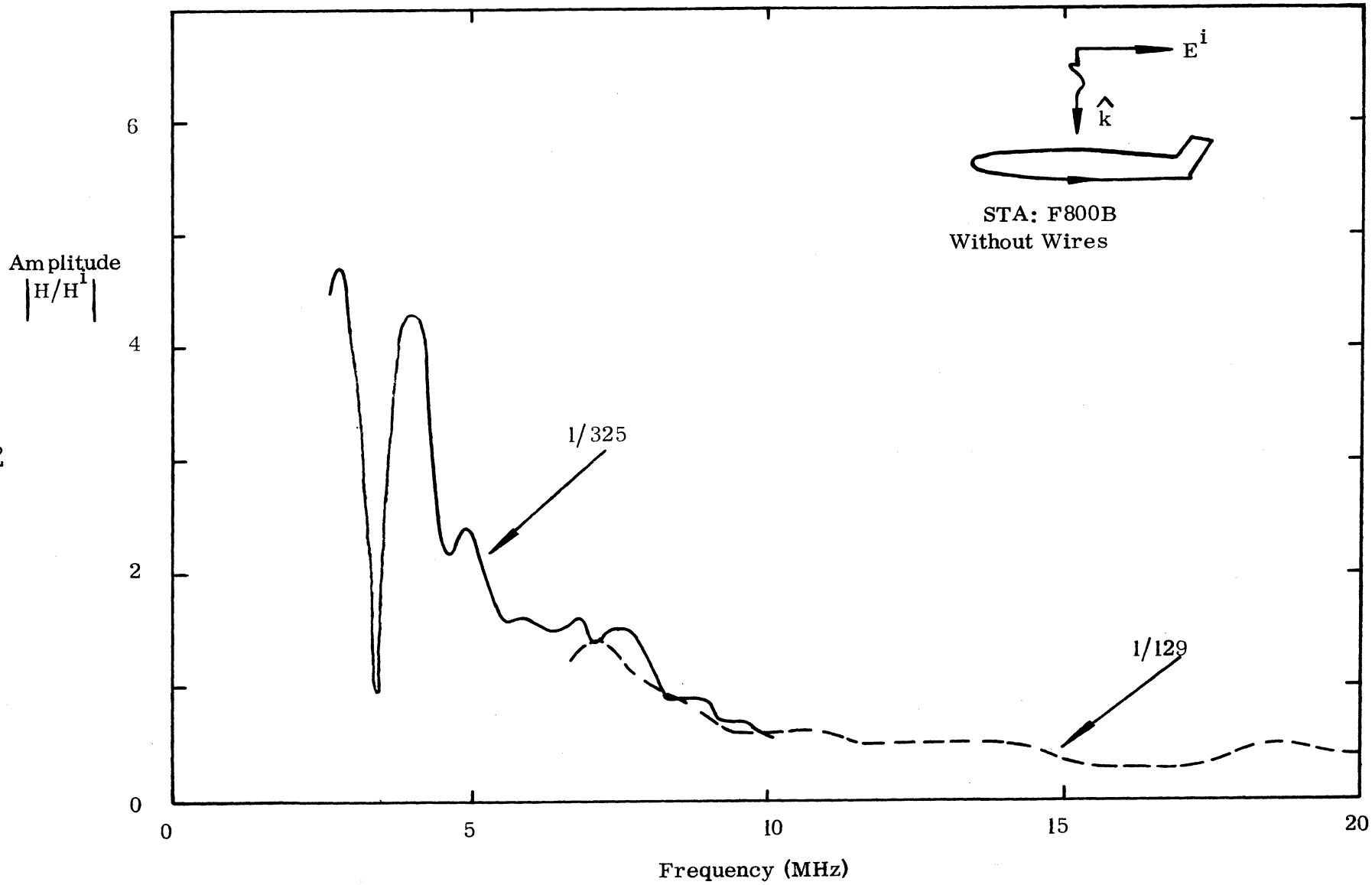

Figure 16a. Current density at STA:F800B, symmetric excitation, without HF wires.

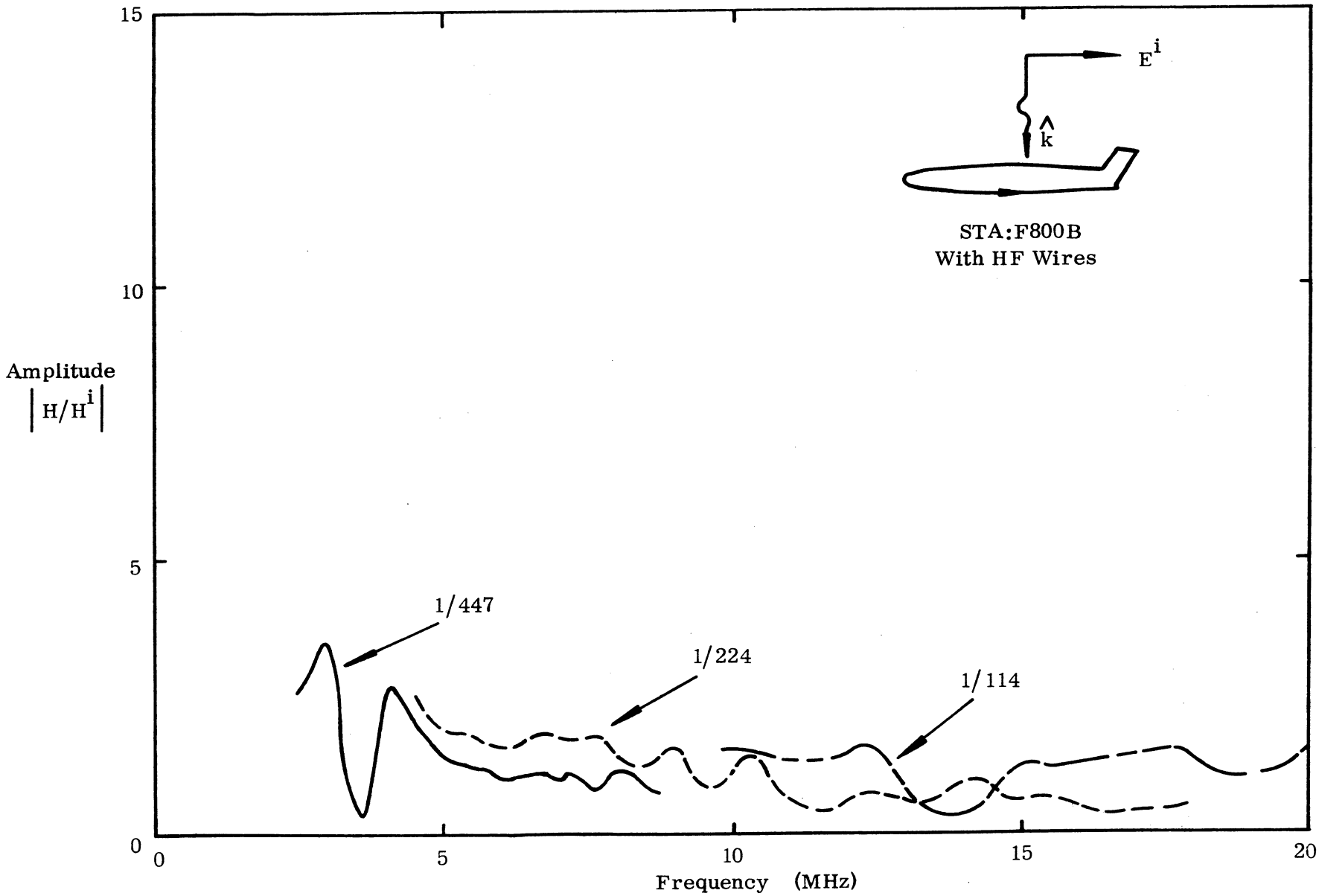

Figure 17a. Current density at STA:F800B, symmetric excitation, with HF wires.

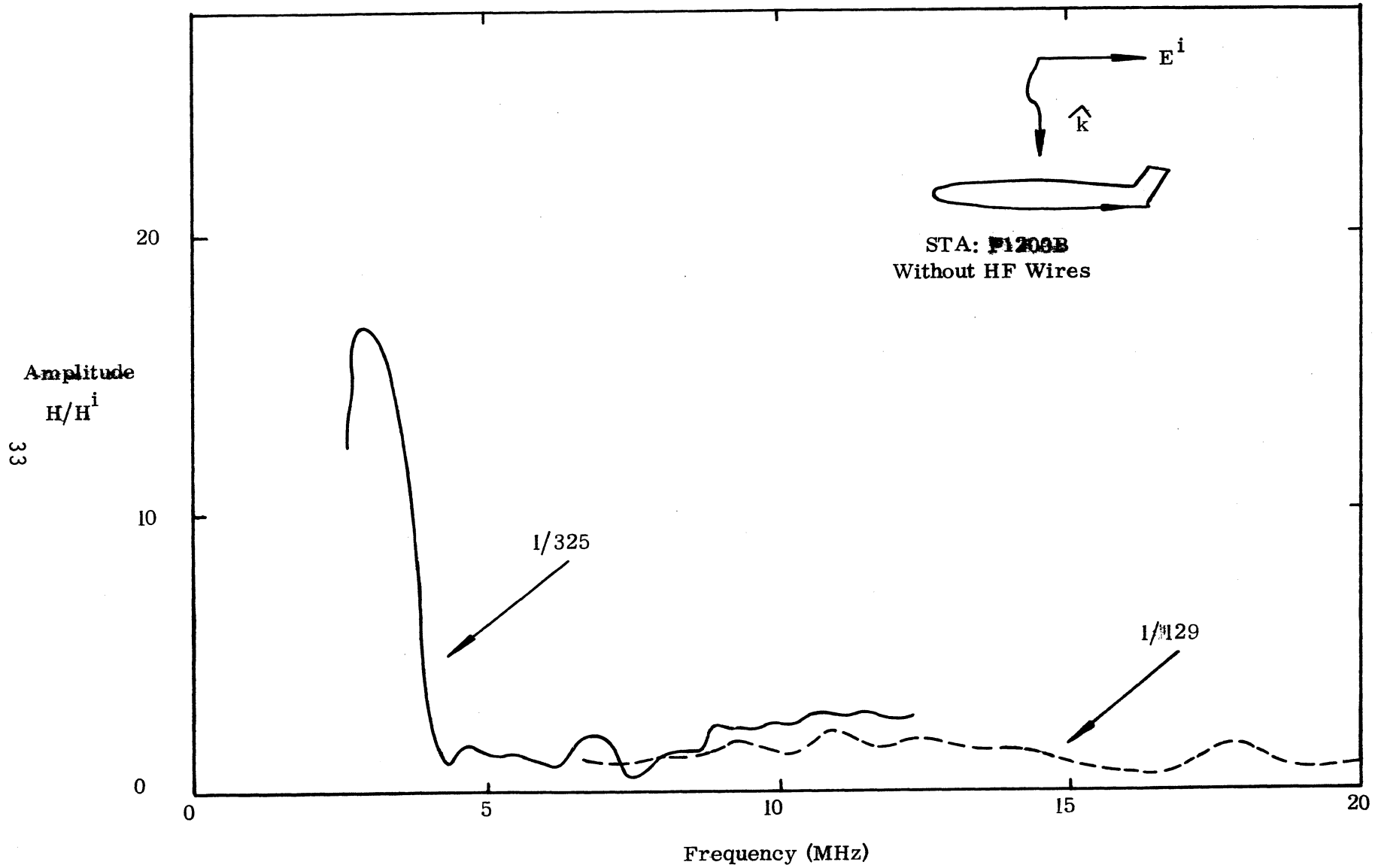

Figure 18a. Current density at STA:F1200B, symmetric excitation, without HF wires.

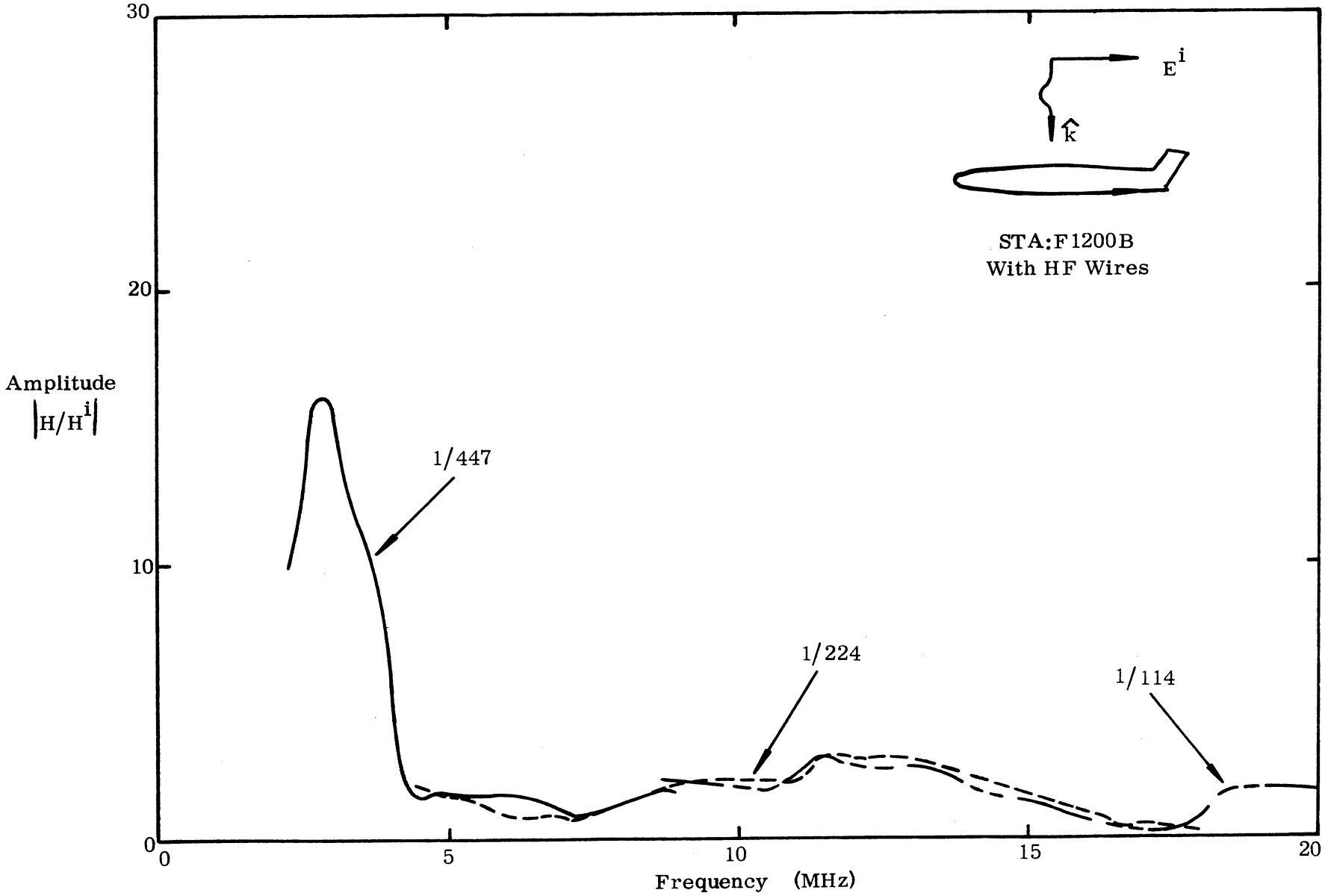

Figure 19a. Current density at STA:F1200B, symmetric excitation, with HF wires.

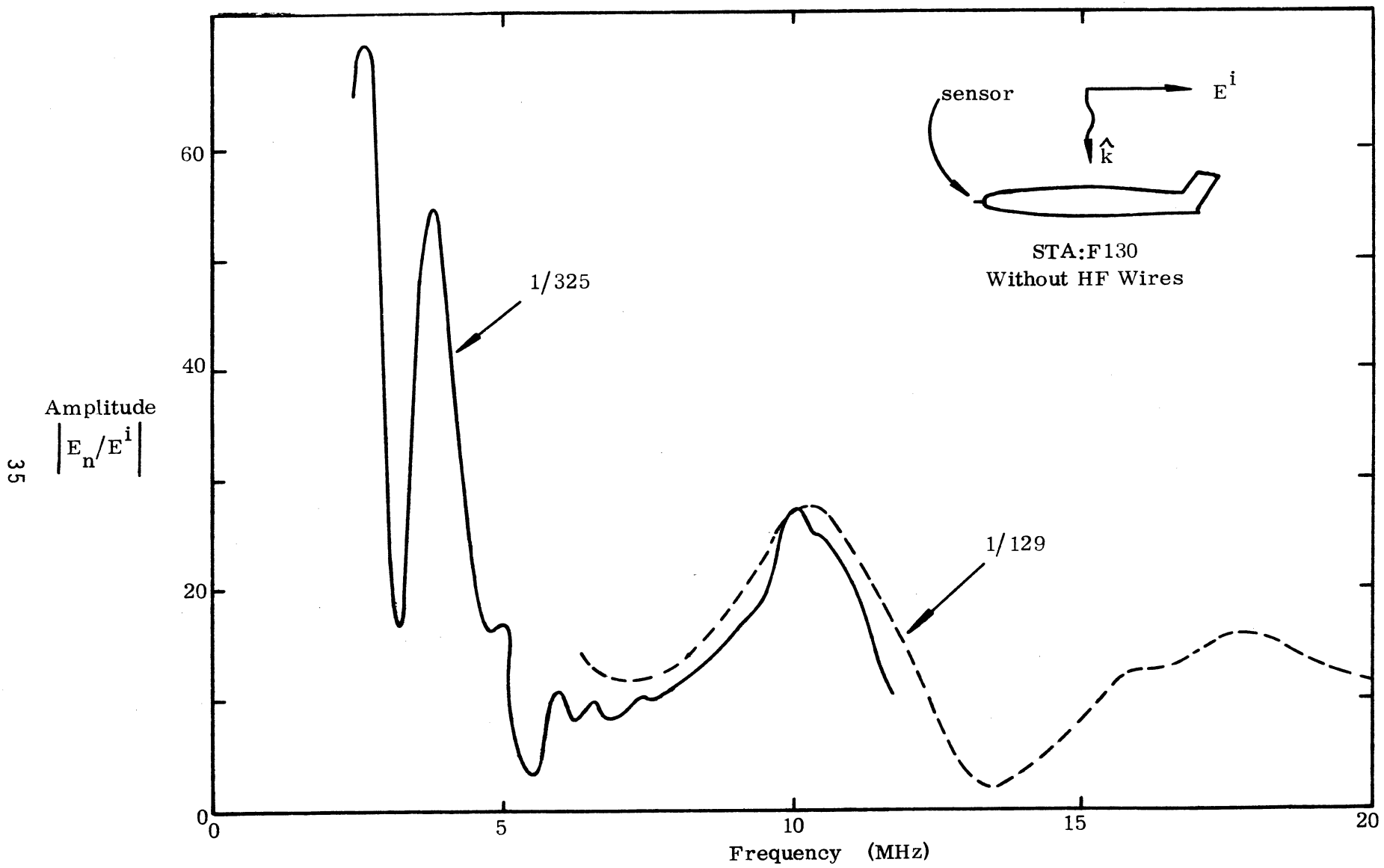

Figure 20a. Charge density at STA:F130, symmetric excitation, without HF wires.

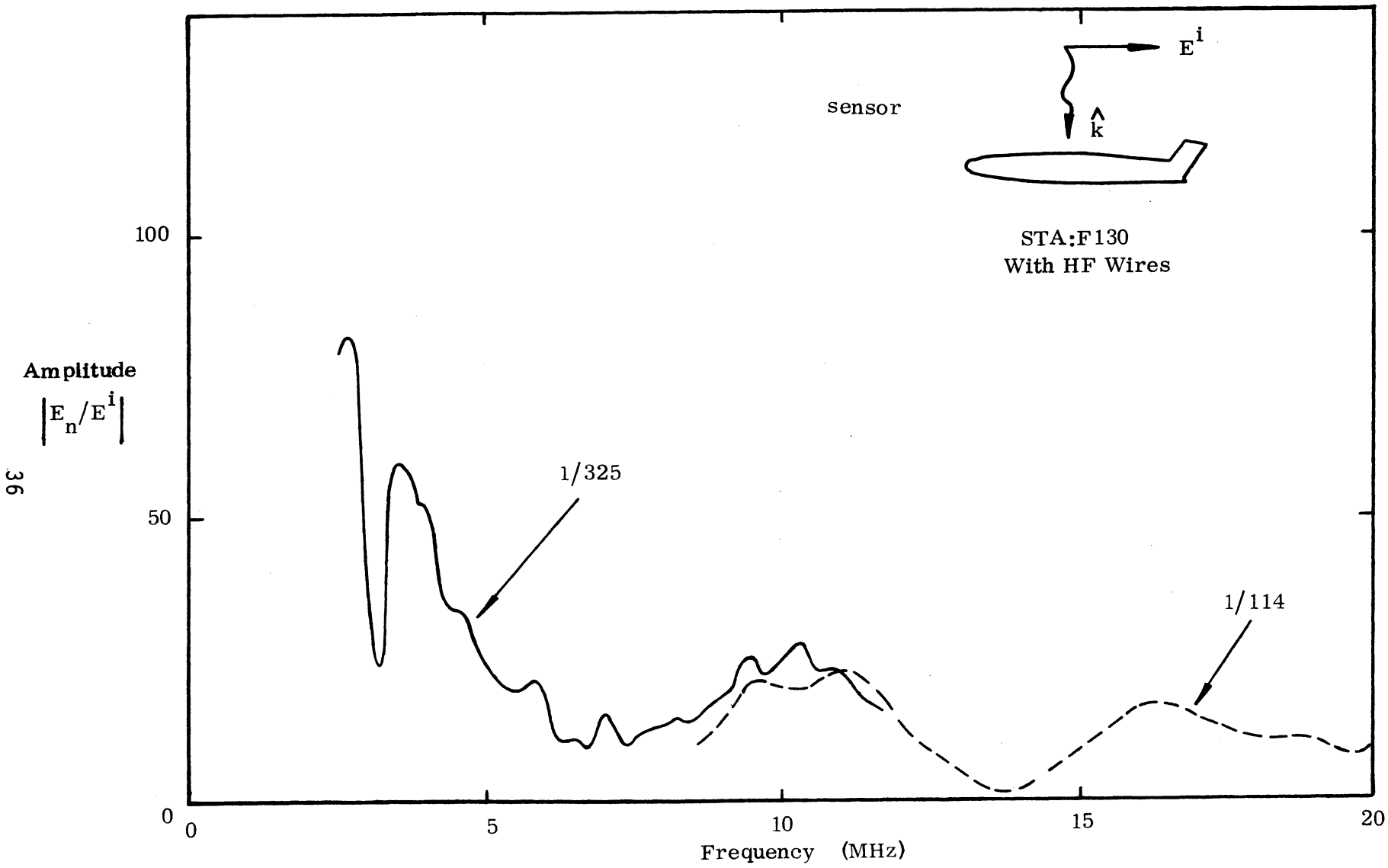

Figure 21a. Charge density at STA:F130, symmetric excitation, with HF wires.

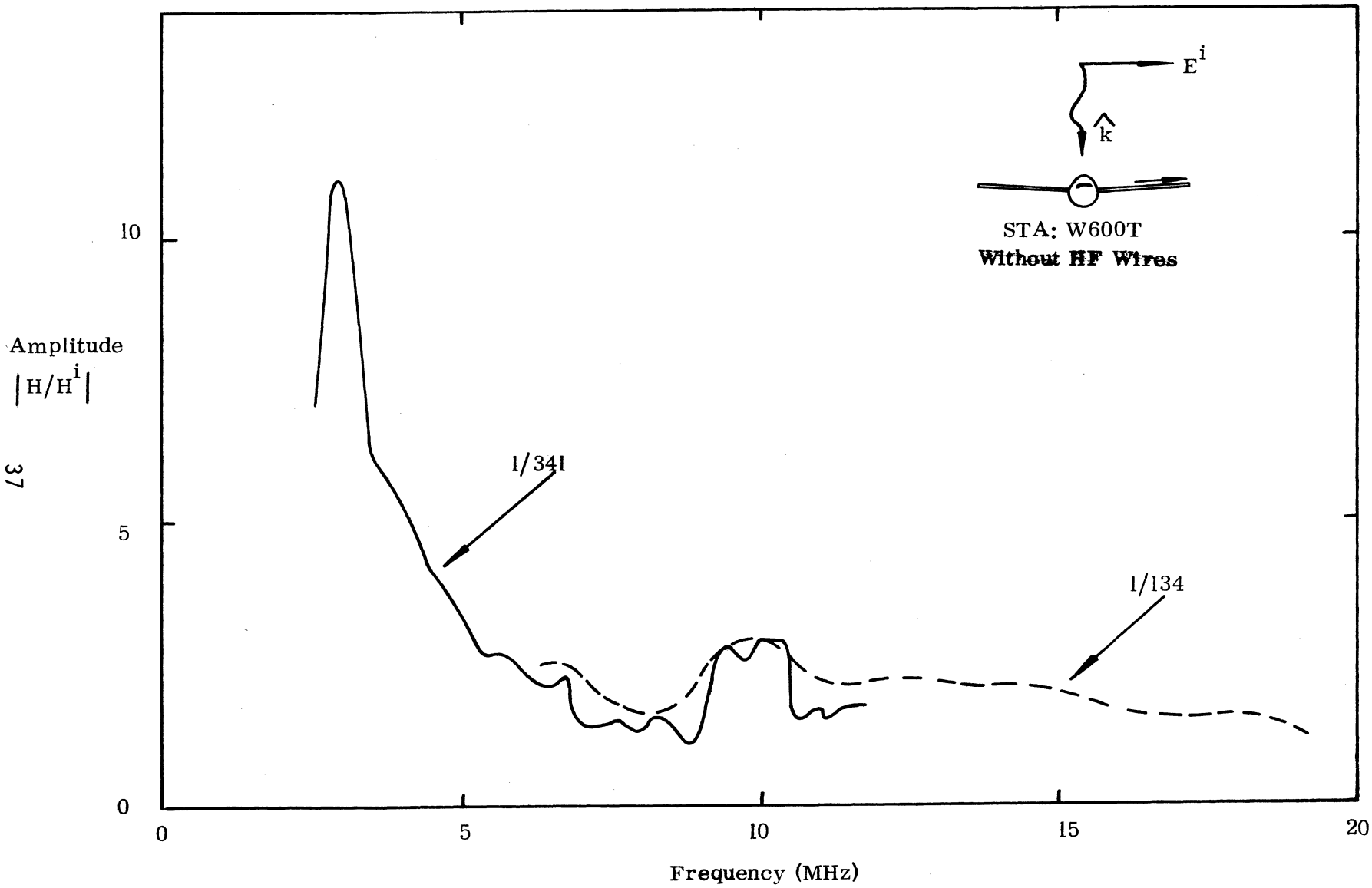

Figure 22a. Current density at STA:W600T, anti-symmetric excitation, without HF wires.

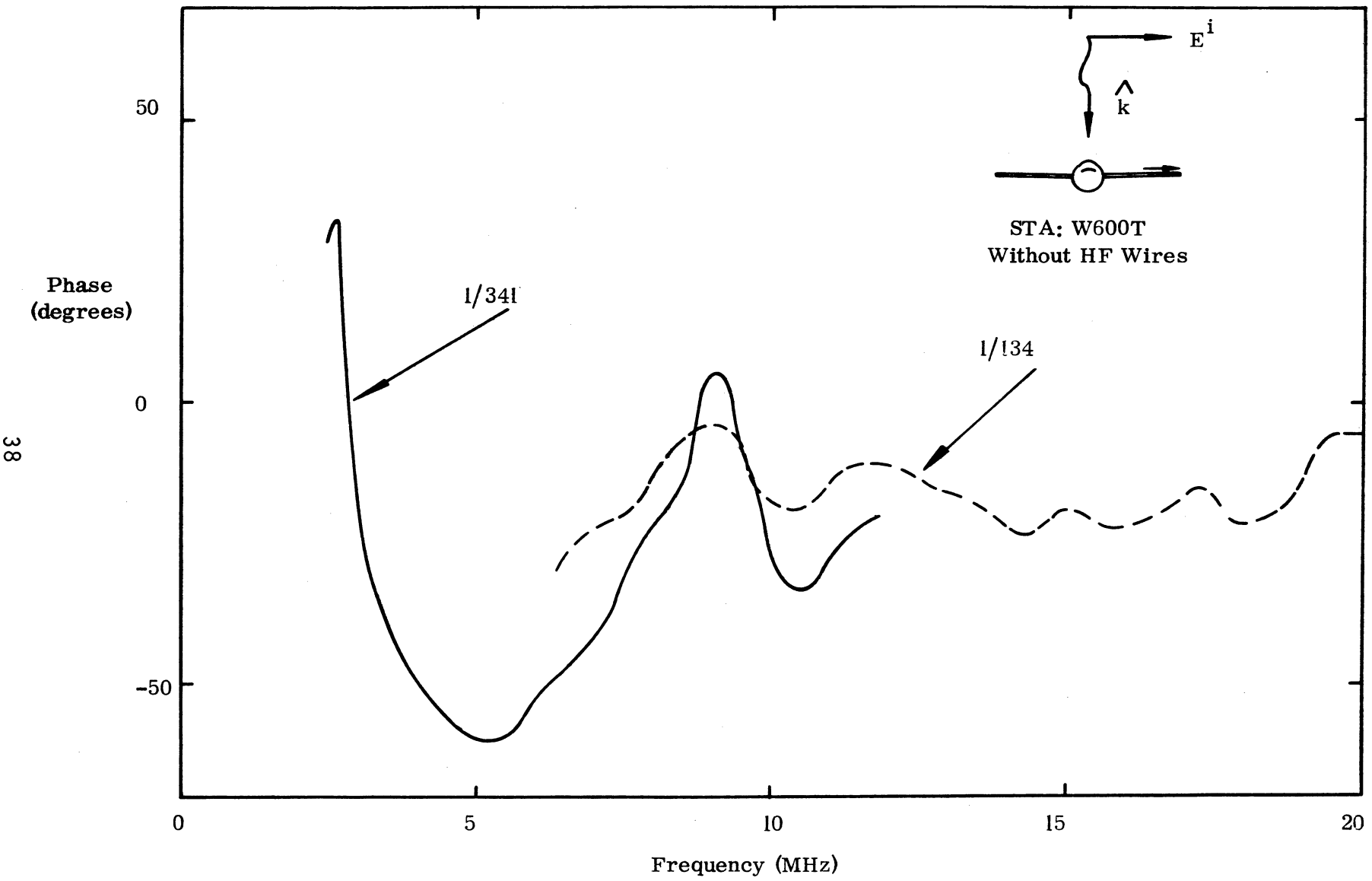

Figure 22b. Current phase at STA:W600T, anti-symmetric excitation, without HF wires.

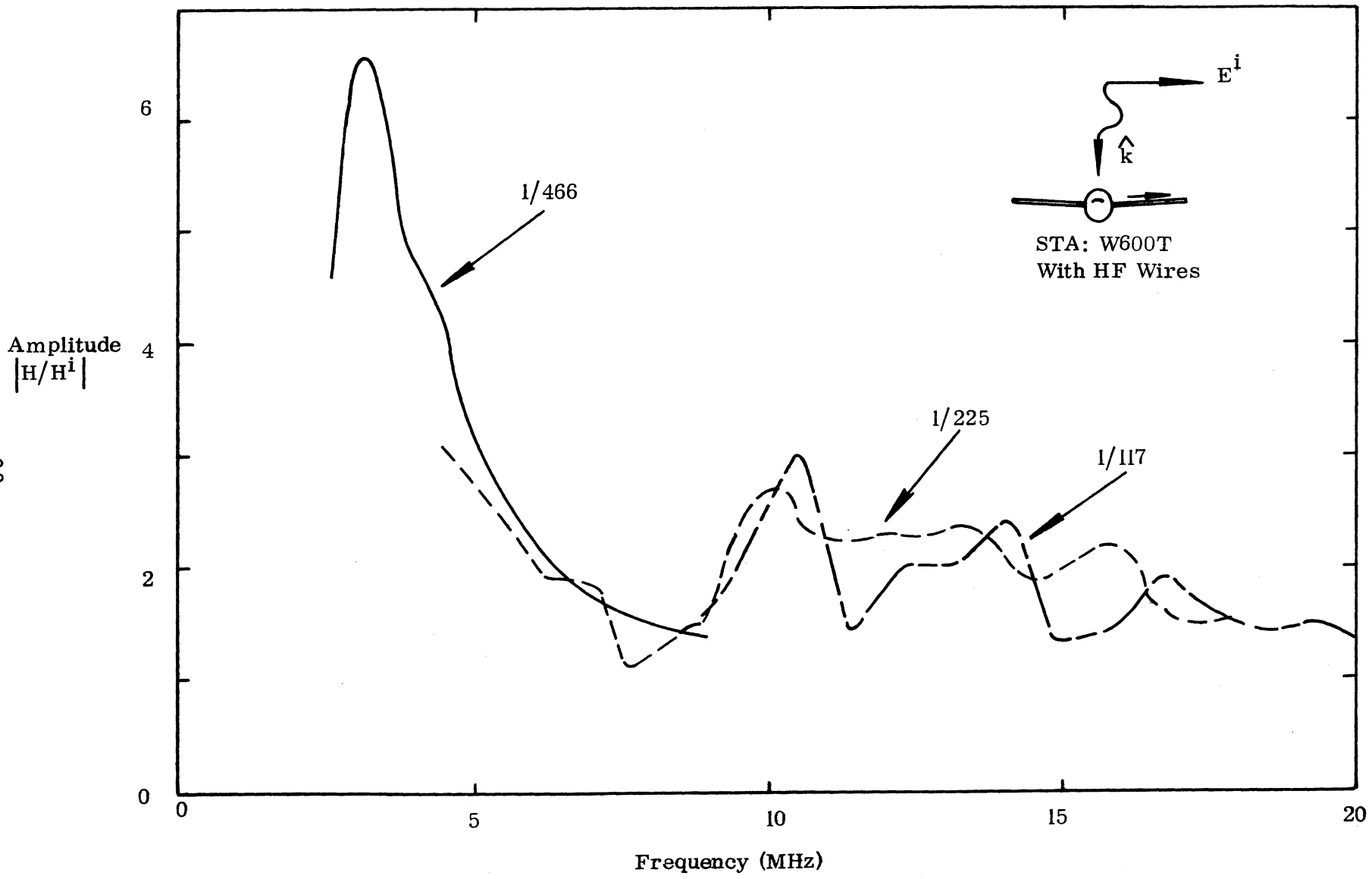

Figure 23a. Current density at STA:W600T, anti-symmetric excitation, with HF wires.

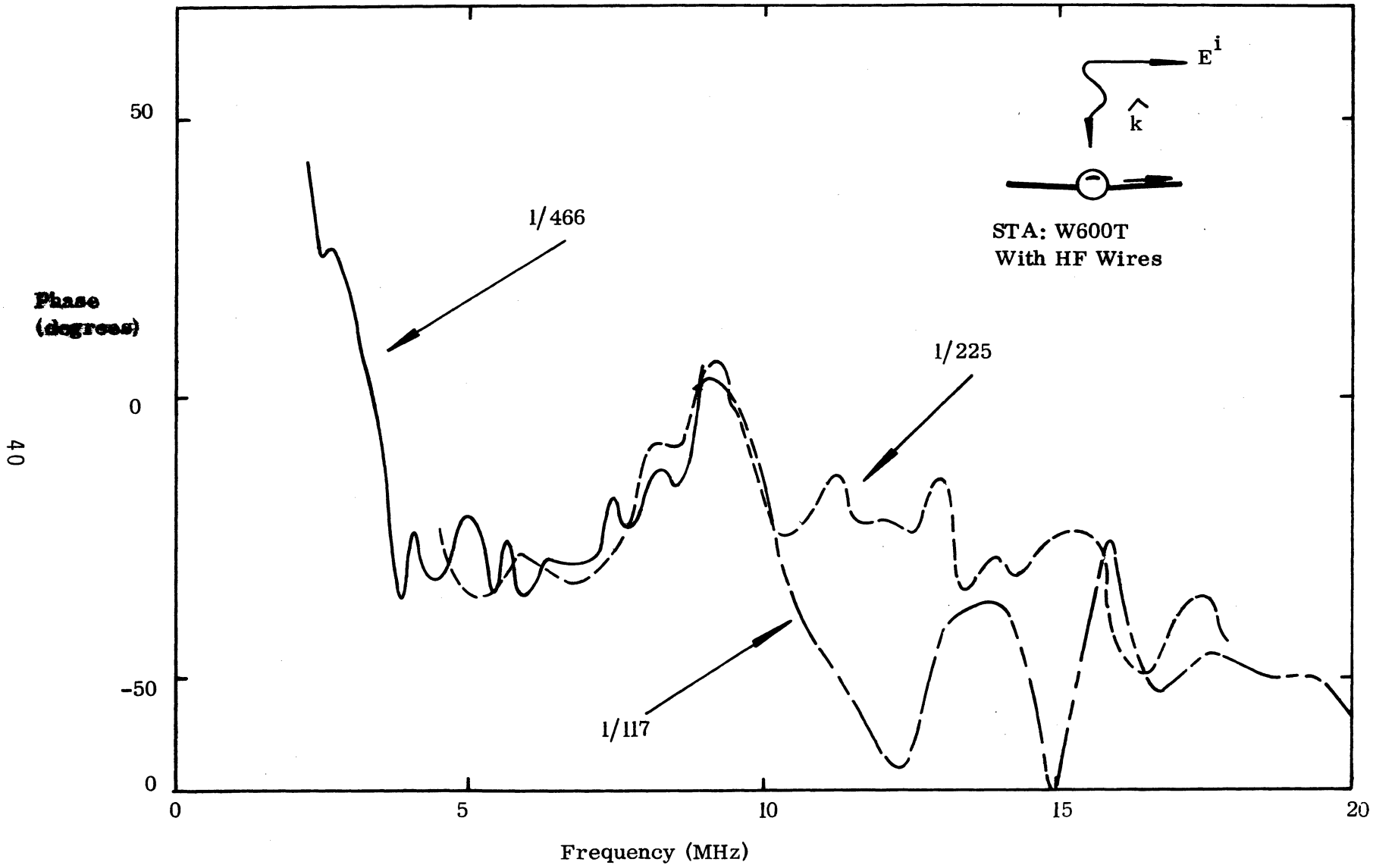

Figure 23b. Current phase at STA:W600T, anti-symmetric excitation, with HF wires.

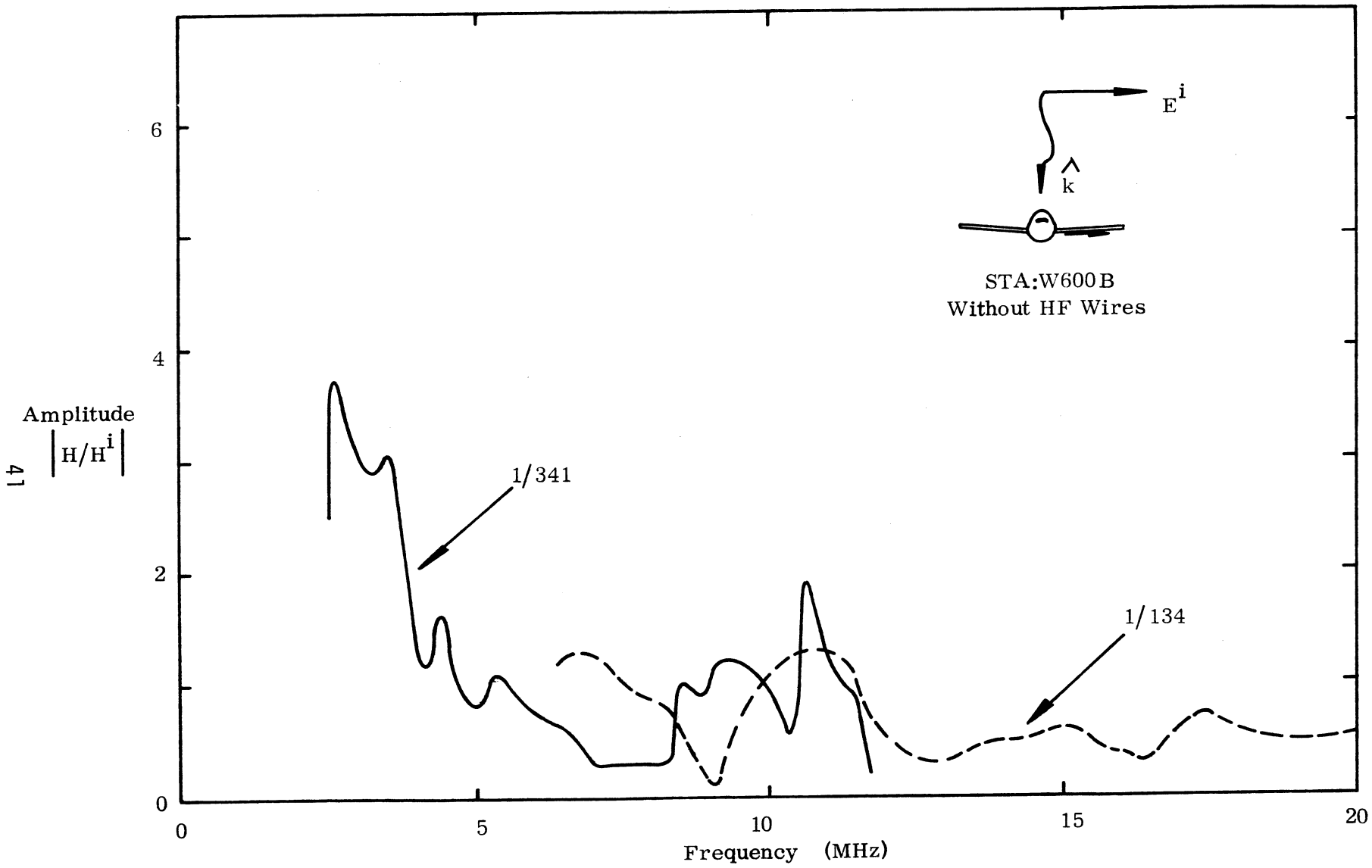

Figure 24a. Current density at STA:W600B, anti-symmetric excitation, without HF wires.

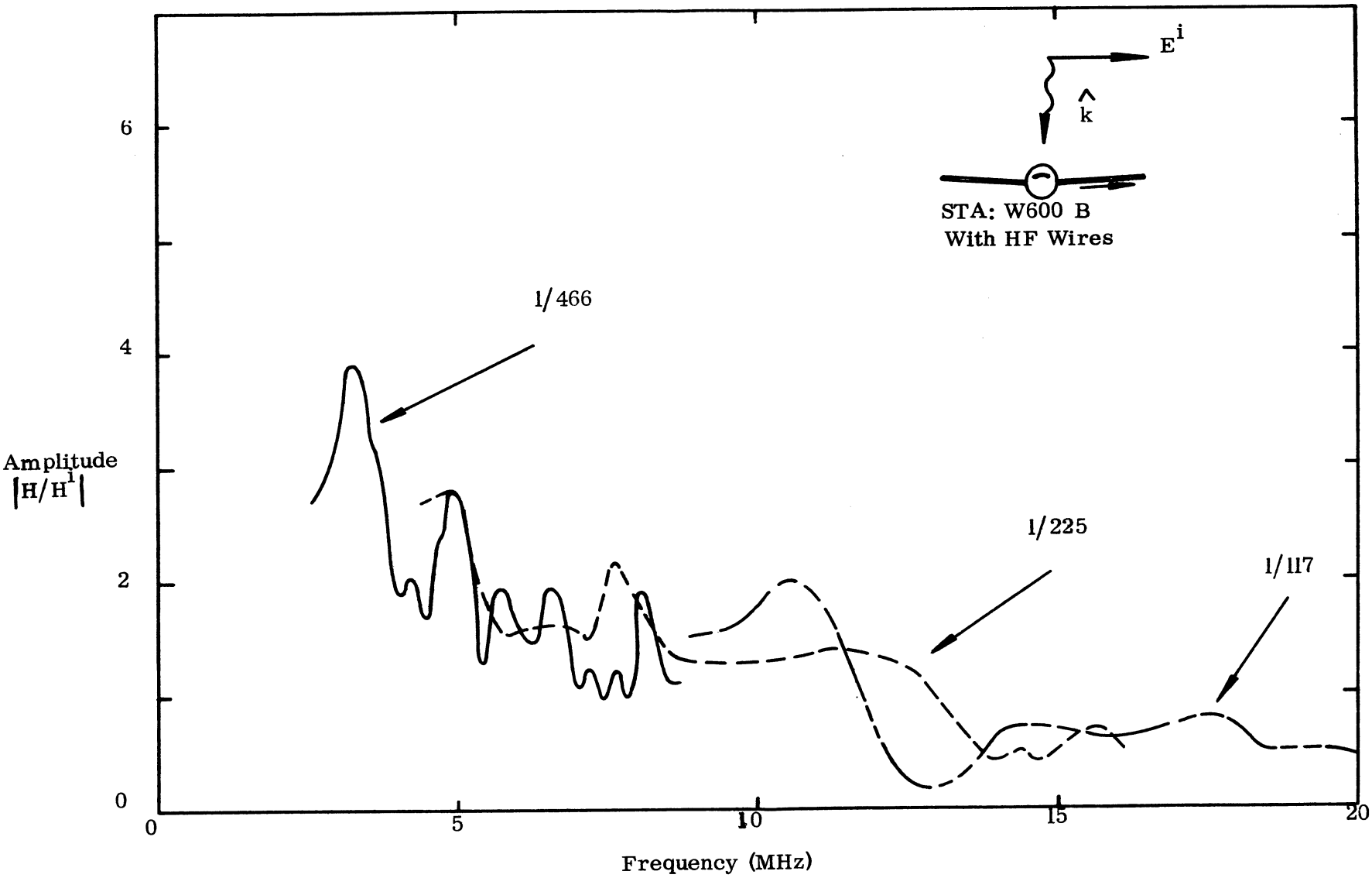

Figure 25a. Current density at STA:W600B, anti-symmetric excitation, with HF wires.

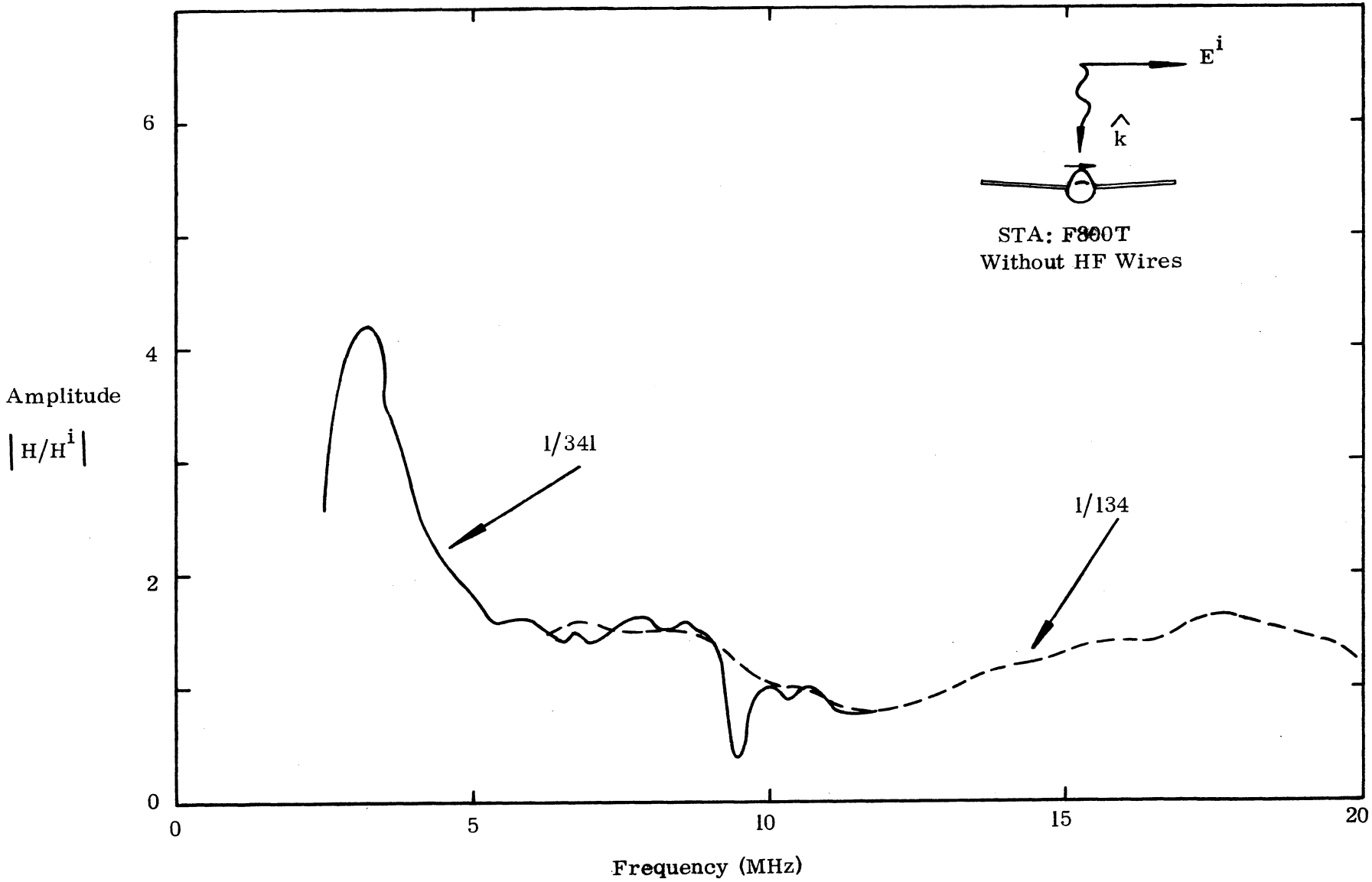

Figure 26a. Current density at STA:F800T, anti-symmetric excitation, without HF wires.

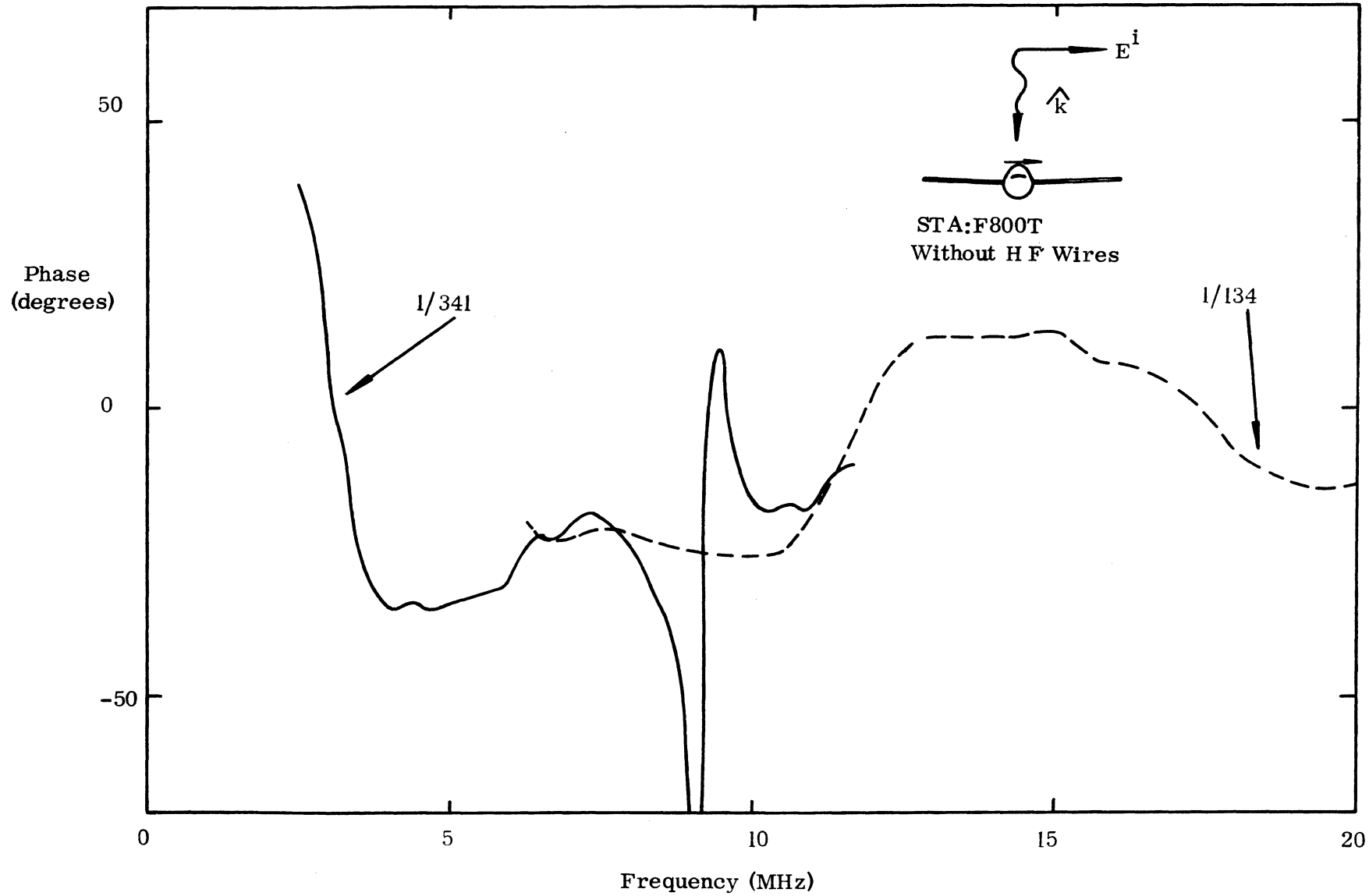

Figure 26b. Current phase at STA:F800T, anti-symmetric excitation, without HF wires.

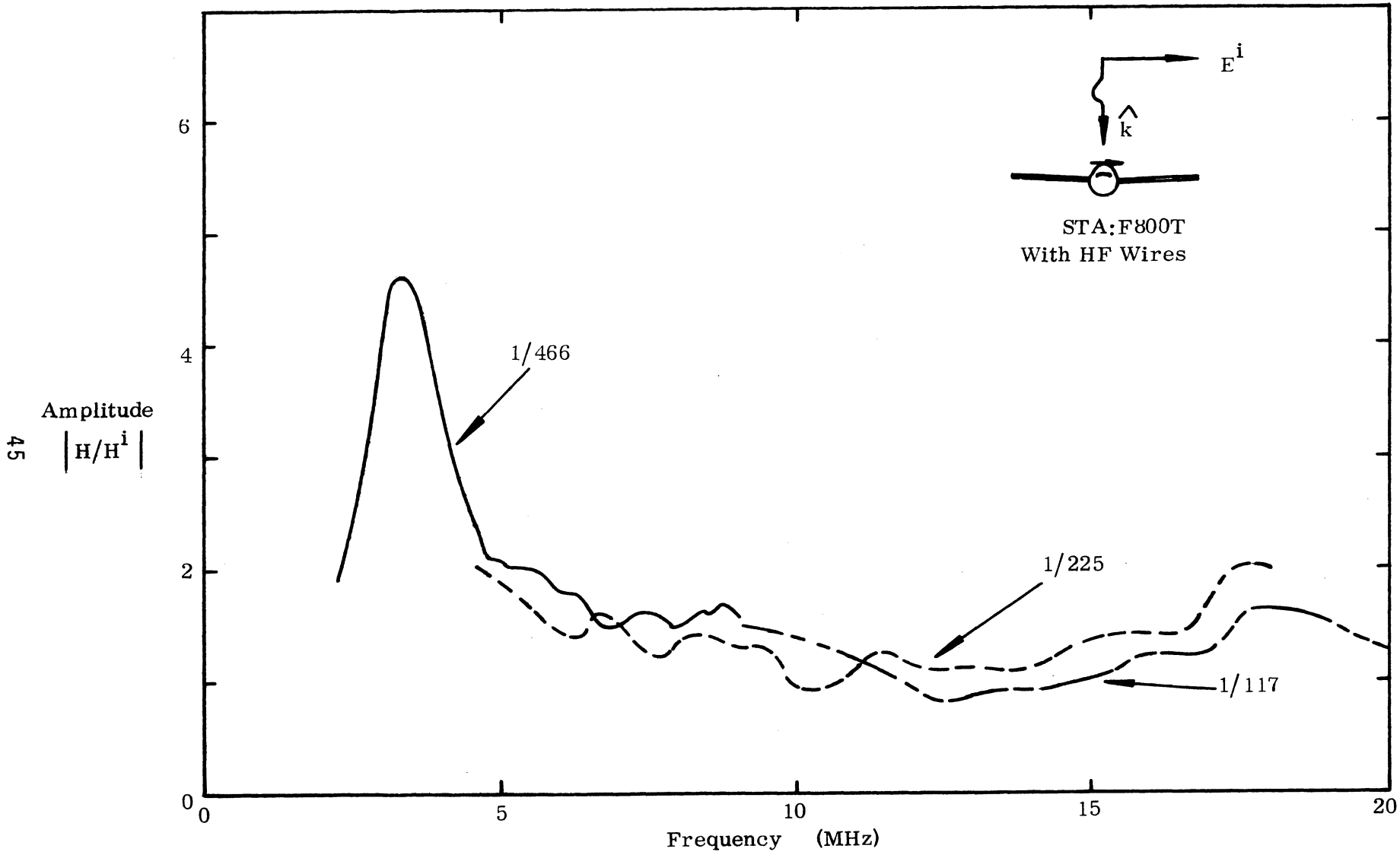

Figure 27a. Current density at STA:F800T, anti-symmetric excitation, with HF wires.

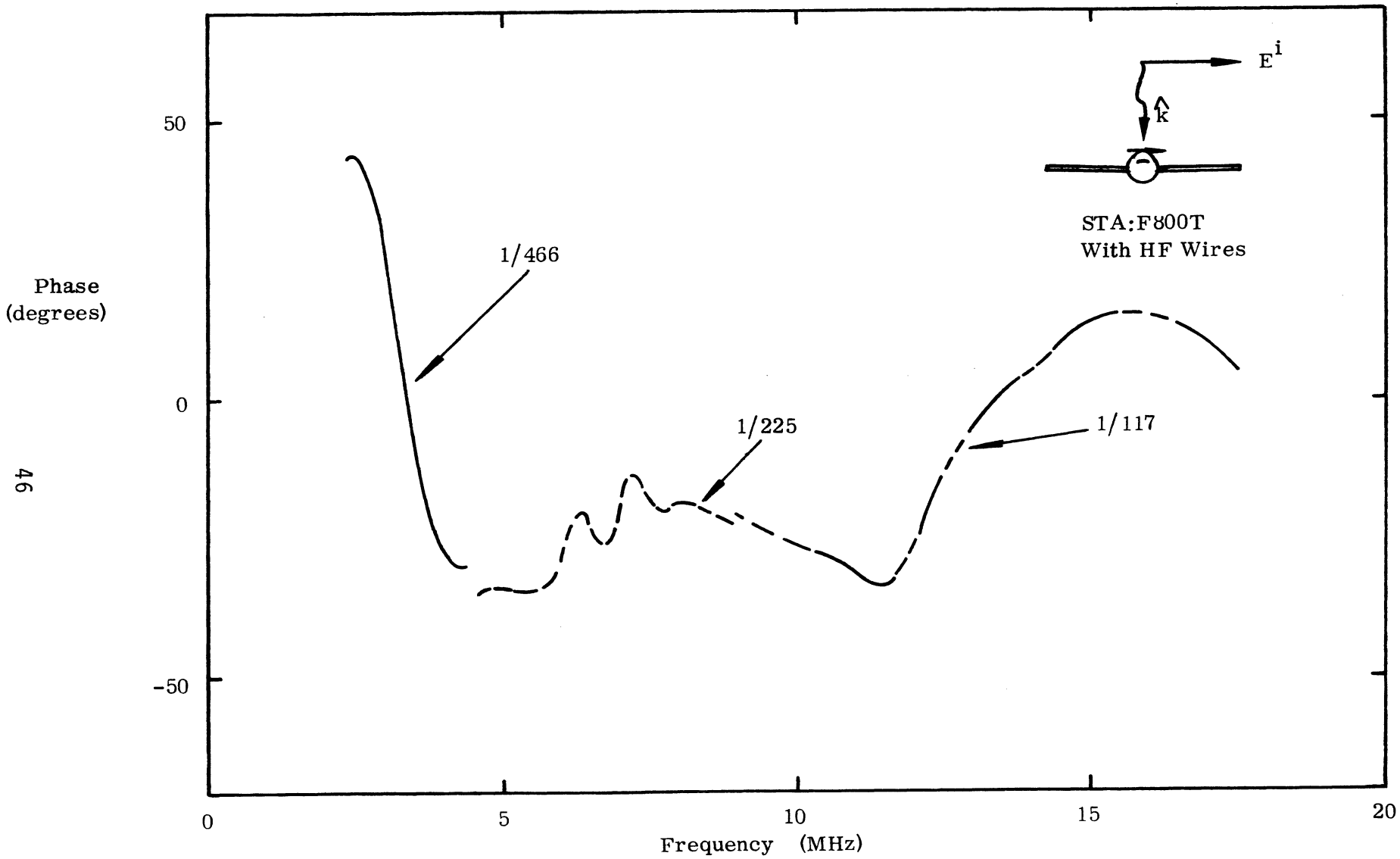

Figure 27b. Current phase at STA:F800T, anti-symmetric excitation, with HF wires.

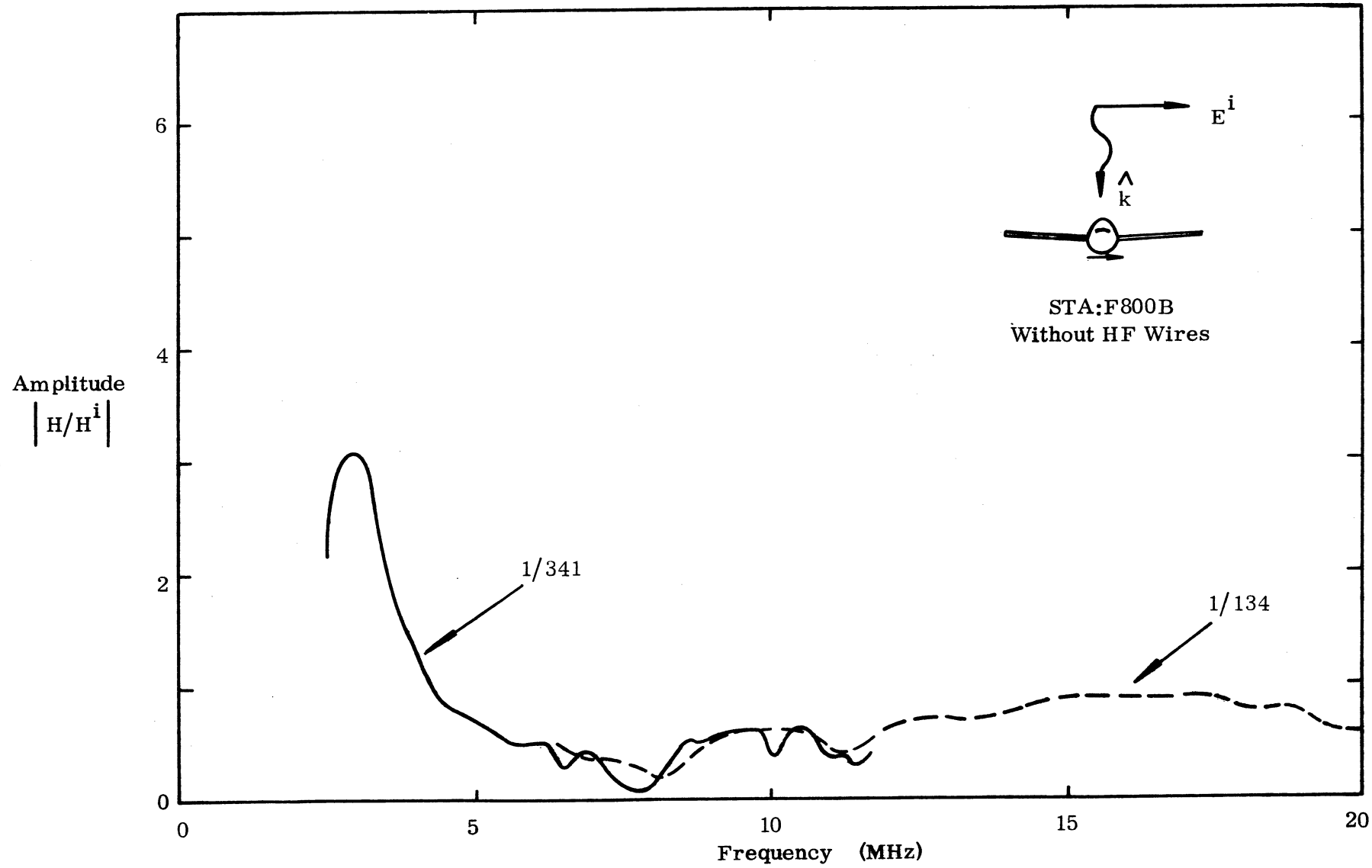

Figure 28a. Current density at STA:F800B, anti-symmetric excitation, without HF wires.

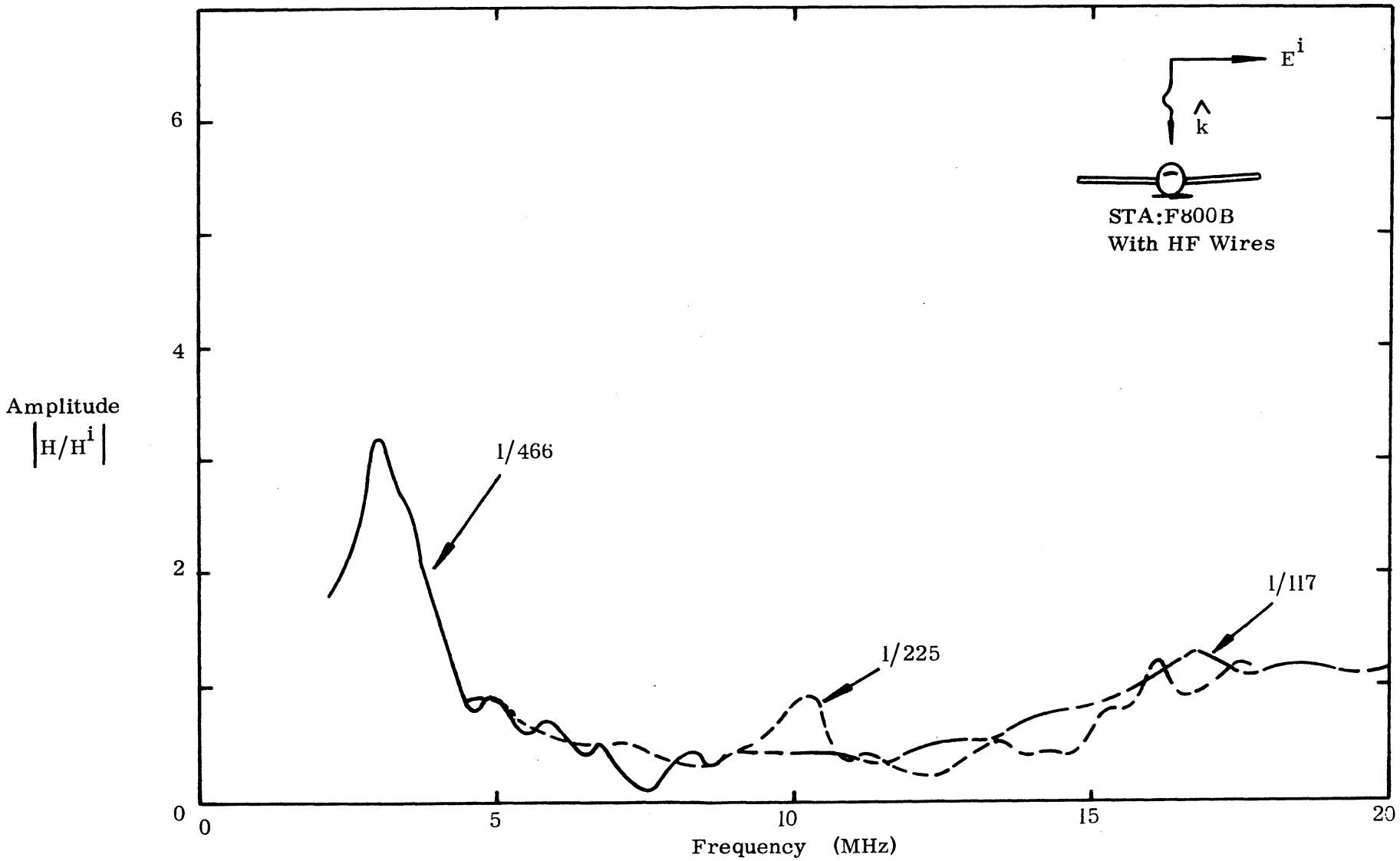

Figure 29a. Current density at STA:F800B, anti-symmetric excitation, with HF wires.

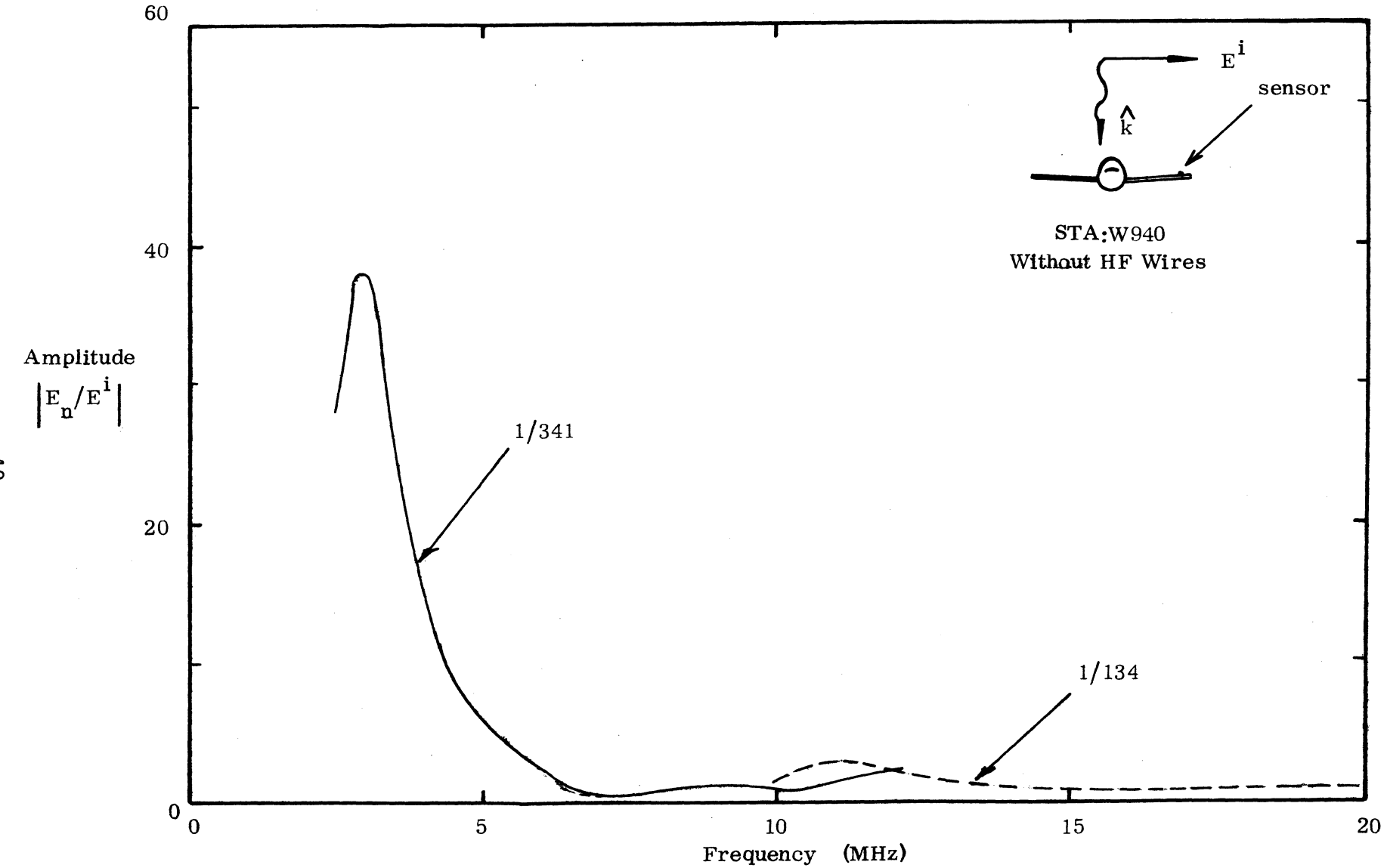

Figure 30a. Charge density at STA:W940, anti-symmetric excitation, without HF wires.

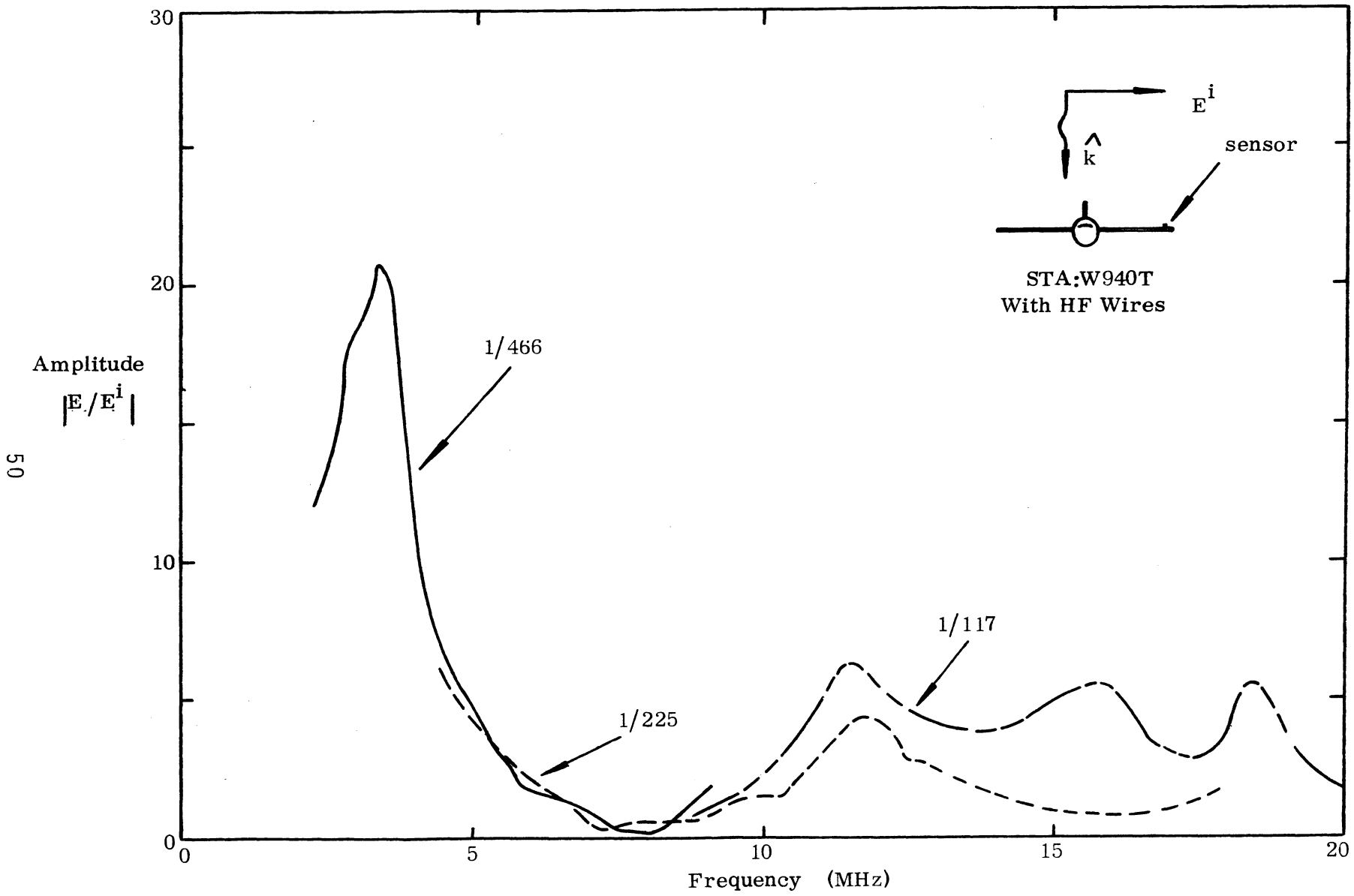

Figure 31a. Charge density at STA:W940T, anti-symmetric excitation, with HF wires.

SECTION III

GROUND PLANE MEASUREMENTS AT NORMAL INCIDENCE

This section presents the measured surface currents and charges on models of the EC-135 aircraft in the presence of a perfectly conducting ground plane. Top-side incidence was always used and, depending on the particular measurement, the incident electric vector was either parallel to the fuselage (symmetric excitation) or perpendicular to the fuselage (antisymmetric excitation). The measurements were made using 1/325 to 1/114 scale model aircraft by scanning the frequency over the bands 0.45 to 1.1 GHz and 2.0 to 4.0 GHz. The data presented here cover 1.38 to 35 MHz and are for models with and without HF wires stretched from the vertical stabilizer of the model to the top of the fuselage near the cockpit.

1. Facilities and Equipment

For these measurements, a vertical ground plane 4 feet high and 12 feet wide was erected in the chamber. A framework of 2 x 4s was used to support a 4 x 12 foot 0.030 inch thick aluminum sheet whose side edges were then imbedded into the absorber walls of the chanber to reduce current reflections from the vertical edges. Since the incident field is horizontally polarized, the currents on the sheet are also horizontal.

The first tests made on the new ground plane were surface scans at a fixed frequency over an area 0.8 by 0.8 m square and there the field amplitude was constant to within $\pm$ 0.5 dB. However, when the frequency was scanned with the test sensor at the center of the ground plane, amplitude oscillations on the order of 3 dB appeared on the X-Y recorder trace. This was obviously a source of concern, and after numerous tests and measurements (and arguments on how a matched horn antenna can reradiate a part of the received signal) it was concluded that energy was being reflected by the ground plane back into the horn and then reradiated in- or out-of-phase depending upon the frequency. To reduce this interaction, about 60 percent of the ground plane was covered with an absorber with particular attention paid to feathering the absorber edge

near to the center of the plate so as not to introduce adverse current reflections. This reduced the ground plane-horn interaction to about 1.5 dB, and yet a further reduction was obtained by changing the reference signal pickup from a directional coupler located ahead of the transmitter horn to a sensor mounted on the ground plane. This change did not reduce horn-ground plane interaction per se, but did smooth out the recorder traces since both the reference and the test signals increased or decreased simultaneously.

Figure 32 shows the frontal view of the absorber-covered ground plane with a model aircraft mounted at the center. The aircraft is out of proportion--the model shown appears over two feet long, although the largest model used was 1/114 scale and about half the size shown. Figure 33 shows a side view of the same and emphasizes the placement of the reference and test sensors. To accommodate the reference and the (bottom) test sensors, holes 3/8 inches in diameter and spaced 5 cm apart were drilled throughout the ground plane in an x-y coordinate lattice whose center is at the center of the sheet. The holes spanned 80 cm horizontally and vertically.

By moving the MGL-S8A(R) sensor (the one with connector underneath) through all the mounting positions (holes) and recording the frequency response at each position, vertical and horizontal surface scans were obtained. Figure 34 shows the reduced data for 0.5 and 1.0 GHz. Measurements were also made in the 2 to 4 GHz band with similar results.

Figure 35 shows the block diagram of the instrumentation used in measurements of the model aircraft near the ground plane. The arrangement is similar to that used earlier in free-space measurements, the main difference being that the reference signal is now taken from a sensor (MGL-S7A(R)) mounted on the ground plane rather than from a directional coupler located ahead of the horn.

2. Models

For the measurements, five different models were used ranging in scale from 1/114 to 1/325. These are the same as previously used for obtaining the free-space data, but because they have been reworked and repainted, some of the scaling factors

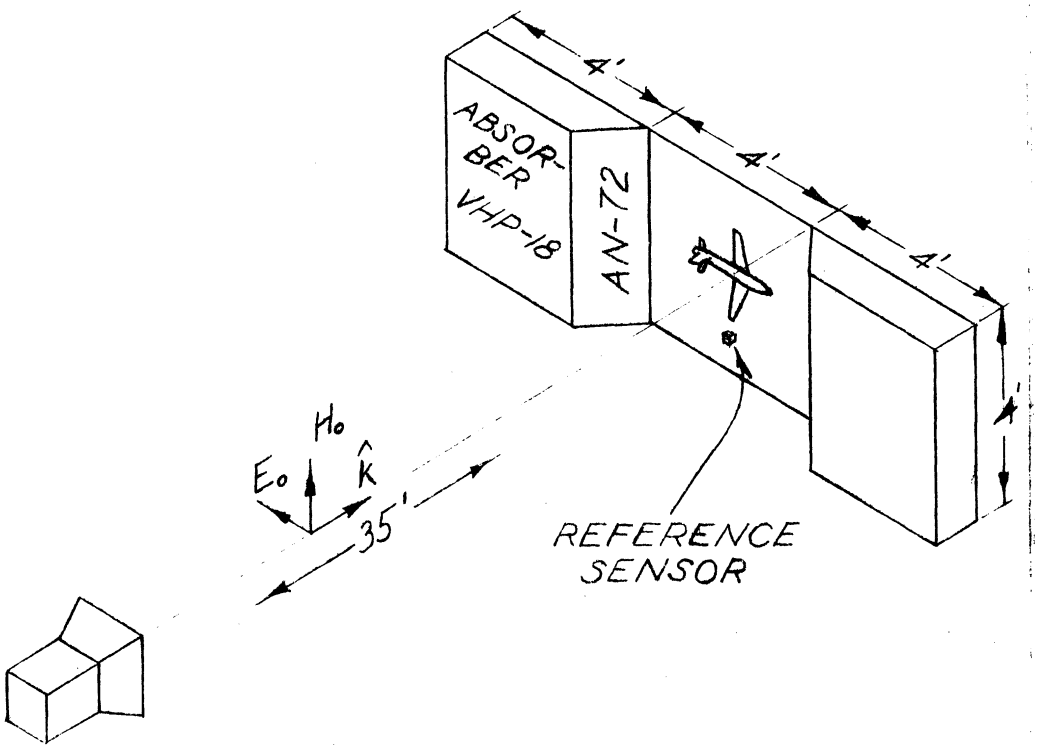

Figure 32. Frontal view of the absorber covered ground plane. The ground plane and the transmitting antenna are inside the anechoic chamber (not shown).

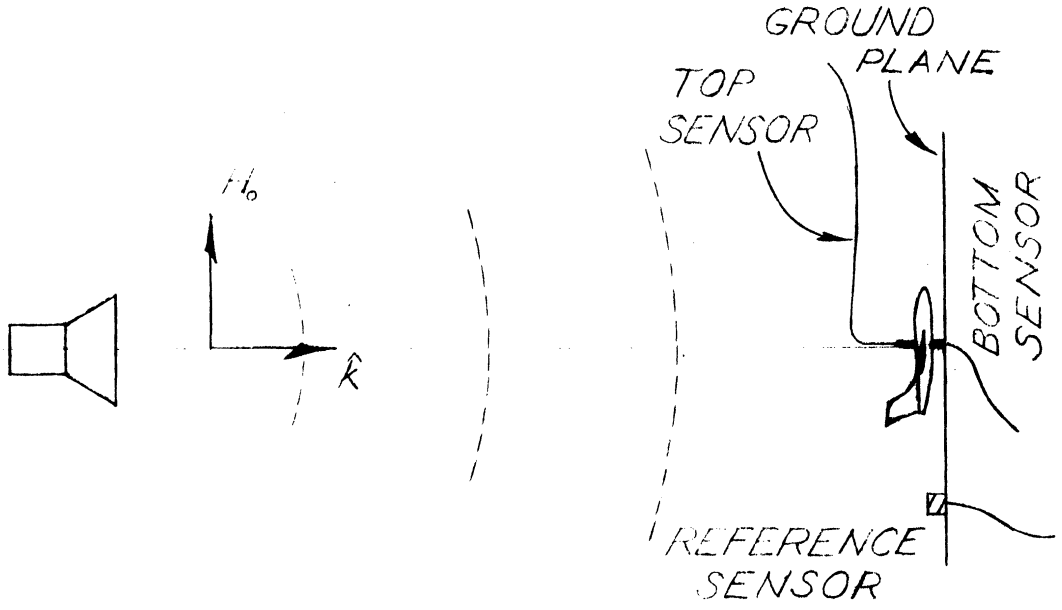

Figure 33. Sideview sketch showing the locations of the sensors (not to scale).

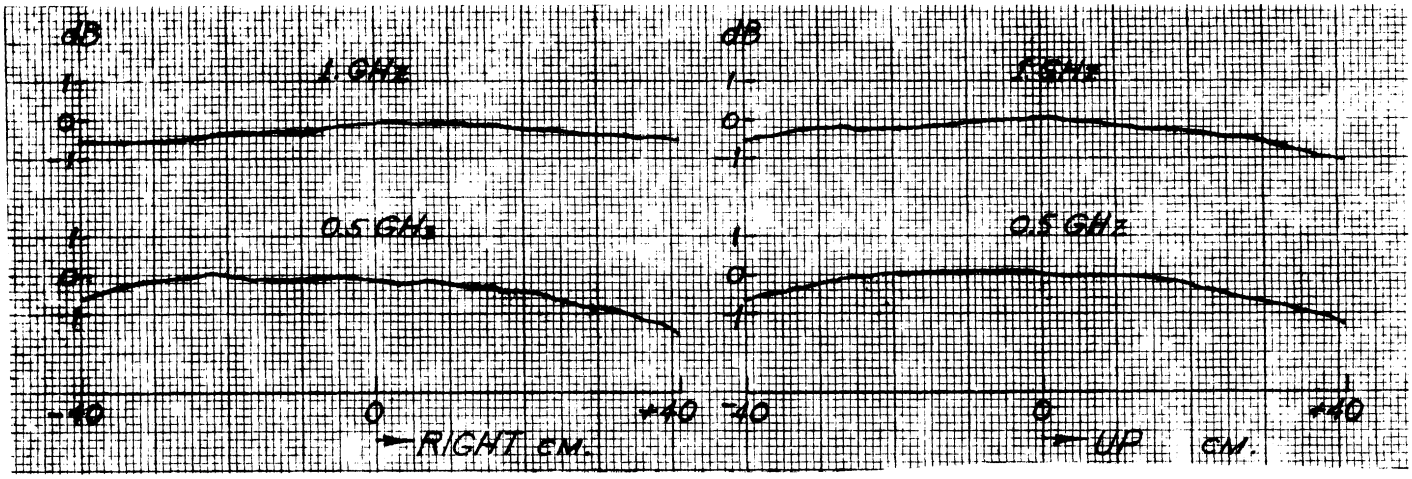

Figure 34. Vertical and horizontal surface scans made with MGL-S8A(R).

differ from those originally given. All models are in the "wheels-up" configuration and have wheel wells and doors taped over with adhesive copper tape. There are two 1/325 scale models, one with HF wires and one without. There is only one 1/216 scale model and for this the wires were attached or removed as required. The 1/129 model is without HF wires and the 1/114 model is with them. Figure 2 shows the locations where these wires are attached and also indicates how they are connected, i.e., open circuit or short circuit condition. To raise the models an appropriate distance above the metal ground plane, four styrofoam blocks were used with each model--two under the fuselage and one under each wingtip. The height of these blocks was chosen to simulate the 1.22 m fuselage-to-ground clearance on a full-scale EC-135 aircraft.

The vital statistics of models are summarized in Table 3. Amongst other things, the relative nose-to-wing and the wing-to-fuselage center distances are given. Such information is helpful in interpreting the measured data and, in particular, explaining the presence of the second resonance peak near 4 MHz.

3. Measurements and Sensors Used

The measurements are for the same aircraft body locations or stations used in the free-space measurements, plus additional measurements for the current on the ground plane under the fuselage of the model. The latter measurements are designated by numbers such as F800G, where "G" implies ground plane measurement. Figure 3 shows the locations of the stations, and for specifying them the following convention

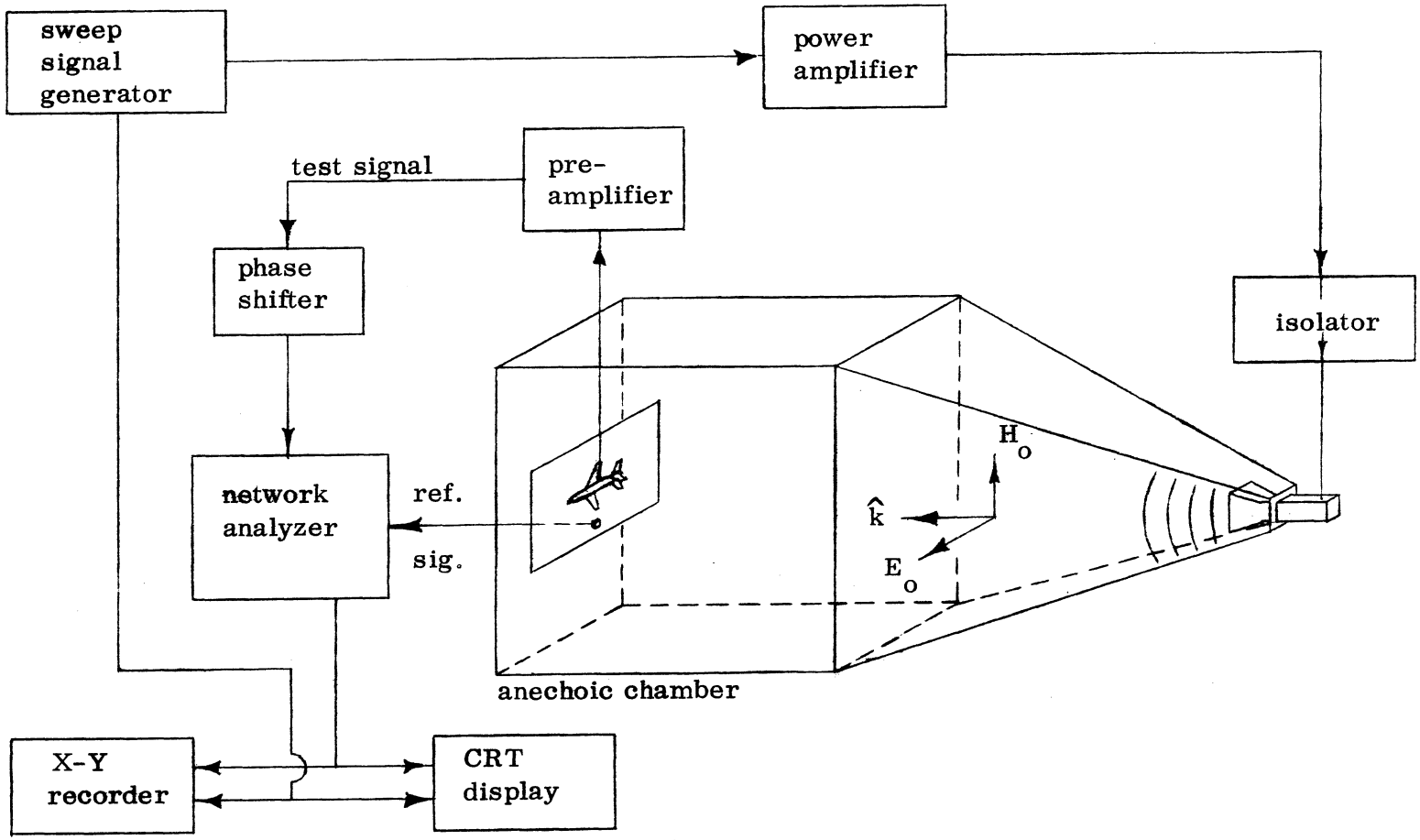

Figure 35. Surface field measurement facility with vertical ground plane.

Table 3

EC-135 MODELS USED

EC-135 Model	Fuselage Scale	Wing Span Scale	Material	Fuselage Diameter at Station			Wing Thickness at W600	With HF Wires	Without HF Wires	a/L	b/L	$\frac{(a+b)}{L}$
				400 (cm)	800 (cm)	1200 (cm)						
325	1/324.5	1/340.3	metal	1.15	1.19	1.15	0.23	X	X	0.4305	0.5000	0.9305
216	1/216.0	1/225.3	metal	1.80	1.77	1.76	0.28	X		0.3902	0.5307	0.9209
129	1/129.2	1/134.4	plastic	3.01	3.03	3.02	0.59		X	0.3983	0.4807	0.8790
114	1/114.0	1/117.3	plastic	3.50	3.44	3.35	0.30	X		0.3780	0.5621	0.9402

Full Scale Dimensions of EC-135:

Overall length (with boom)	41.53m
Overall length (without boom)	41.17m
Fuselage length (without boom)	39.27m
Wing Span	39.89m
Fuselage clearance	1.22m

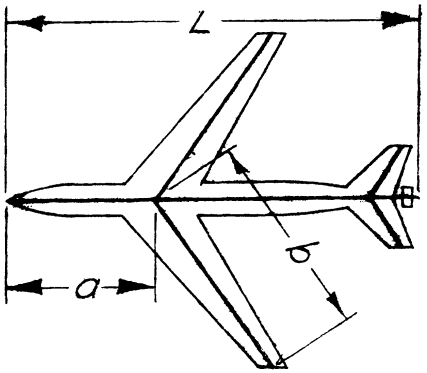

has been adopted: F1200T is the Fuselage station, located on the Top, with 1200 (the number used by the Air Force) indicating the distance in inches from the nose, but with the nose already at 130 instead of 0. Other letters used in station designations are W, B, and G, and refer to Wing, Bottom, and Ground positions, respectively. Four different magnetic sensors and one charge probe were used in making these measurements, with the MGL-S7A(A) used for reference. For the top measurements, our own free space 3.2 mm diameter shielded loop probe was used (figure 33), and for the bottom measurements, a similar but straight probe. The MGL-S8A(R) was used to measure the current on the ground plane, and at the nose and wingtips the charge was measured using a 2 mm extension of the center conductor of a 0.020 inch diameter coax. In all the measurements precautions were taken to minimize the sensor lead interaction with the electromagnetic field.

4. Incident Field Calibration

Since it is almost impossible to achieve a flat or even uniform measurement system response over a wide frequency range, the incident field should be measured everytime a sensor or other component in the system is changed. The number of station measurements made per calibration varied. For example, at the F400T, F800T, and F1200T stations, only one calibration run was made for each model and frequency band, while for the bottom stations F400B, F800B, and F1200B, a new calibration run was made for each station.

(a) Top Sensor

This is the same one used in the free-space model measurements. Its signal lead extends vertically to the ceiling on the illuminated side of the ground plane, but since the lead is perpendicular to the incident electric field, its interaction or disturbance is negligible. For calibration of this sensor and the rest of the system, the loop was moved against the ground plane (with the model removed) and the calibration field $\underline{H}_c$ recorded on the X-Y chart recorder. Hence, the incident field $\underline{H}_o$ is

$$\underline{H}_o = 1/2\, \underline{H}_c. \qquad (1)$$

(b) Bottom Sensor

As can be seen in figure 33, this sensor goes through a small hole in the ground plane. Behind the ground plane the sensor is attached to a precision slide which provides accurate positioning. In measurements of the current at STA:F800B, for example, the model is first mounted on the ground plane and then the sensor is moved out until the loop barely touches the model at this station. To record the calibration field, the model is removed and the field recorded. If h is the distance (or clearance) from the ground plane to what was STA:F800B, the incident field can be written as

$$\underline{H}_o = \frac{\underline{H}_c}{2\cos(kh)}$$

where k is the wave number. Then,

$$\underline{H}_o = \frac{\underline{H}_c}{2\cos(12fh)} \tag{2}$$

where f is now the frequency in GHz and h is the distance in centimeters.

(c) Wing Measurements

The wing measurement data are for anti-symmetric excitation only, for which the incident magnetic vector is parallel to the fuselage. To measure the wing current, the top and bottom loops were both rotated 34 degrees, the estimated average swept-back angle for the wings. The incident field is then given by

$$\underline{H}_o = \frac{\underline{H}_c}{2\cos 34^o \cos(kh)}$$

i.e.,

$$\underline{H}_o = \frac{\underline{H}_c}{1.6581\cos(12fh)} \tag{3}$$

where f is the frequency in GHz and h is the displacement of the sensor from the ground plane where the calibration measurement is made. For the wing top measurements, the sensor was always moved against the ground plane and hence h = 0. For the wing bottom measurement, the sensor was left at the wing station location (with the model removed) and hence h is the ground to station distance for the particular model used.

(d) Charge Sensors

Since the 2 mm extension of the center conductor of the 0.020 inch coax requires a base or image plane, a 10 x 10 cm image plane was used to obtain the calibration field. Figure 36 shows its implementation. An L-shaped bracket, made out of 0.020 inch thick brass, was taped to the ground plane perpendicular to the incident electric vector. A coax with center conductor extended was then inserted through the holes previously drilled and carefully taped with conductive tape to cover the loop created on the underside of the image plane. A loop as seen in figure 36 will respond to the magnetic field, and if not properly hidden, would affect the electric field measurements.

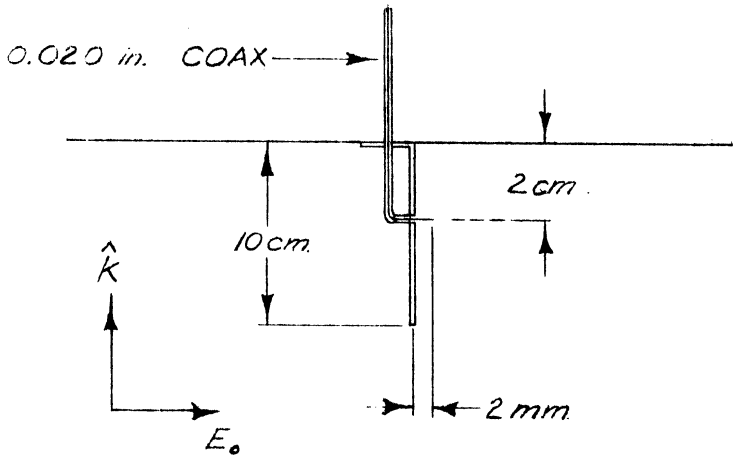

Figure 36. Image plane for calibration of charge probes.

To verify that the field measured on this small image plane is the same as that measured on a larger sheet, frequency scans were run as the size of the image plane was increased in four increments to $25 \times 25\ cm^2$. When compared to the trace for the 10 x 10 cm plane, the recordings typically deviated ± 0.25 dB over the 0.45 to 1.10 GHz range scanned, and the maximum deviation observed was 0.5 dB. Such variations are within the measurement repeatability tolerances and, hence, a 10 x 10 cm plate is of sufficient size for the present application.

When a plane wave of strength $\underline{E}_o$ and $e^{i\omega t}$ time dependence is incident perpendicularly on a perfectly conducting ground plane, the sum of the incident and reflected

field is

$$\underline{E} = 2i\underline{E}_o \sin(kd),$$

where d is the distance from the ground plane where $\underline{E}$ is observed. The factor i in the equation implies a 90 degree phase shift. If $\underline{E}_c$ represents the calibration voltage measured on the image plane, the incident field $\underline{E}_o$ is then

$$\underline{E}_o = \frac{\underline{E}_c}{2i\sin(kd)}$$

i.e.,

$$\underline{E}_o = \frac{\underline{E}_c}{2i\sin(12fd)} \tag{4}$$

The charge measurements on the models were made at two stations: the nose (F130, symmetric excitation) and the wingtip (W940T, antisymmetric excitation). For both measurements, the coax lead was brought away from the model at station F870B and then directly through a hole in the ground plane. The station F870B was selected as a result of the following test. A model was mounted on the ground plane as if for measuring the current at STA:1200T, but this time a shorting strap to simulate the lead that is present in charge measurements was connected from the bottom of the fuselage to the ground plane. Measurements were then made as the position of the shorting strap was changed, and of the points tested, the STA:F870B was found to have least effect on the current on the top of the fuselage. In antisymmetric excitations, the charge is zero at any symmetric point on the fuselage and, hence, STA:F870B was also acceptable.

5. Reduction of Data

Two methods of data reduction were employed for the data presented here. For the low frequency range, typically 1 to 9 MHz, the data were reduced manually by picking discrete frequency values, writing down the dB and phase data in a table, and performing the necessary mathematical operations using a hand calculator. Points were chosen uniformly spaced in frequency, plus extra points at peaks and other places where the resulting curves were inadequate. The actual points where the data were reduced are

shown on the curves. At the higher frequencies the analog data was first digitized using a Computek Tablet interfaced with a PDP-11 computer where the data was stored on the disc. From there it was copied to MTS (The University of Michigan AMDAHL 470 V/6 machine) and further processed using codes based on formulas presented in Section III, para. 4. The reduced data from MTS was then plotted on a desk-top digital plotter covering the frequency range 0 to 40 MHz

A correction for the integrating effect of a probe was applied only to the measured data for the charge at the nose (STA:F130). It was assumed that the nose can be approximated as the tip of a prolate spheroid, and using the static solution and the assumption that the 2 mm long monopole responds to the electric field value at its center, i.e., 1 mm from the surface, the following correction factors γ were obtained and applied to the data:

Scale	γ
1/114	1.621
1/129	1.701
1/216	2.174
1/325	2.755

In contrast to the free-space data previously given for the current, no corrections to account for the integrating effect of the probe have been applied to the present data. The reason is that with a ground plane present, the illuminating signal can be considered as two plane waves traveling in opposite directions and for this case an appropriate correction procedure has not been developed. Judging from the free-space correction data, the correction factor would be at most 1.2 for the 1/325 model and at most 1.15 for the 1/114 model. This factor would apply to the scattered component of the field only and is, therefore, applicable to the curves presented only when $H^{scat} \gg H_o$, i.e., $H/H_o > 10$.

6. Data

The surface current and charge data presented has been normalized to the incident field strength H_o or E_o and scaled to the full scale frequencies. Figures designated XXa contain amplitude data, and those designated XXb contain the corresponding phase data. Note that the phase is relative to the incident phase at the ground plane surface. Also, the first pair of figures for a given station is for the model without HF wires, followed by the data for the model with wires. Table 4 summarizes the data and can be used as a guide to quickly locate a particular set.

All the measurements that were made under this task are included. Most of the results appear excellent and quite consistent, yet there are some "rotten apples" indicating that something abnormal may have happened when the data was taken. Because the reduction of the data lags the measurements by a couple of months, it is impractical to repeat the measurements in question. Where abnormalities in data occur and there is an apparent reason for the effects, comments have been entered on the figures.

Table 4

DATA SELECTION CHART

Station Number	J or Q	Without HF wires		With HF wires	
		Symmetric (Figure)	Anti-symmetric (Figure)	Symmetric (Figure)	Anti-symmetric (Figure)
F400T	J	37a, b 38a, b	-------	39a 40a, b	------
F800T	J	41a, b 42a, b	61a, b 62a, b	43a 44a, b	63a 64a, b
F1200T	J	45a, b 46a, b	—------	47a 48a, b	-------
F400B	J	49a, b 50a, b	-------	51a 52a, b	-------
F800T	J	53a, b 54a, b	65a, b 66a, b	55a 56a, b	67a 68a, b
F1200B	J	57a, b 58a, b	-------	59a 60a, b	-------
W600T	J	------	69a, b 70a, b	-------	71a 72a, b
W600B	J	------	73a, b 74a, b	-------	75a 76a, b
F130	Q	77a, b 78a, b	------	79a 80a, b	-------
W940T	Q	------	81a, b 82a, b	-------	83a 84a, b
F400G	J	------	-------	-------	-------
F800G	J	85a, b 86a, b	89a, b 90a, b	-------	-------
F1200G	J	87a, b 88a, b	91a, b	-------	-------

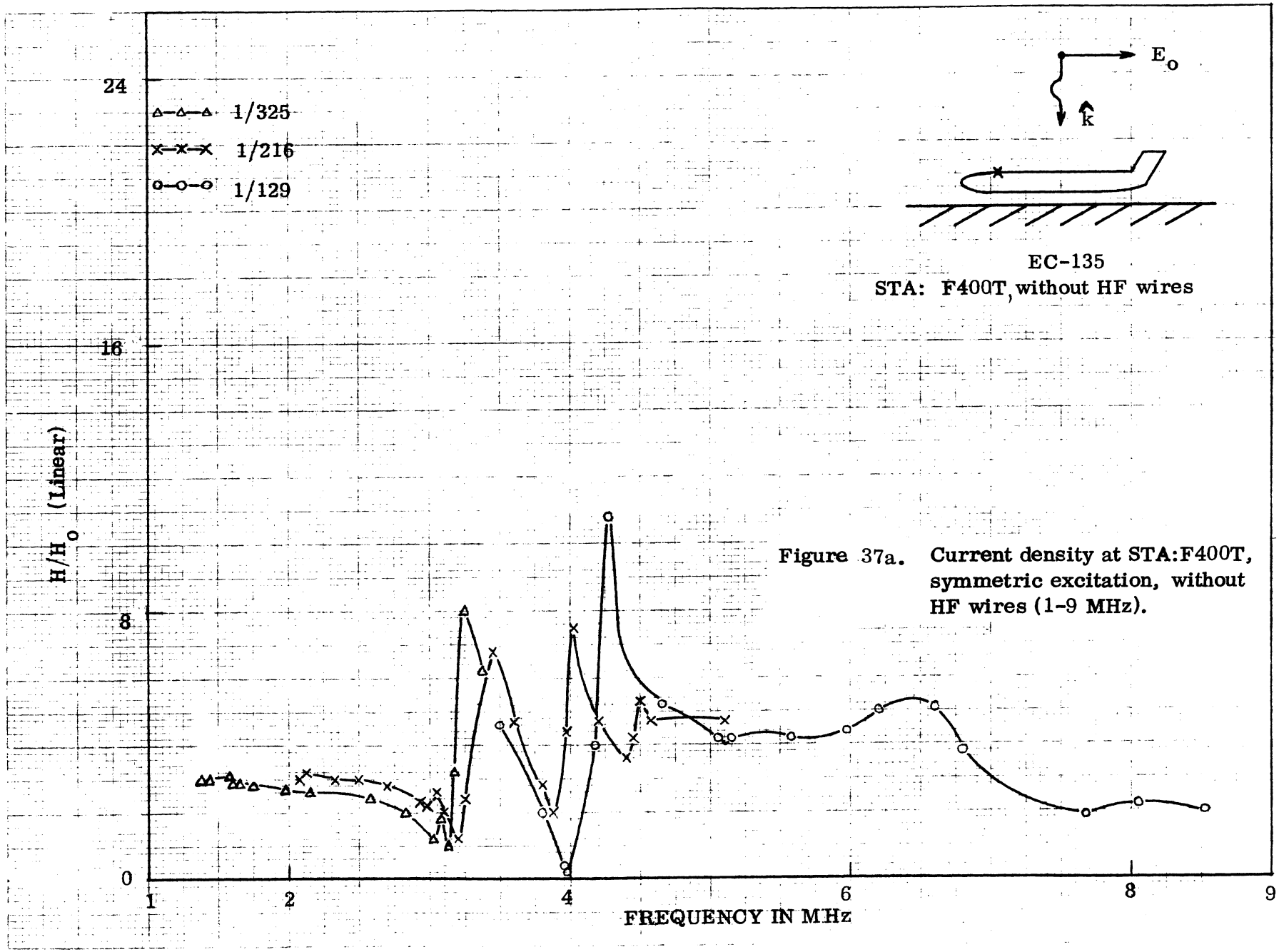

Figure 37a. Current density at STA:F400T, symmetric excitation, without HF wires (1-9 MHz).

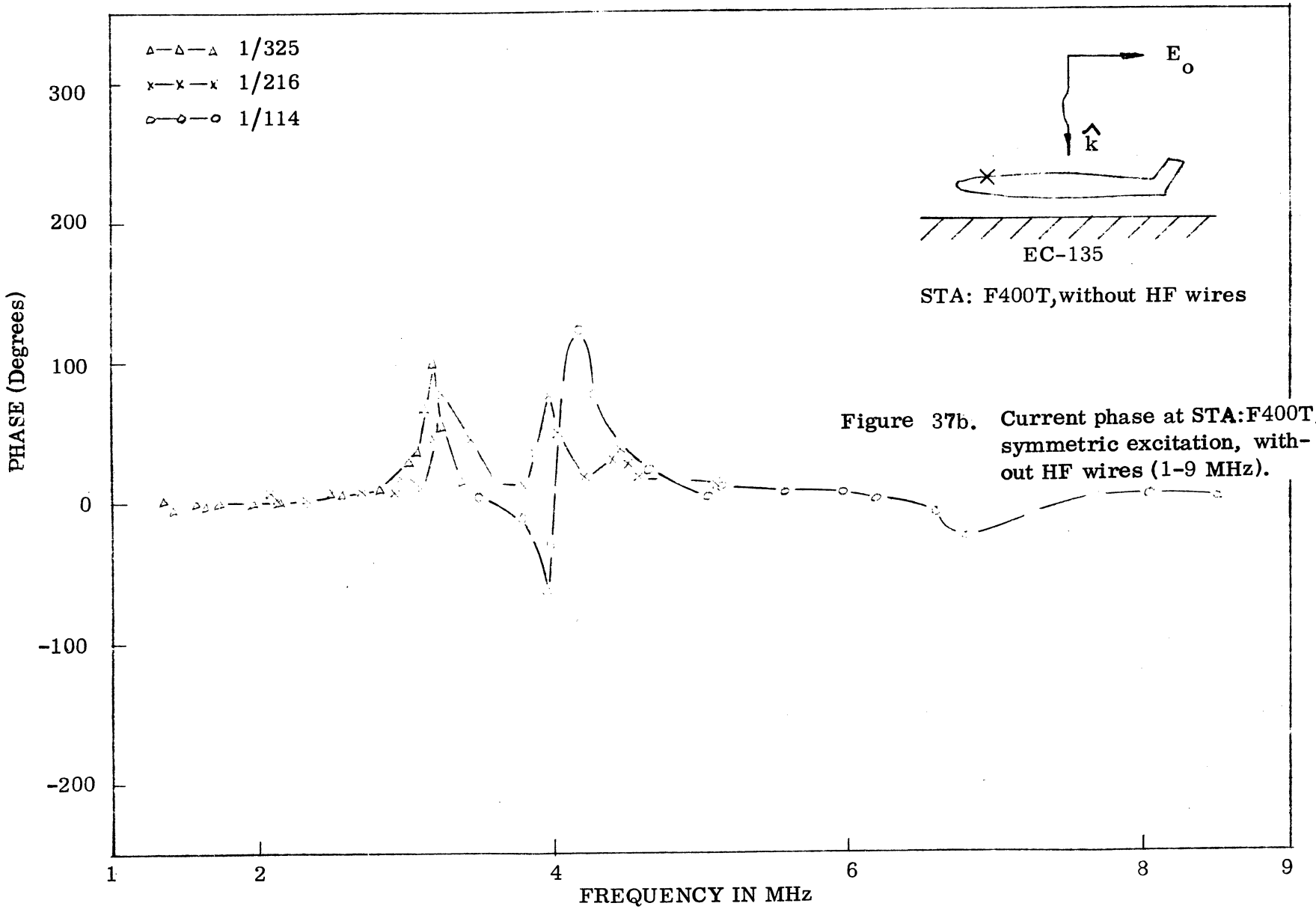

Figure 37b. Current phase at STA:F400T, symmetric excitation, without HF wires (1-9 MHz).

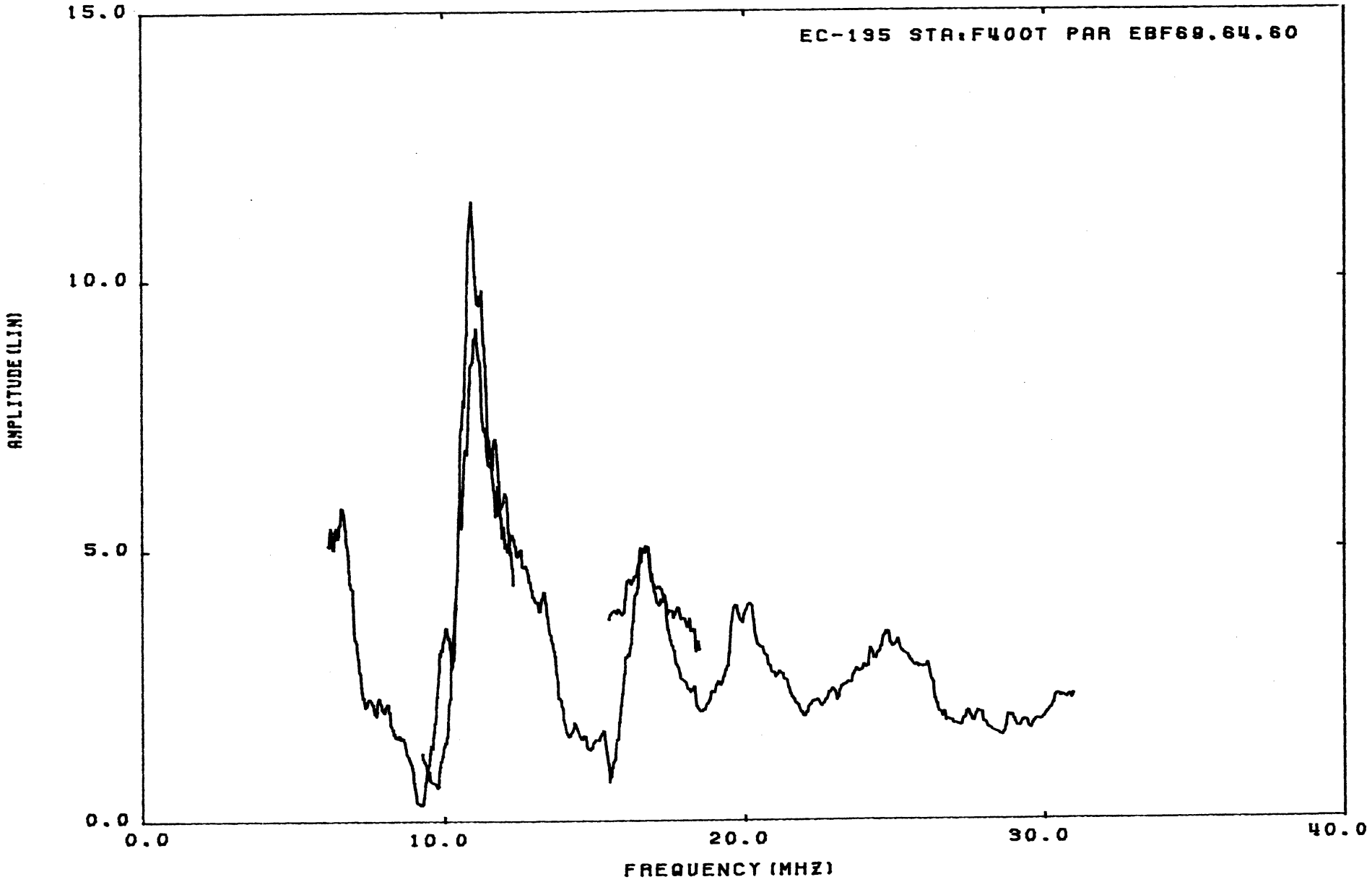

Figure 38a. Current density at STA:F400T, symmetric excitation, without HF wires (0-40 MHz).

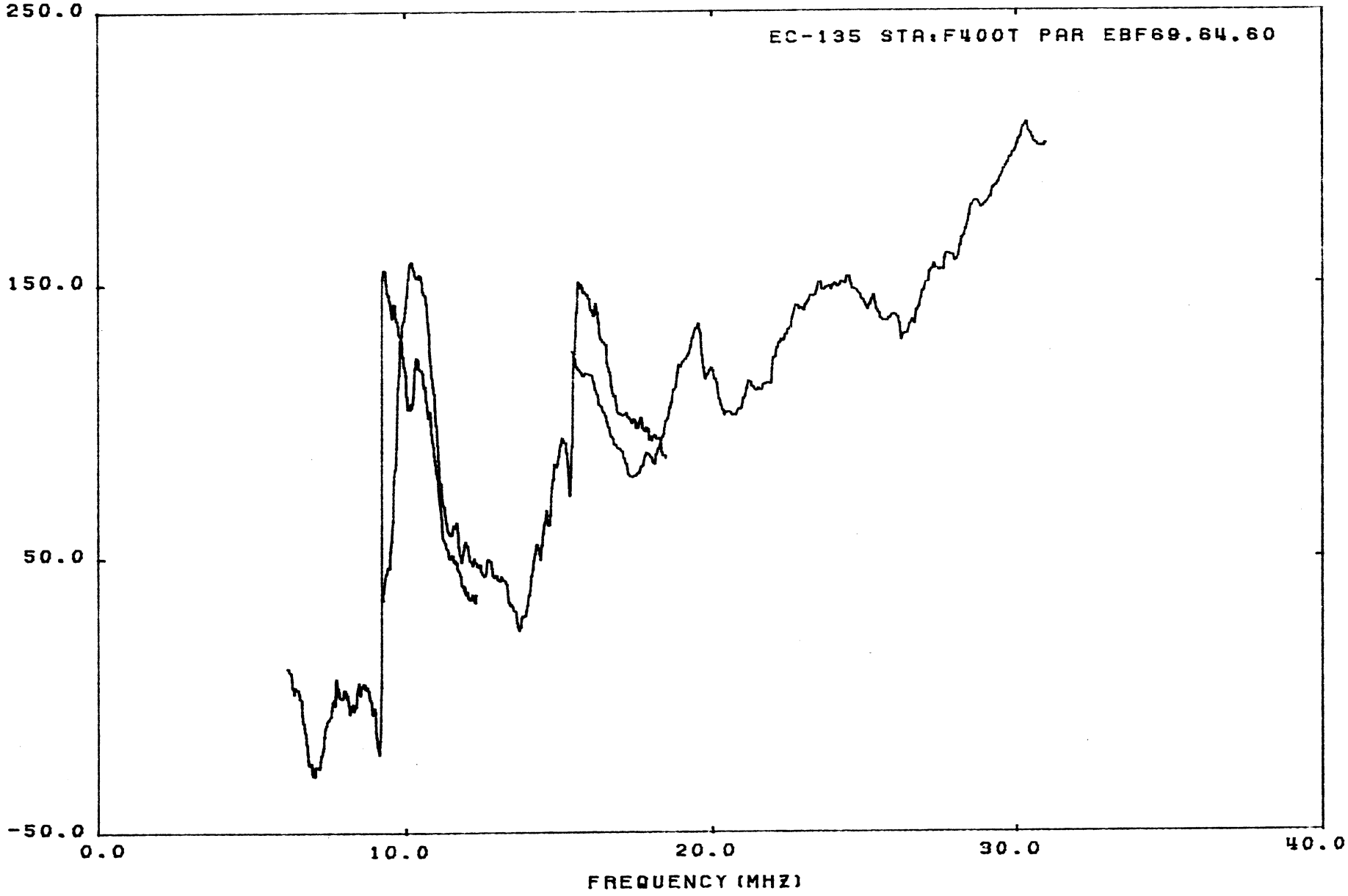

Figure 38b. Current phase at STA:F400T, symmetric excitation, without HF wires (0-40 MHz).

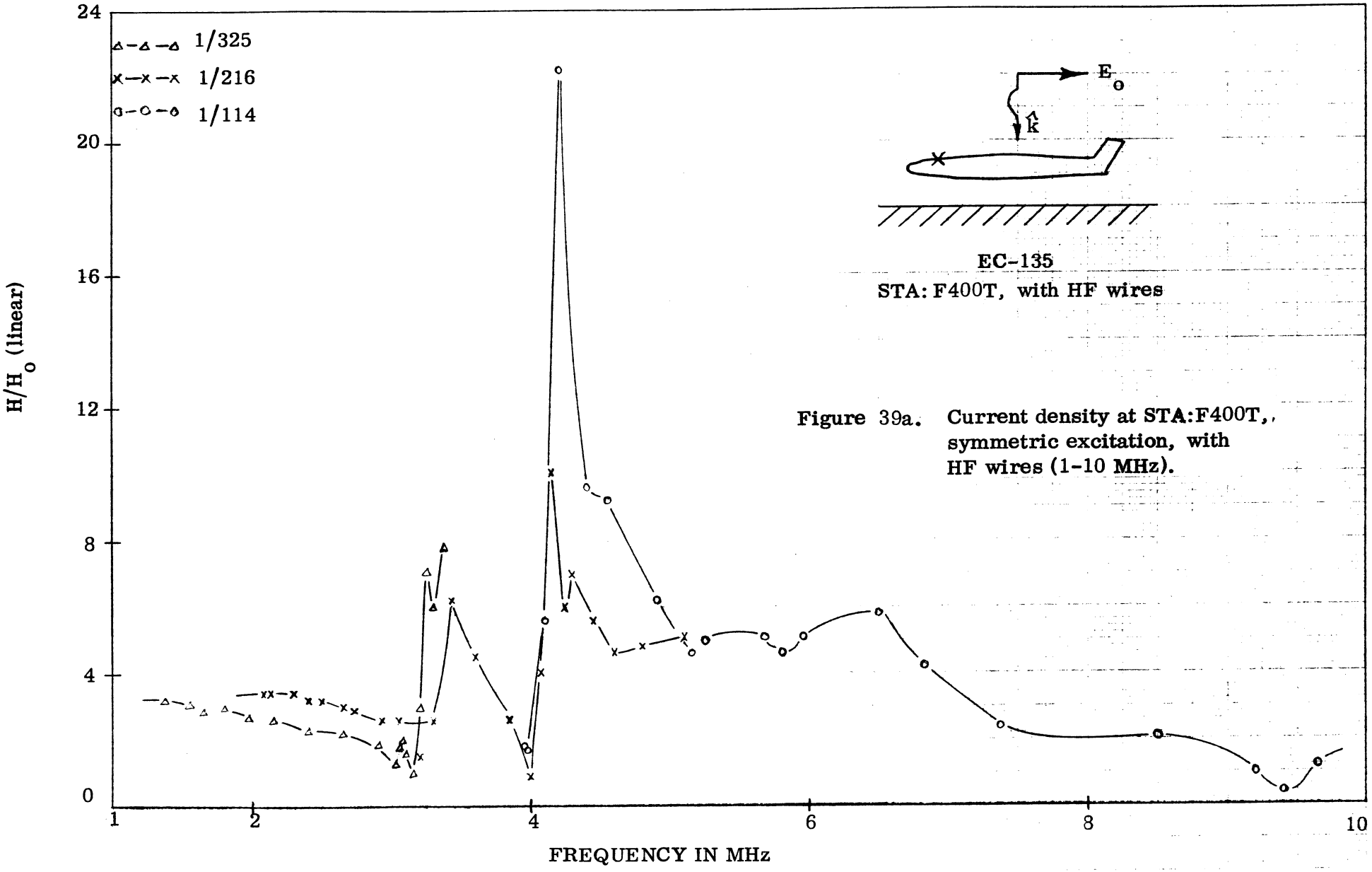

Figure 39a. Current density at STA:F400T,, symmetric excitation, with HF wires (1-10 MHz).

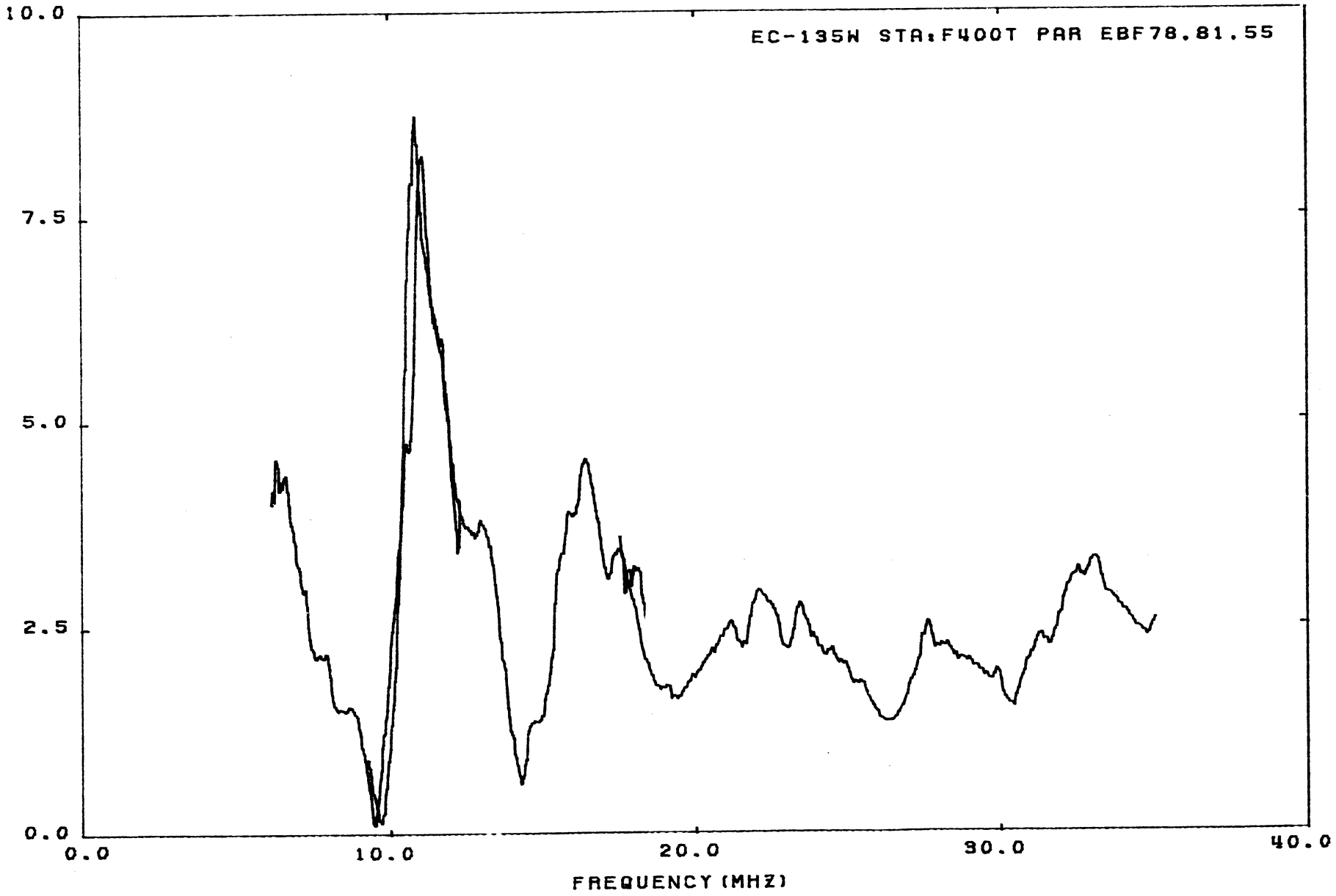

Figure 40a. Current density at STA:F400T, symmetric excitation, with HF wires (0-40 MHz).

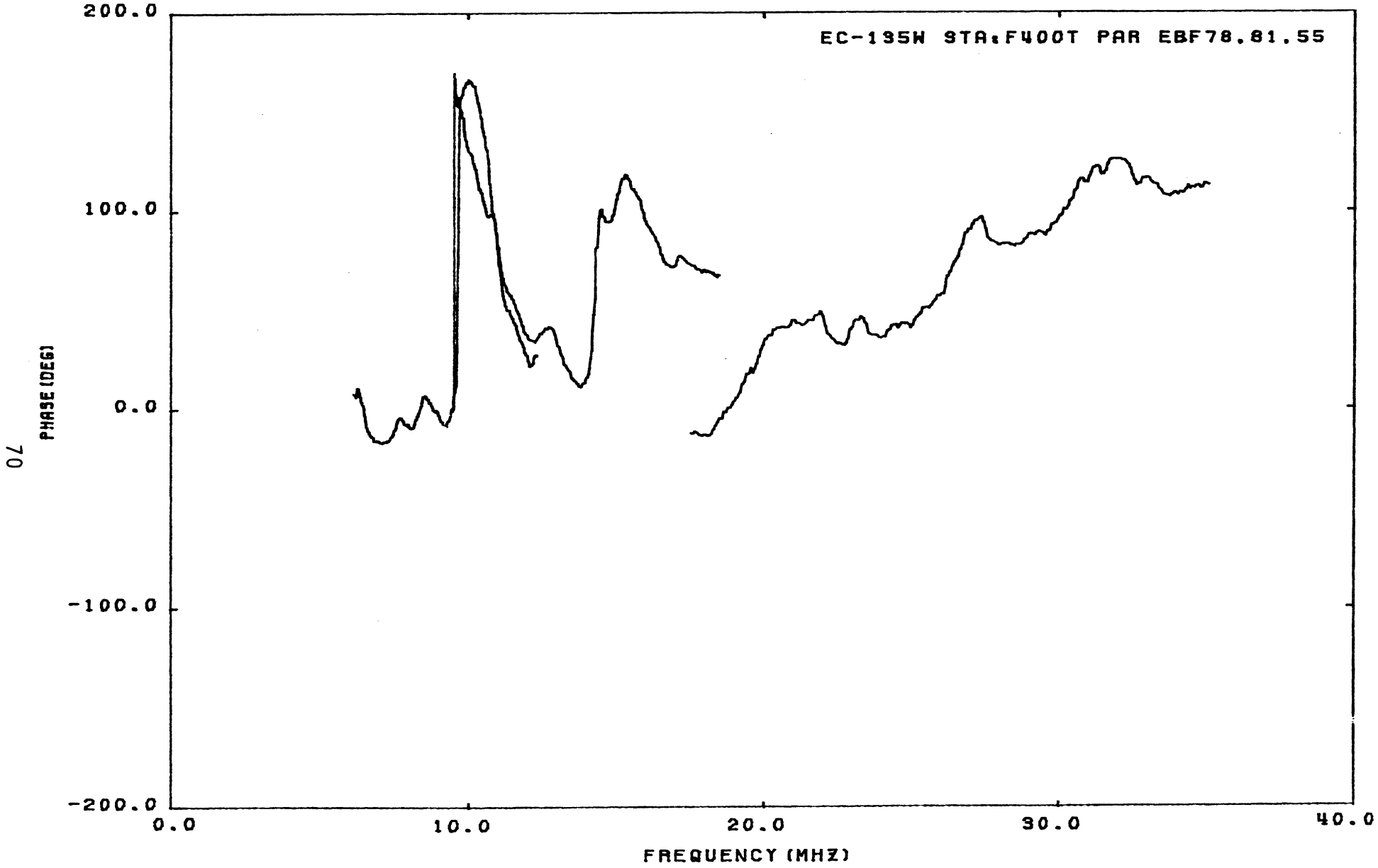

Figure 40b. Current phase at STA:F400T, symmetric excitation, with HF wires (0-40 MHz).

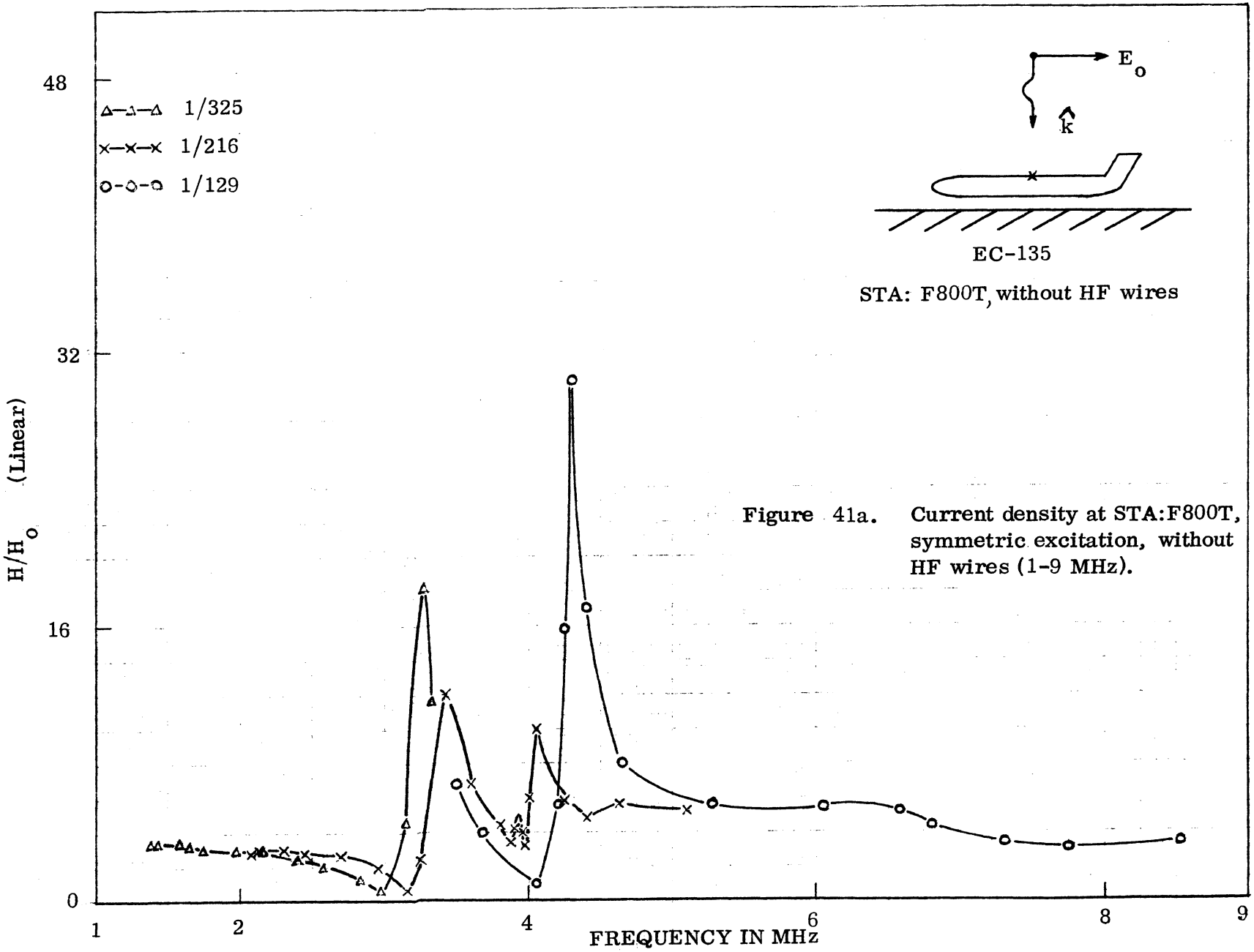

Figure 41a. Current density at STA:F800T, symmetric excitation, without HF wires (1-9 MHz).

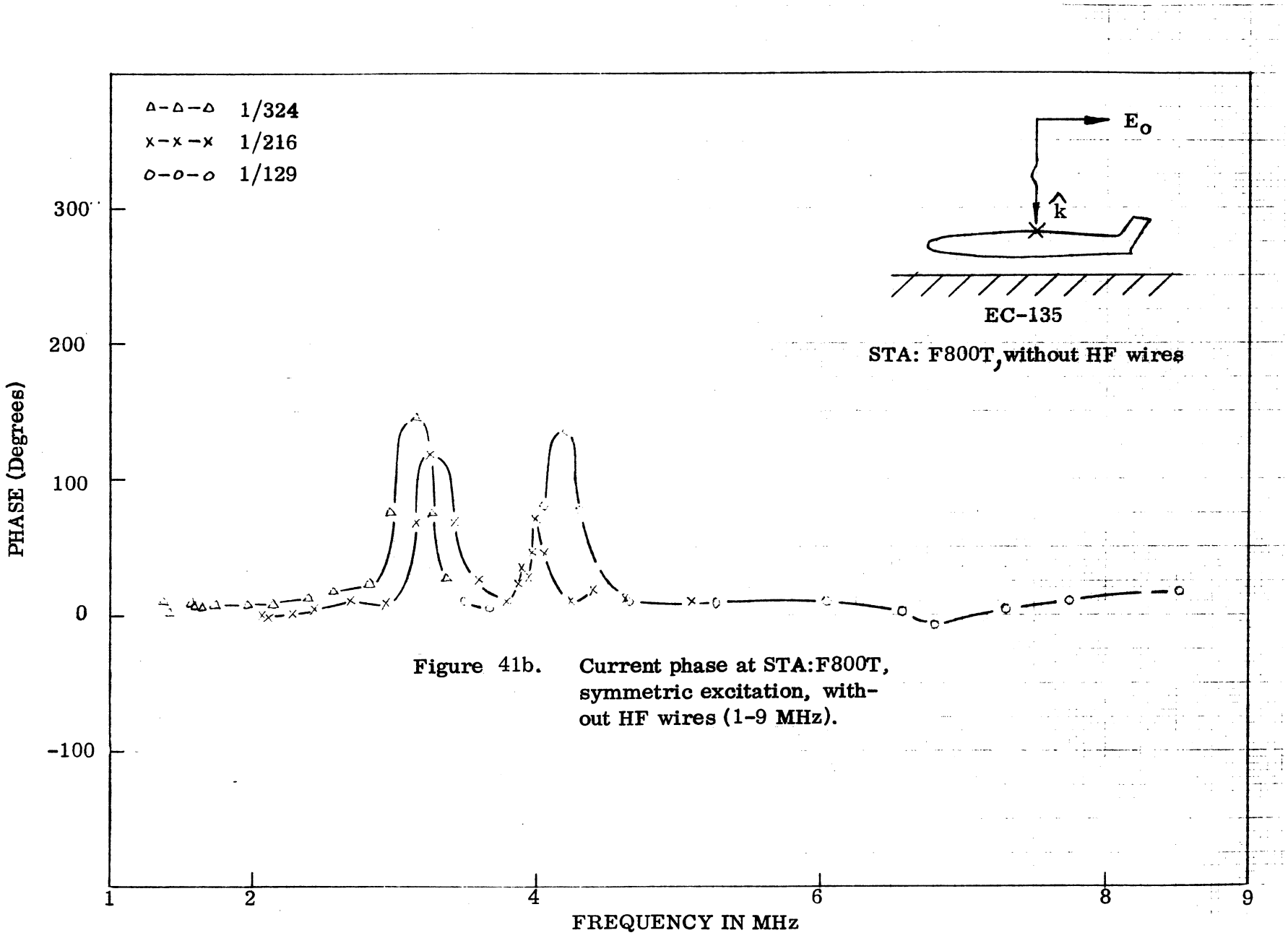

Figure 41b. Current phase at STA:F800T, symmetric excitation, without HF wires (1-9 MHz).

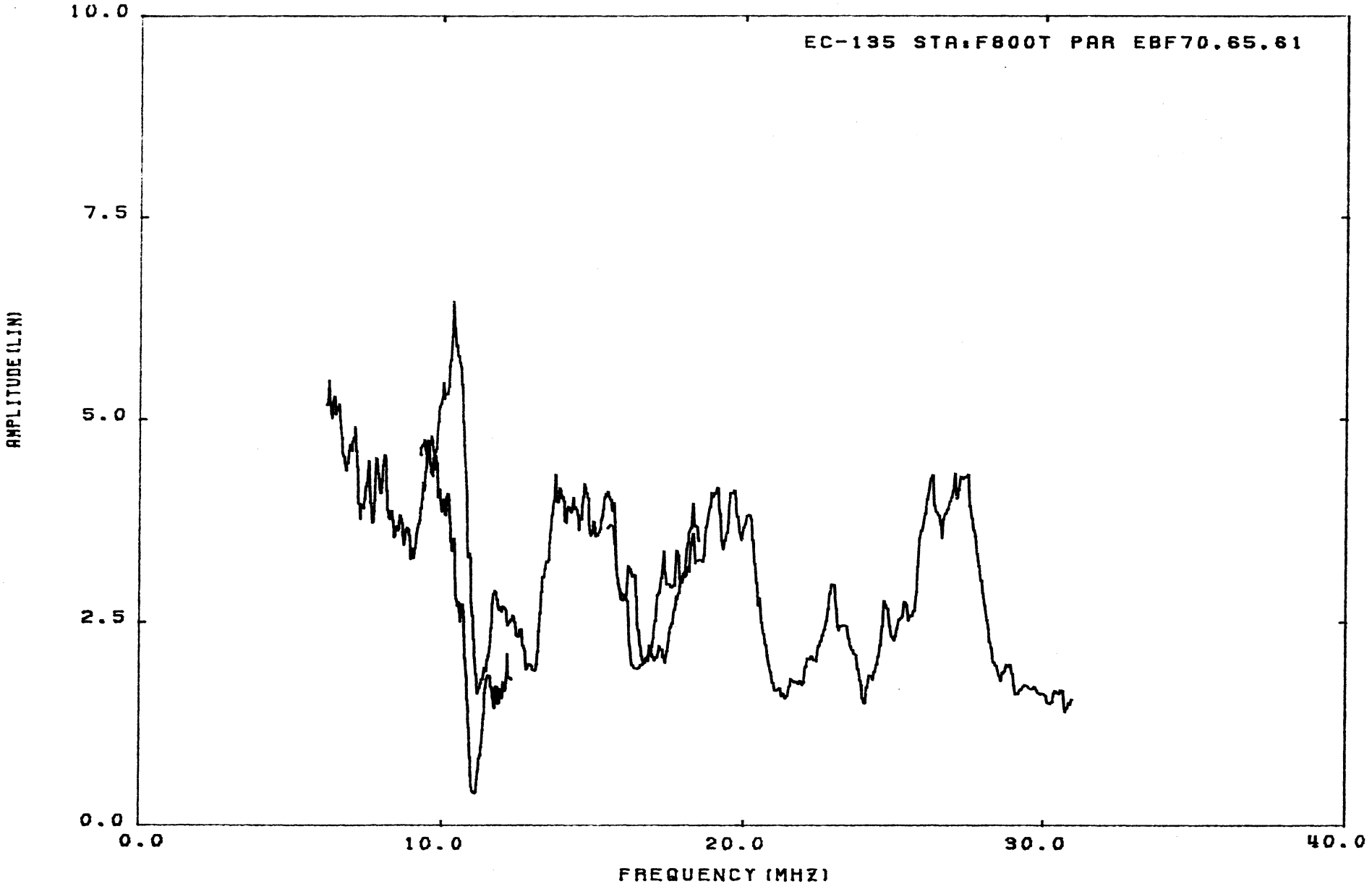

Figure 42a. Current density at STA:F800T, symmetric excitation, without HF wires (0-40 MHz).

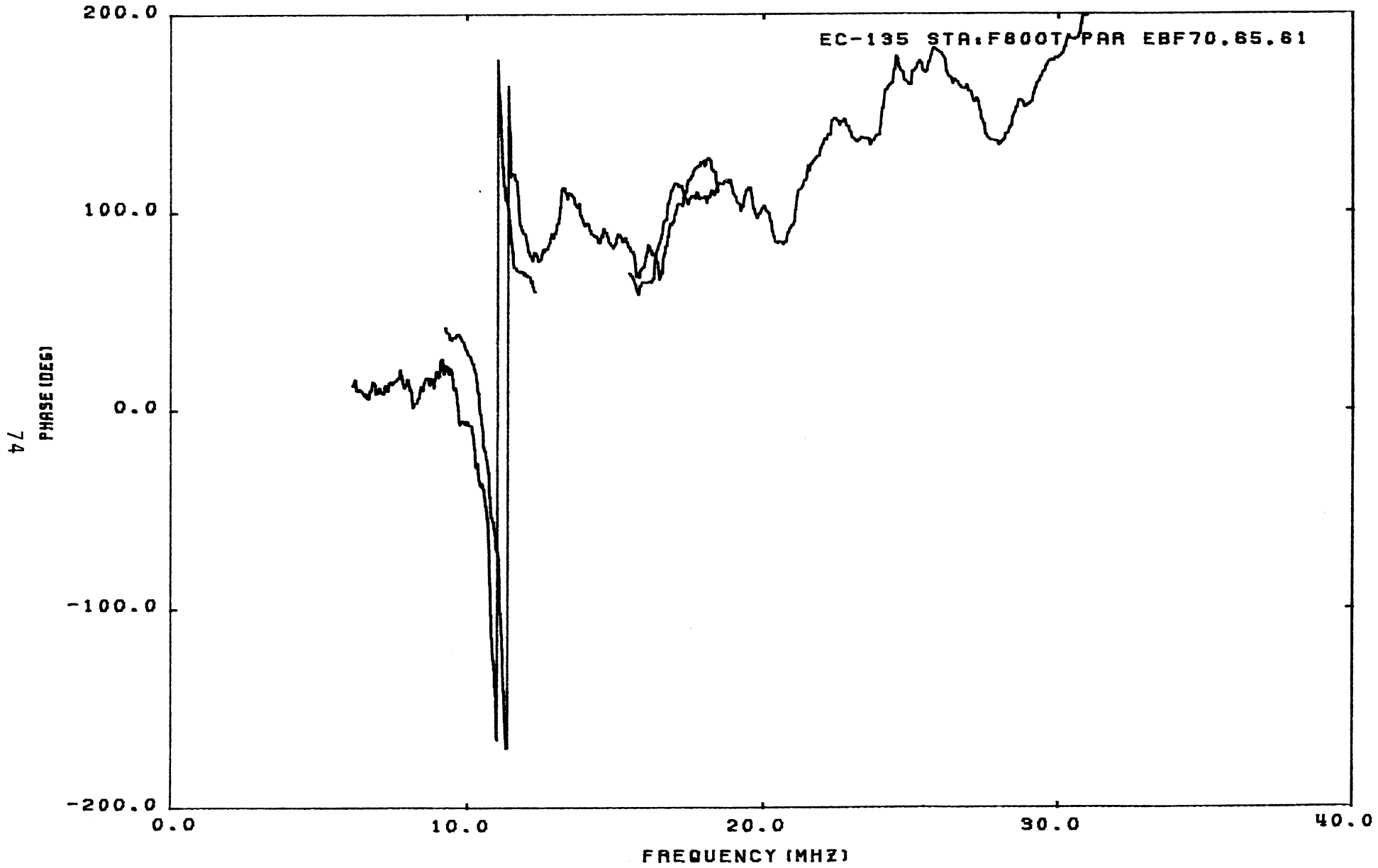

Figure 42b. Current phase at STA:F800T, symmetric excitation, without HF wires (0-40MHz).

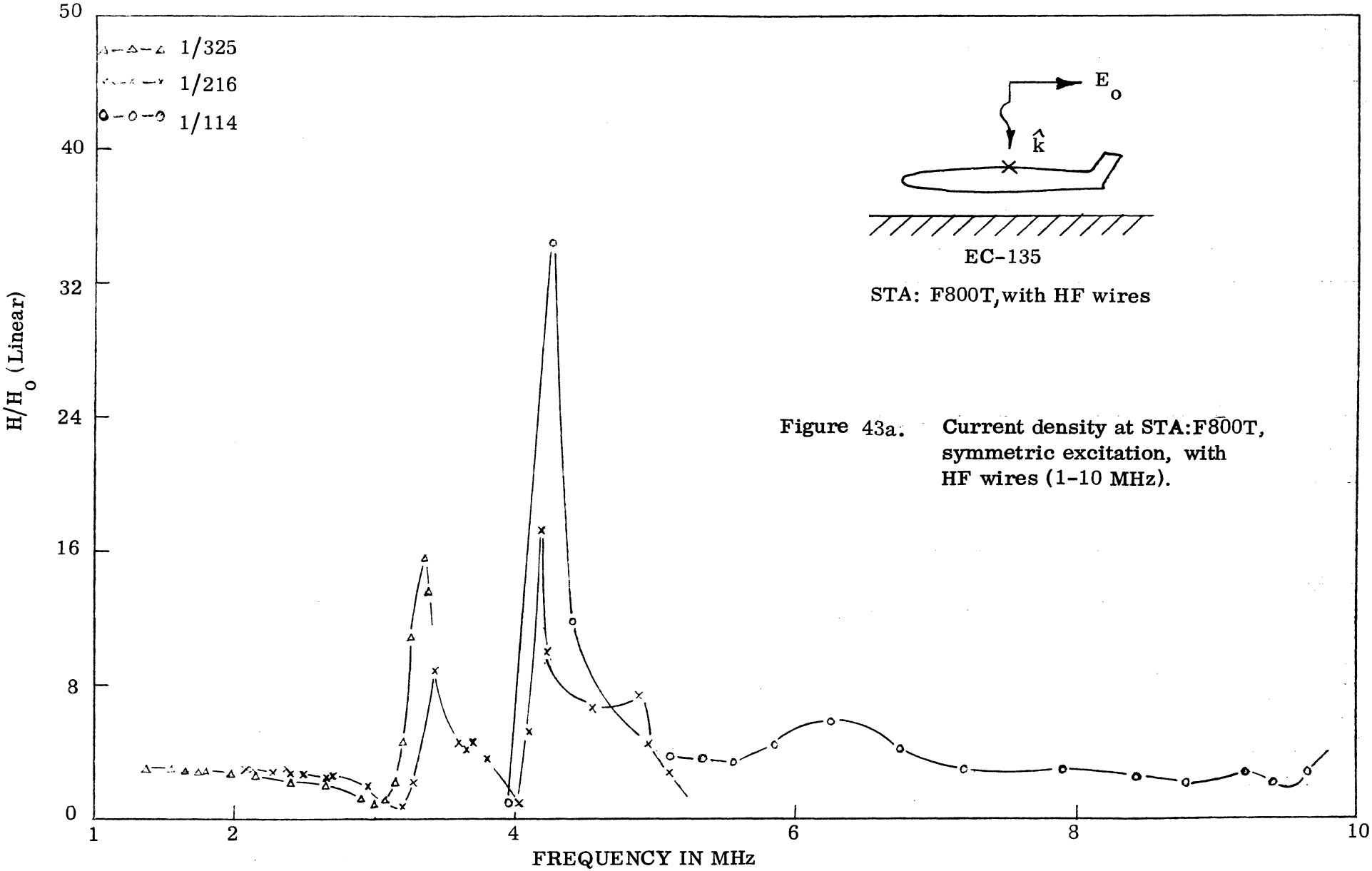

Figure 43a. Current density at STA:F800T, symmetric excitation, with HF wires (1-10 MHz).

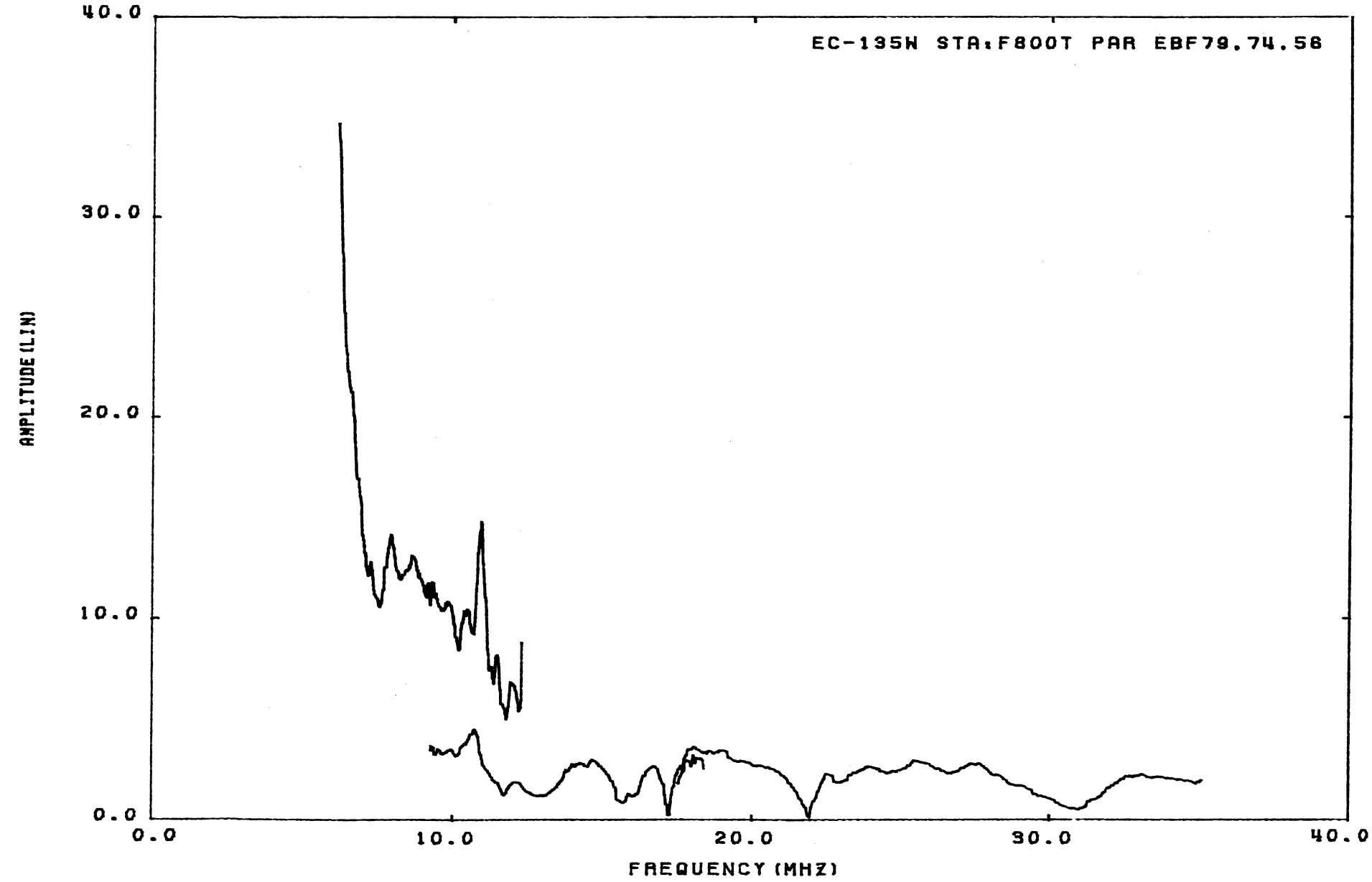

Figure 44a. Current density at STA:F800T, symmetric excitation, with HF wires (0-40 MHz).

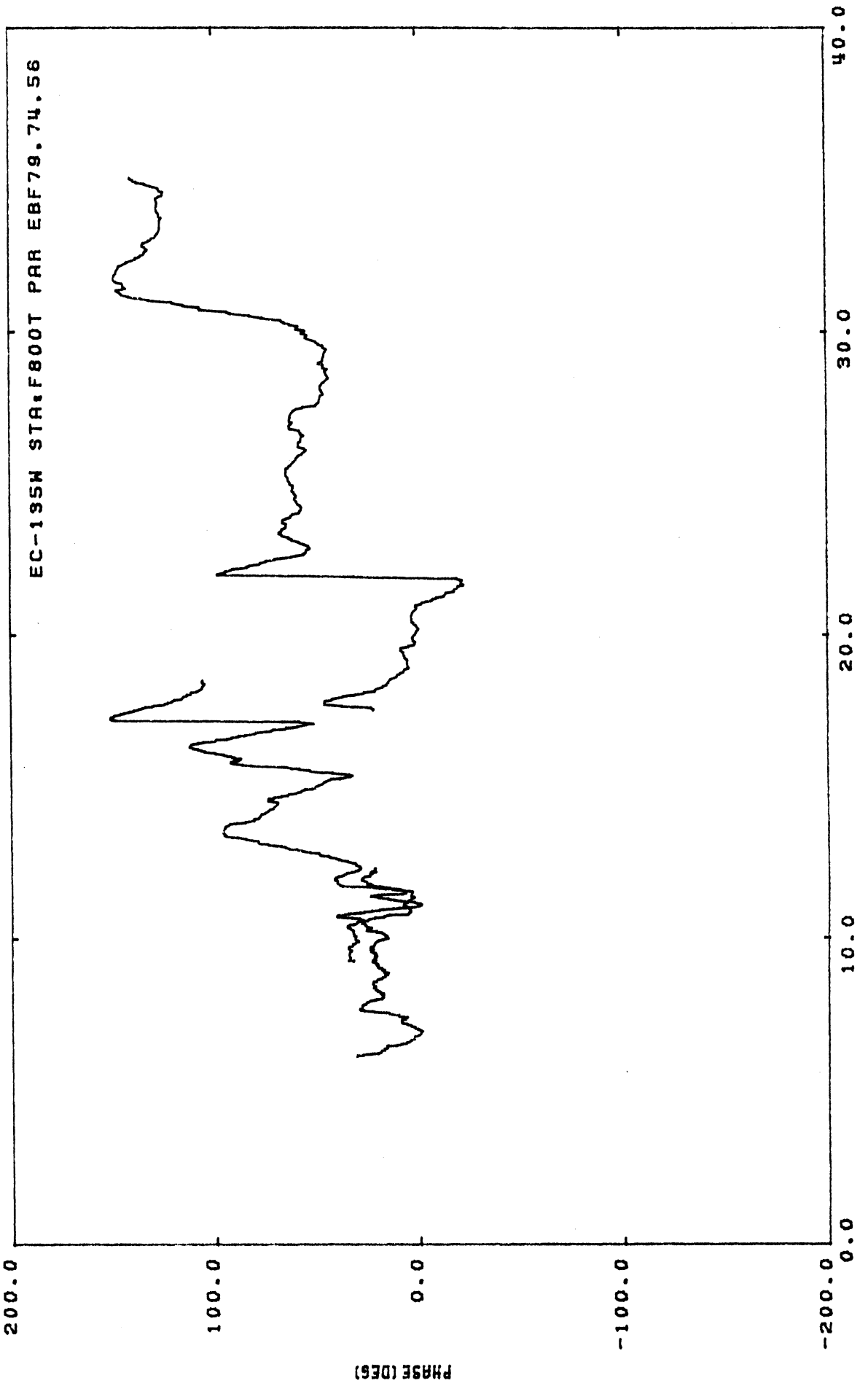

Figure 44b. Current phase at STA:F800T, symmetric excitation, with HF wires (0-40 MHz).

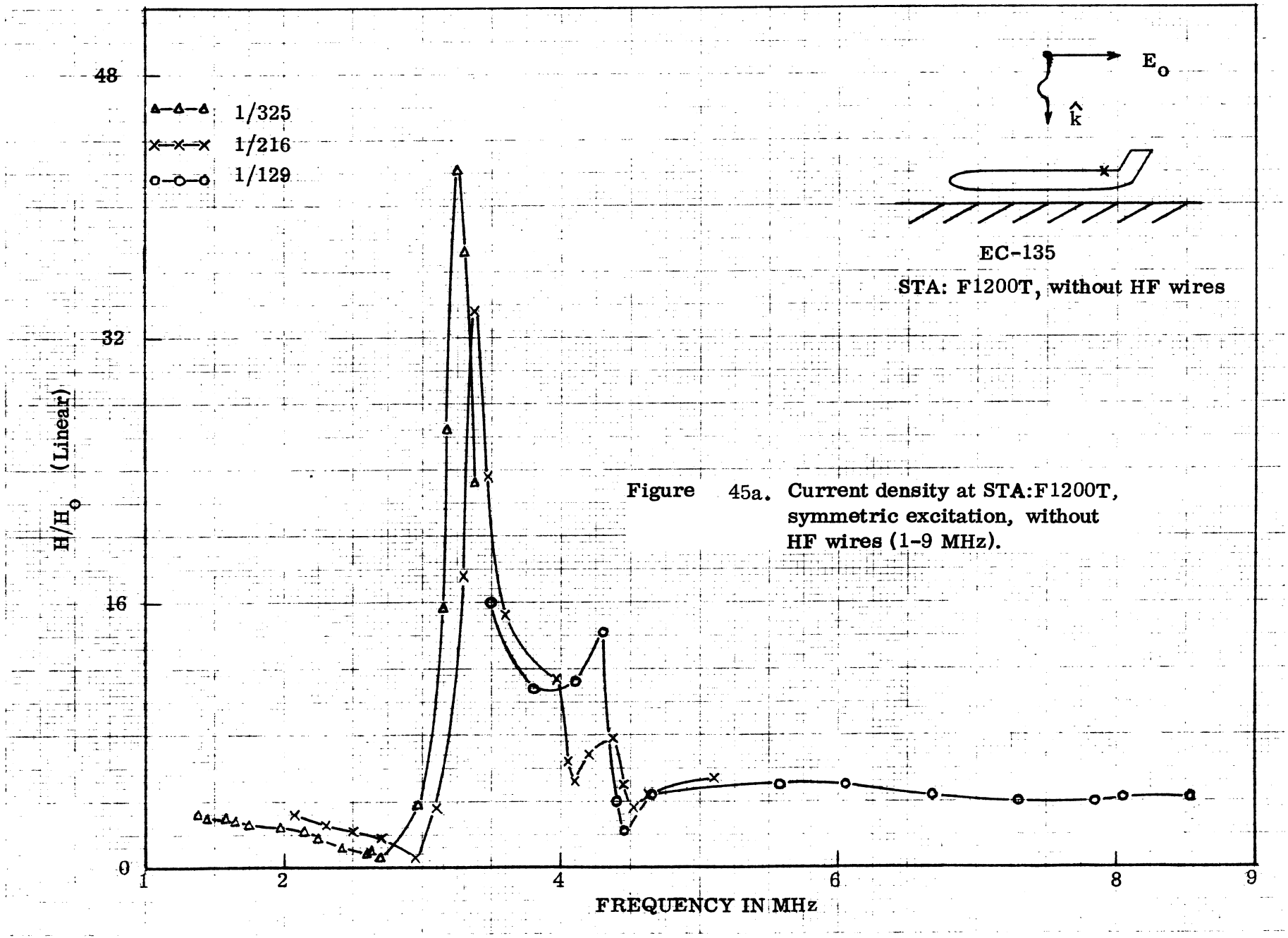

Figure 45a. Current density at STA:F1200T, symmetric excitation, without HF wires (1-9 MHz).

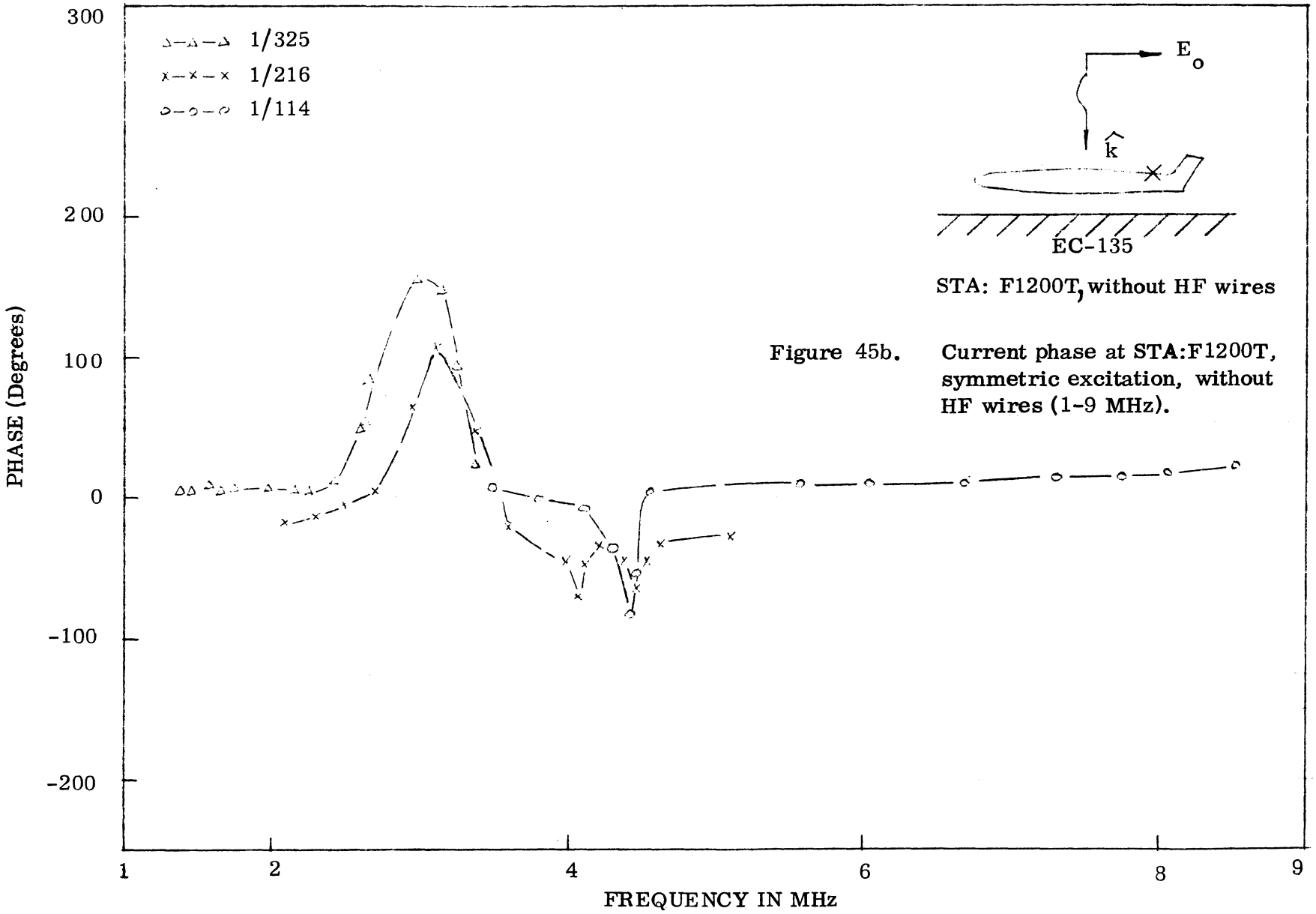

Figure 45b. Current phase at STA:F1200T, symmetric excitation, without HF wires (1-9 MHz).

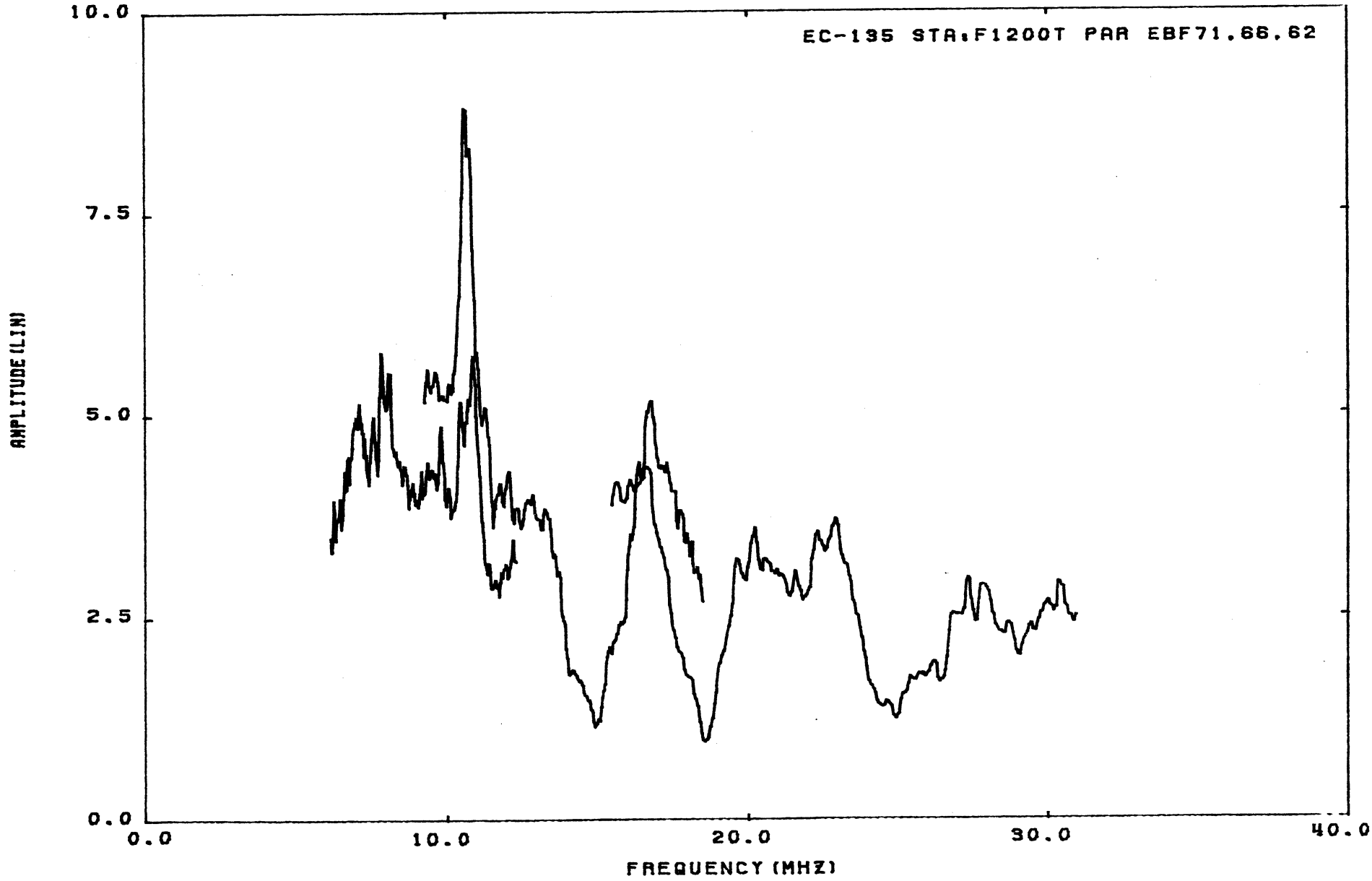

Figure 46a. Current density at STA:F1200T, symmetric excitation, without HF wires (0-40 MHz).

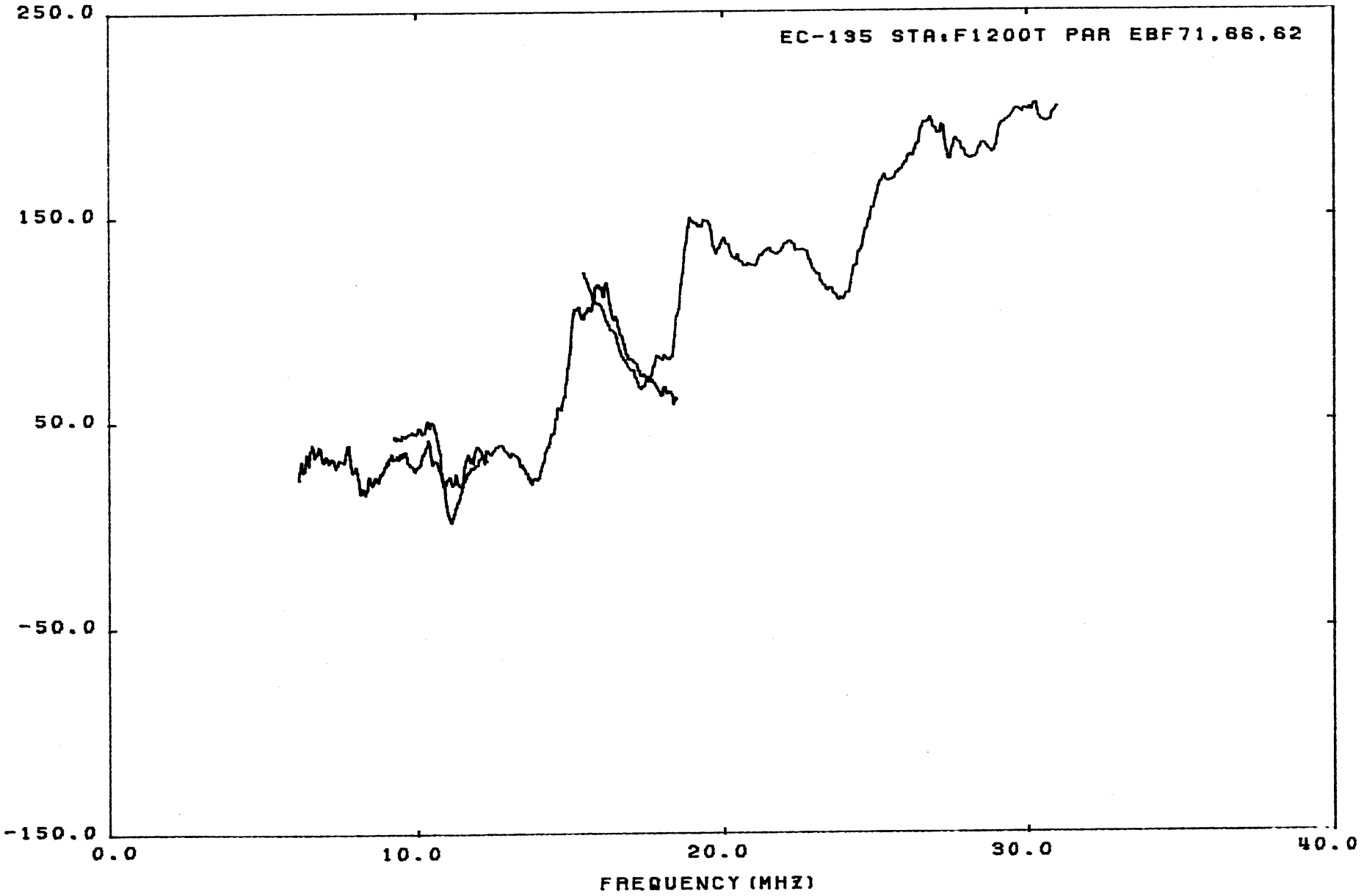

Figure 46b. Current phase at STA:F1200T, symmetric excitation, without HF wires (0-40 MHz).

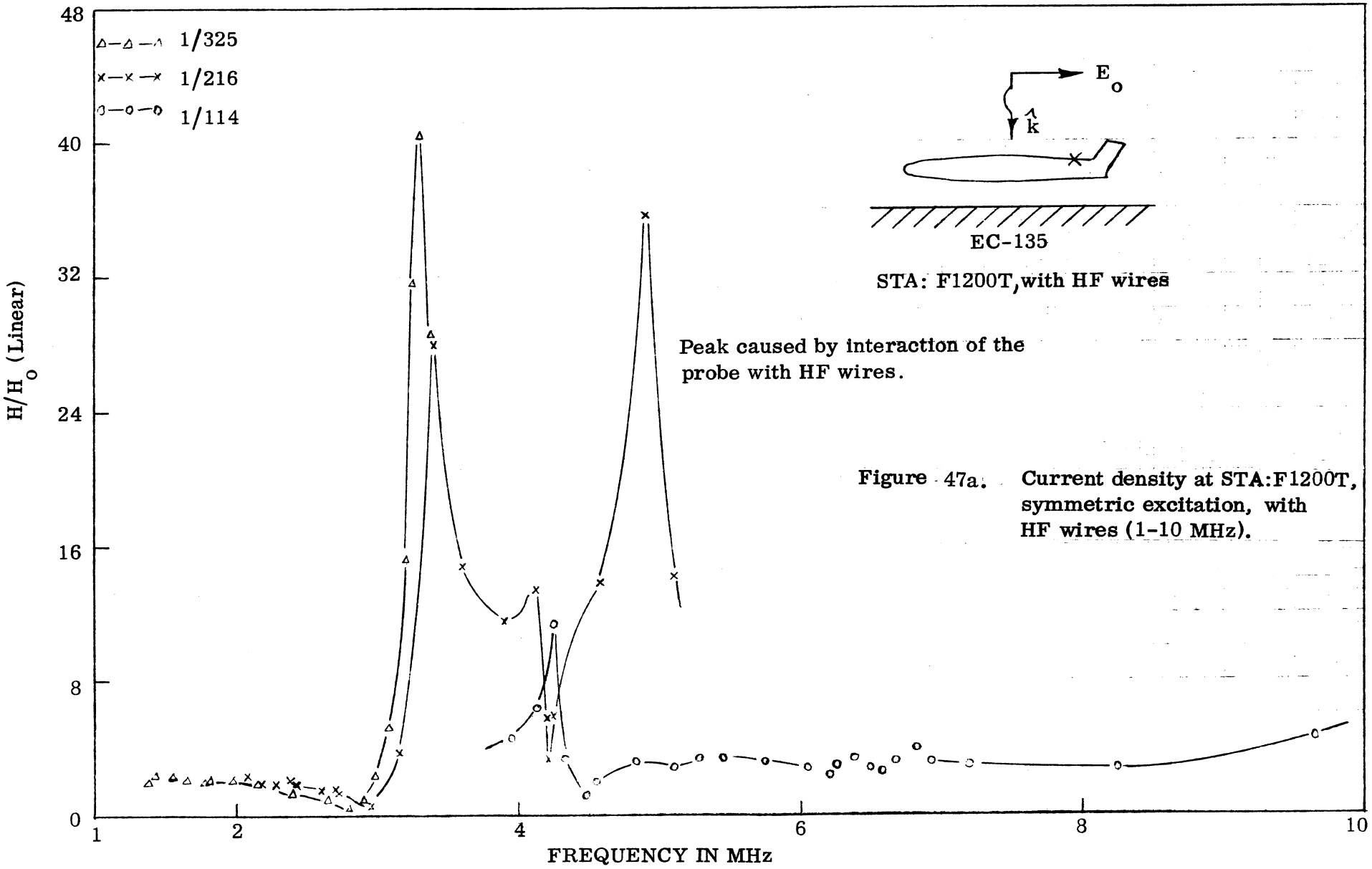

Figure 47a. Current density at STA:F1200T, symmetric excitation, with HF wires (1-10 MHz).

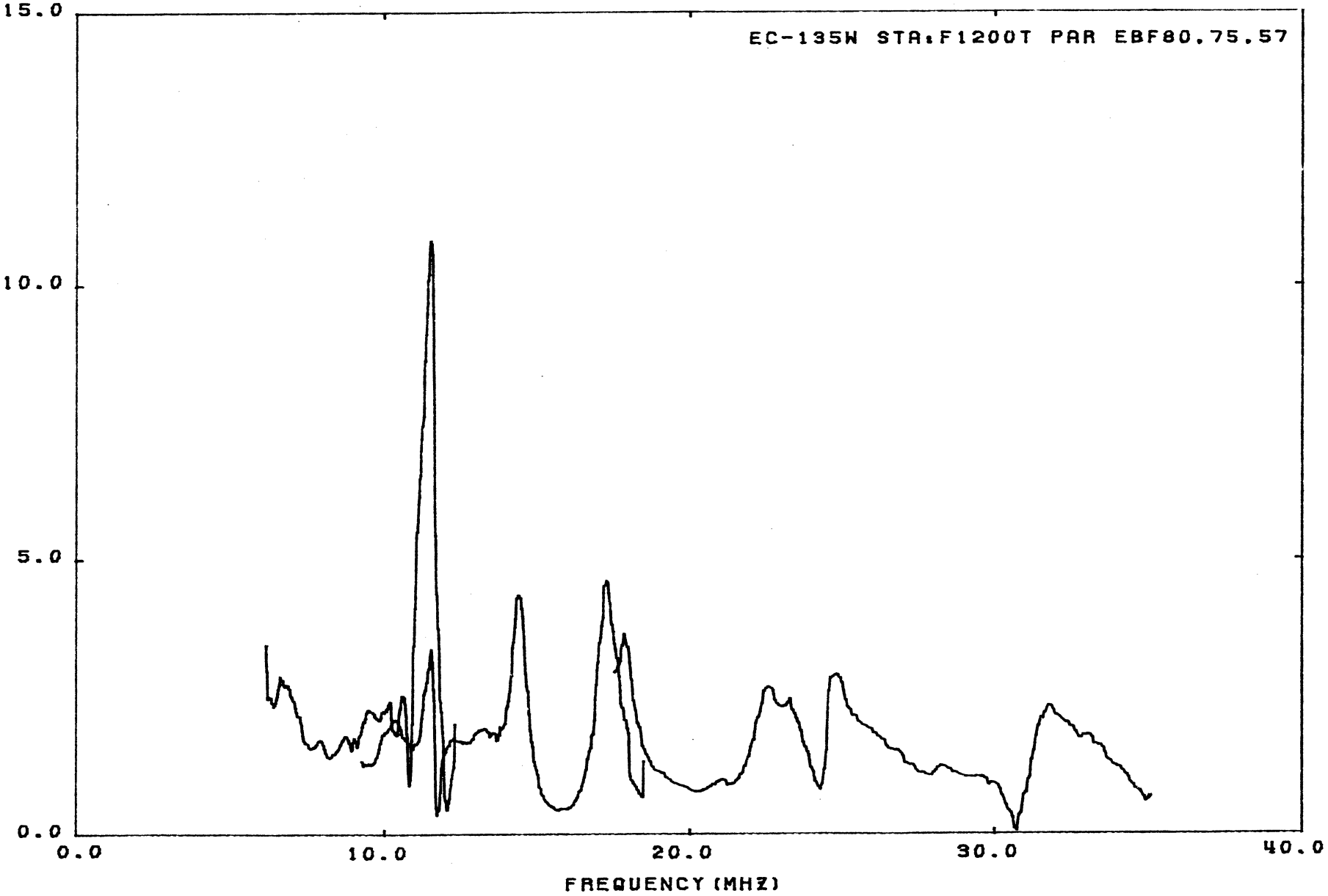

Figure 48a. Current density at STA:F1200T, symmetric excitation, with HF wires (0-40 MHz).

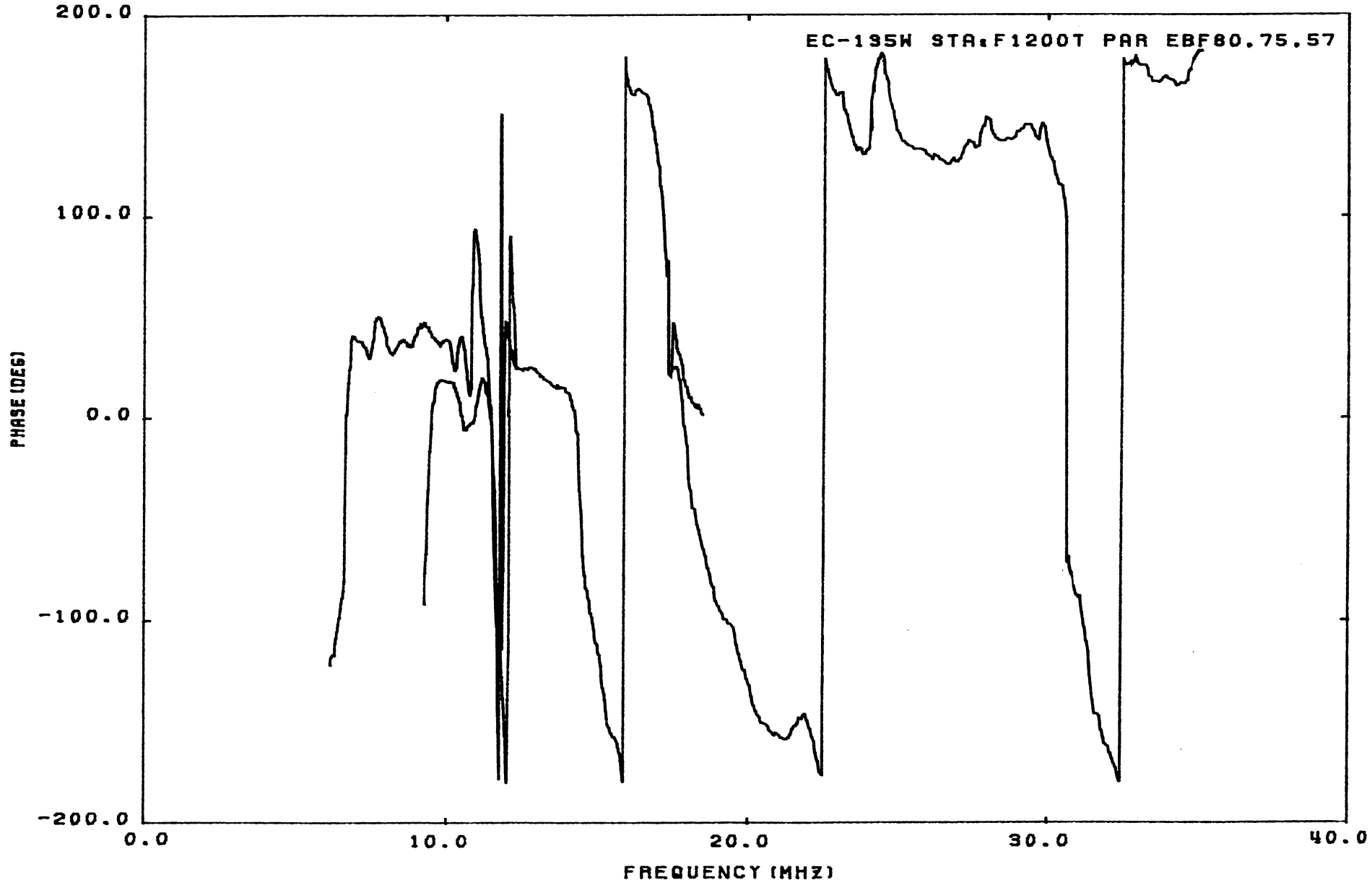

Figure 48b. Current phase at STA:F1200T, symmetric excitation, with HF wires (0-40 MHz).

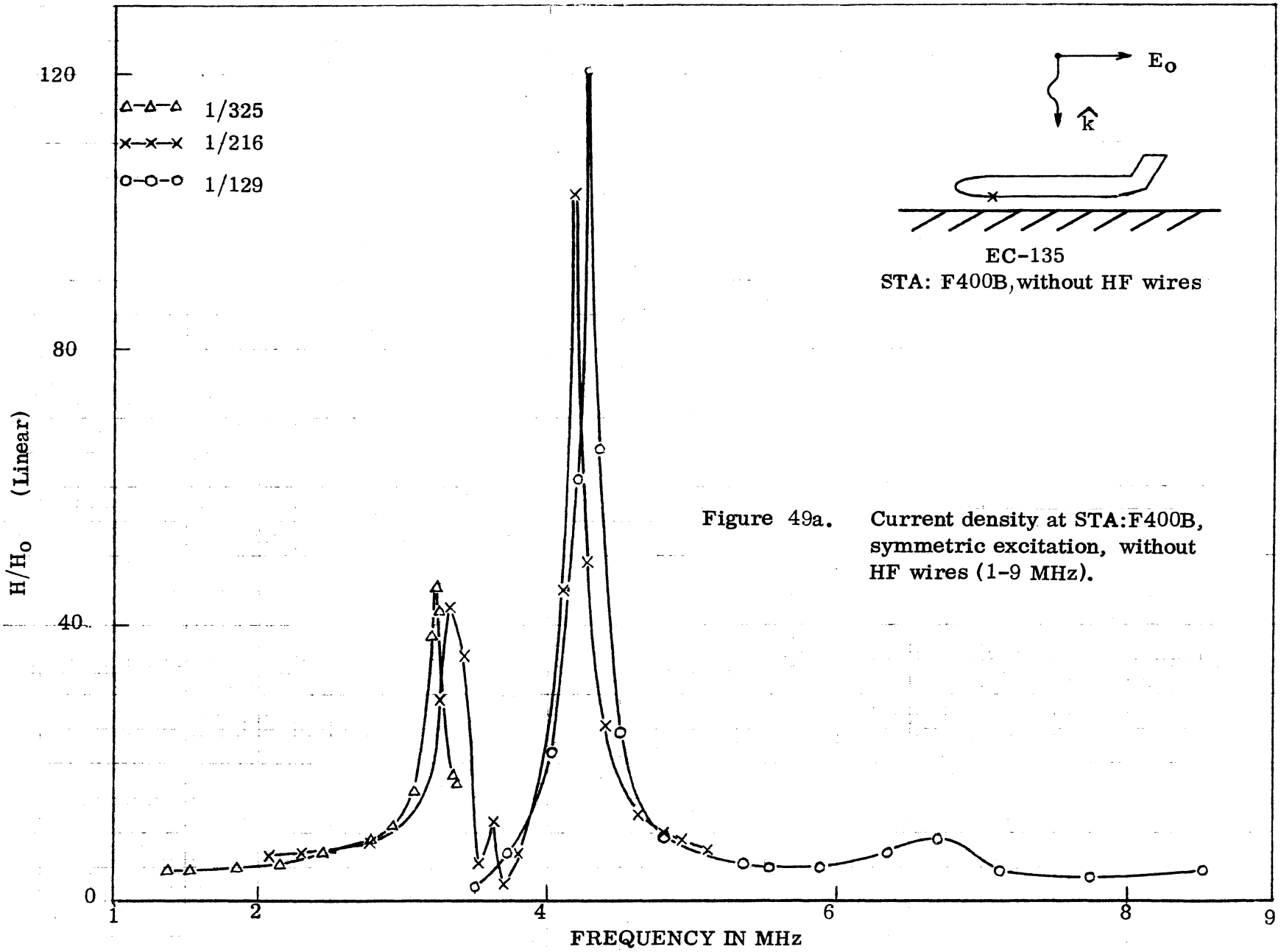

Figure 49a. Current density at STA:F400B, symmetric excitation, without HF wires (1-9 MHz).

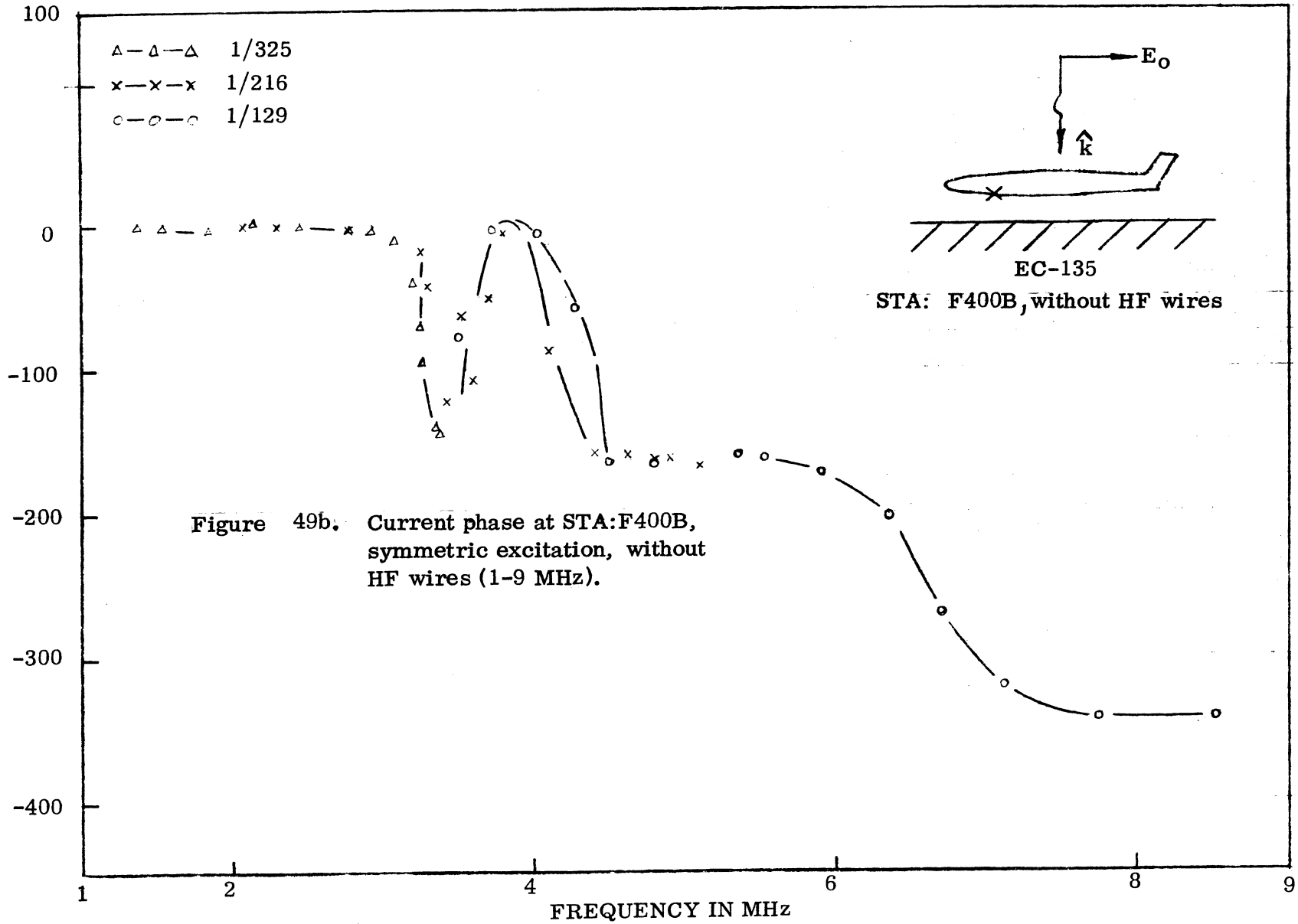

Figure 49b. Current phase at STA:F400B, symmetric excitation, without HF wires (1-9 MHz).

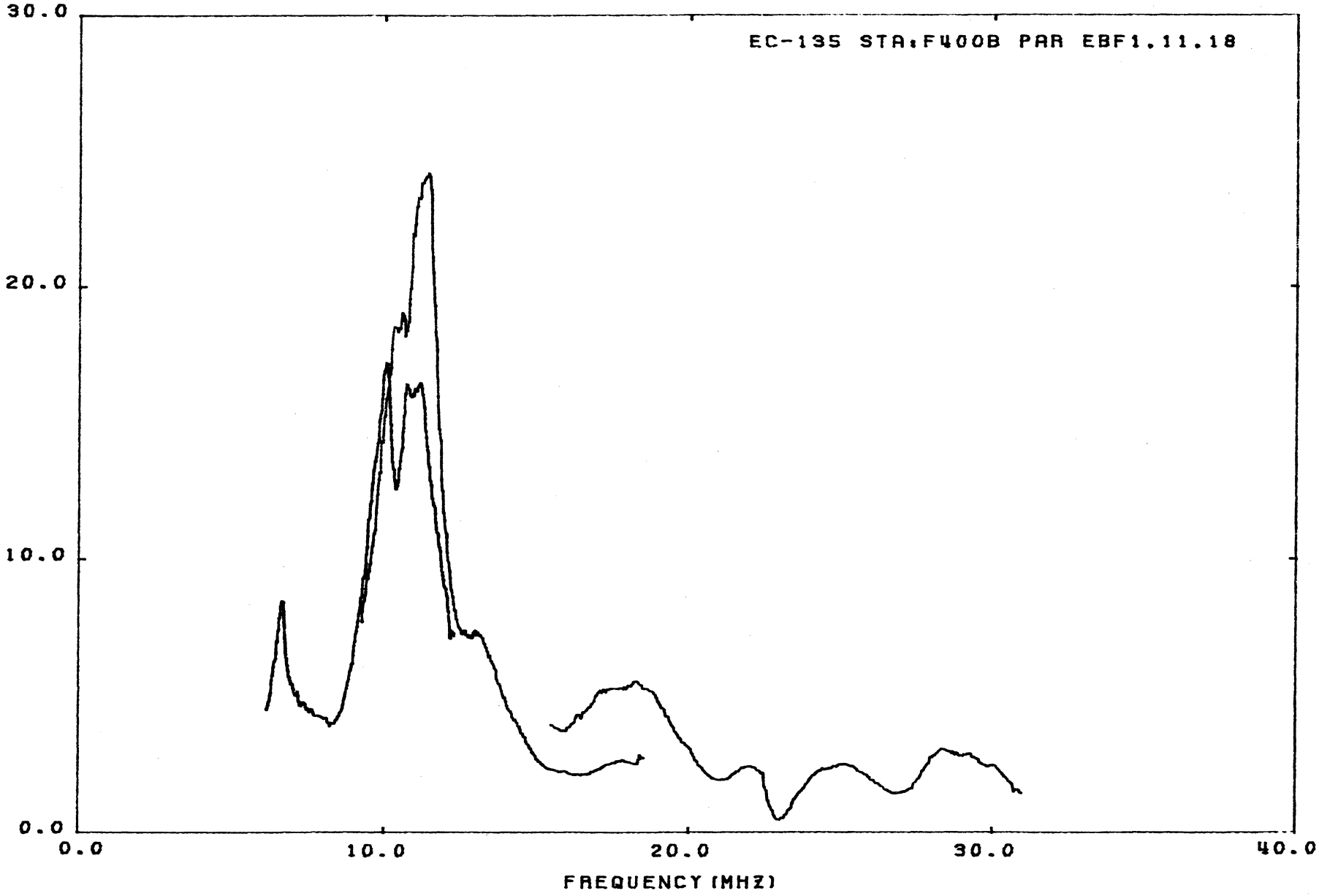

Figure 50a. Current density at STA:F400B, symmetric excitation, without HF wires (0-40 MHz).

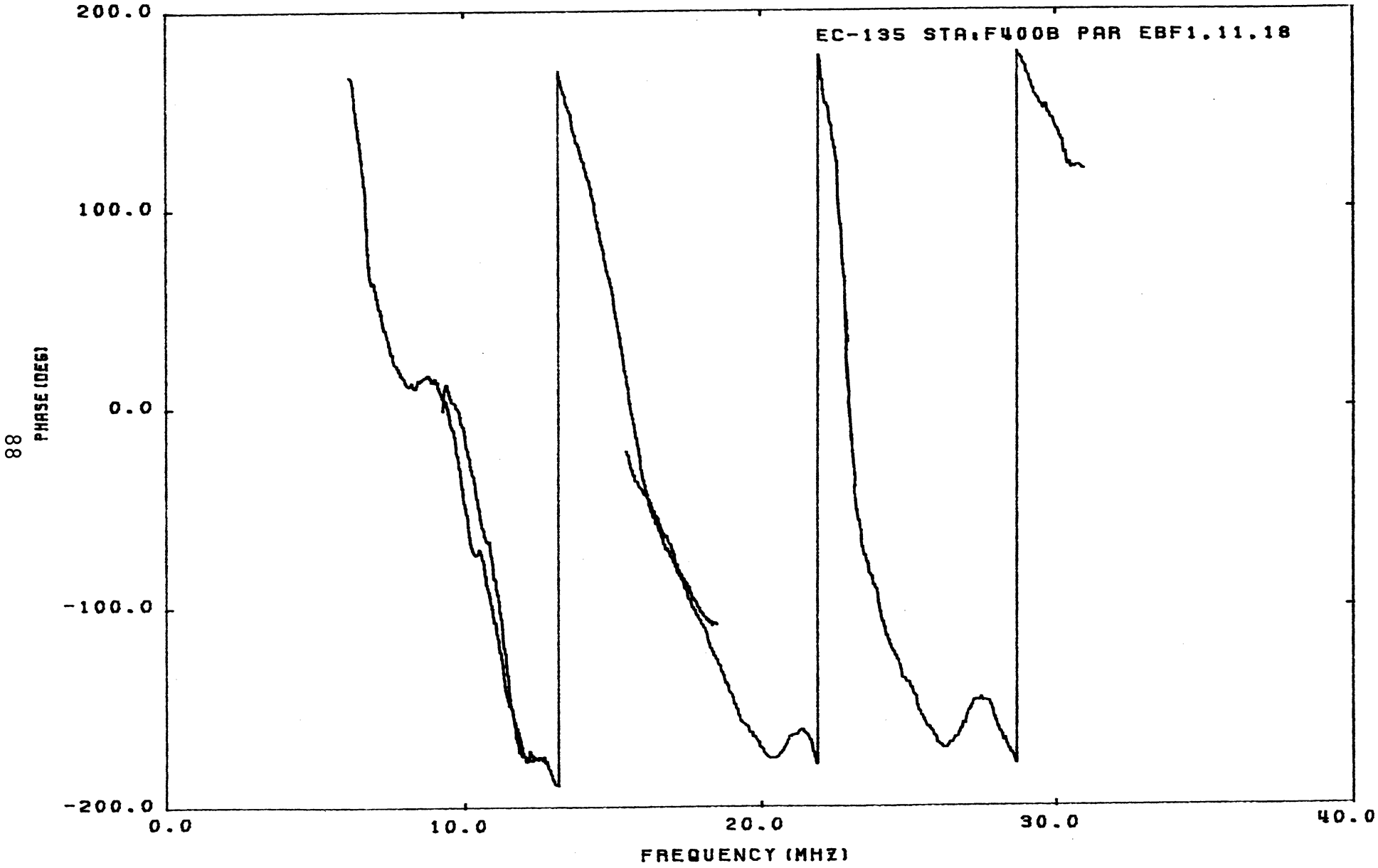

Figure 50b. Current phase at STA:F400B, symmetric excitation, without HF wires (0-40 MHz).

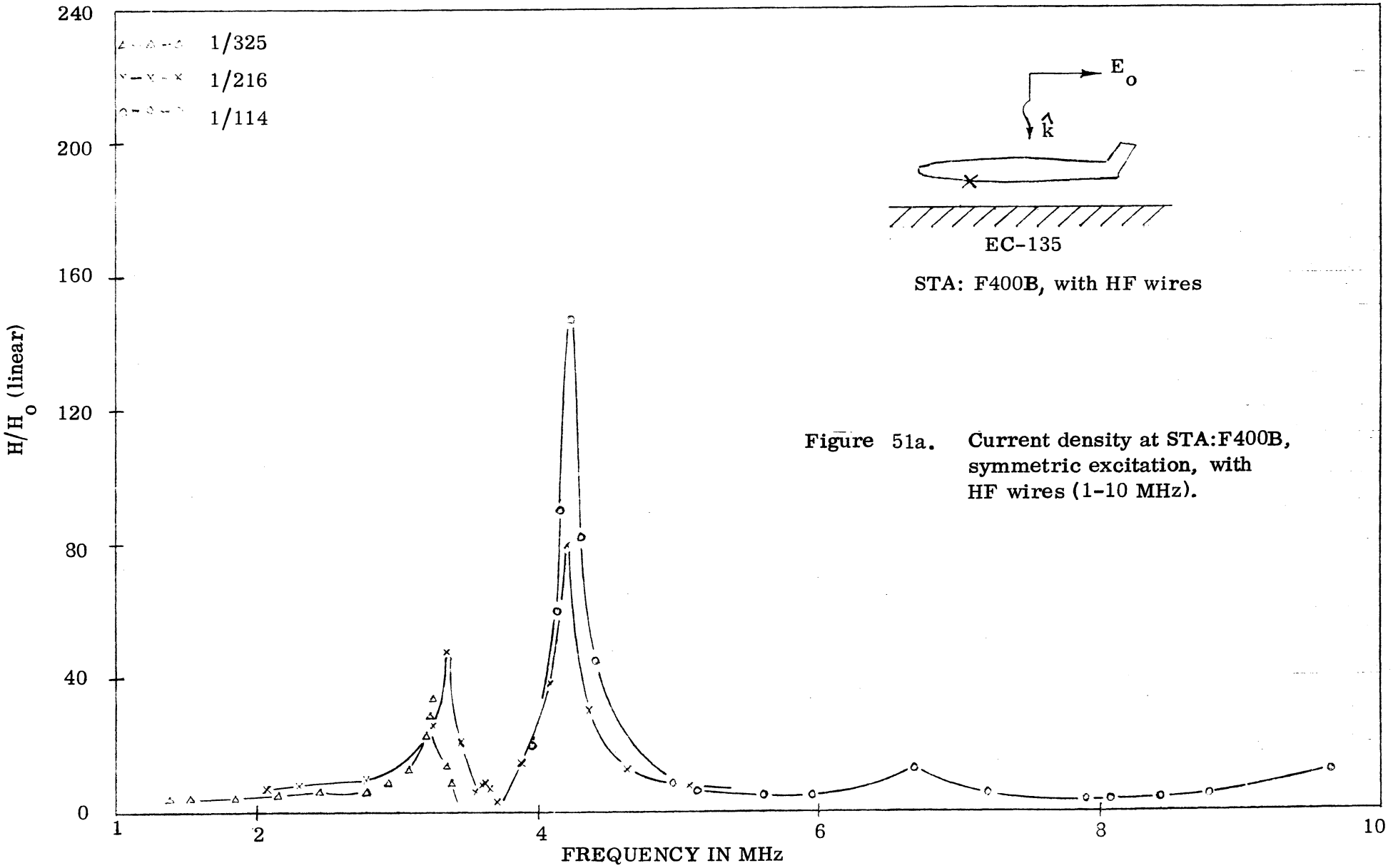

Figure 51a. Current density at STA:F400B, symmetric excitation, with HF wires (1-10 MHz).

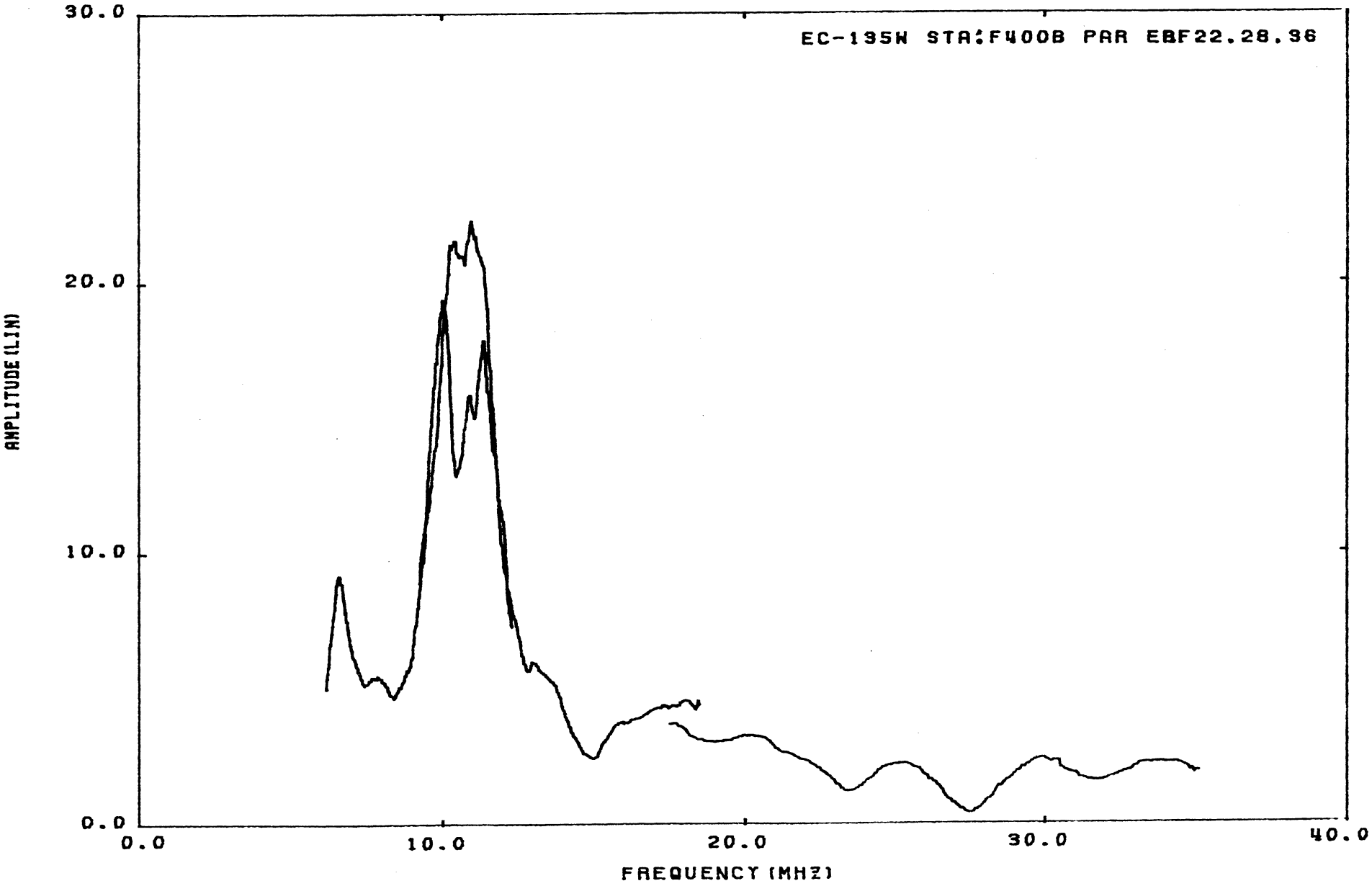

Figure 52a. Current density at STA:F400B, symmetric excitation, with HF wires (0-40 MHz).

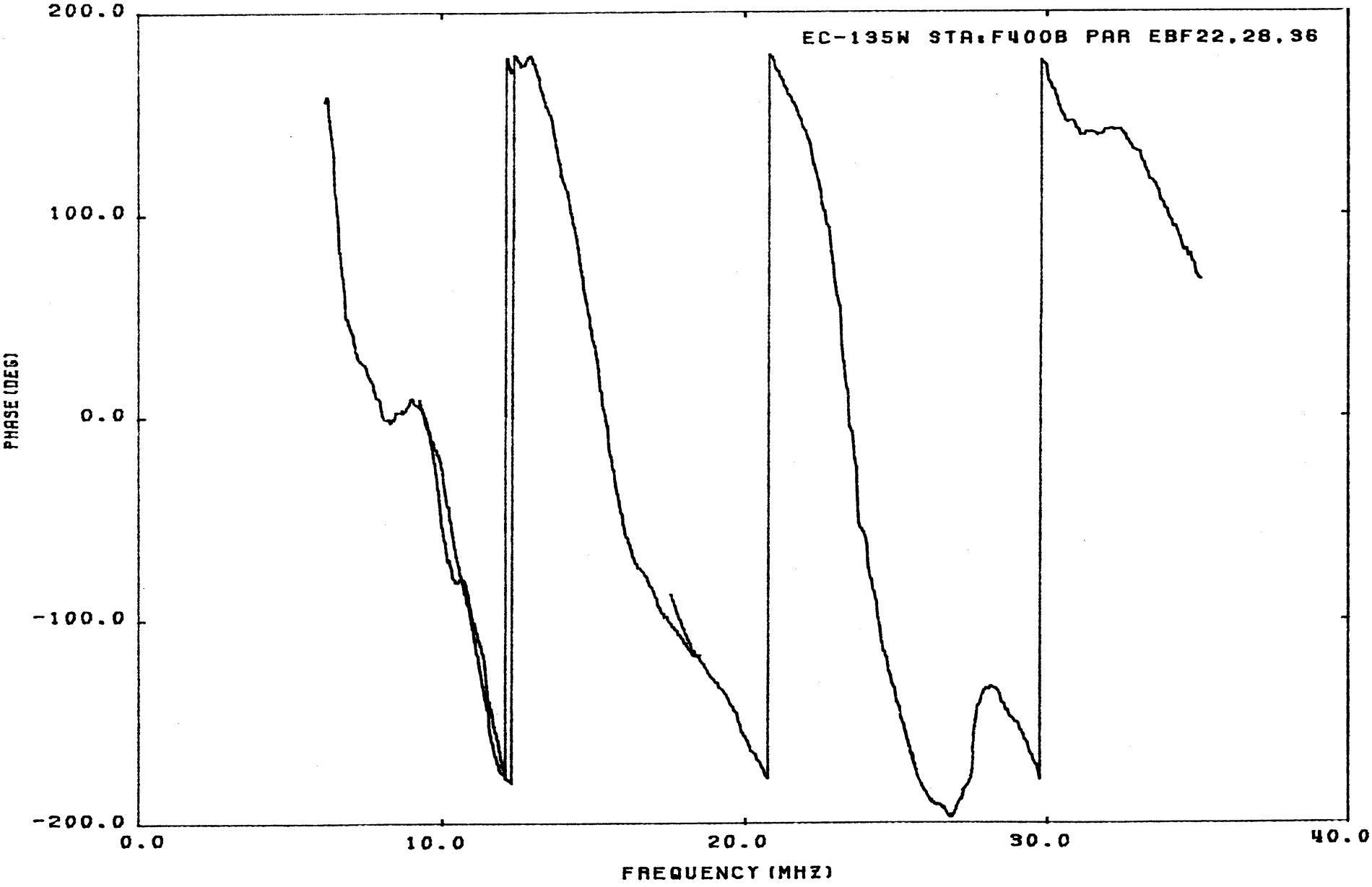

Figure 52b. Current phase at STA:F400B, symmetric excitation, with HF wires (0-40 MHz).

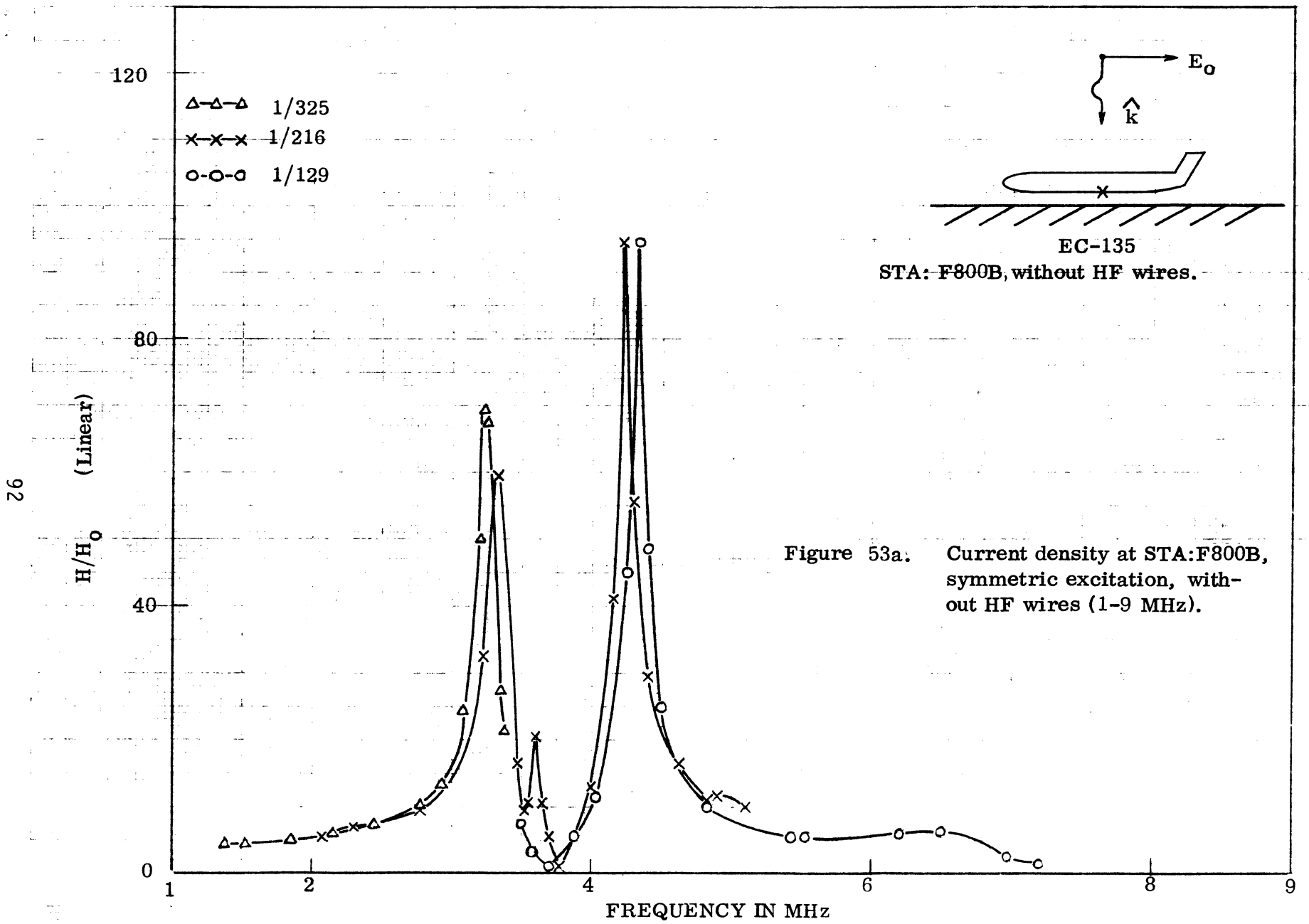

Figure 53a. Current density at STA:F800B, symmetric excitation, without HF wires (1-9 MHz).

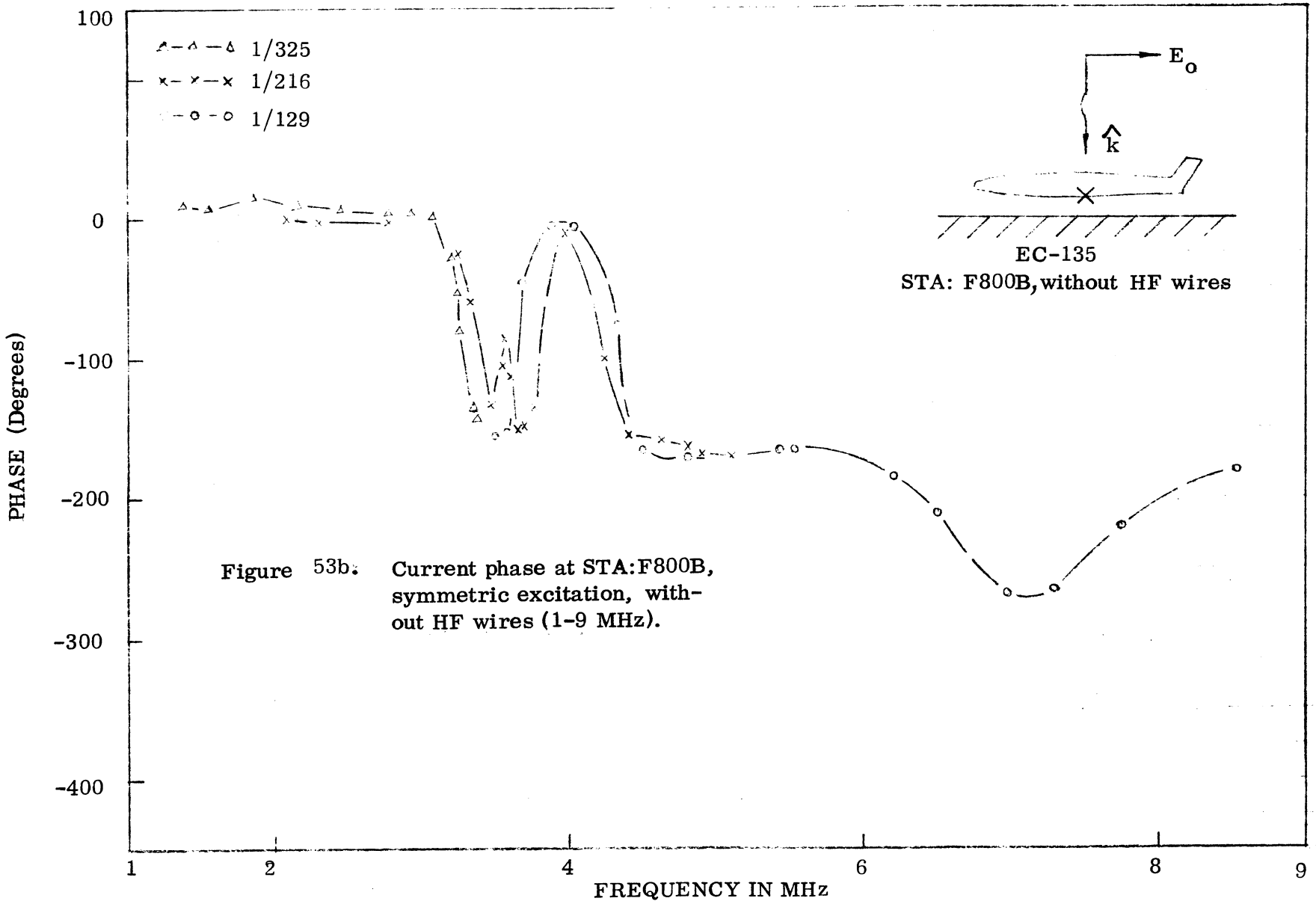

Figure 53b. Current phase at STA:F800B, symmetric excitation, without HF wires (1-9 MHz).

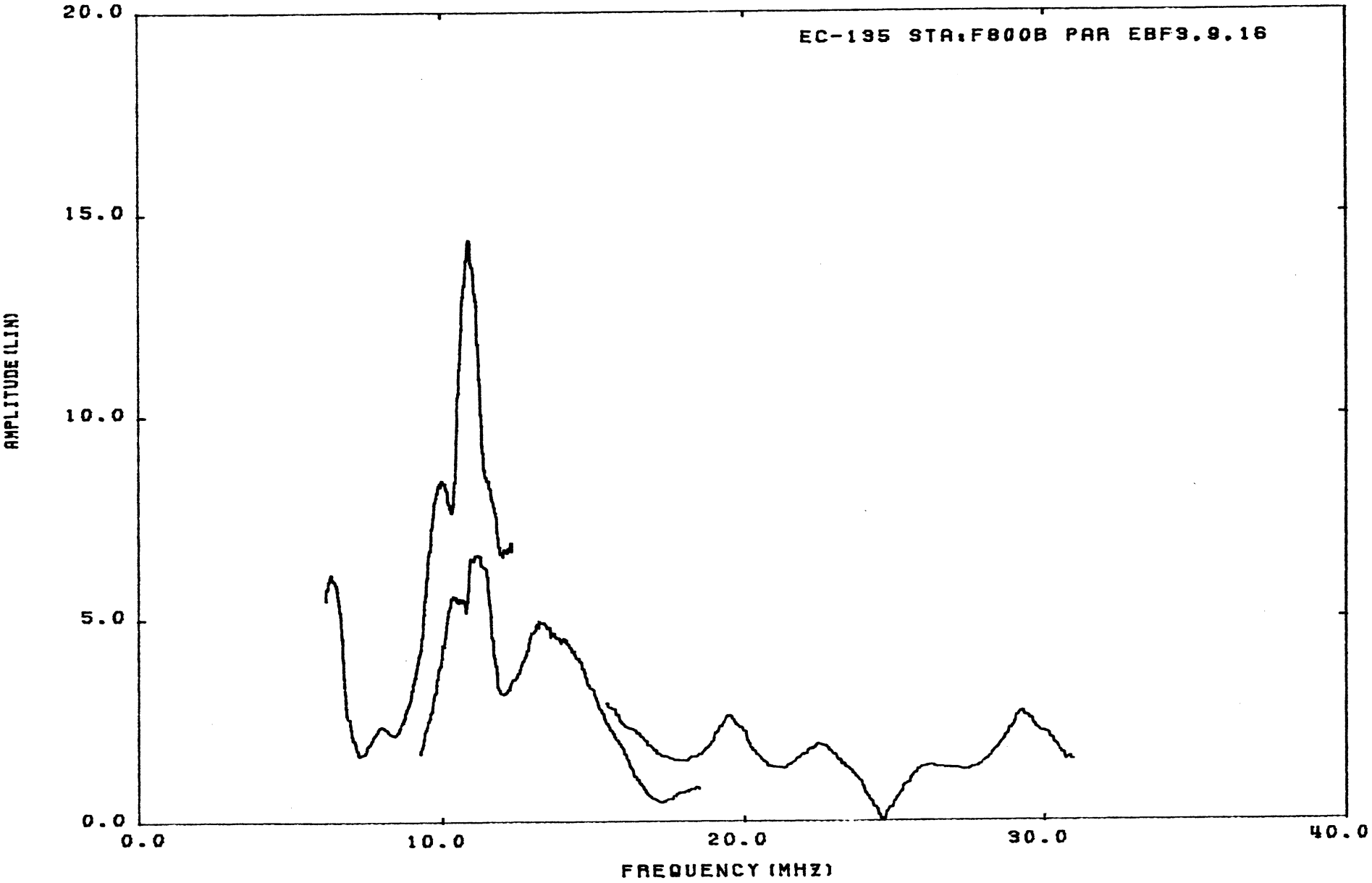

Figure 54a. Current density at STA:F800B, symmetric excitation, without HF wires (0-40 MHz).

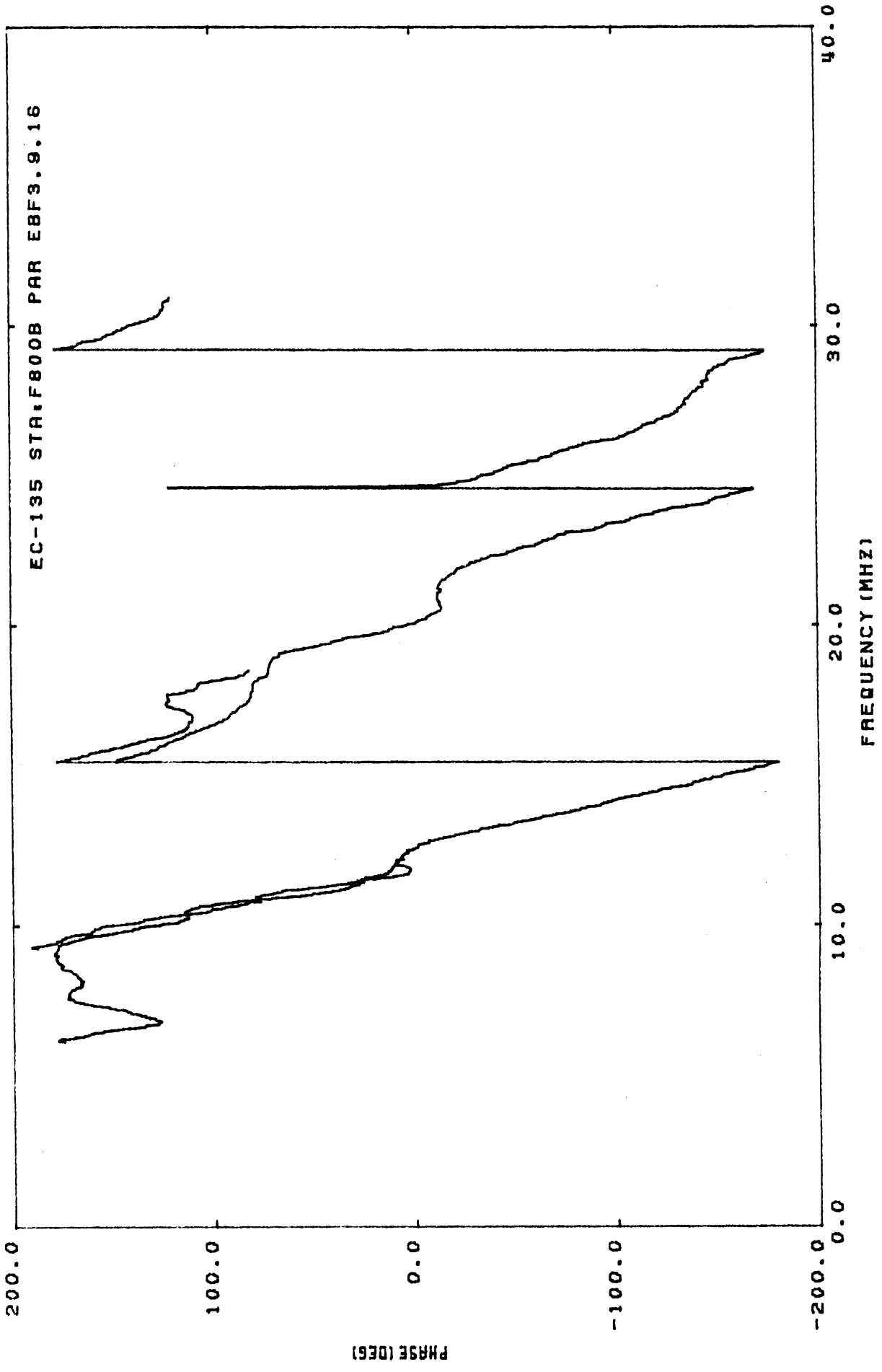

Figure 54b. Current phase at STA:F800B, symmetric excitation, without HF wires (0-40 MHz).

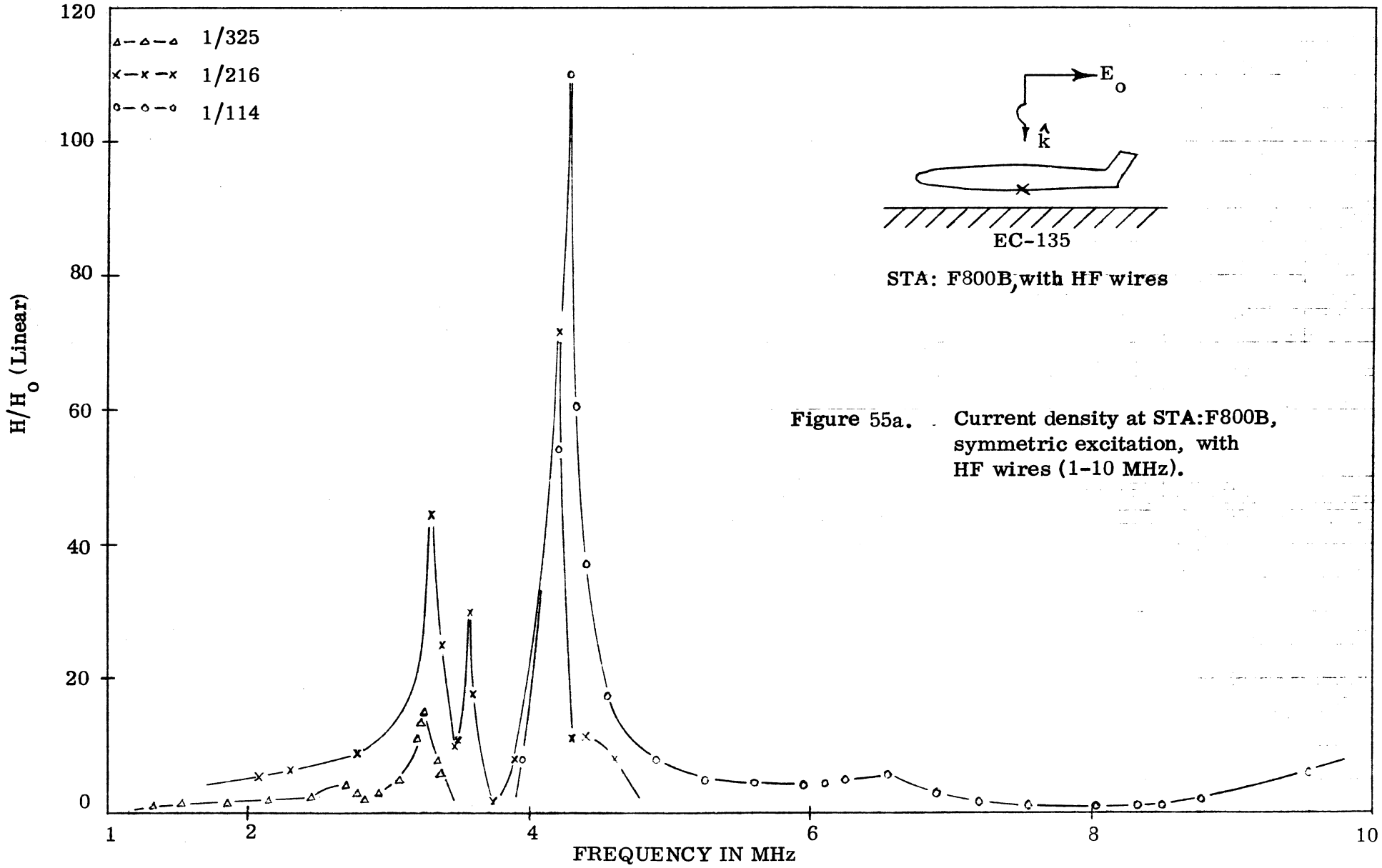

Figure 55a. Current density at STA:F800B, symmetric excitation, with HF wires (1-10 MHz).

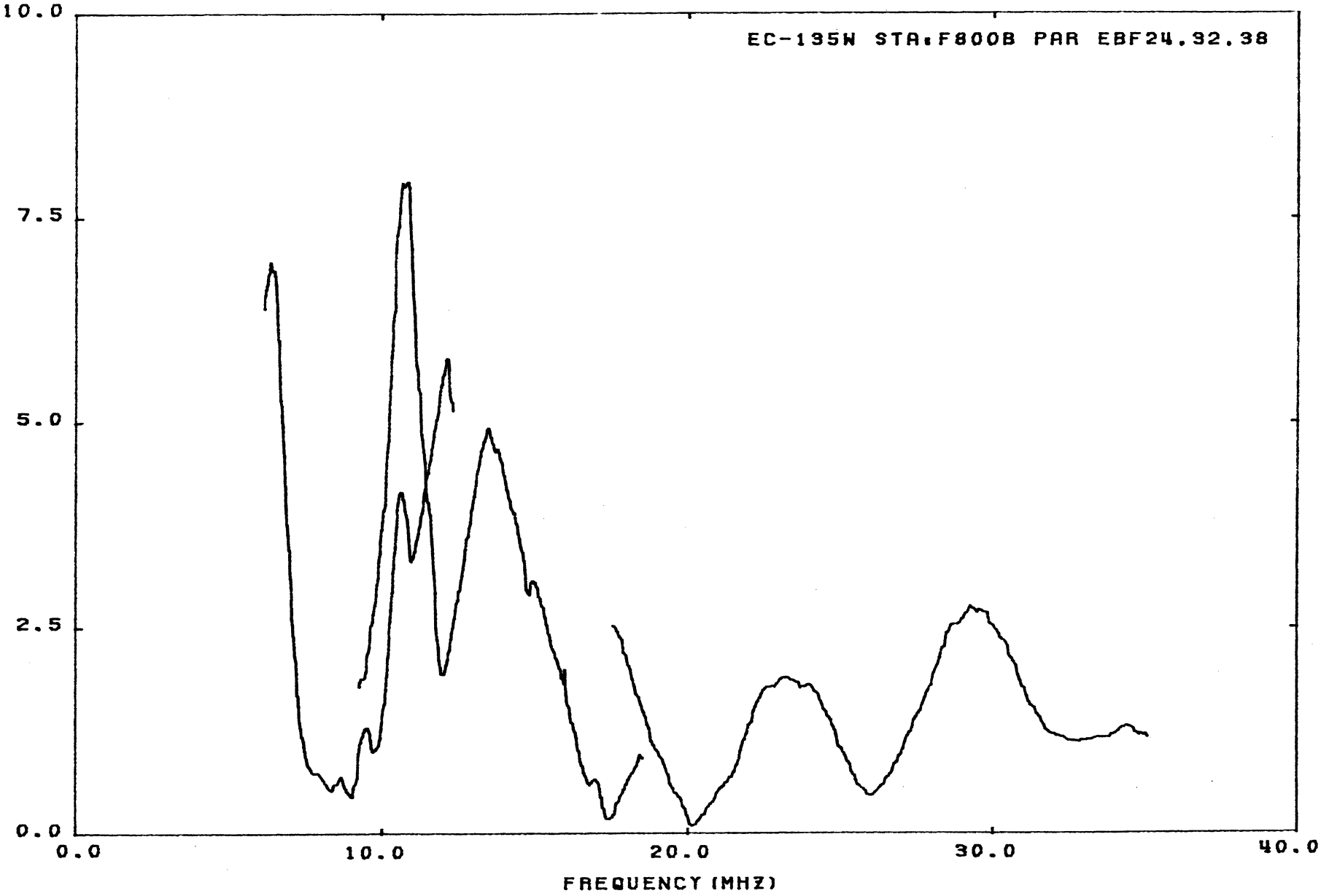

Figure 56a. Current density at STA:F800B, symmetric excitation, with HF wires (0-40 MHz).

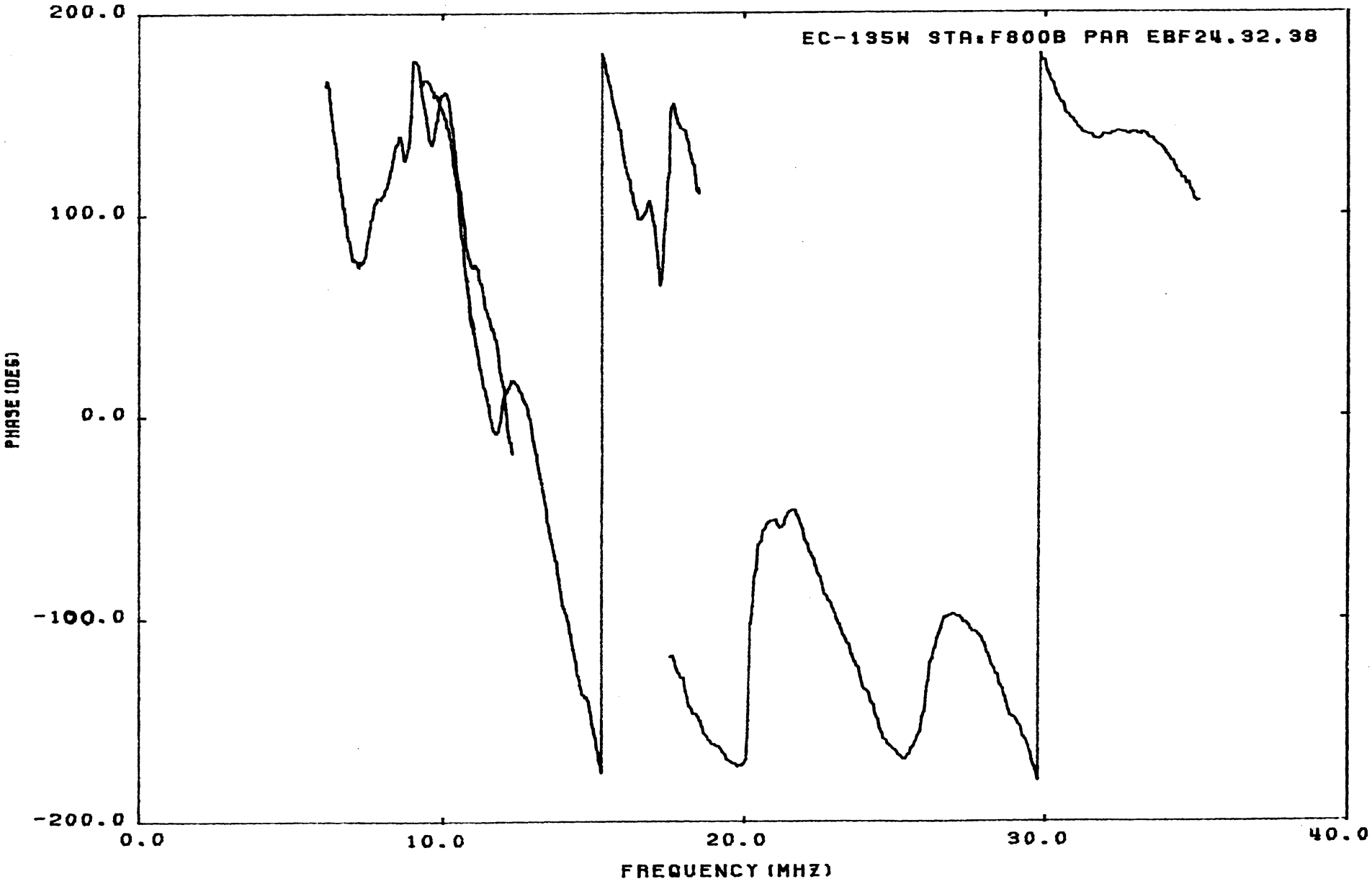

Figure 56b. Current phase at STA:F800B, symmetric excitation, with HF wires (0-40 MHz).

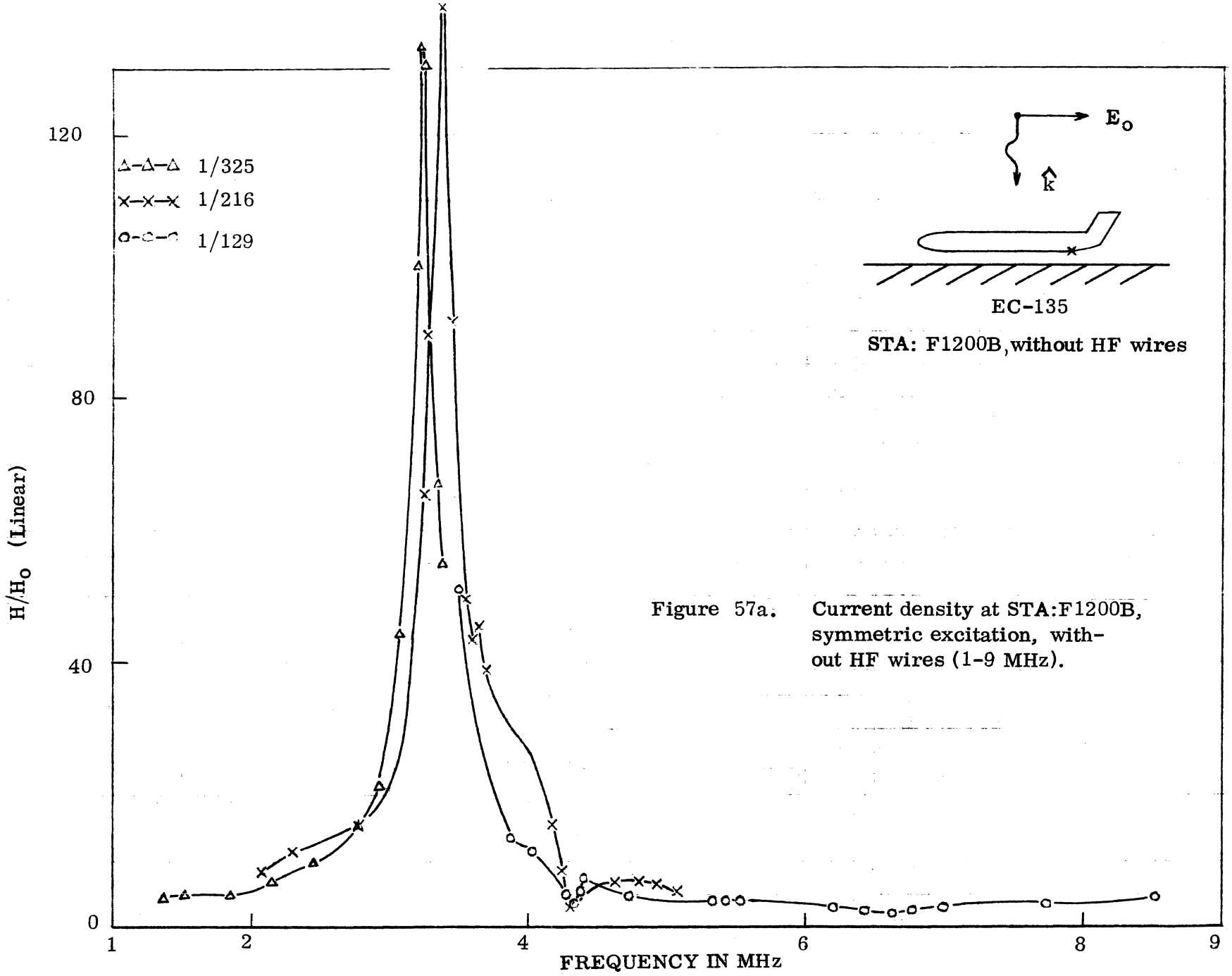

Figure 57a. Current density at STA:F1200B, symmetric excitation, without HF wires (1-9 MHz).

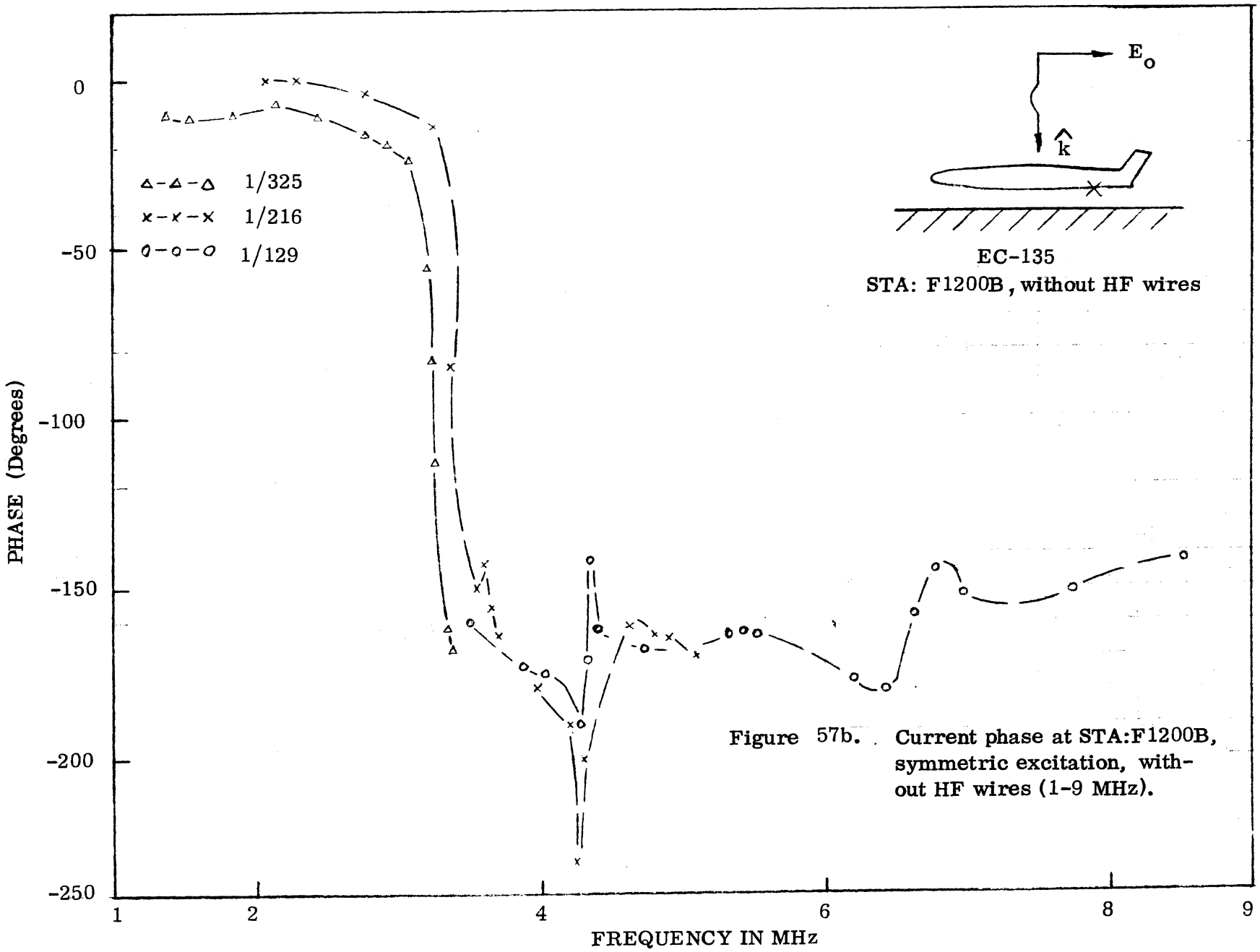

Figure 57b. Current phase at STA:F1200B, symmetric excitation, without HF wires (1-9 MHz).

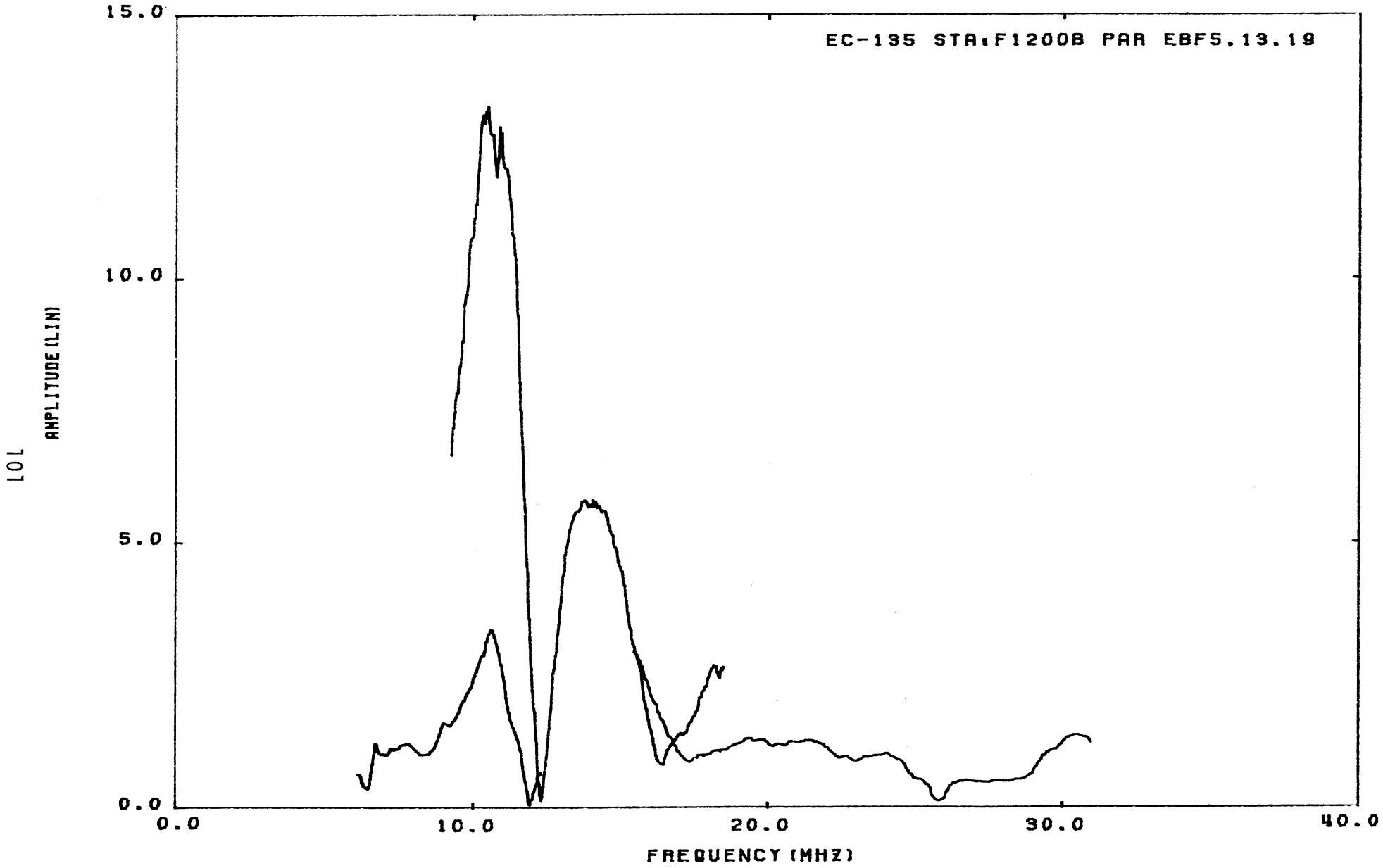

Figure 58a. Current density at STA:F1200B, symmetric excitation, without HF wires (0-40 MHz).

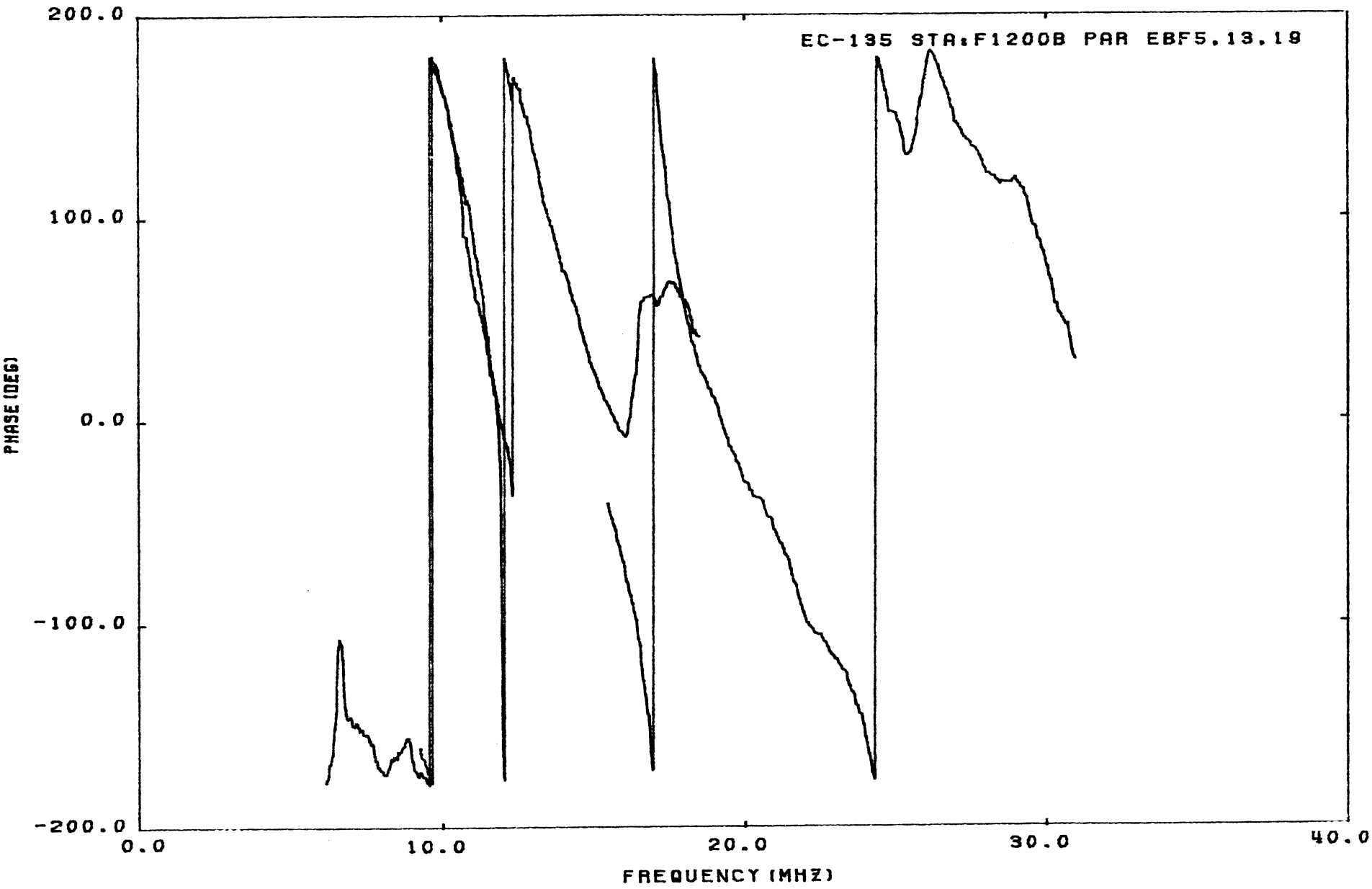

Figure 58b. Current phase at STA:F1200B, symmetric excitation, without HF wires (0-40 MHz).

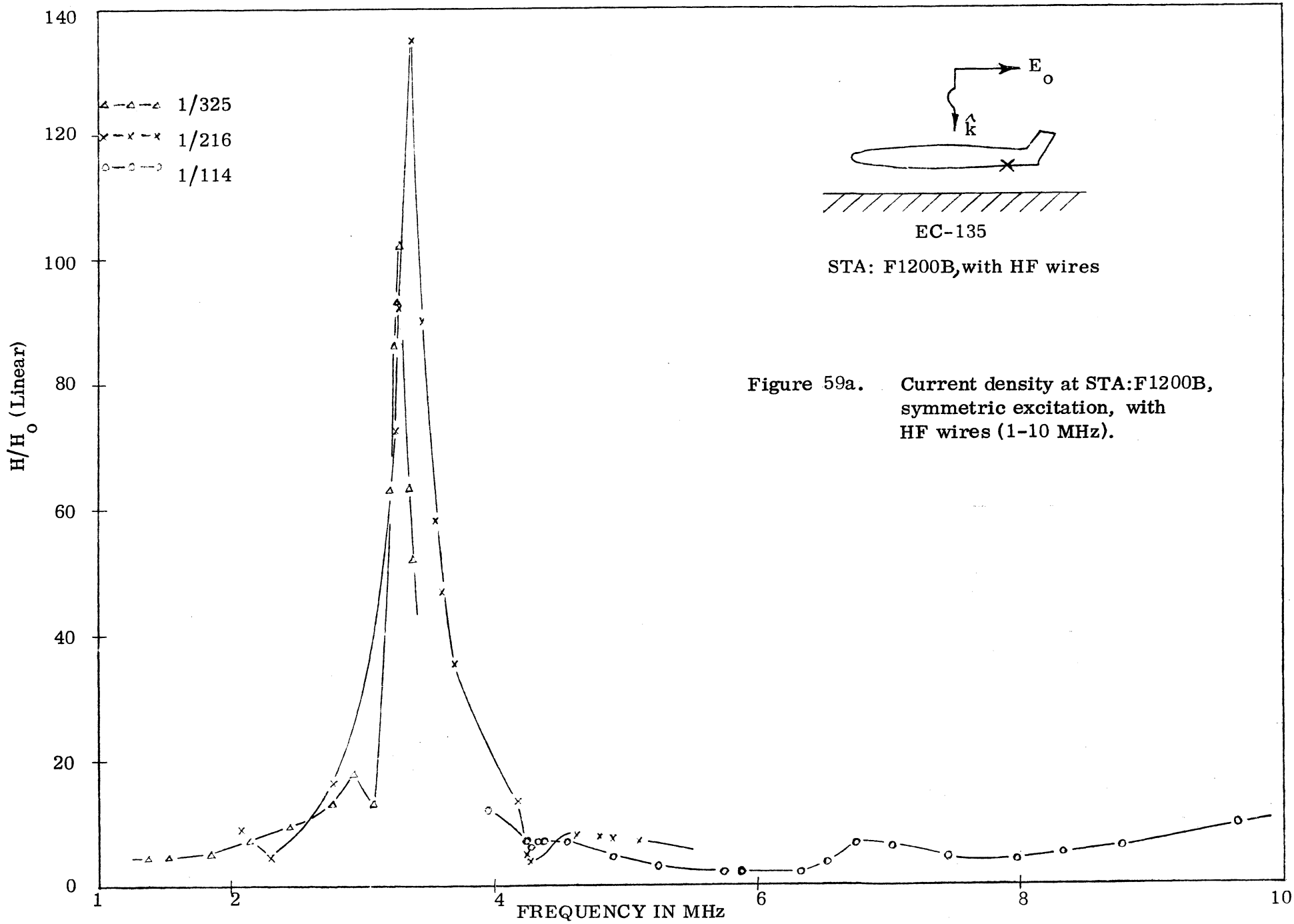

Figure 59a. Current density at STA:F1200B, symmetric excitation, with HF wires (1-10 MHz).

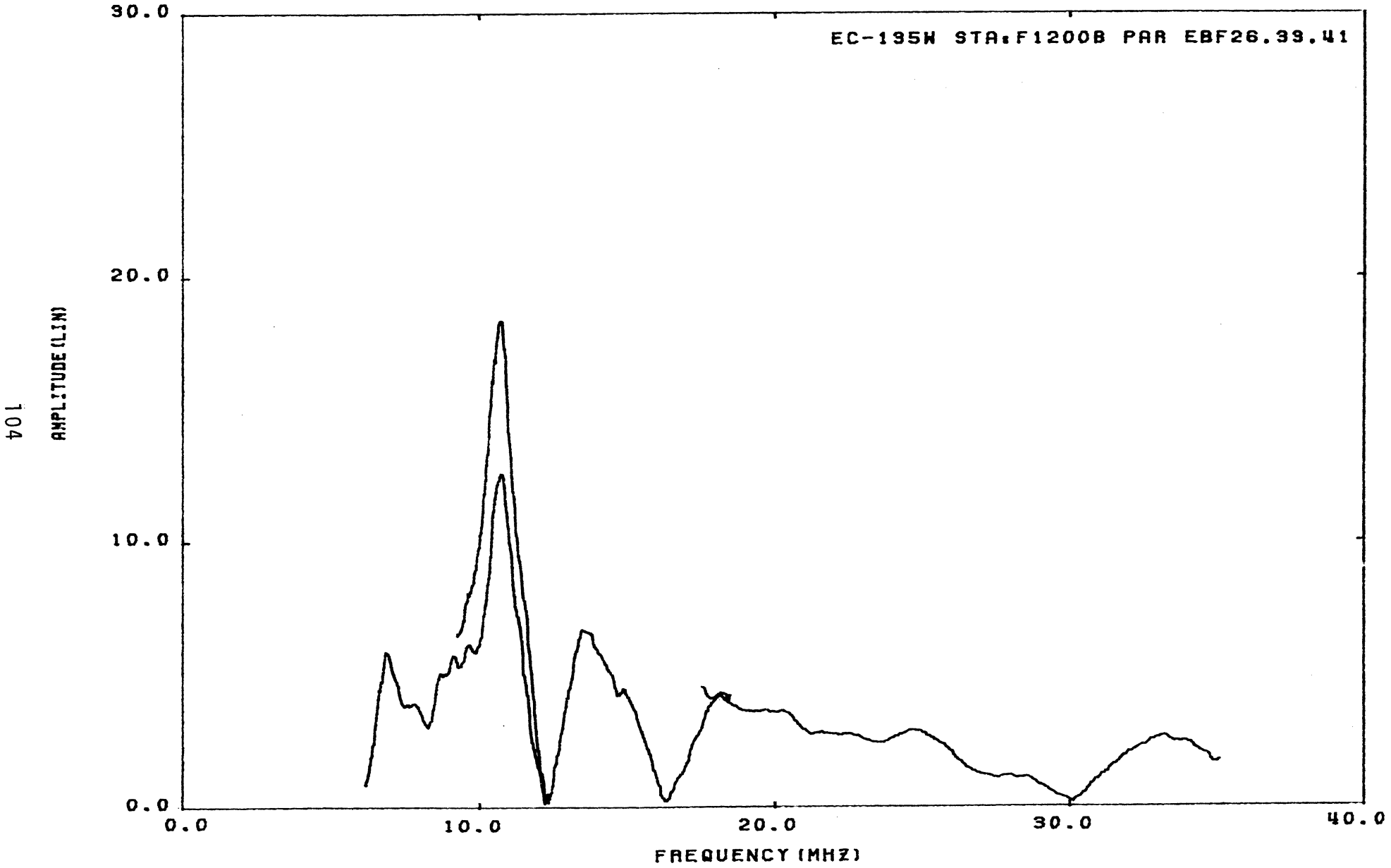

Figure 60a. Current density at STA:F1200B, symmetric excitation, with HF wires (0-40 MHz).

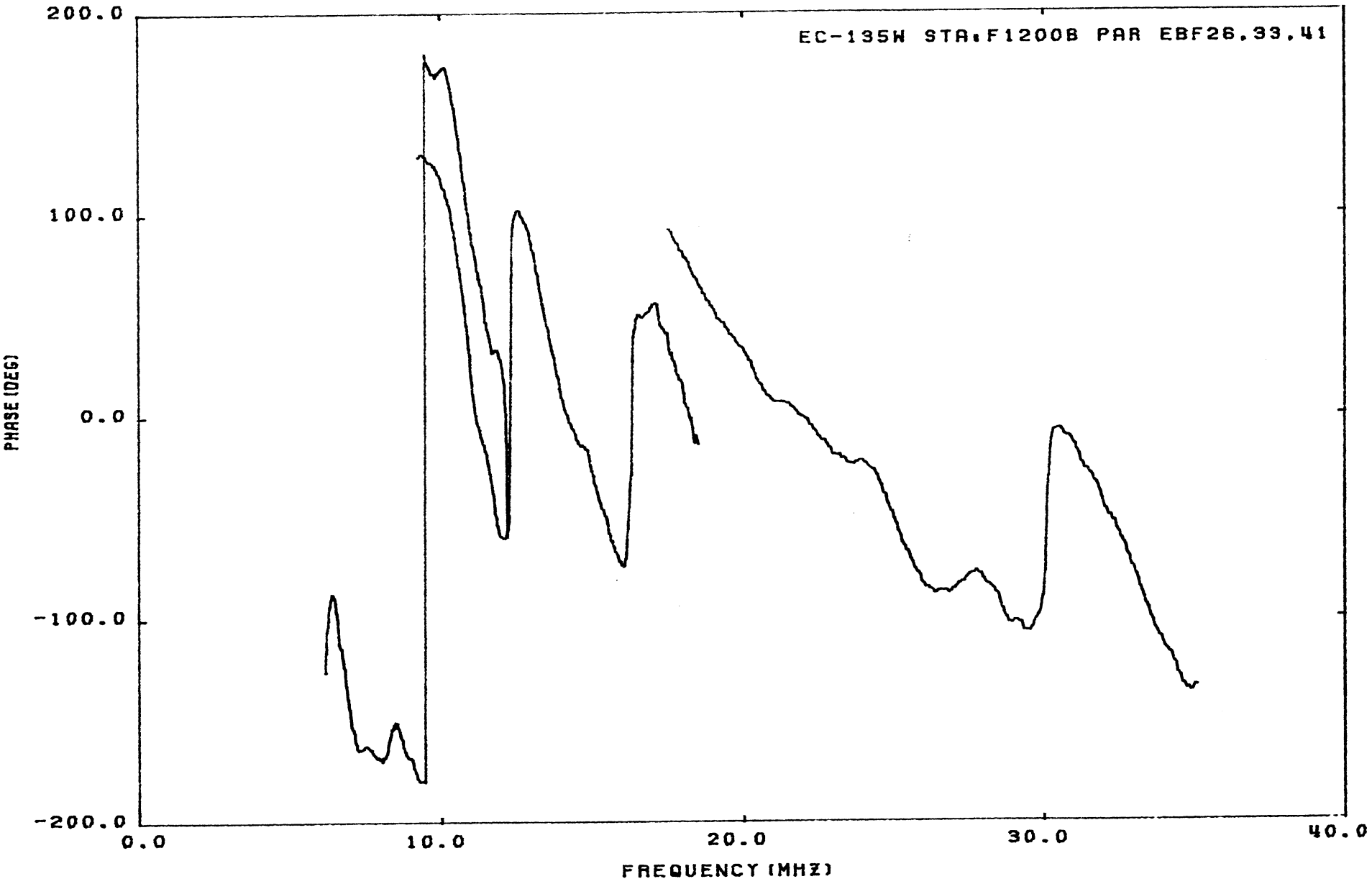

Figure 60b. Current phase at STA:F1200B, symmetric excitation, with HF wires (0-40 MHz).

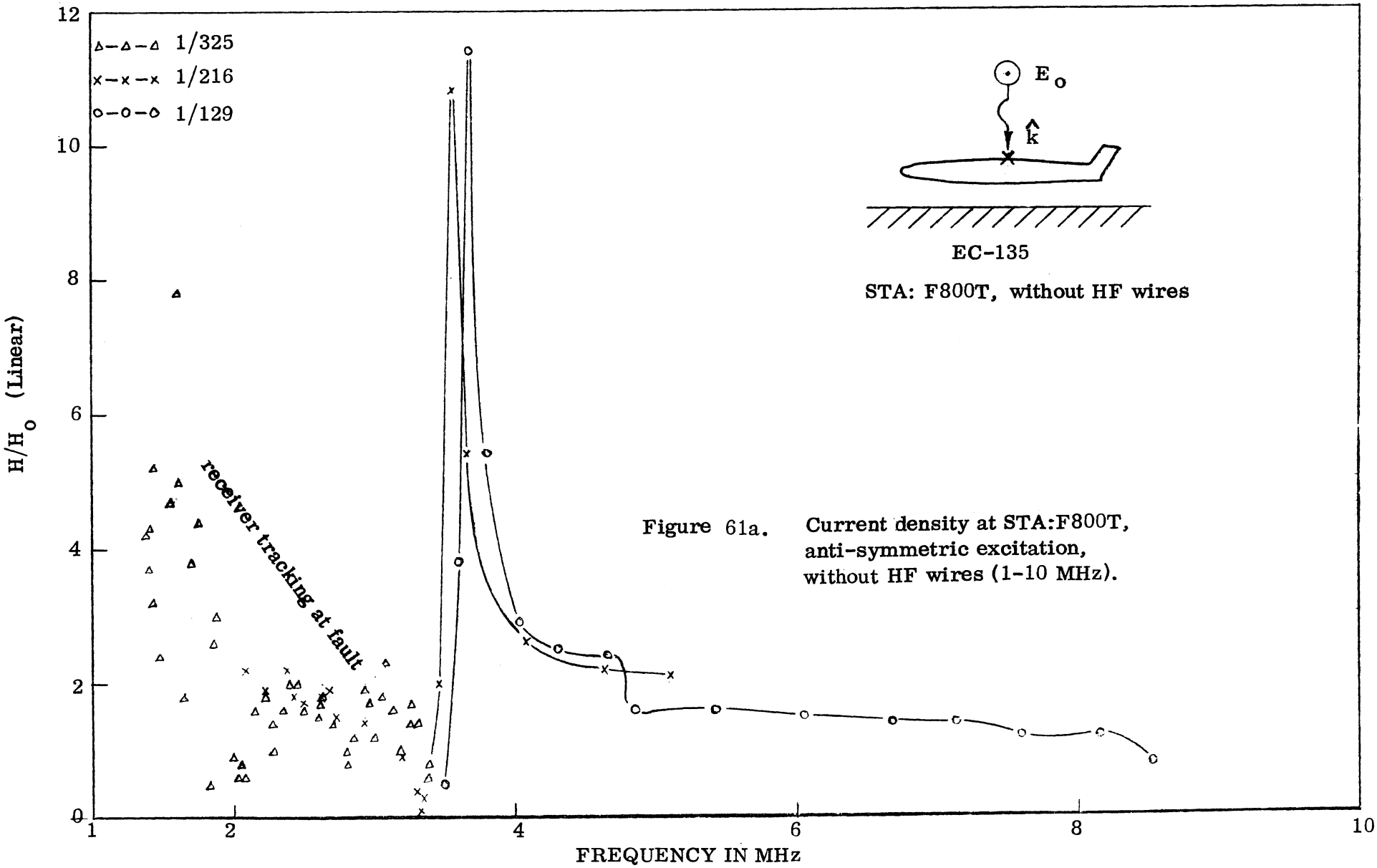

Figure 61a. Current density at STA:F800T, anti-symmetric excitation, without HF wires (1-10 MHz).

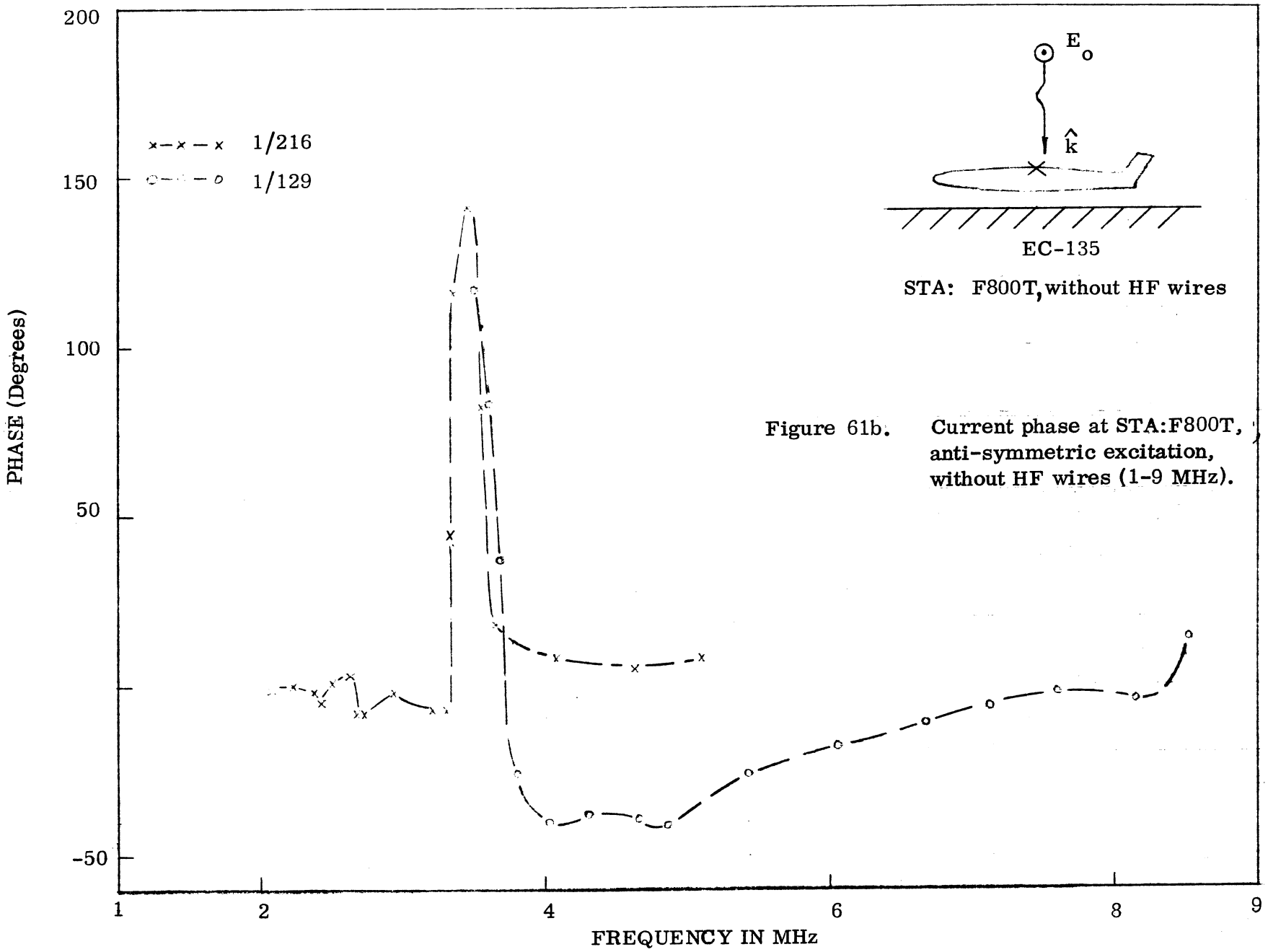

Figure 61b. Current phase at STA:F800T, anti-symmetric excitation, without HF wires (1-9 MHz).

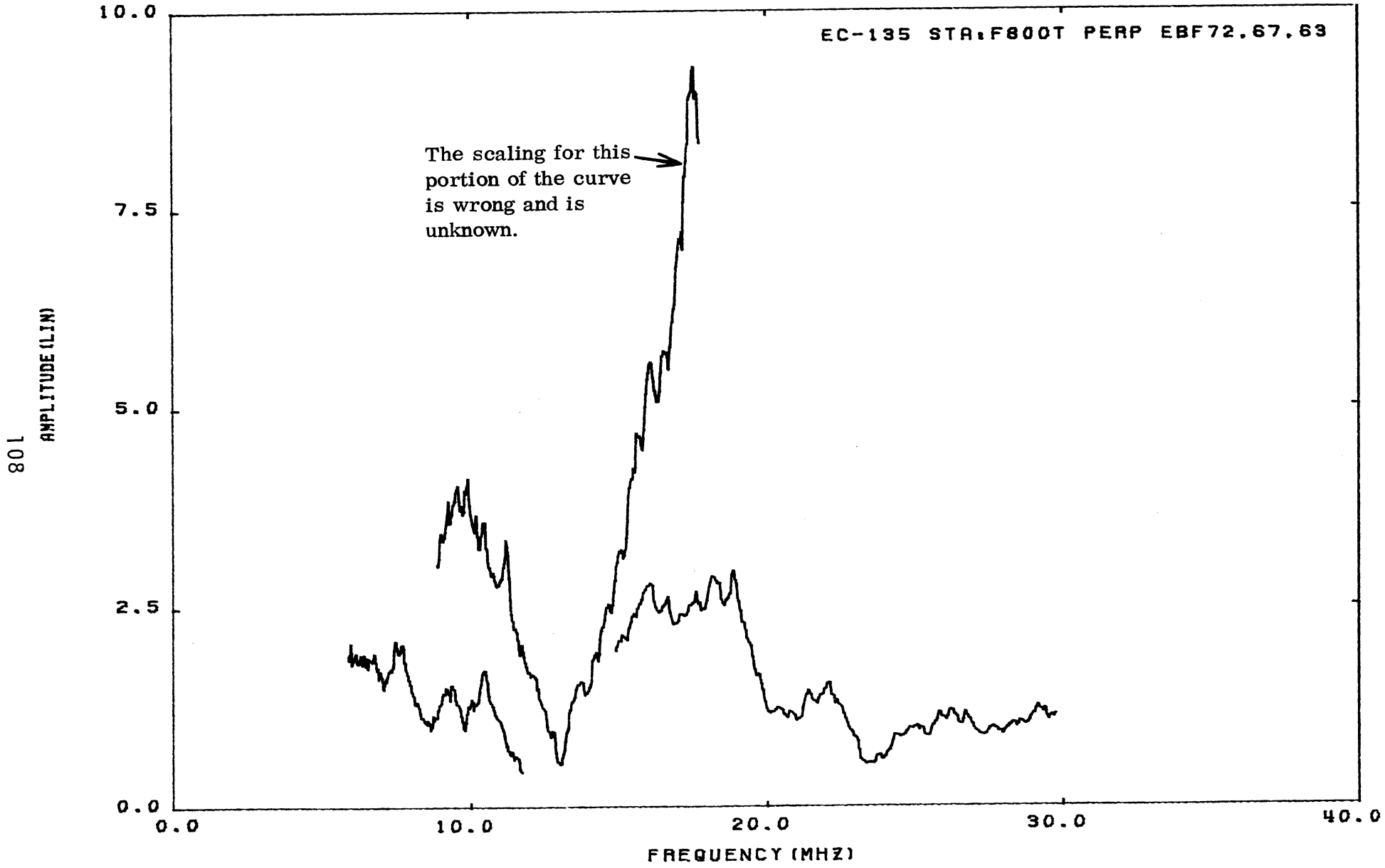

Figure 62a. Current density at STA:F800T, anti-symmetric excitation, without HF wires (0-40 MHz).

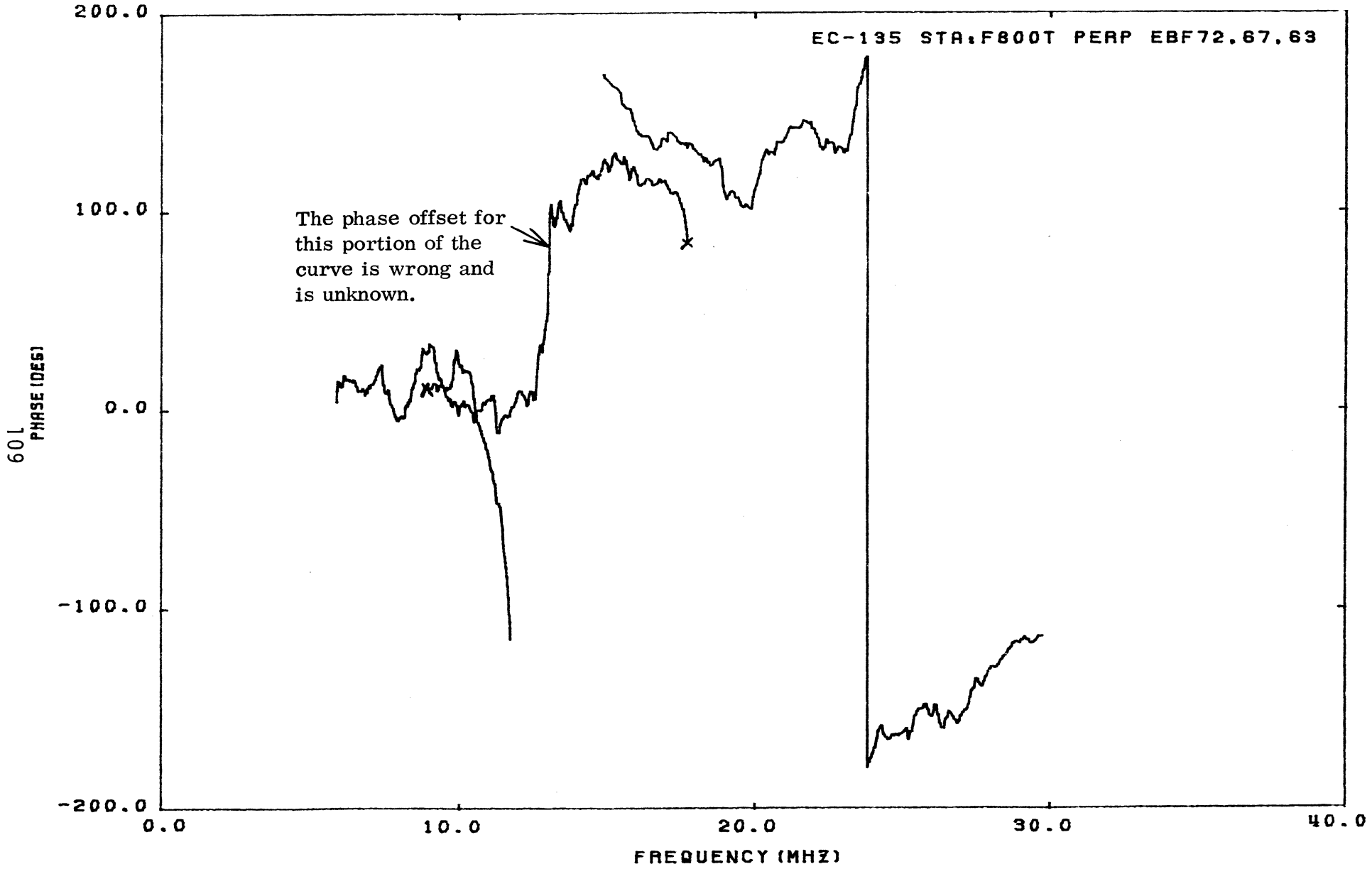

Figure 62b. Current phase at STA:F800T, anti-symmetric excitation, without HF wires (0-40 MHz).

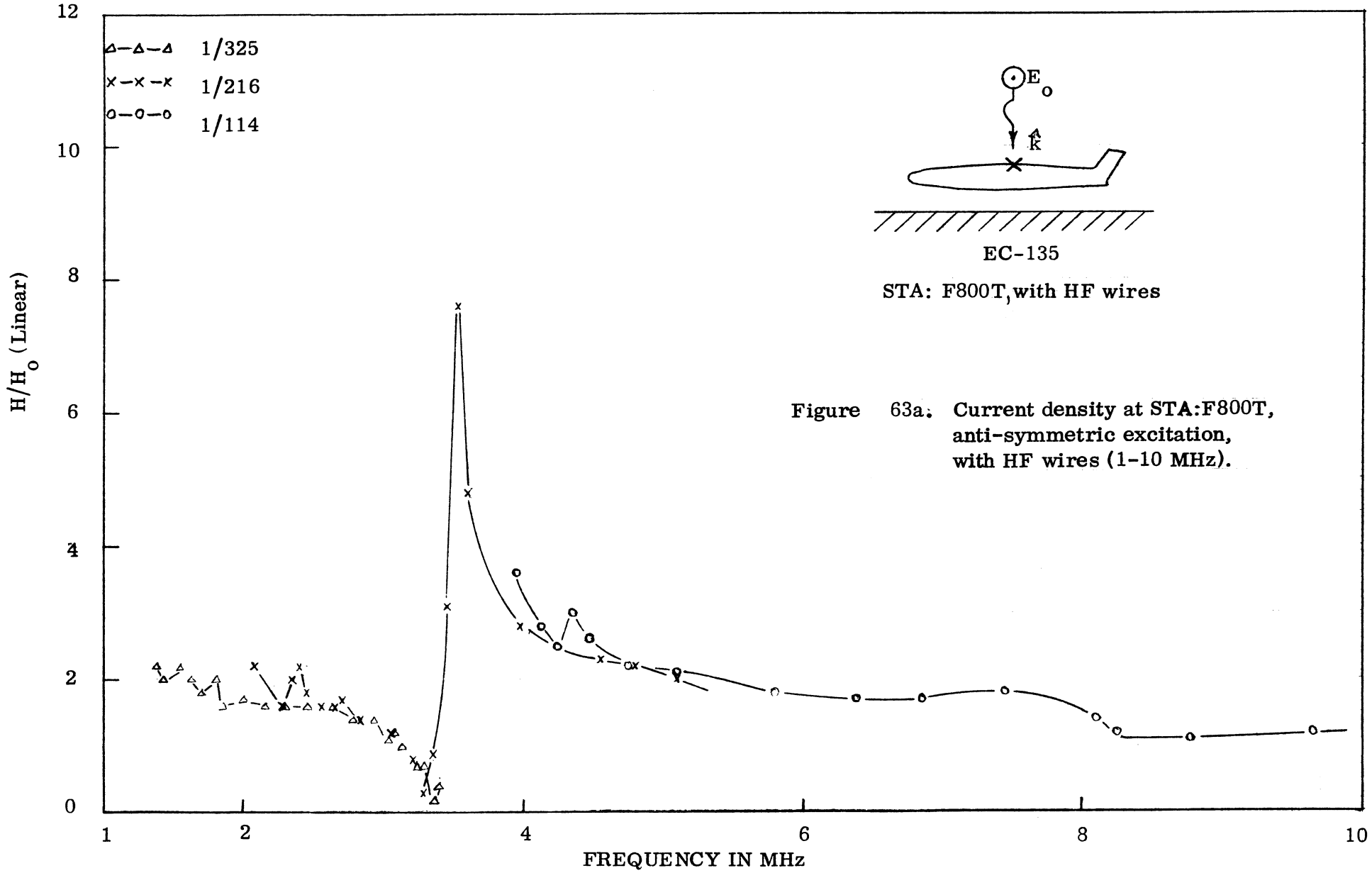

Figure 63a. Current density at STA:F800T, anti-symmetric excitation, with HF wires (1-10 MHz).

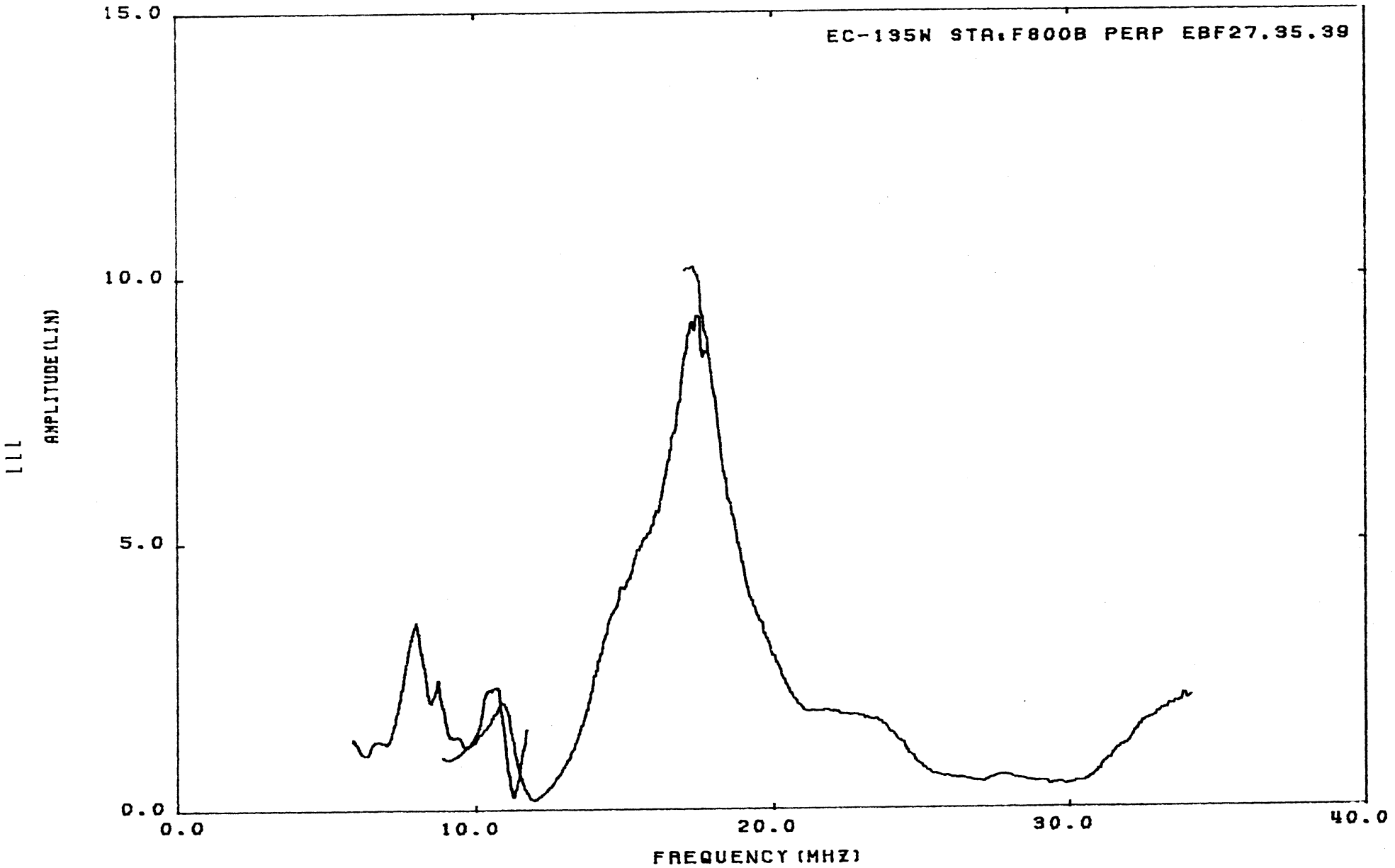

Figure 64a. Current density at STA:F800T, anti-symmetric excitation, with HF wires (0-40 MHz).

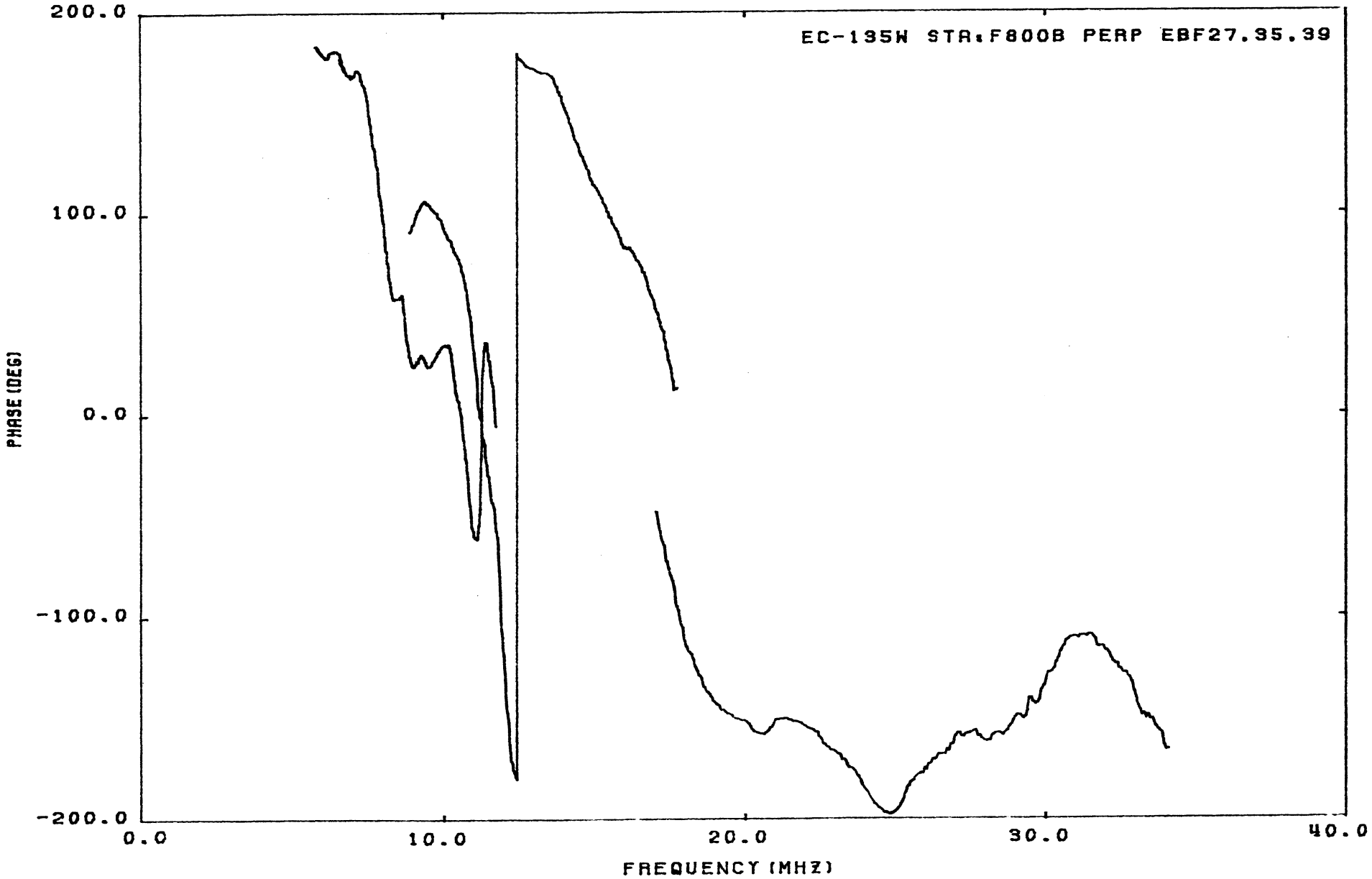

Figure 64b: Current phase at STA:F800T, anti-symmetric excitation, with HF wires (0-40 MHz).

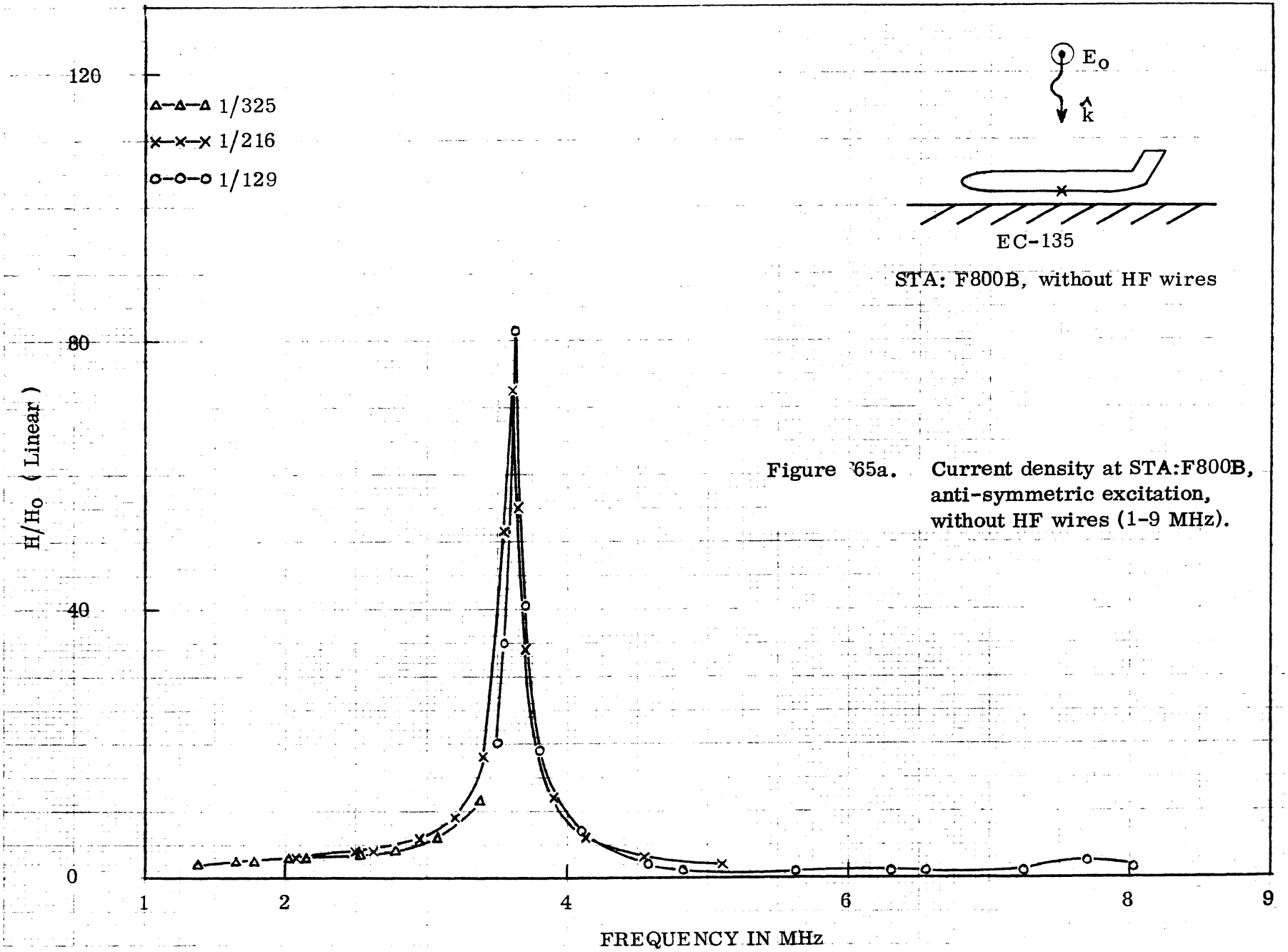

Figure 65a. Current density at STA:F800B, anti-symmetric excitation, without HF wires (1-9 MHz).

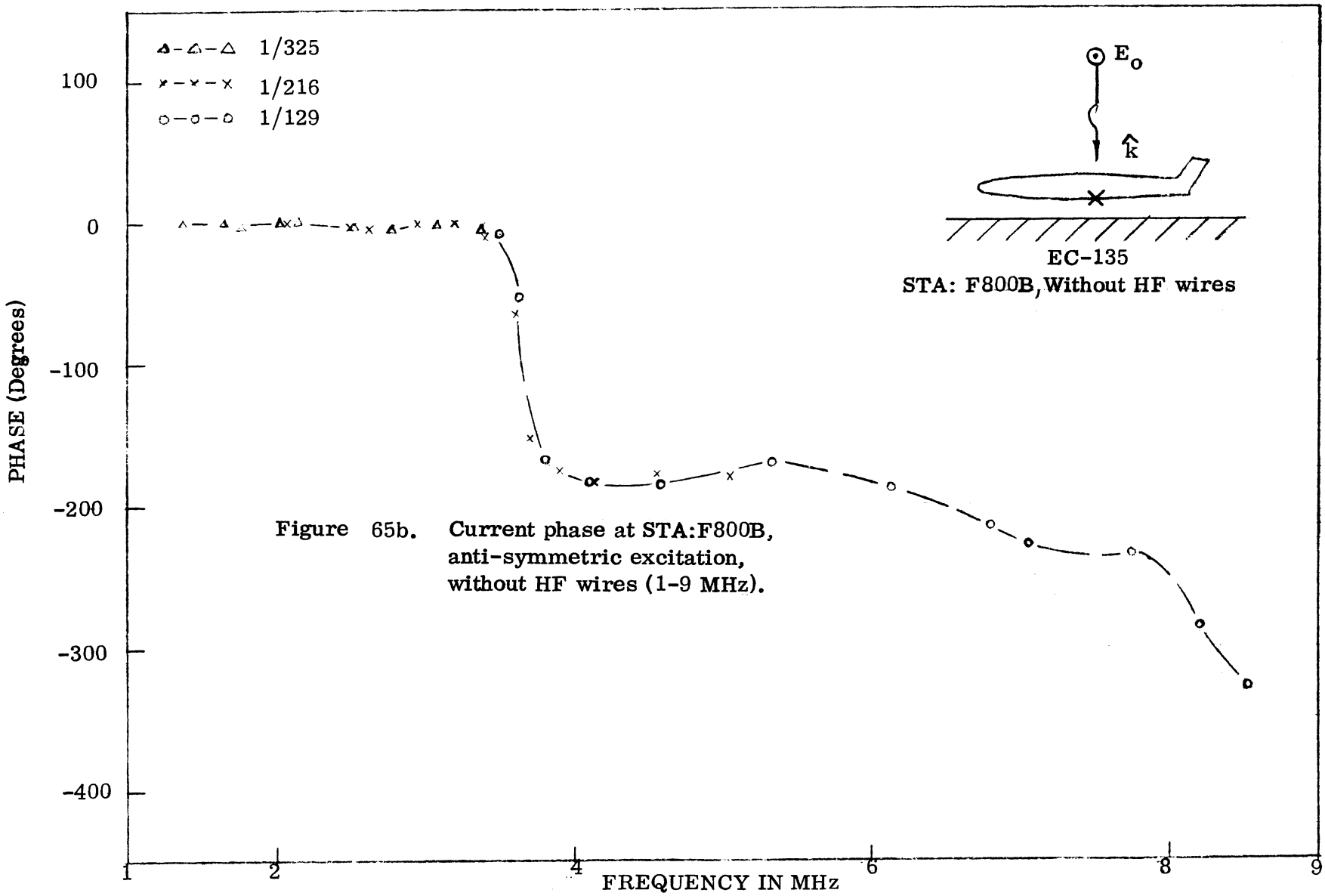

Figure 65b. Current phase at STA:F800B, anti-symmetric excitation, without HF wires (1-9 MHz).

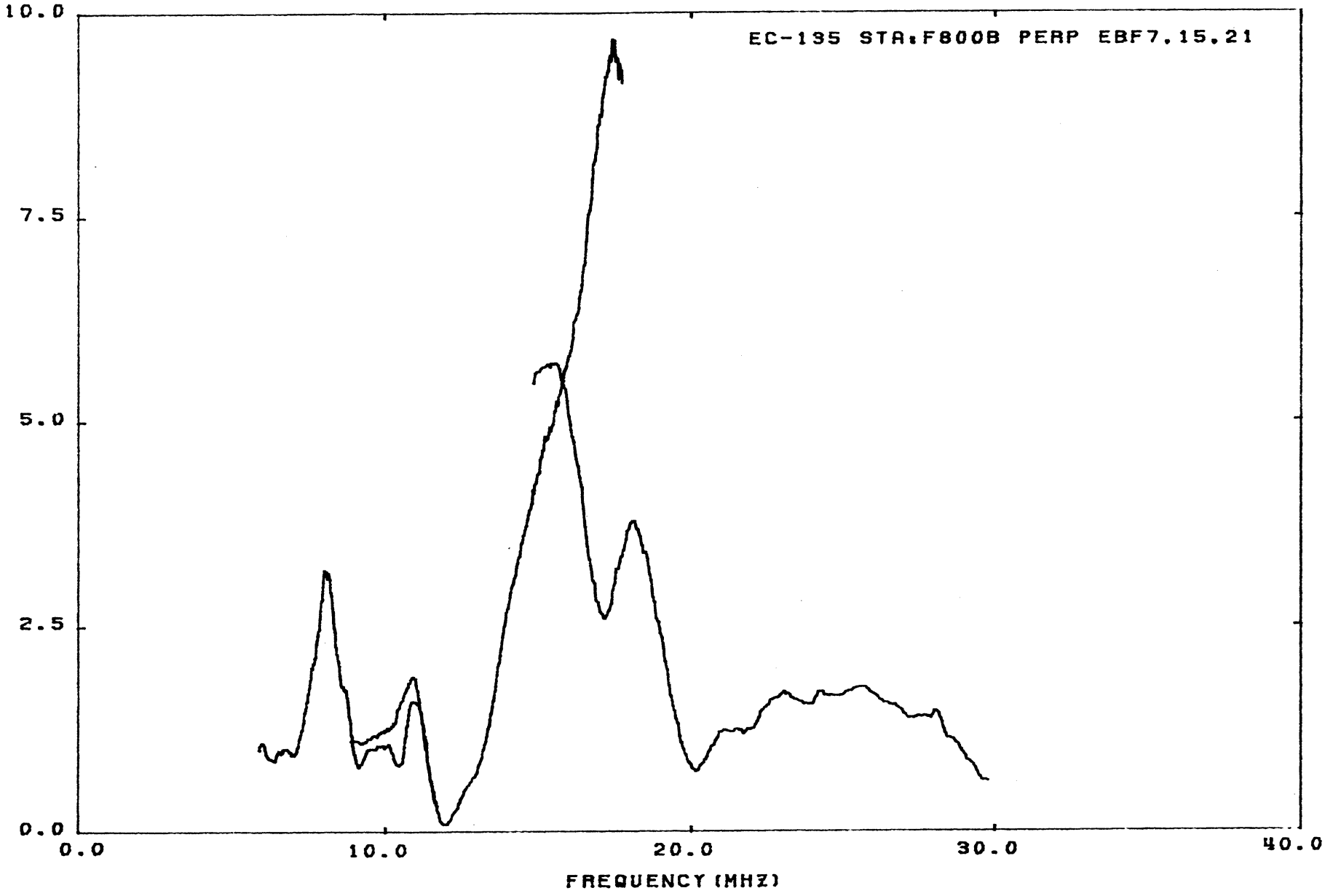

Figure 66a. Current density at STA:F800B, anti-symmetric excitation, without HF wires (0-40 MHz).

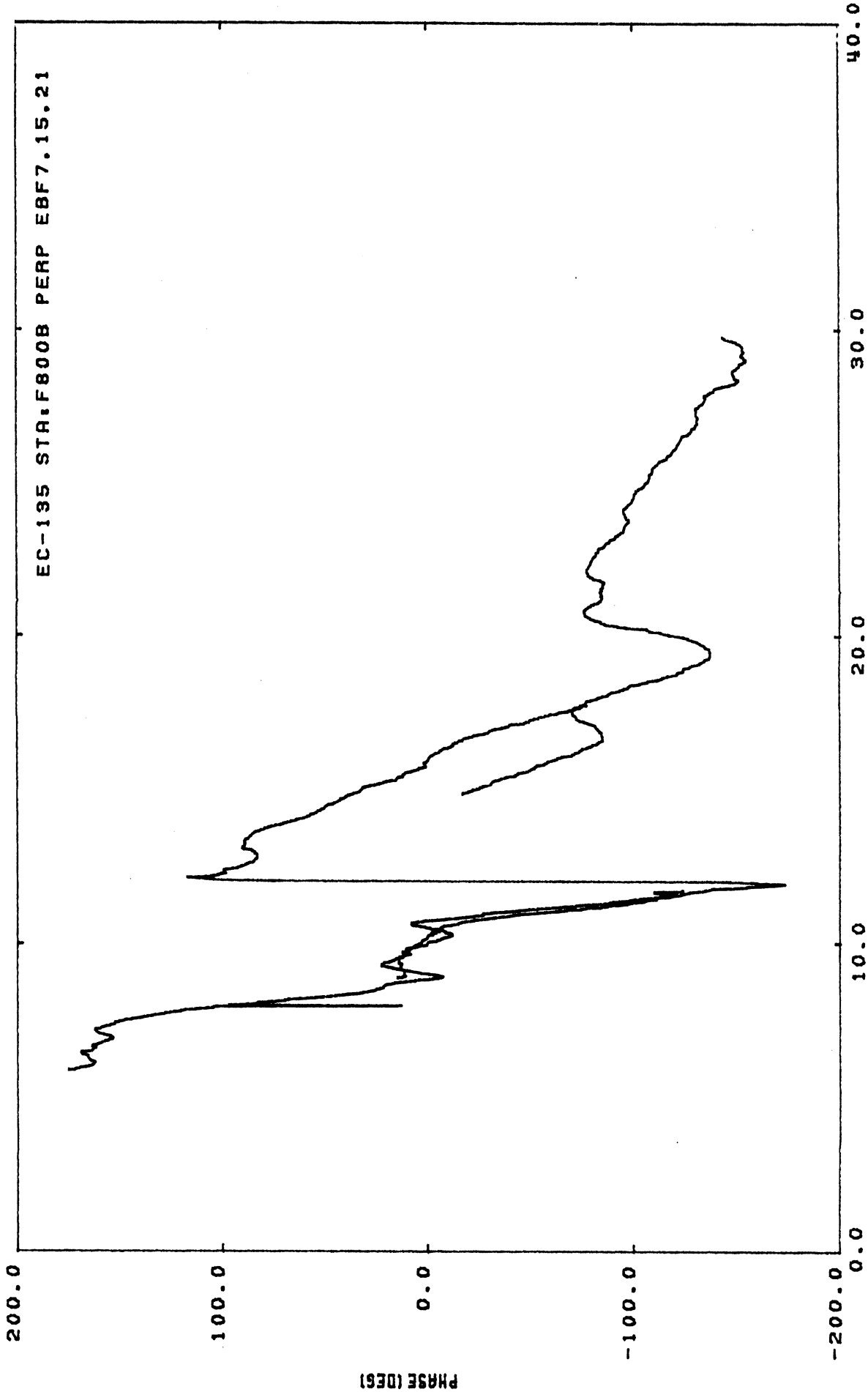

Figure 66b: Current phase at STA:F800B, anti-symmetric excitation, without HF wires (0-40 MHz).

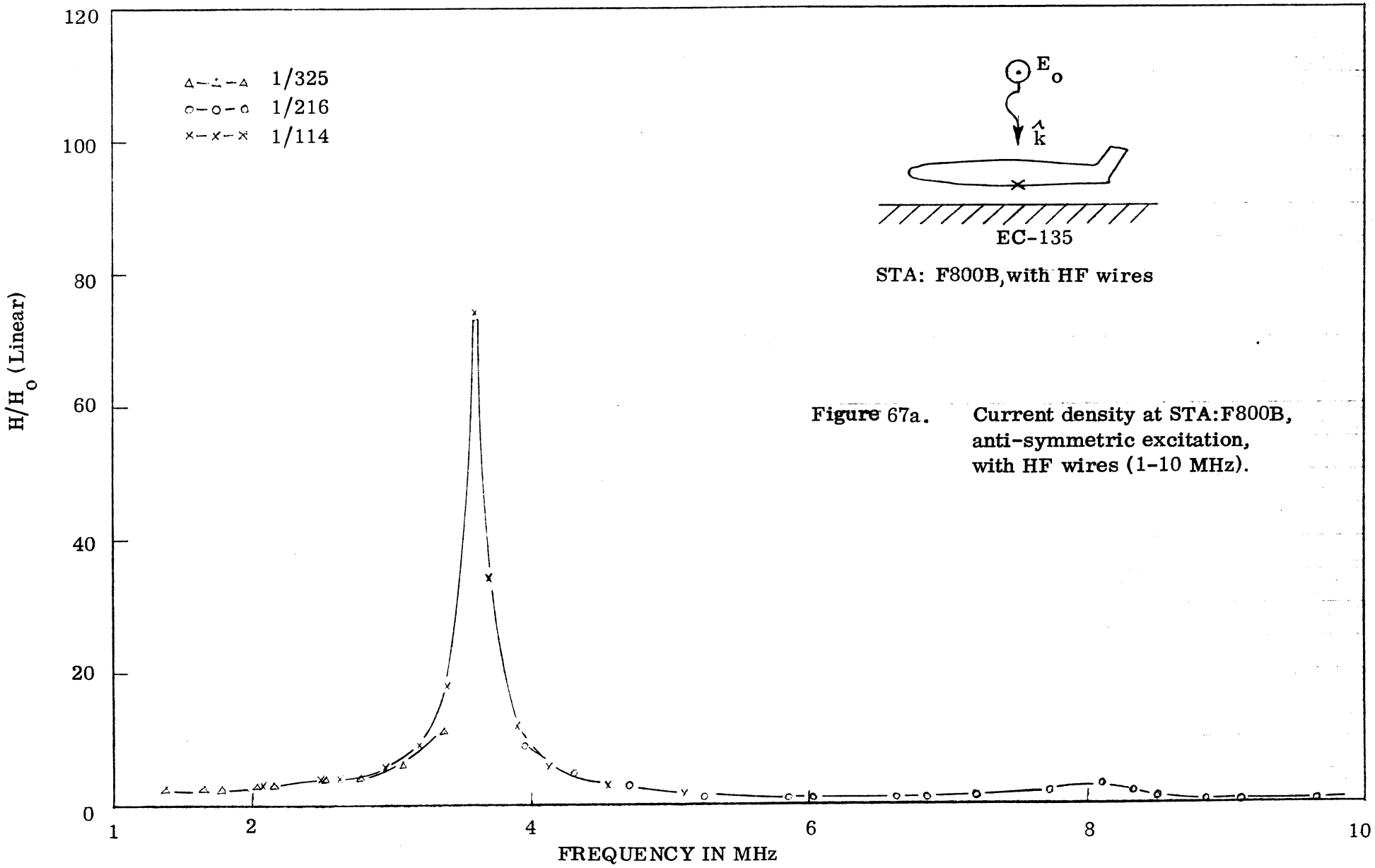

Figure 67a. Current density at STA:F800B, anti-symmetric excitation, with HF wires (1-10 MHz).

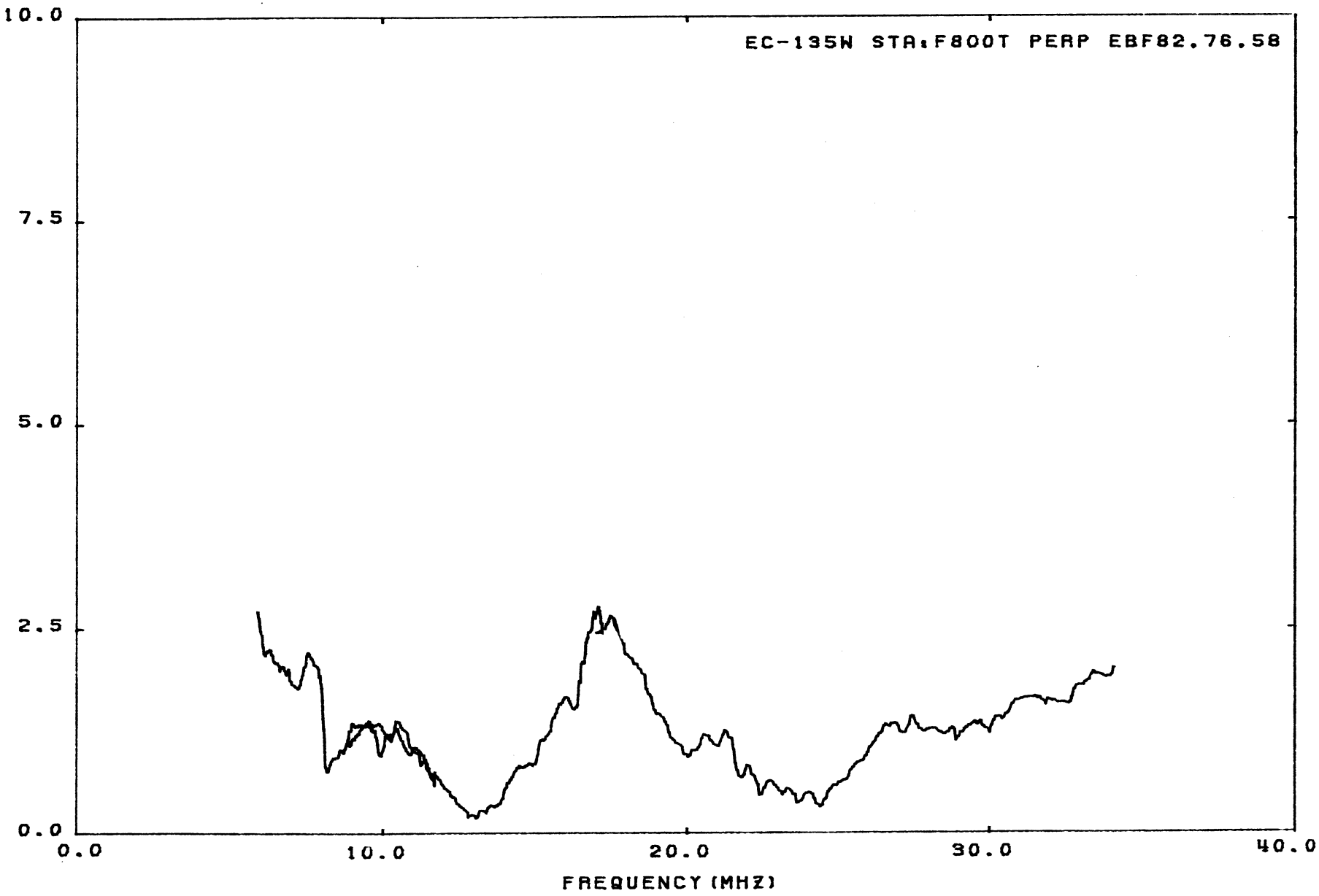

Figure 68a. Current density at STA:F800B, anti-symmetric excitation, with HF wires (0-40 MHz).

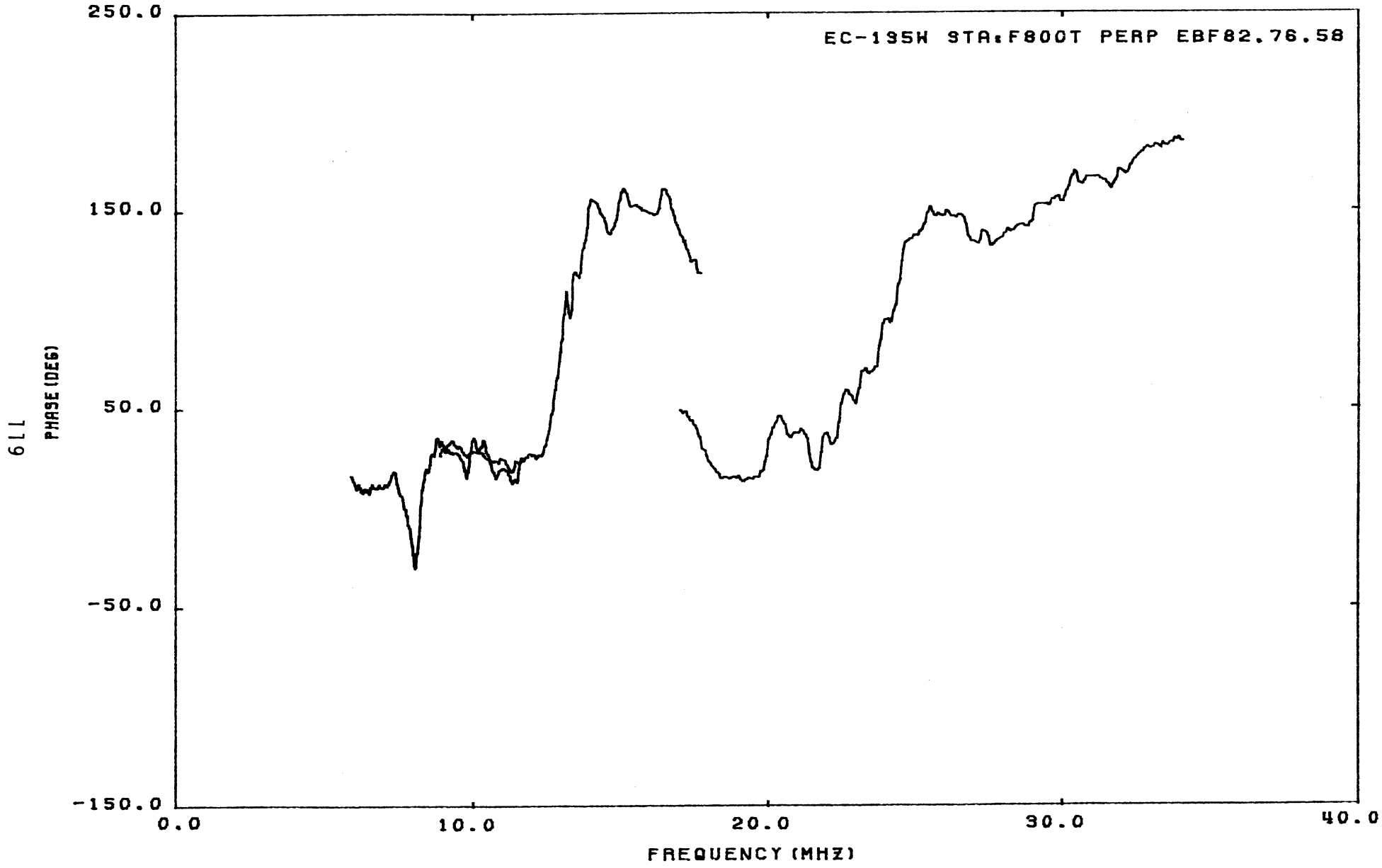

Figure 68b. Current phase at STA:F800B, anti-symmetric excitation, with HF wires (0-40 MHz).

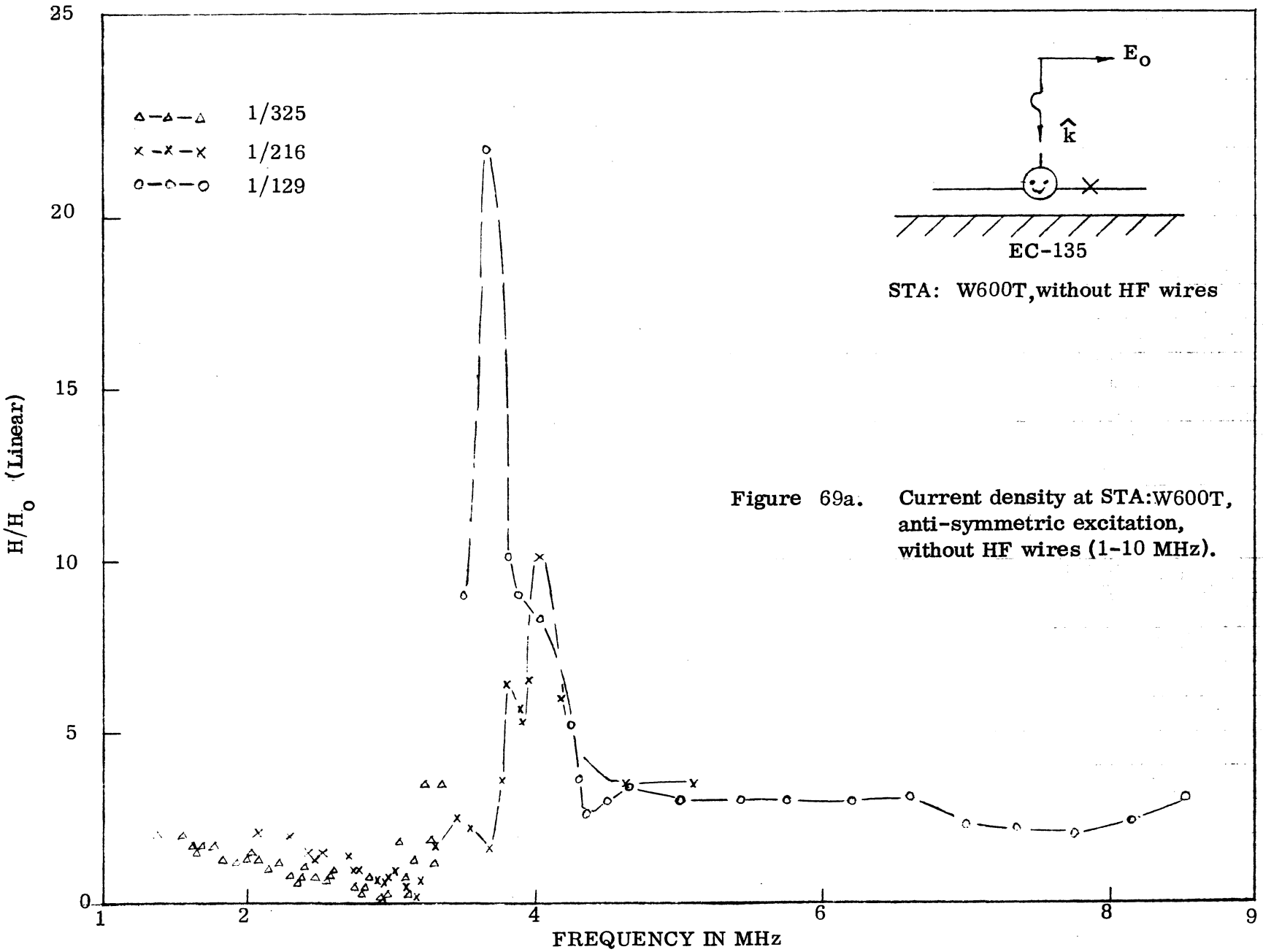

Figure 69a. Current density at STA:W600T, anti-symmetric excitation, without HF wires (1-10 MHz).

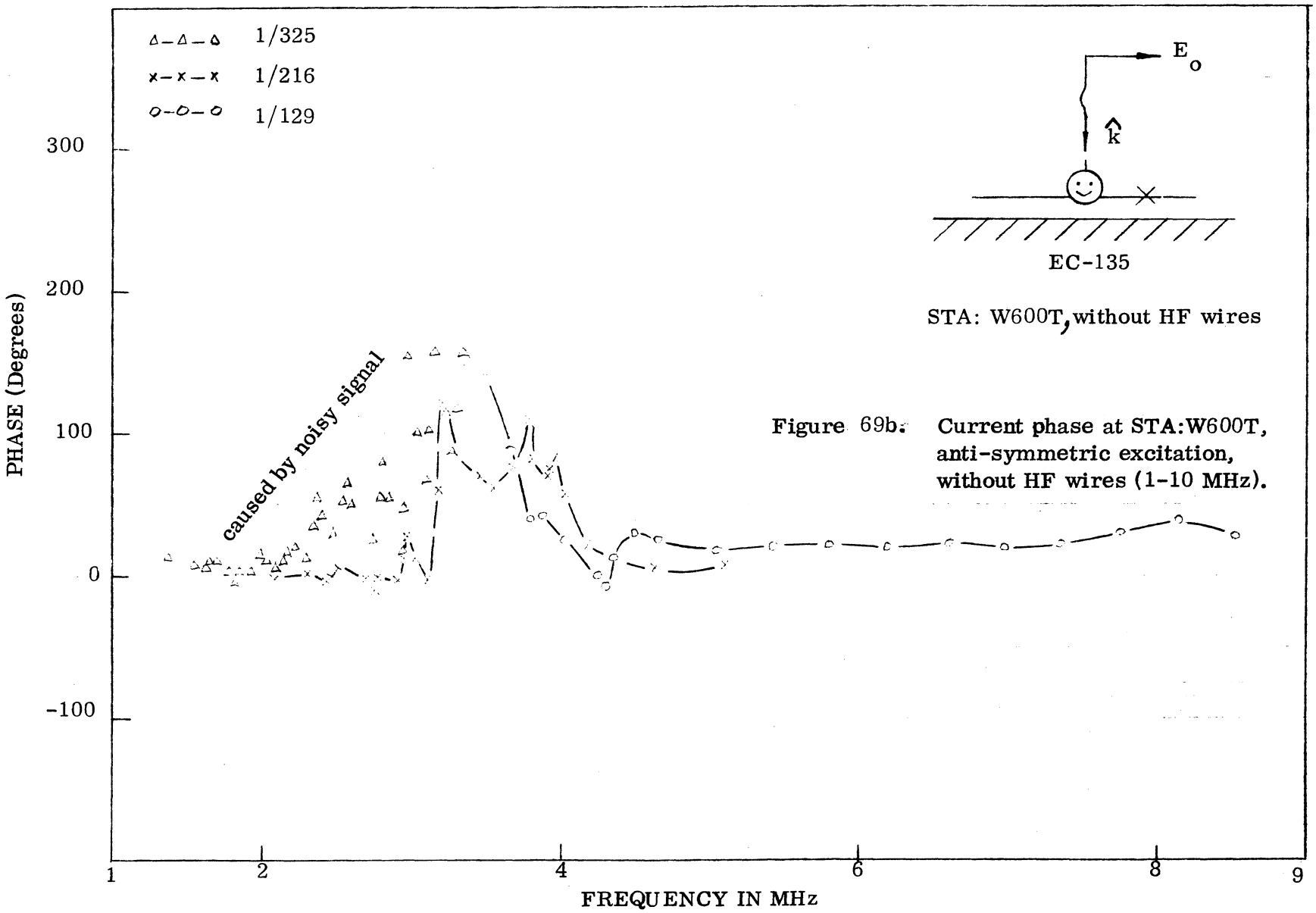

Figure 69b. Current phase at STA:W600T, anti-symmetric excitation, without HF wires (1-10 MHz).

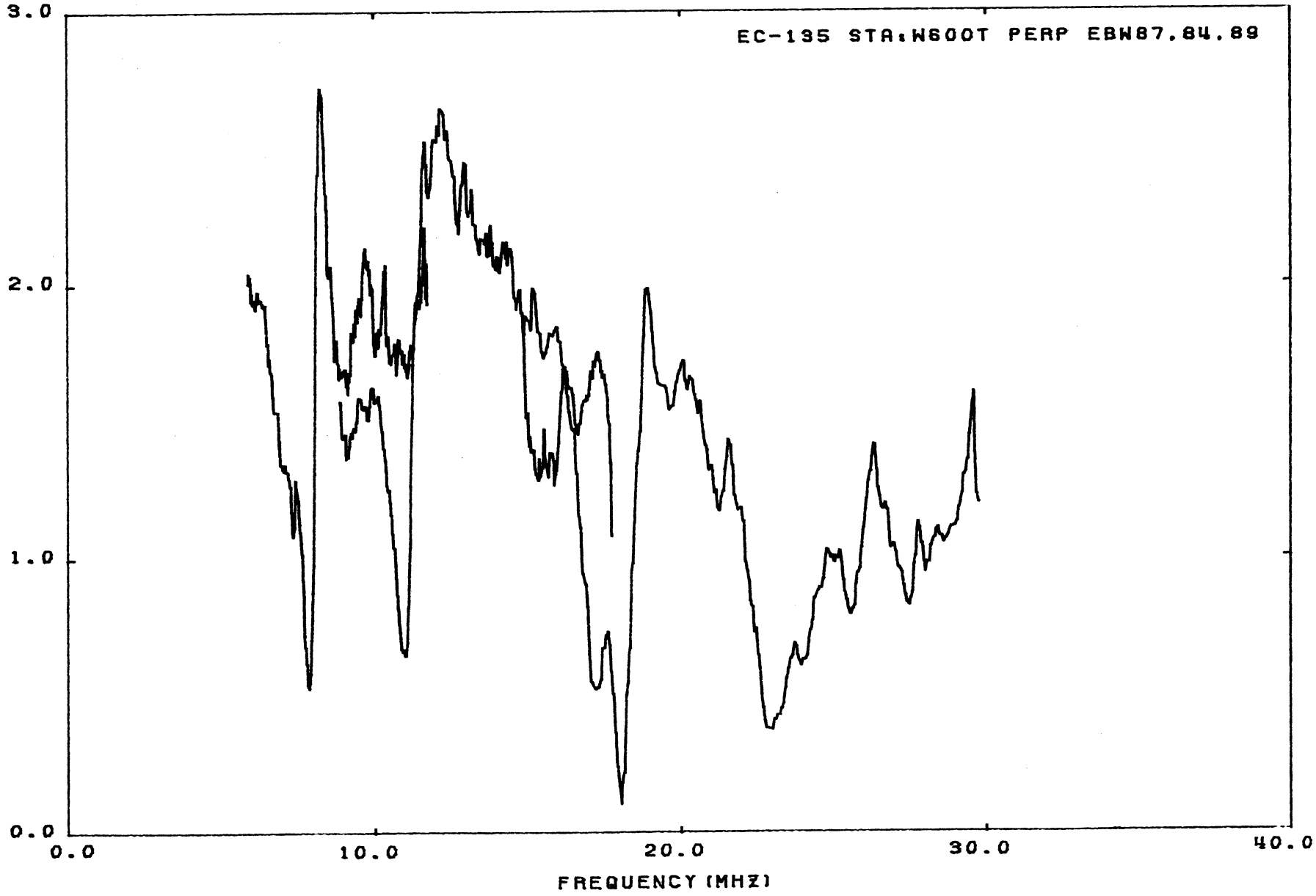

Figure 70a. Current density at STA:W600T, anti-symmetric excitation, without HF wires (0-40 MHz).

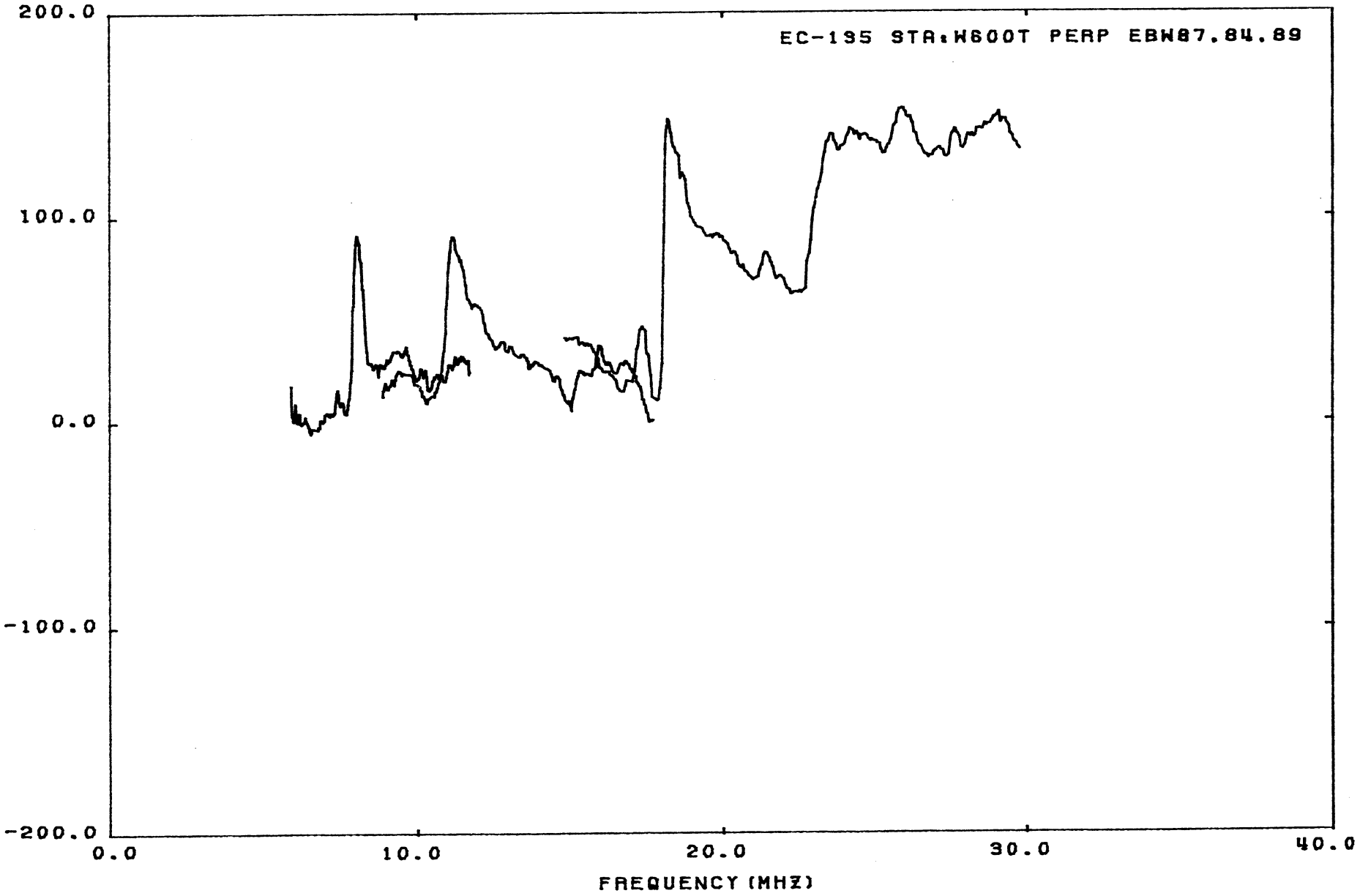

Figure 70b. Current phase at STA:W600T, anti-symmetric excitation, without HF wires (0-40 MHz).

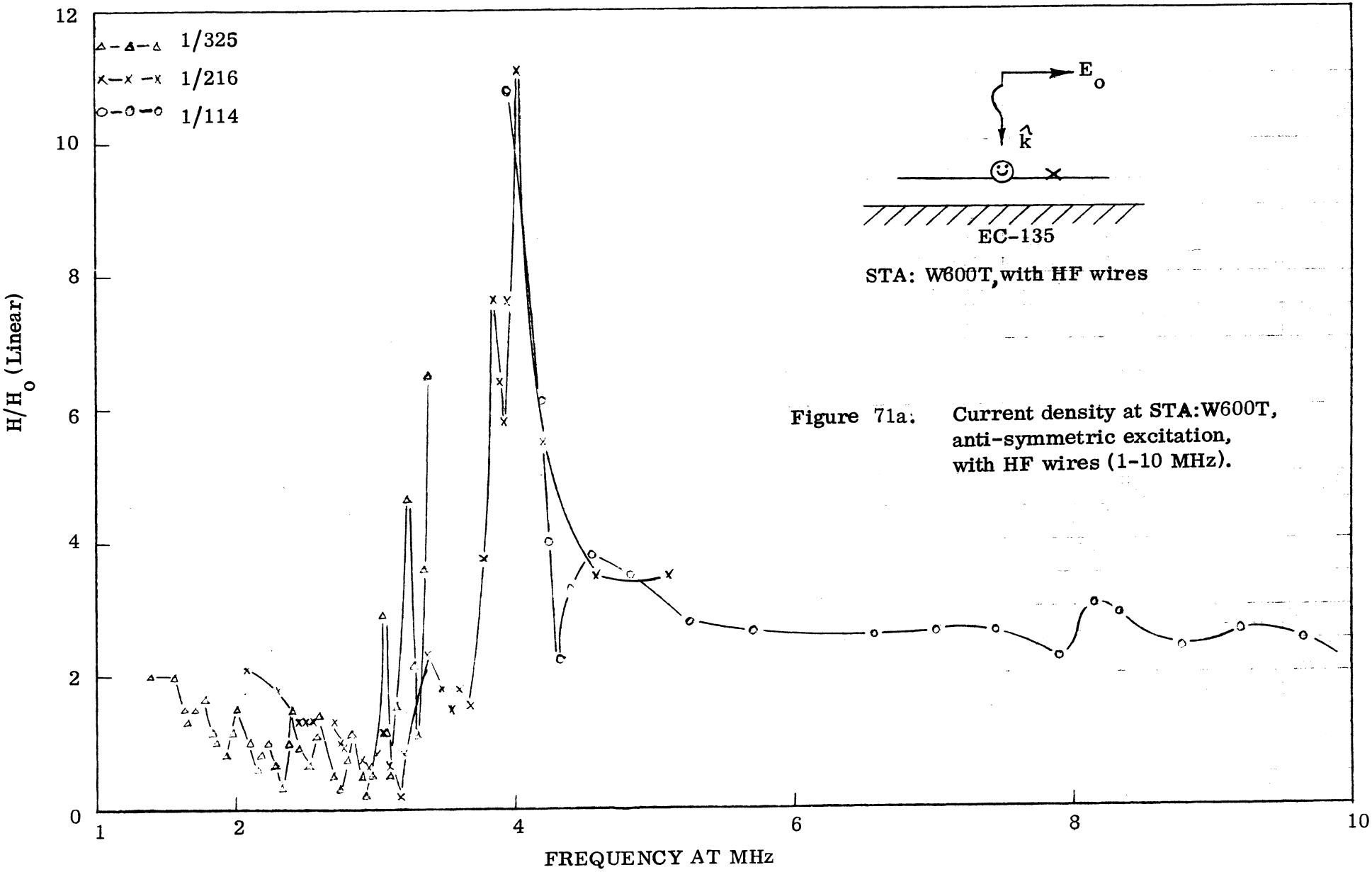

Figure 71a: Current density at STA:W600T, anti-symmetric excitation, with HF wires (1-10 MHz).

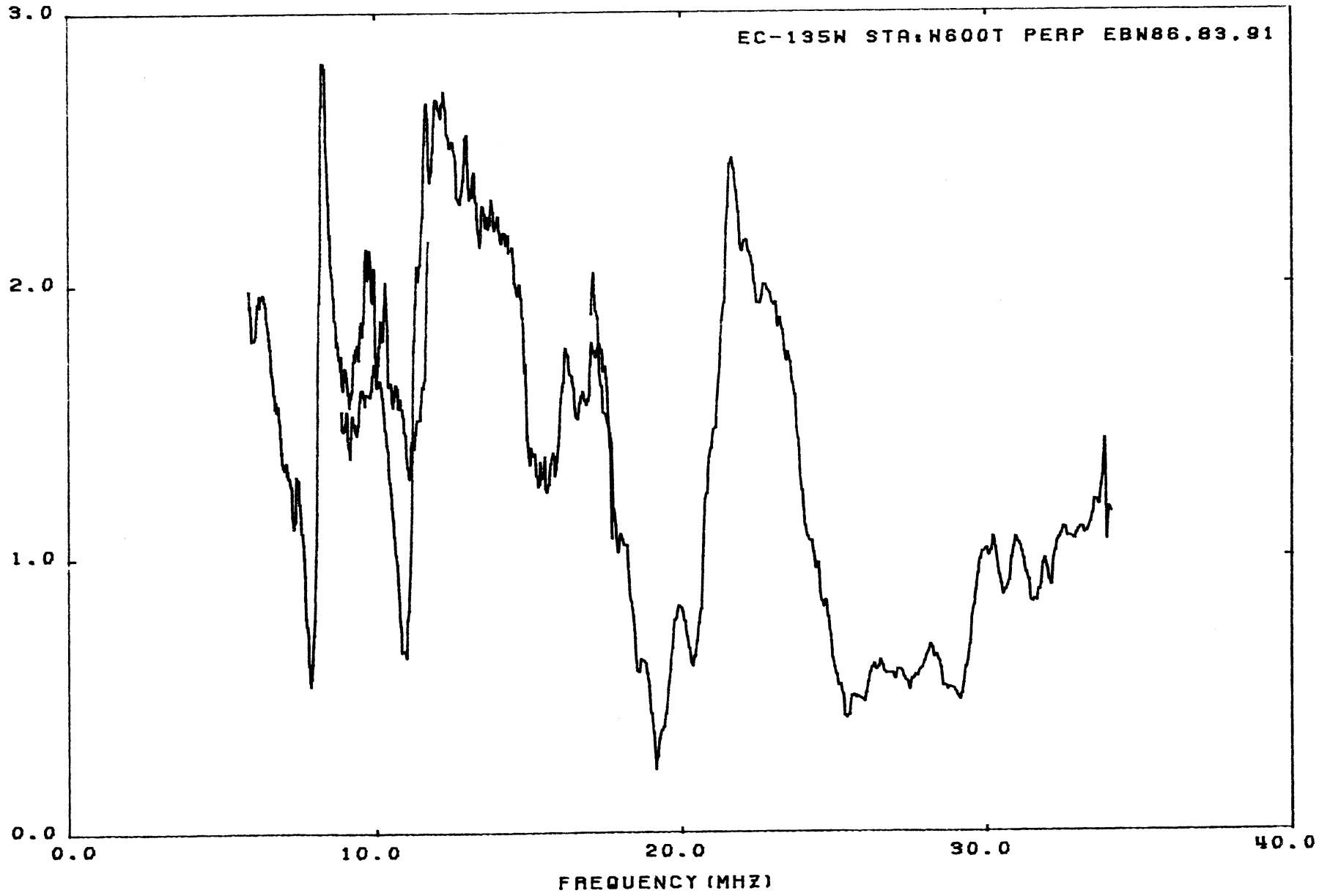

Figure 72a. Current density at STA:W600T, anti-symmetric excitation, with HF wires (0-40 MHz).

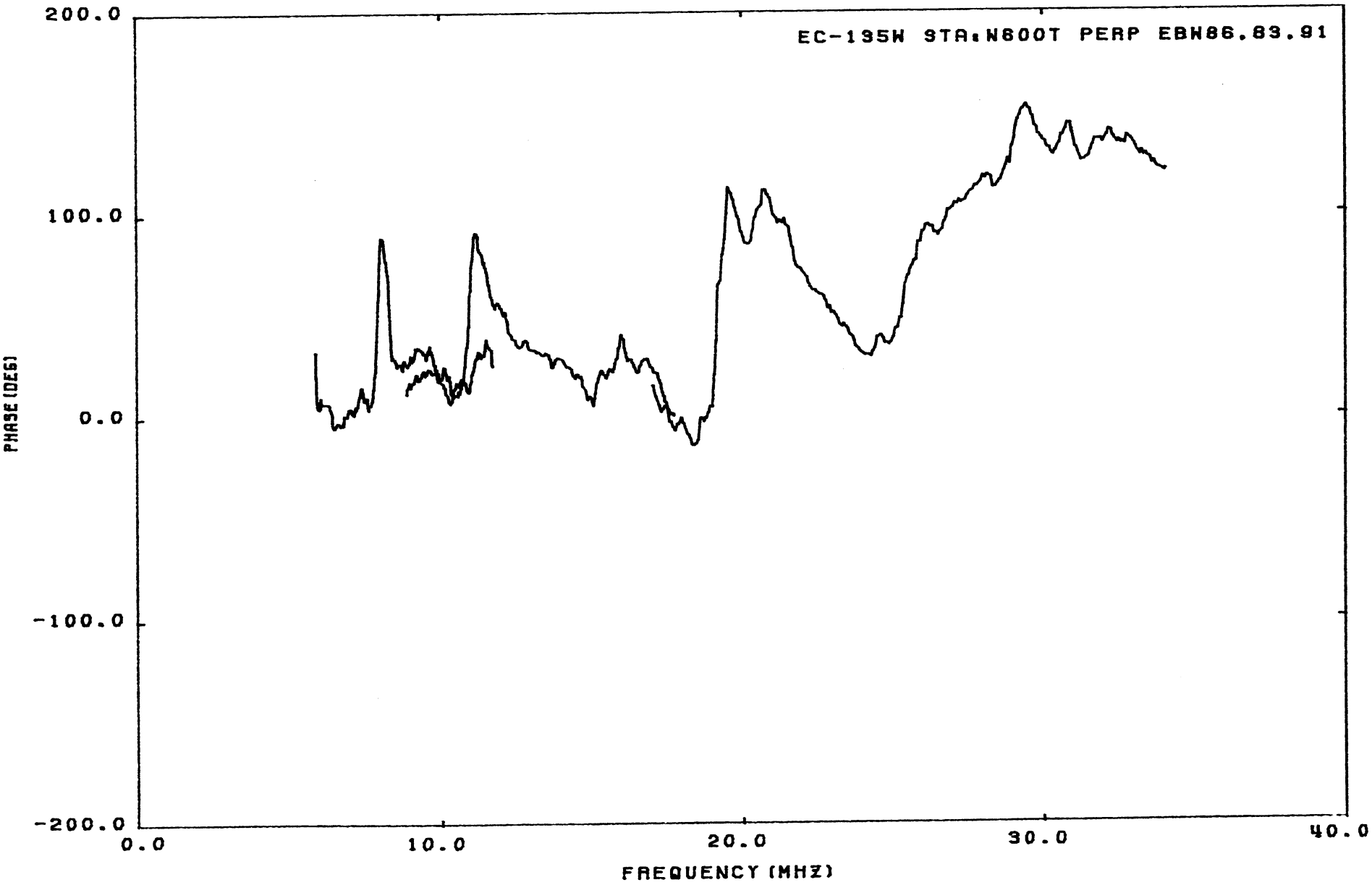

Figure 72b. Current phase at STA:W600T, anti-symmetric excitation, with HF wires (0-40 MHz).

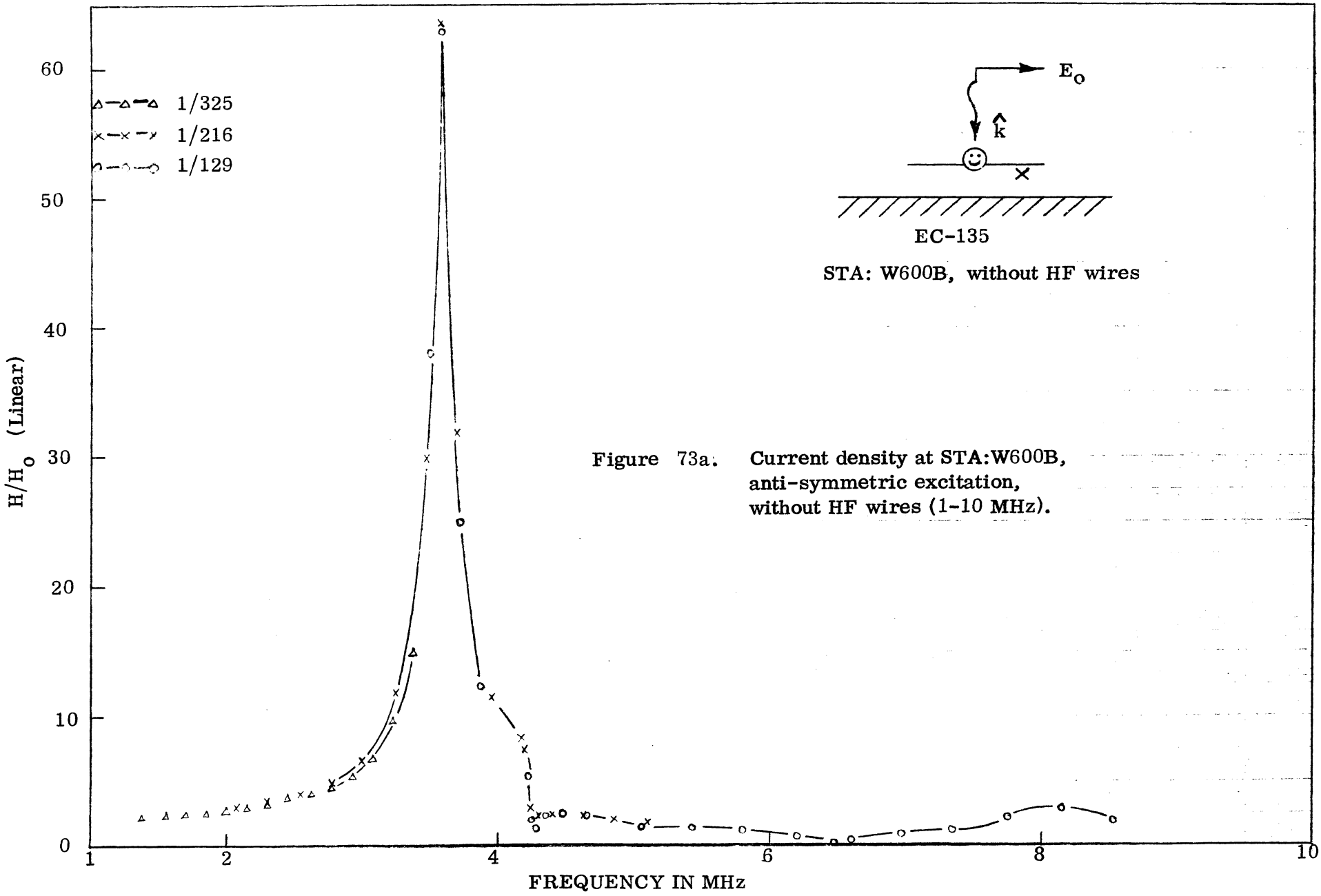

Figure 73a. Current density at STA:W600B, anti-symmetric excitation, without HF wires (1-10 MHz).

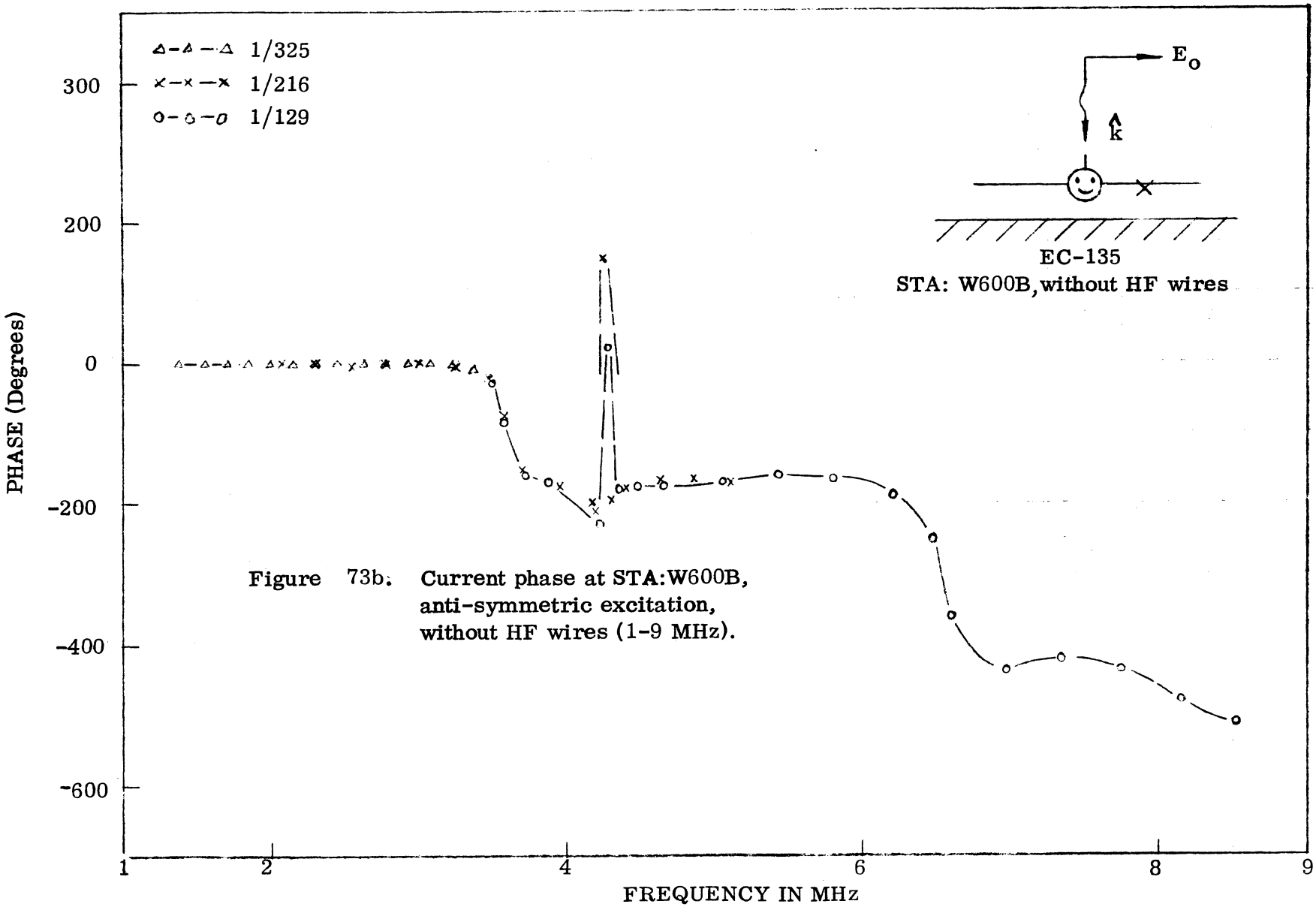

Figure 73b. Current phase at STA:W600B, anti-symmetric excitation, without HF wires (1-9 MHz).

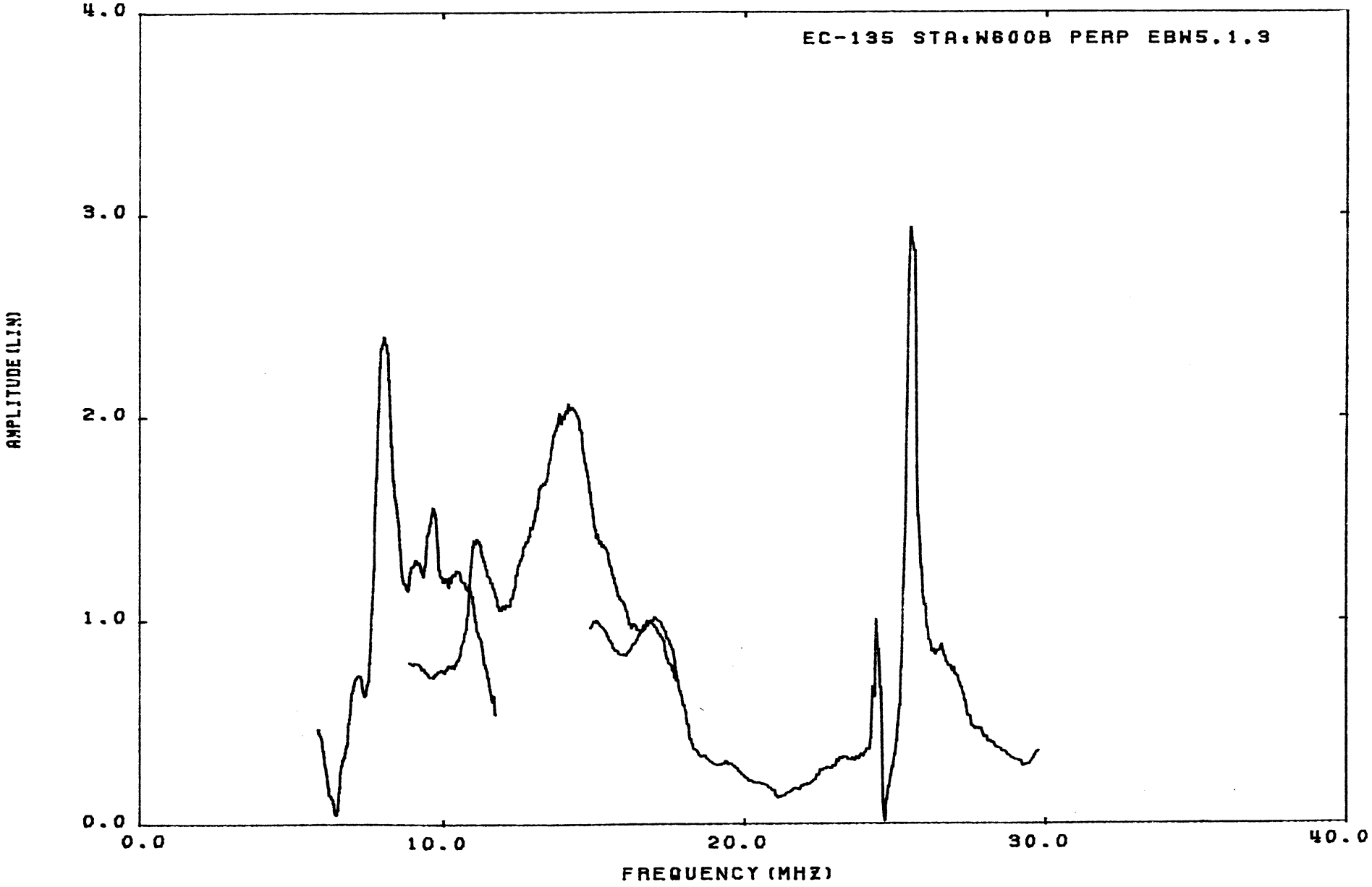

Figure 74a. Current density at STA:W600B, anti-symmetric excitation, without HF wires (0-40 MHz).

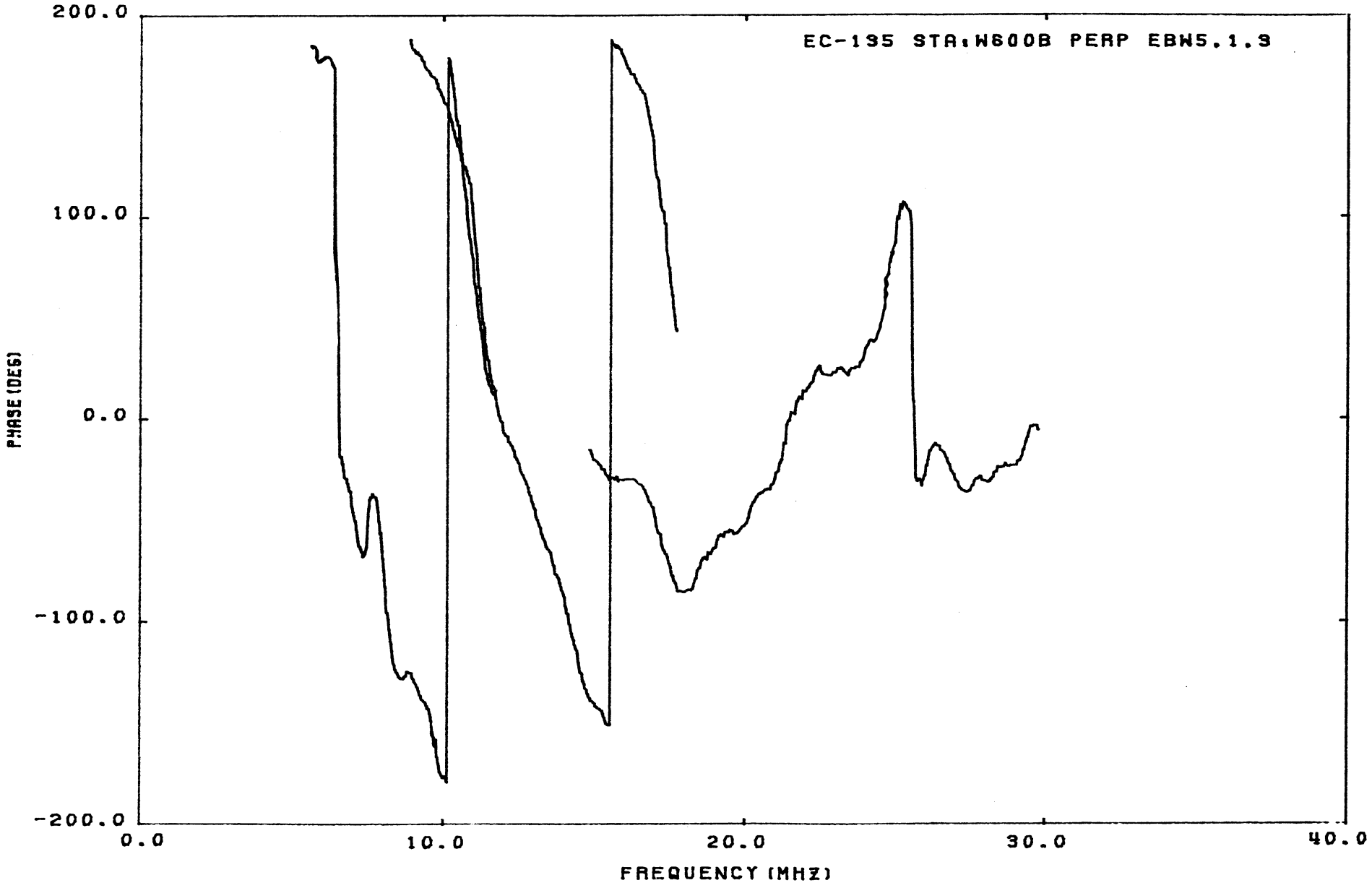

Figure 74b. Current phase at STA:W600B, anti-symmetric excitation, without HF wires (0-40 MHz).

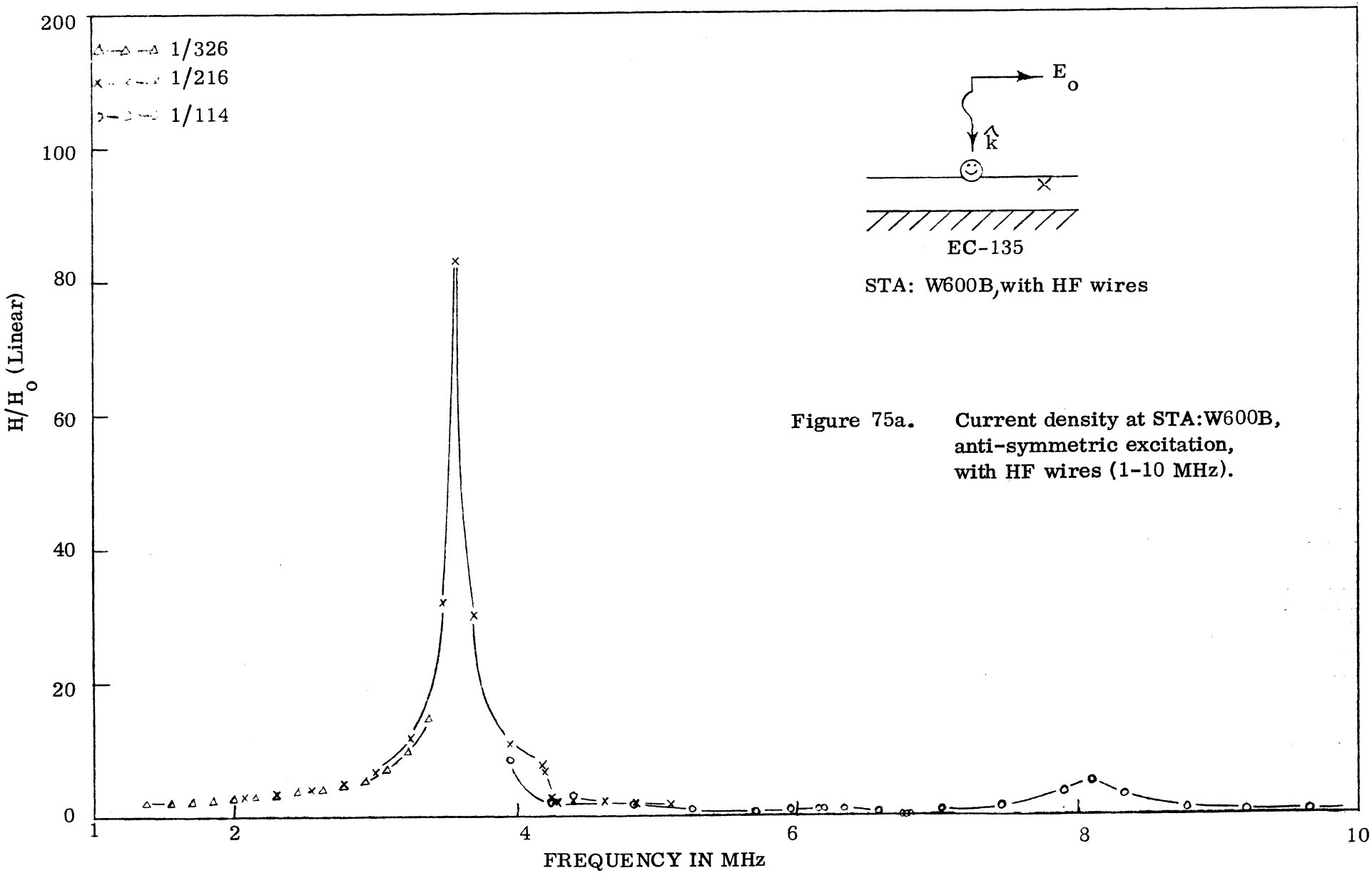

Figure 75a. Current density at STA:W600B, anti-symmetric excitation, with HF wires (1-10 MHz).

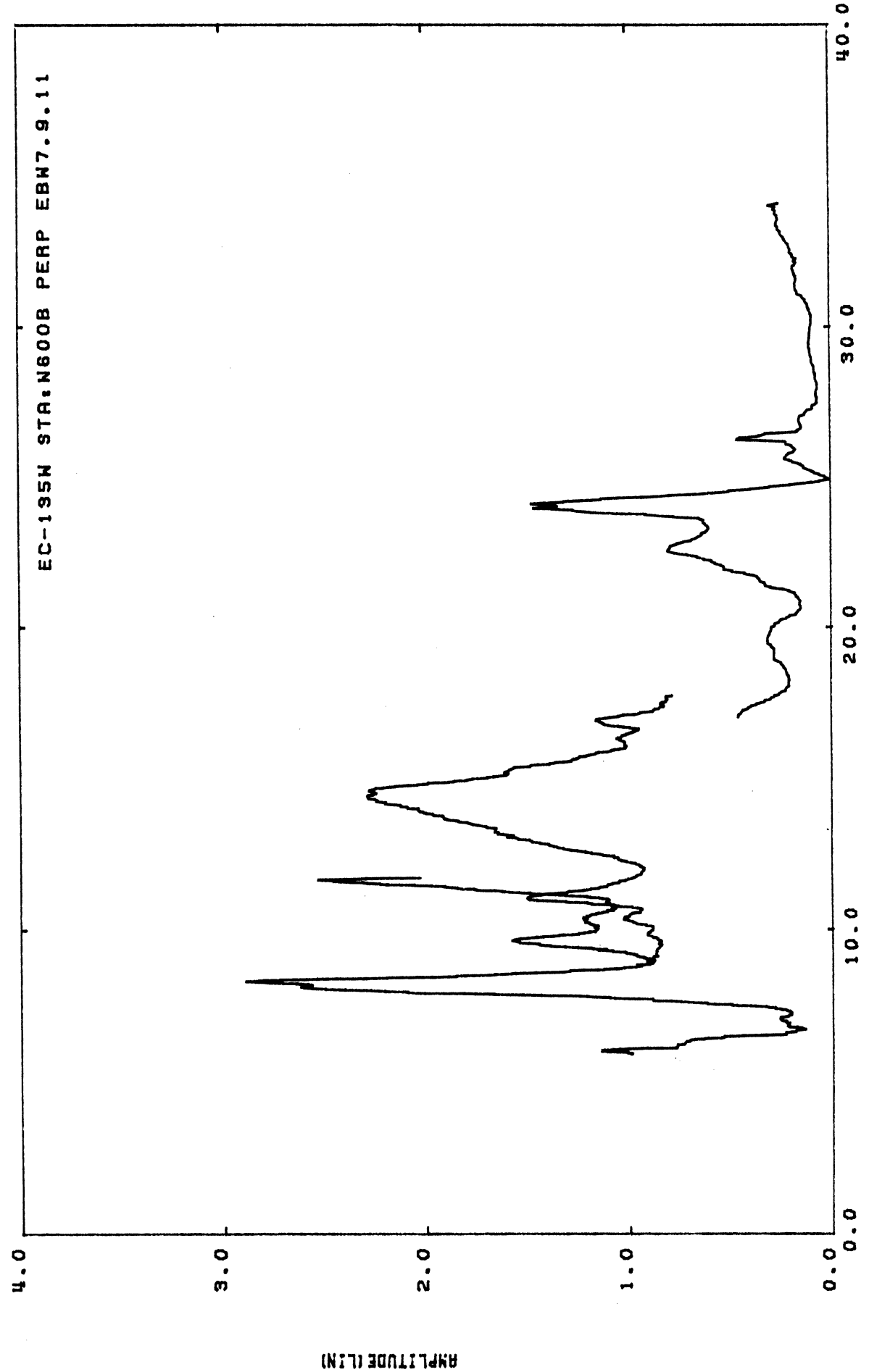

Figure 76a. Current density at STA:W600B, anti-symmetric excitation, with HF wires (0–40 MHz).

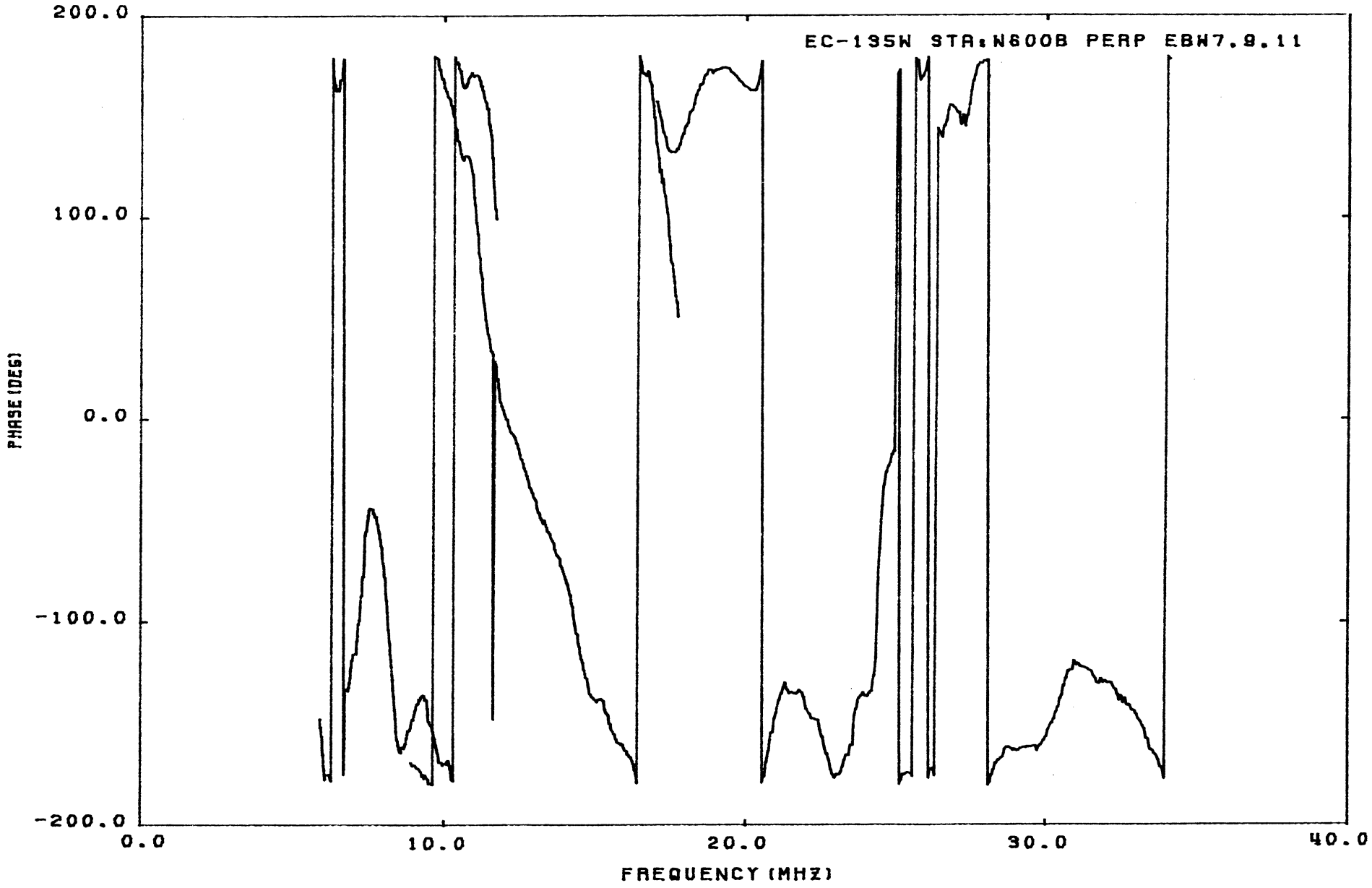

Figure 76b. Current phase at STA:W600B, anti-symmetric excitation, with HF wires (0-40 MHz).

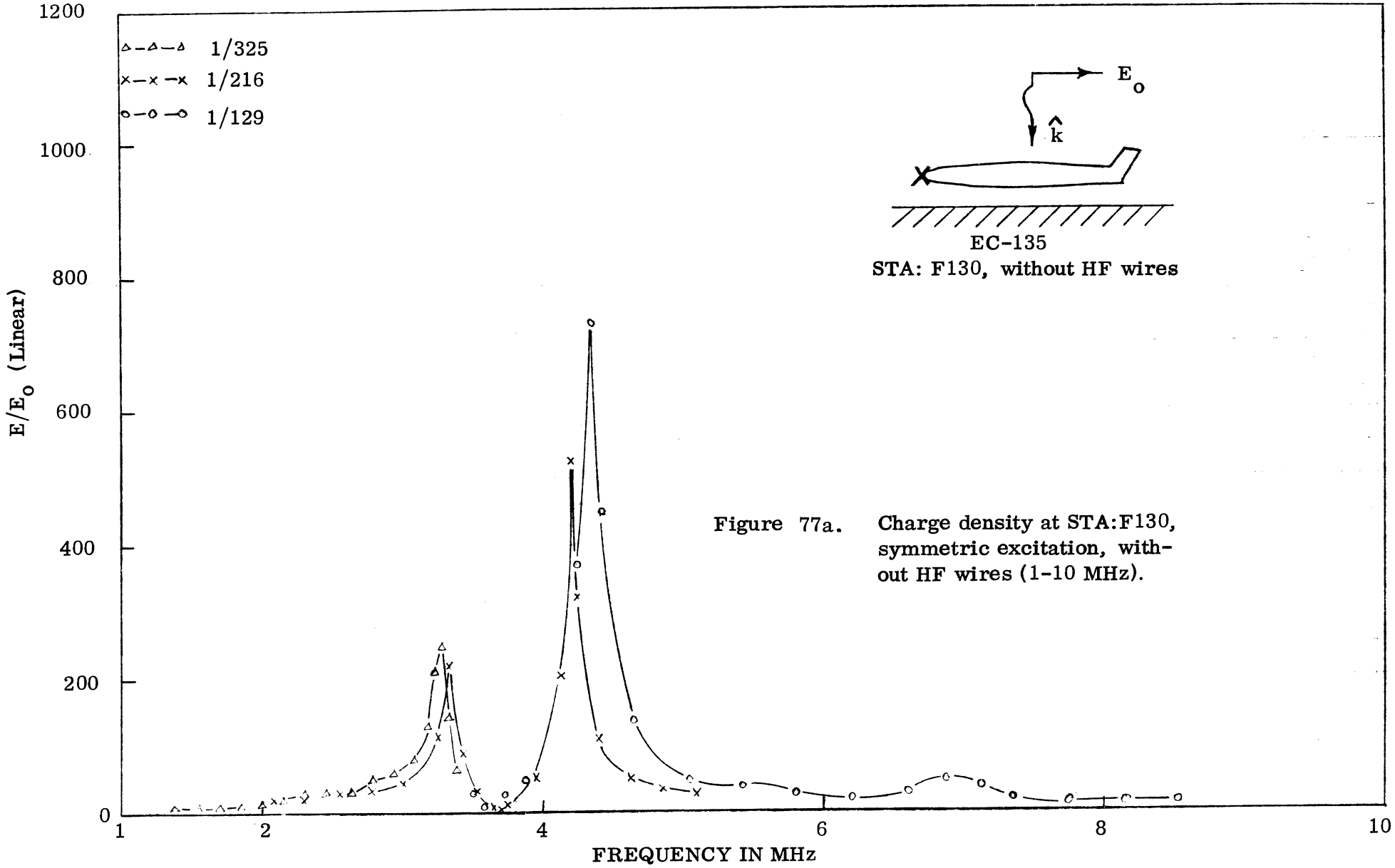

Figure 77a. Charge density at STA:F130, symmetric excitation, without HF wires (1-10 MHz).

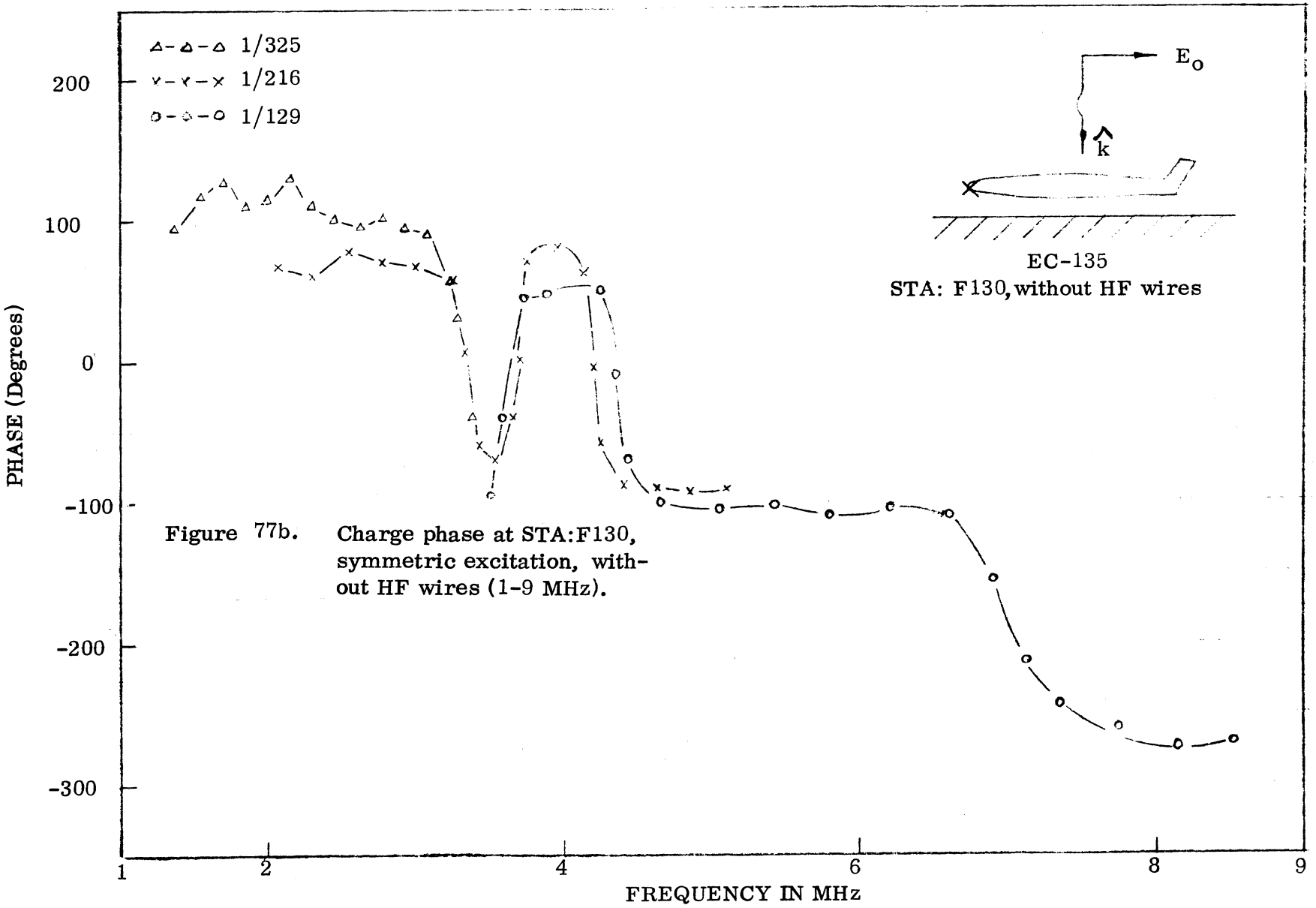

Figure 77b. Charge phase at STA:F130, symmetric excitation, without HF wires (1-9 MHz).

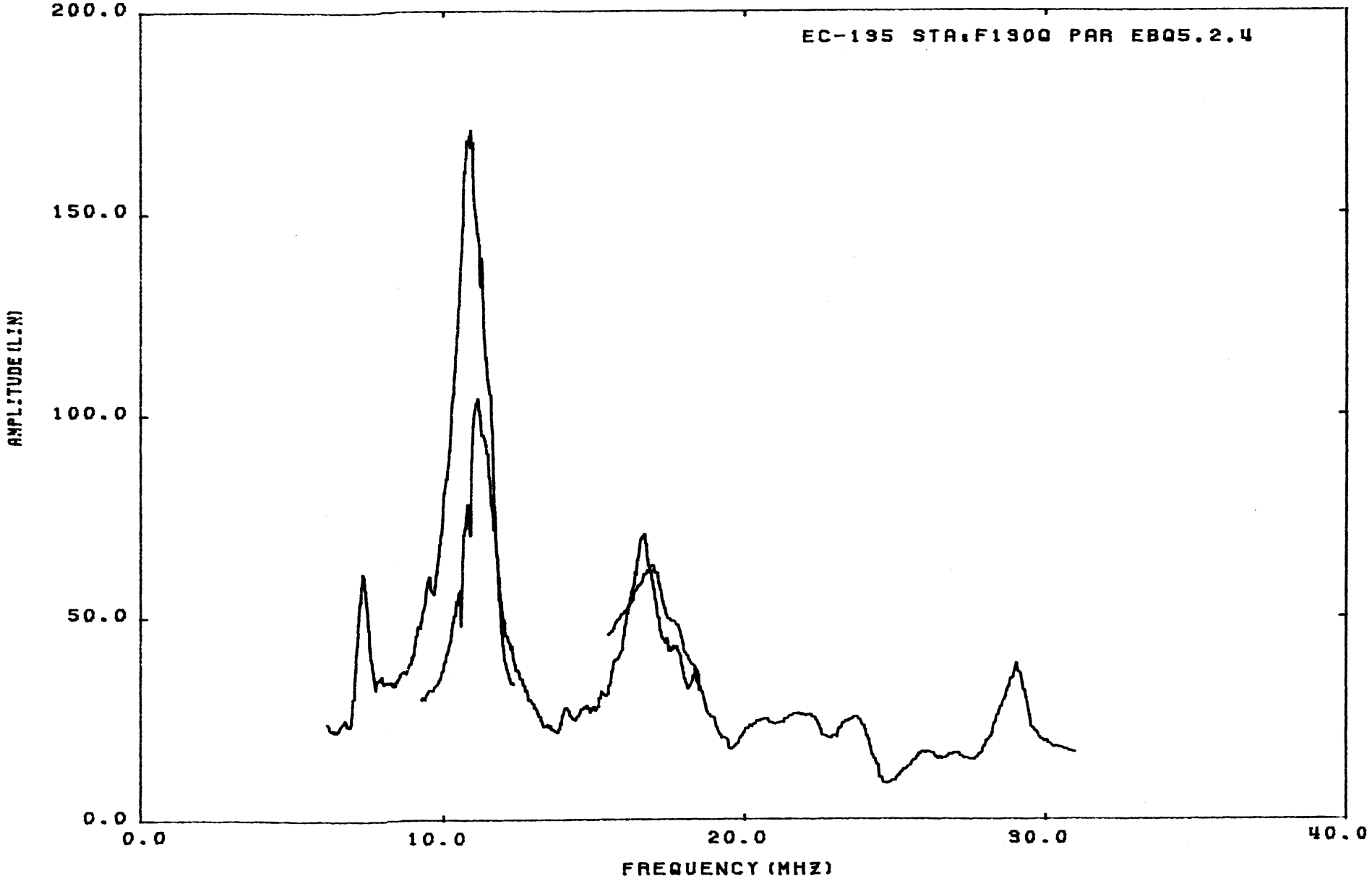

Figure 78a. Charge density at STA:F130, symmetric excitation, without HF wires (0-40 MHz).

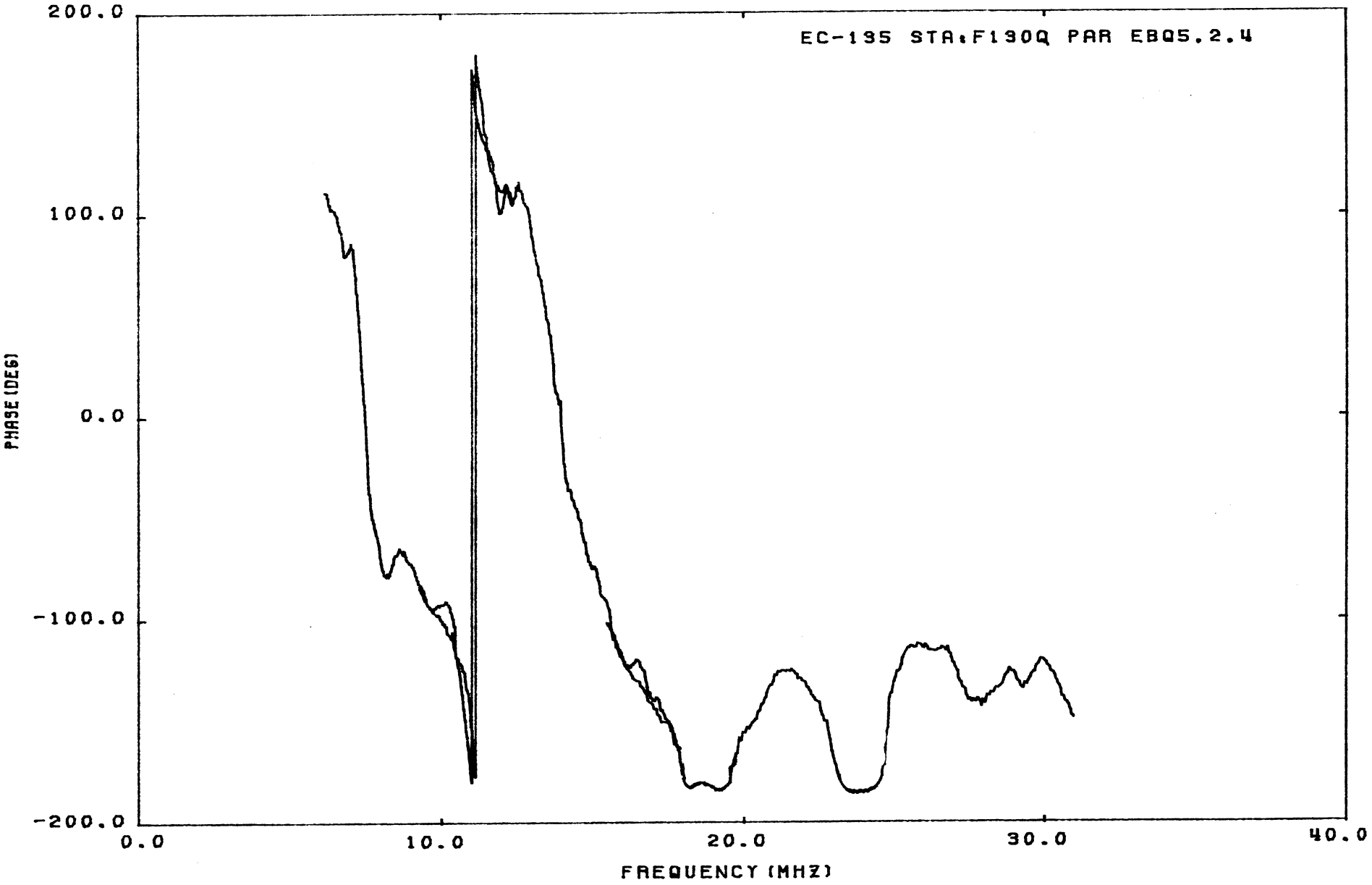

Figure 78b. Charge phase at STA:F130, symmetric excitation, without HF wires (0-40 MHz).

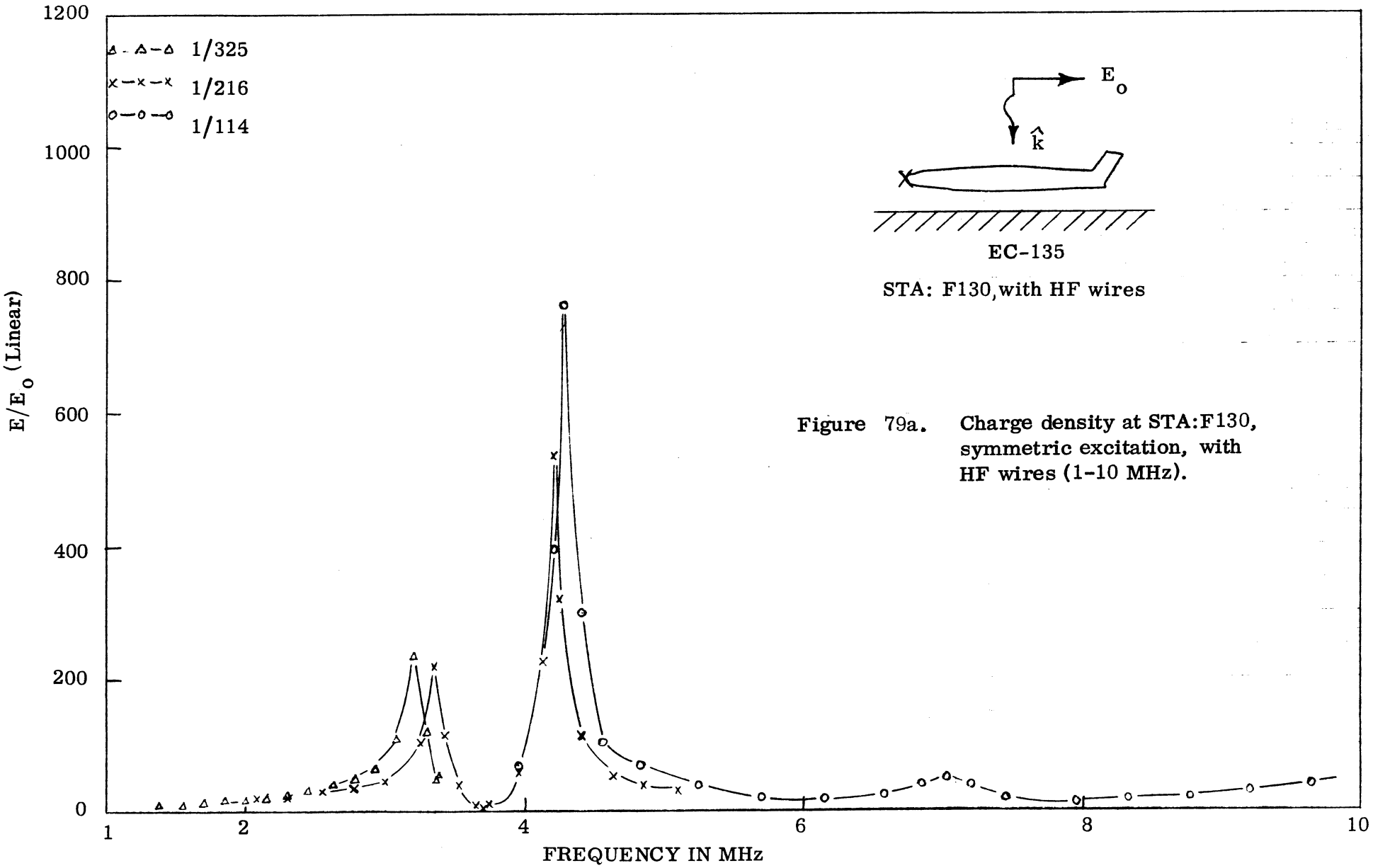

Figure 79a. Charge density at STA:F130, symmetric excitation, with HF wires (1-10 MHz).

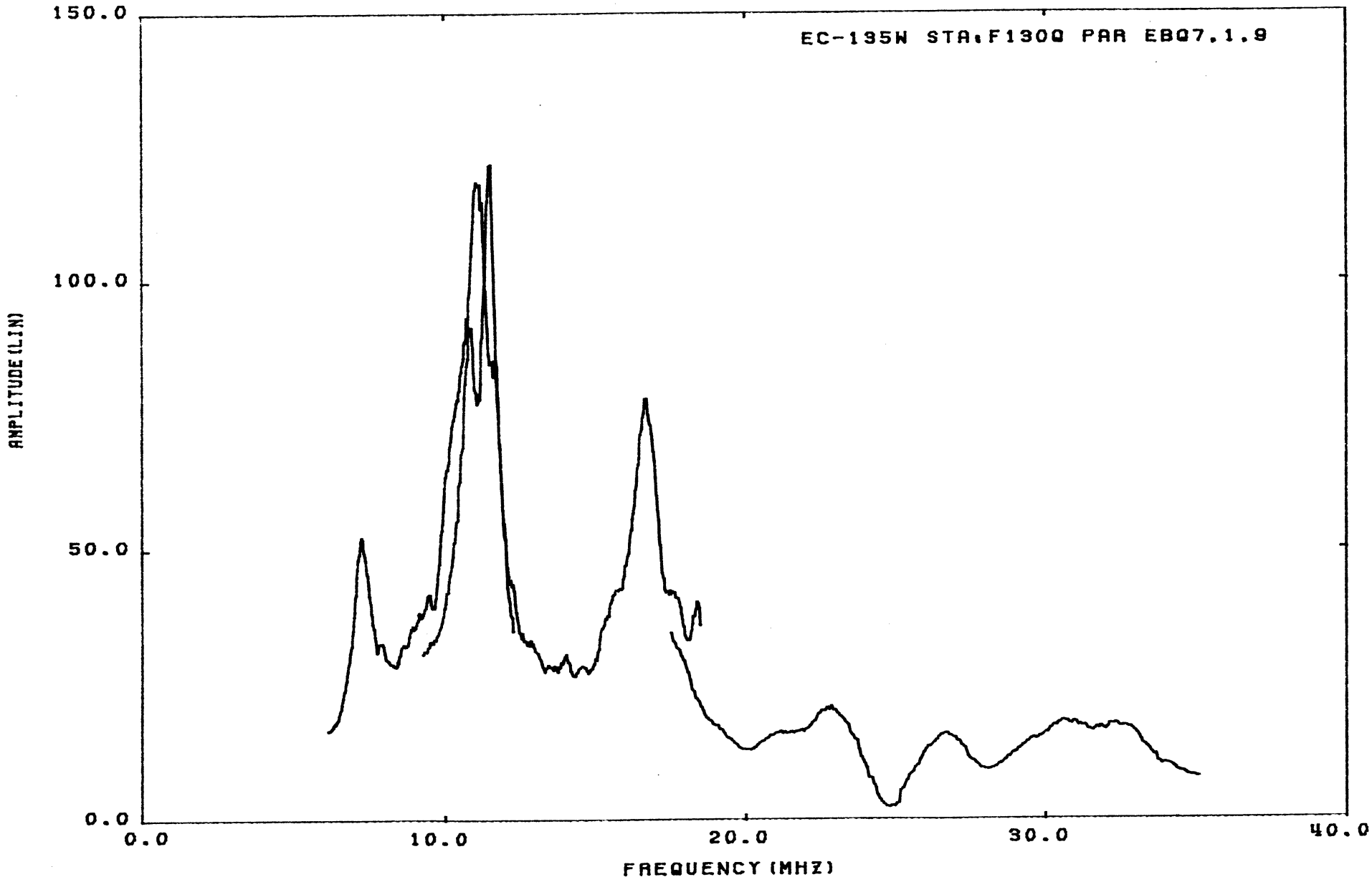

Figure 80a. Charge density at STA:F130, symmetric excitation, with HF wires (0-40 MHz).

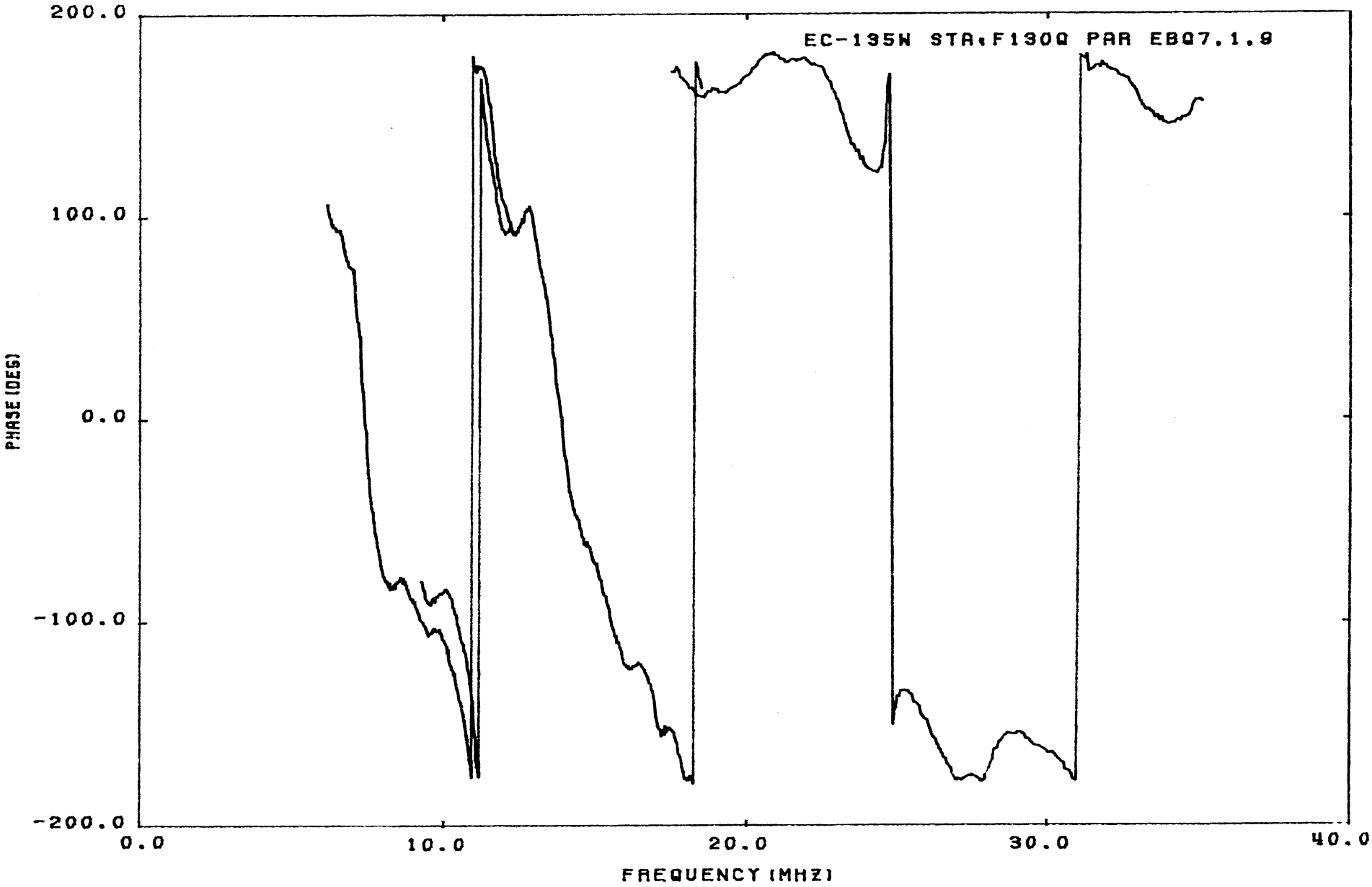

Figure 80b. Charge phase at STA:F130, symmetric excitation, with HF wires (0-40 MHz).

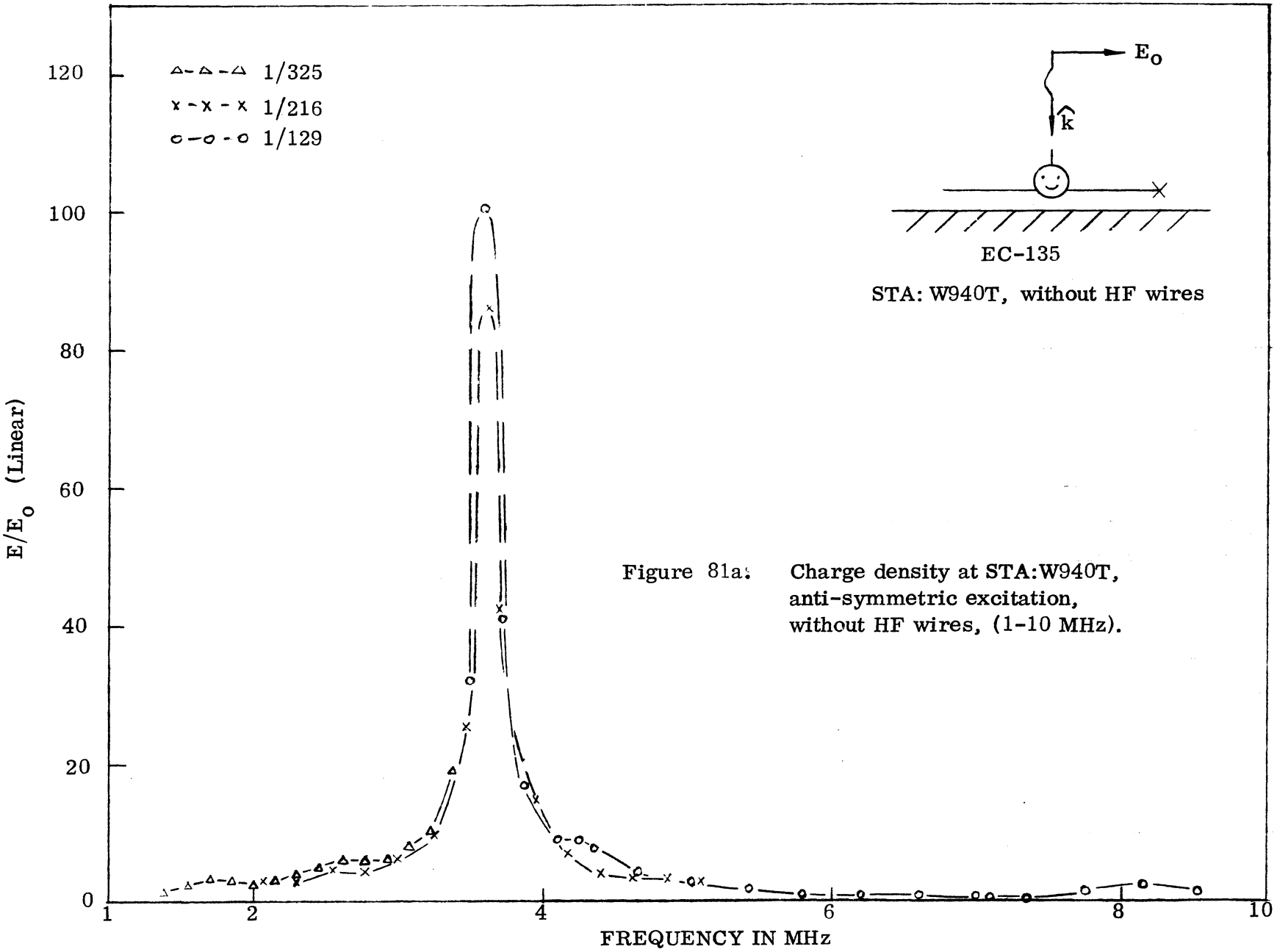

Figure 81a: Charge density at STA:W940T, anti-symmetric excitation, without HF wires, (1-10 MHz).

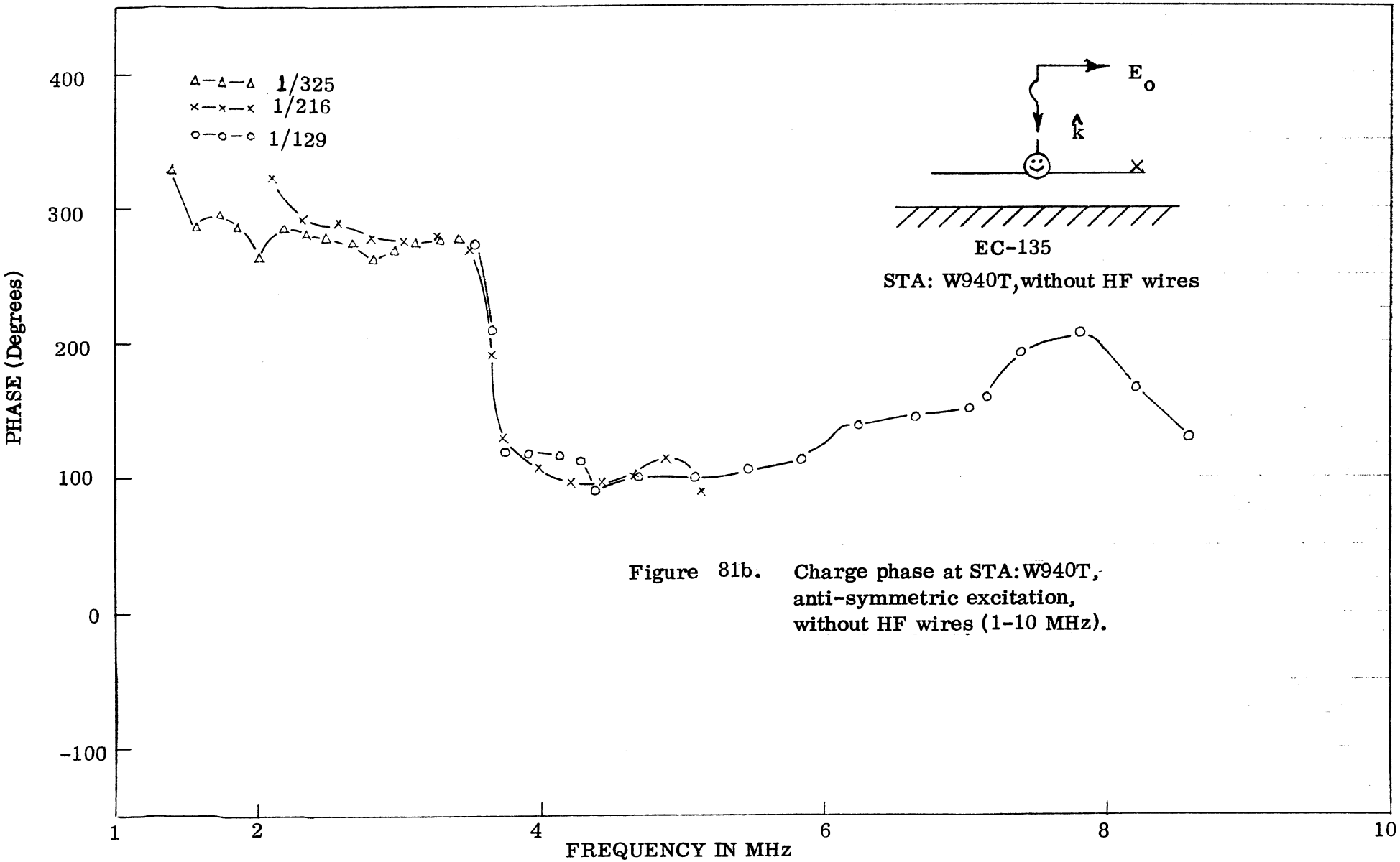

Figure 81b. Charge phase at STA: W940T, anti-symmetric excitation, without HF wires (1-10 MHz).

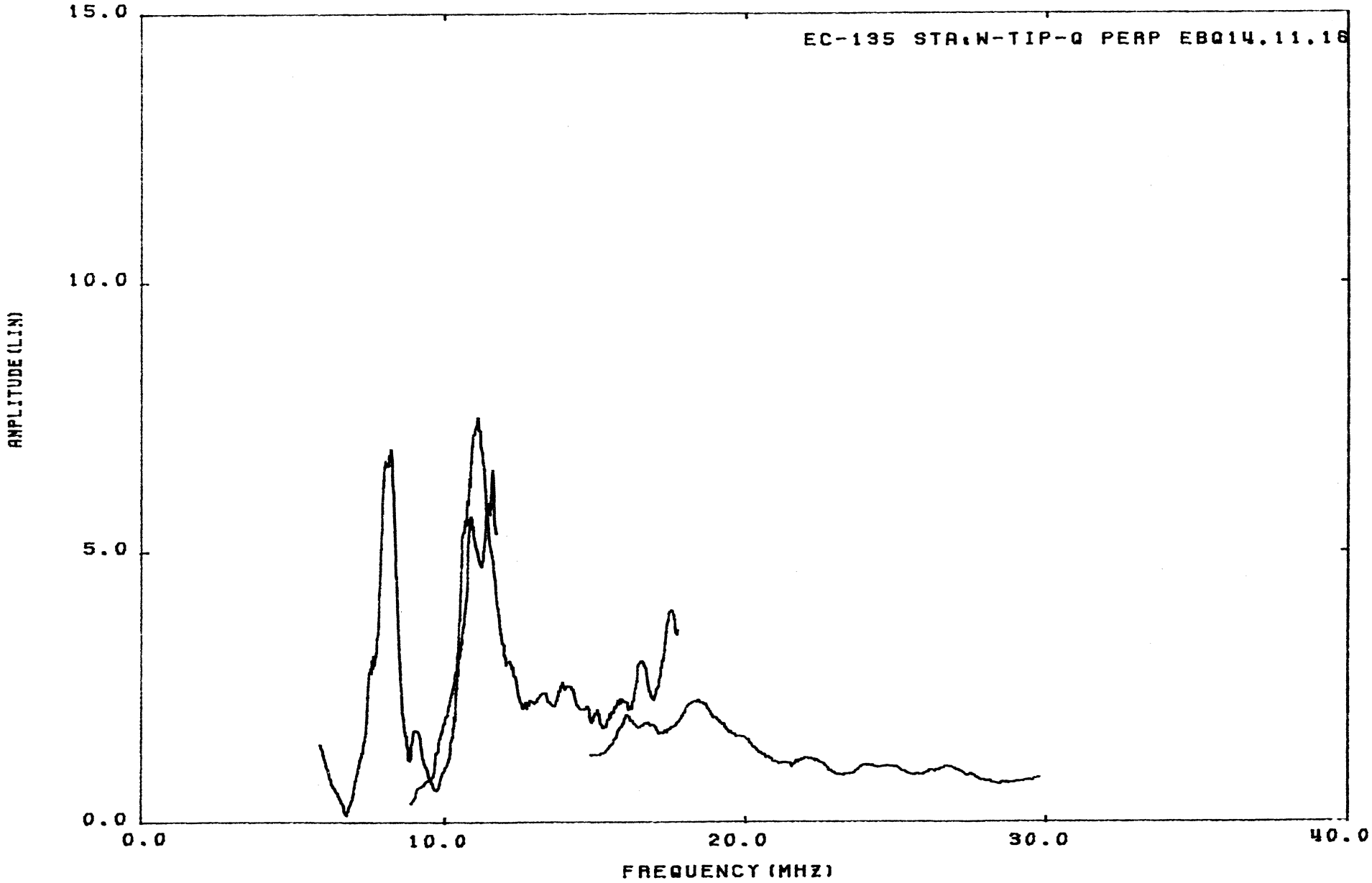

Figure 82a. Charge density at STA:W940T, anti-symmetric excitation, without HF wires (0-40 MHz).

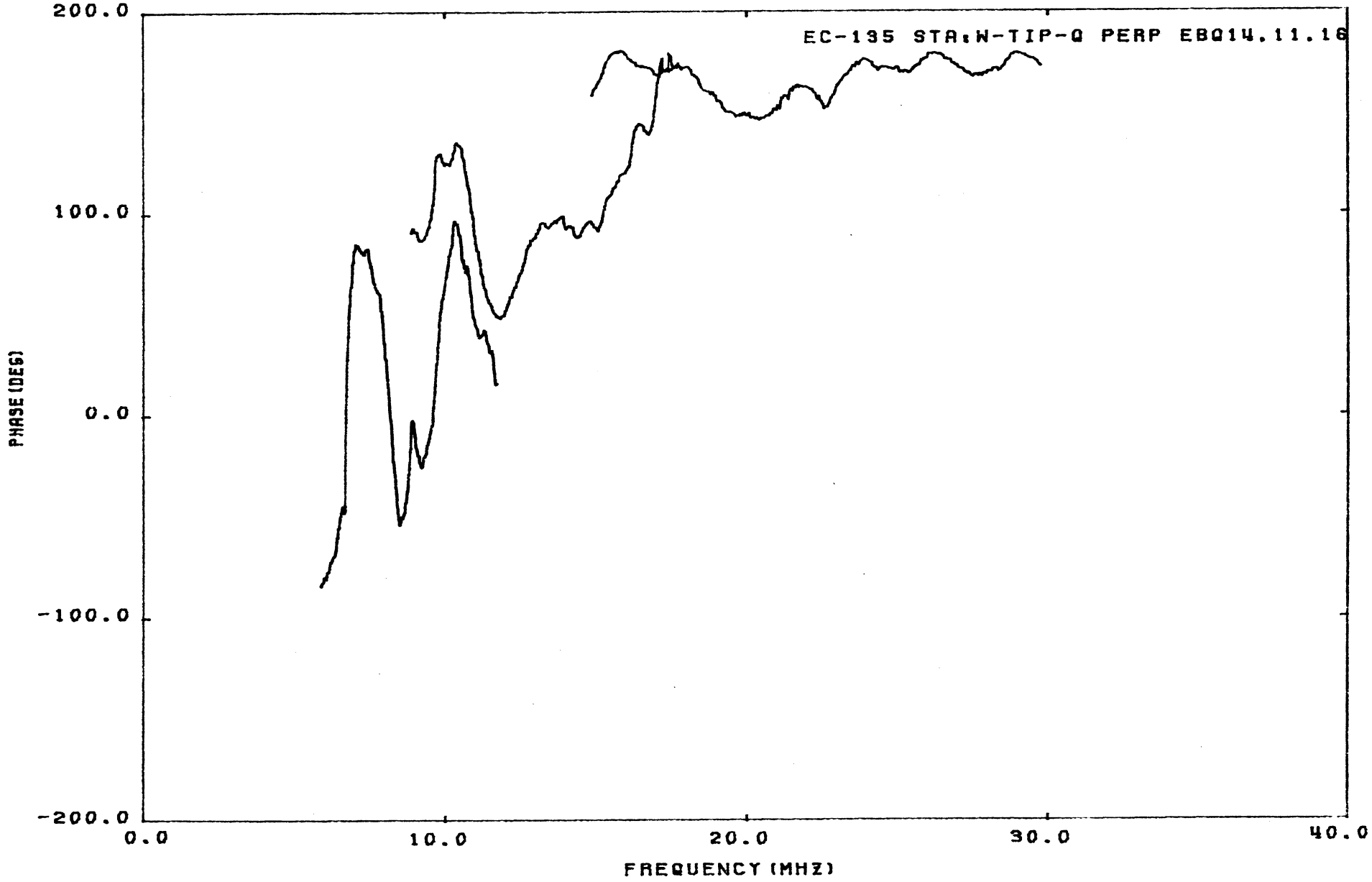

Figure 82b. Charge phase at STA:W940T, anti-symmetric excitation, without HF wires (0-40 MHz).

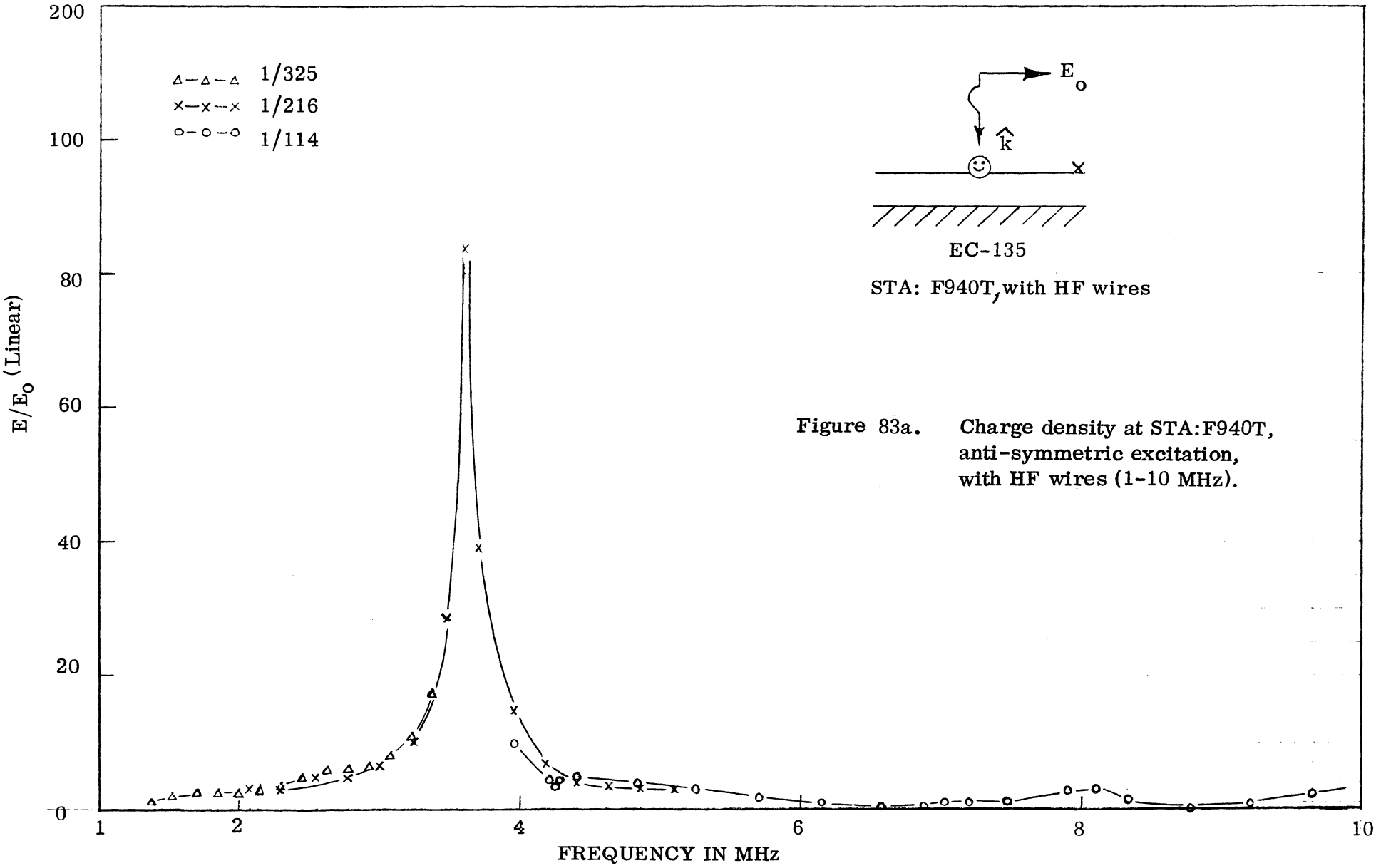

Figure 83a. Charge density at STA:F940T, anti-symmetric excitation, with HF wires (1-10 MHz).

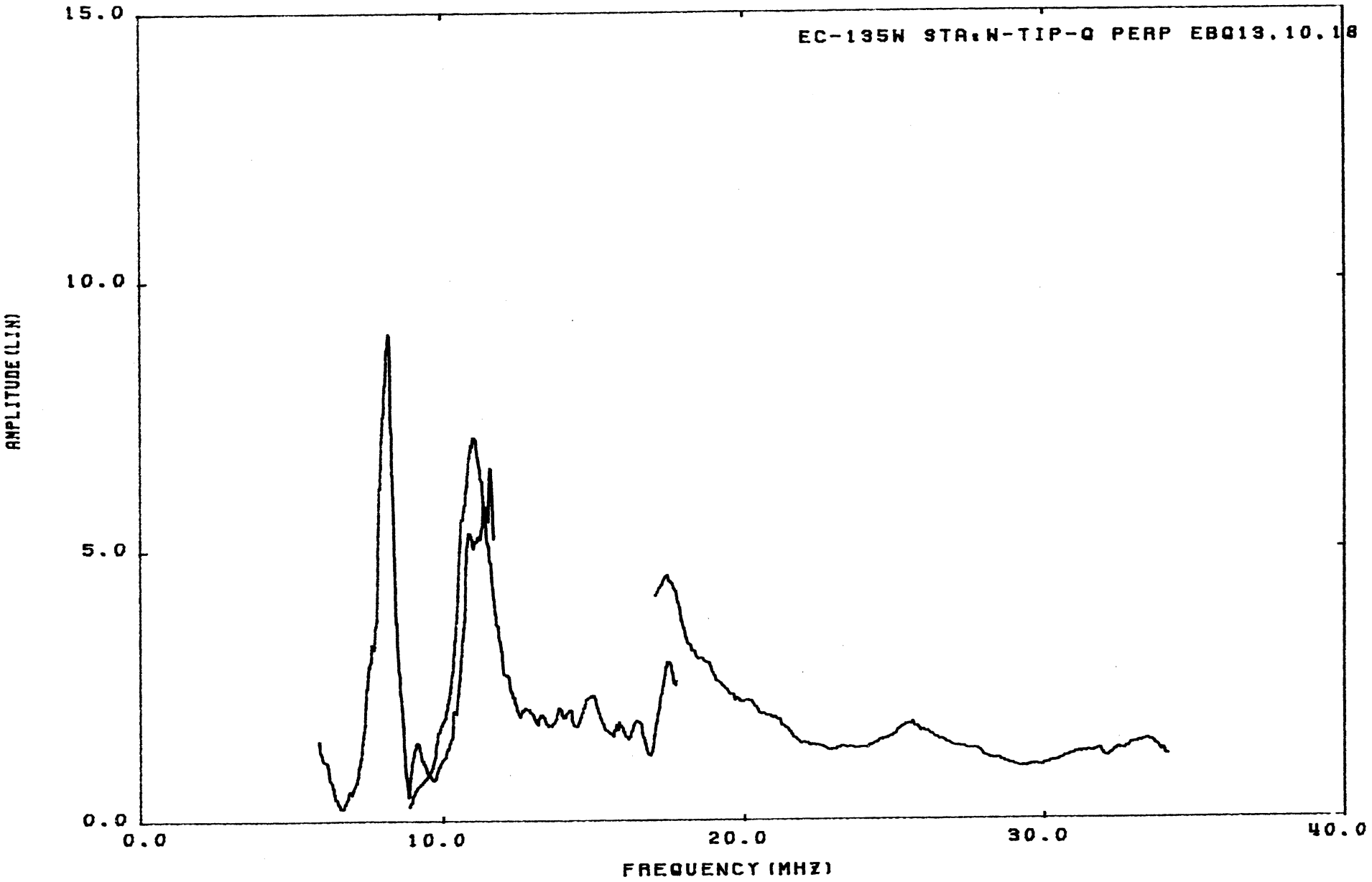

Figure 84a. Charge density at STA:F940T, anti-symmetric excitation, with HF wires (0-40 MHz).

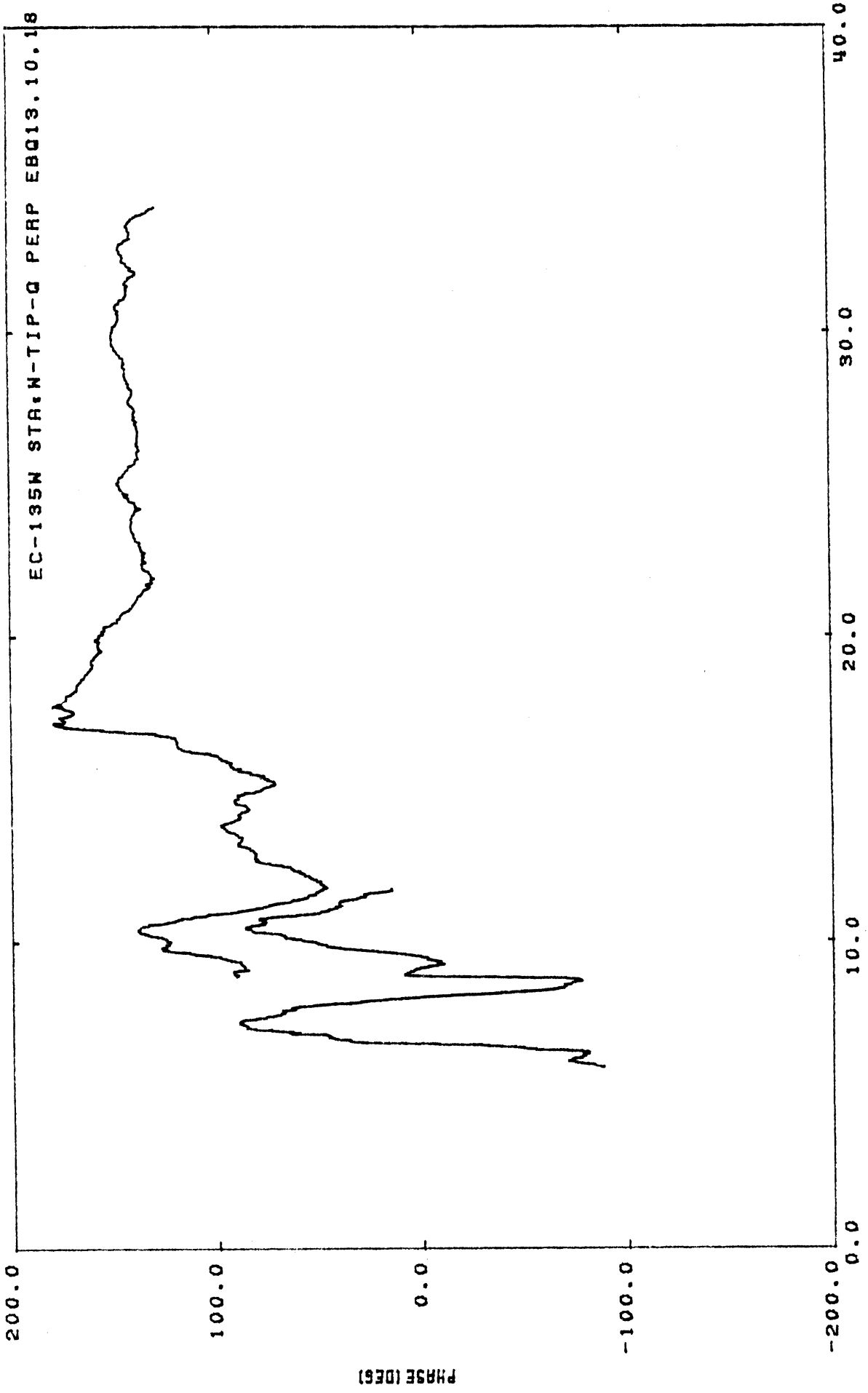

Figure 84b. Charge phase at STA:F940T, anti-symmetric excitation, with HF wires (0-40 MHz).

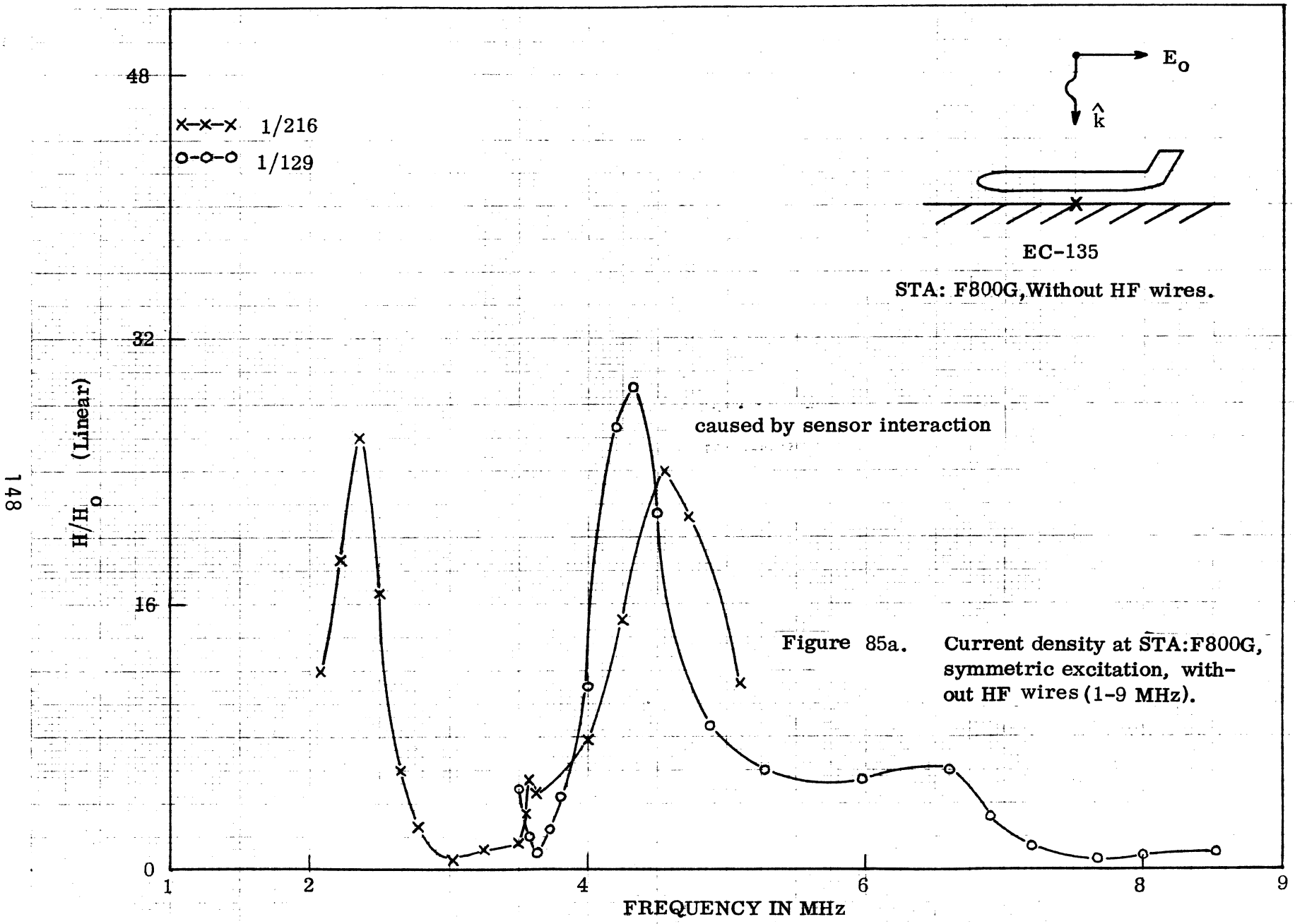

Figure 85a. Current density at STA:F800G, symmetric excitation, without HF wires (1-9 MHz).

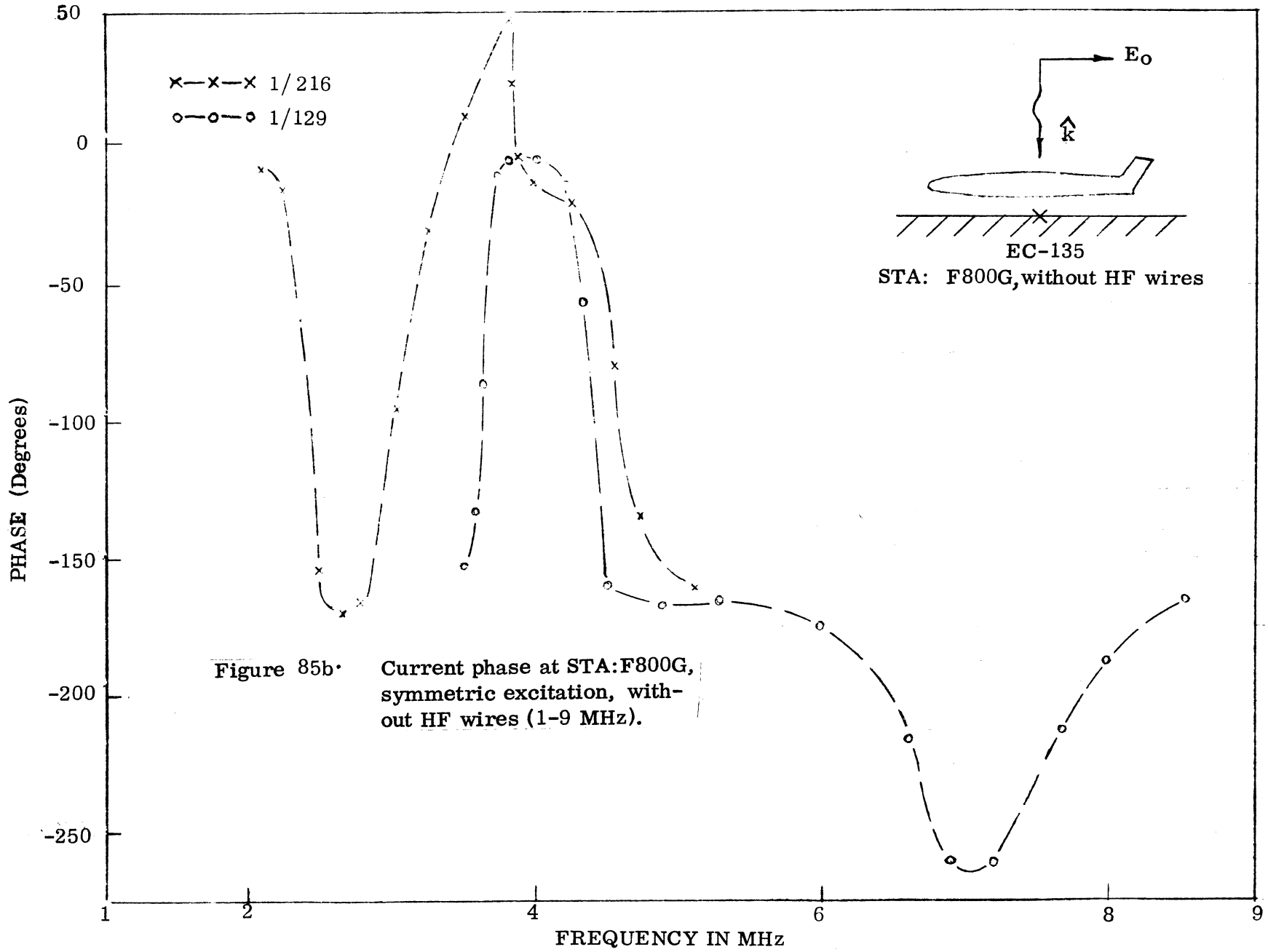

Figure 85b. Current phase at STA:F800G, symmetric excitation, without HF wires (1-9 MHz).

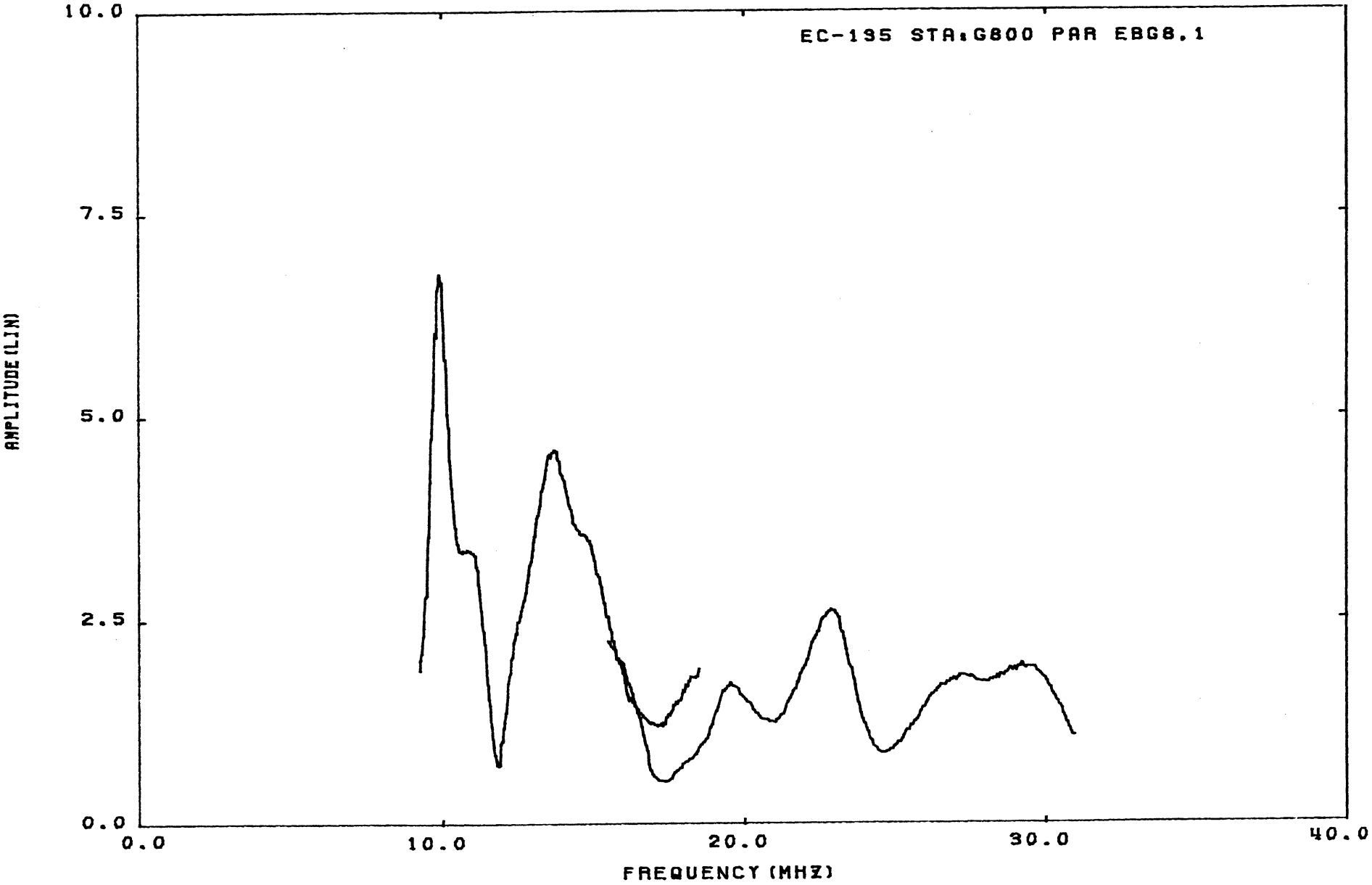

Figure 86a. Current density at STA:F800G, symmetric excitation, without HF wires (0-40 MHz).

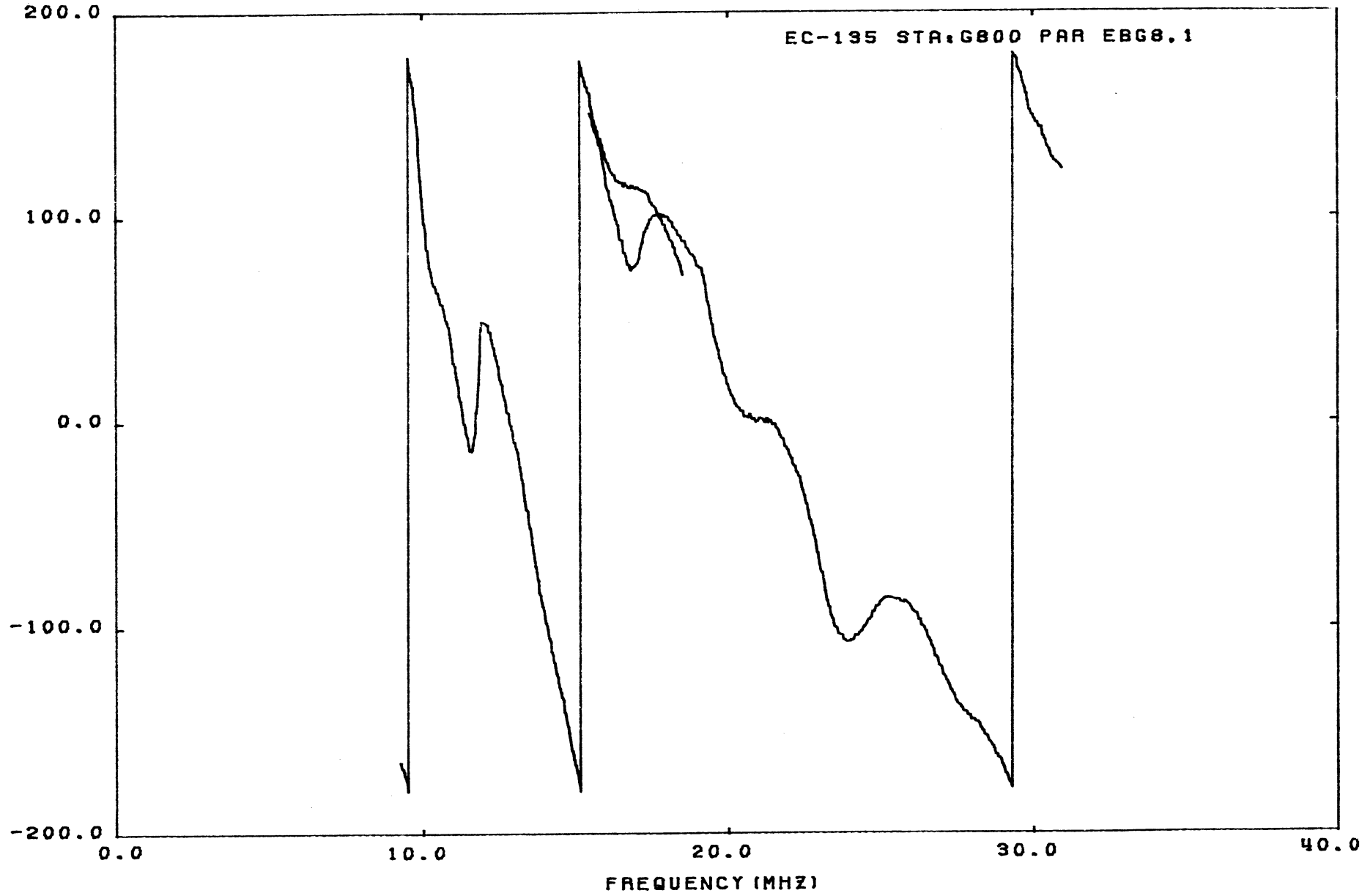

Figure 86b. Current phase at STA:F800G, symmetric excitation, without HF wires (0-40 MHz).

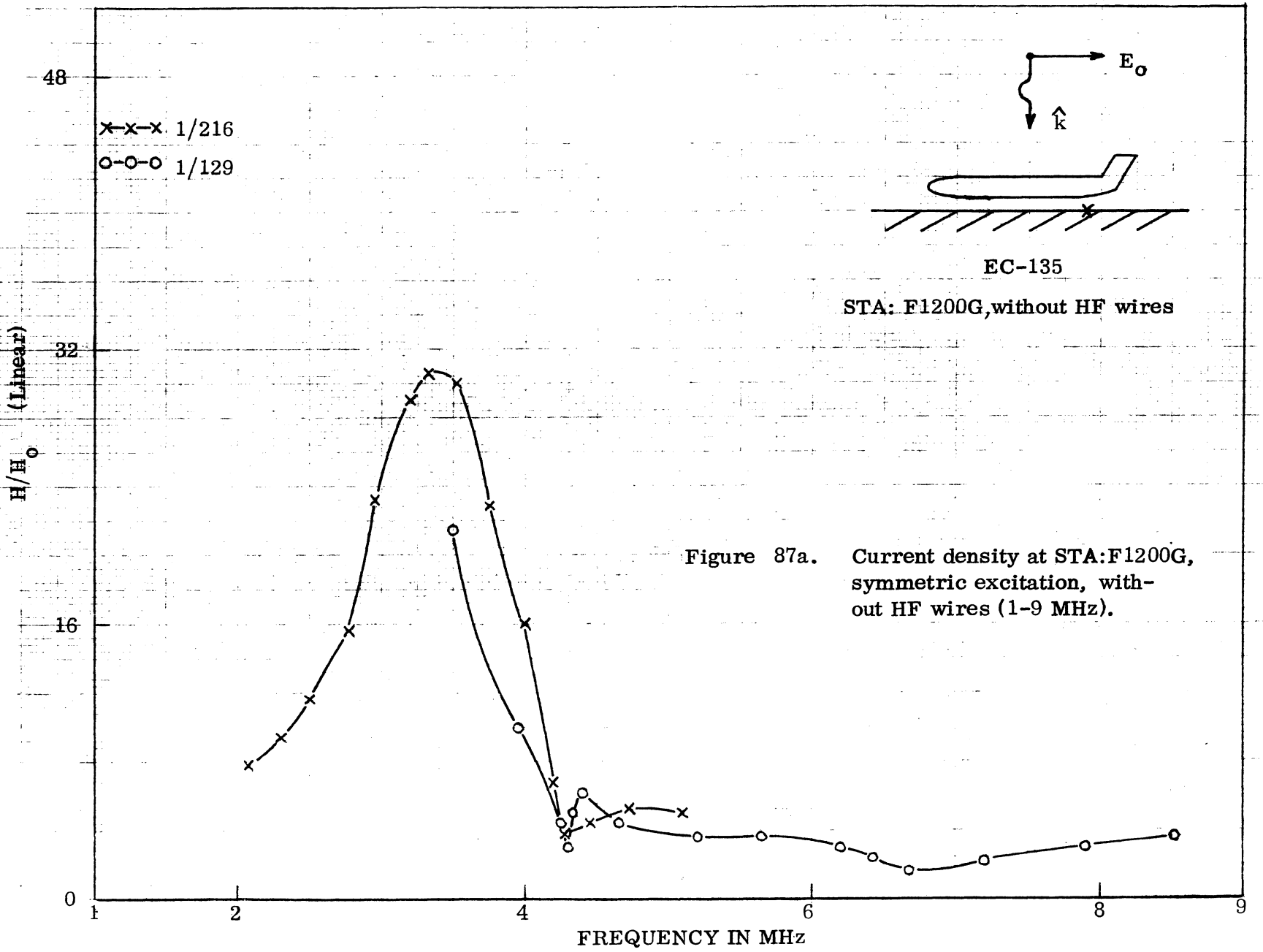

Figure 87a. Current density at STA:F1200G, symmetric excitation, without HF wires (1-9 MHz).

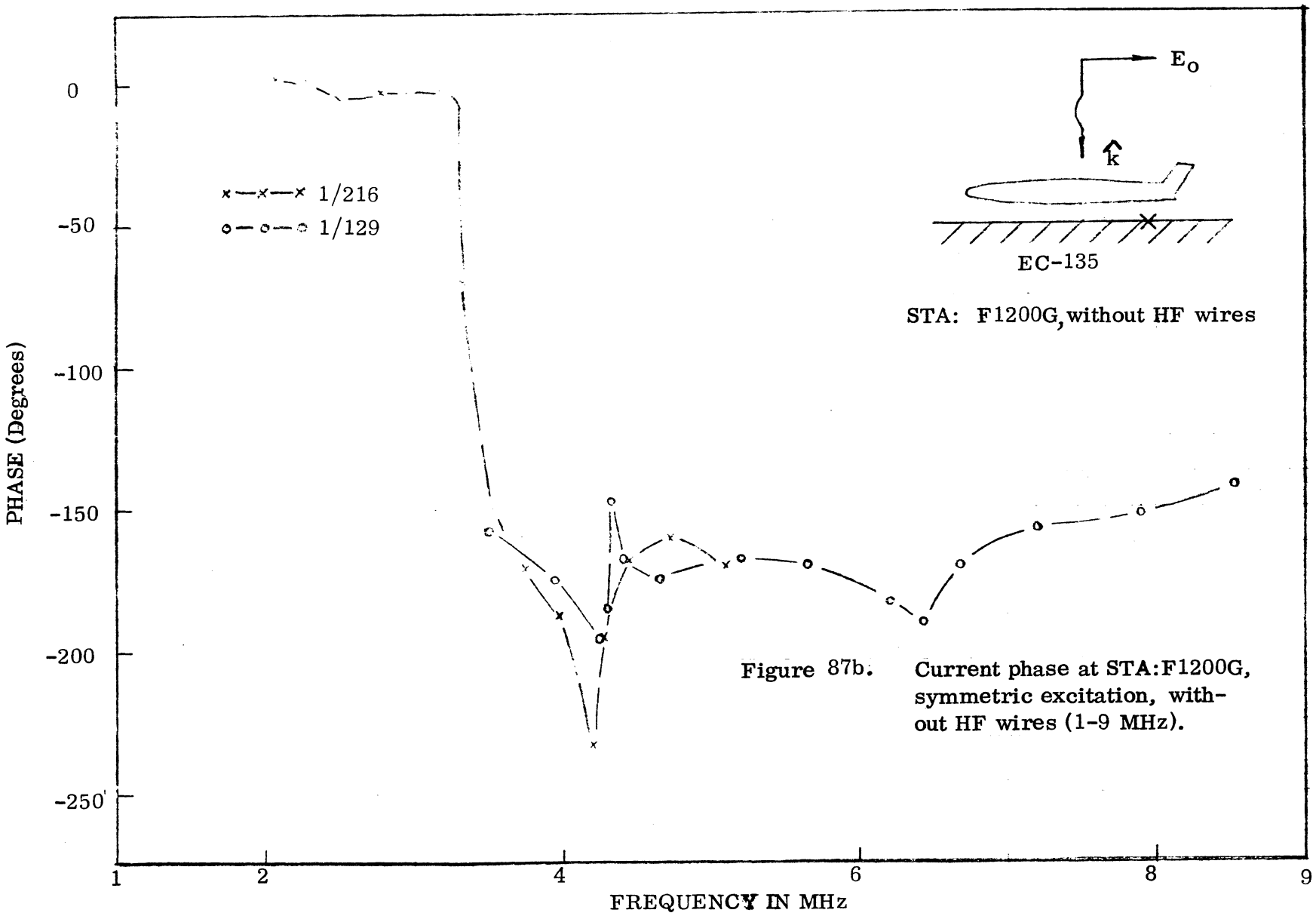

Figure 87b. Current phase at STA:F1200G, symmetric excitation, without HF wires (1-9 MHz).

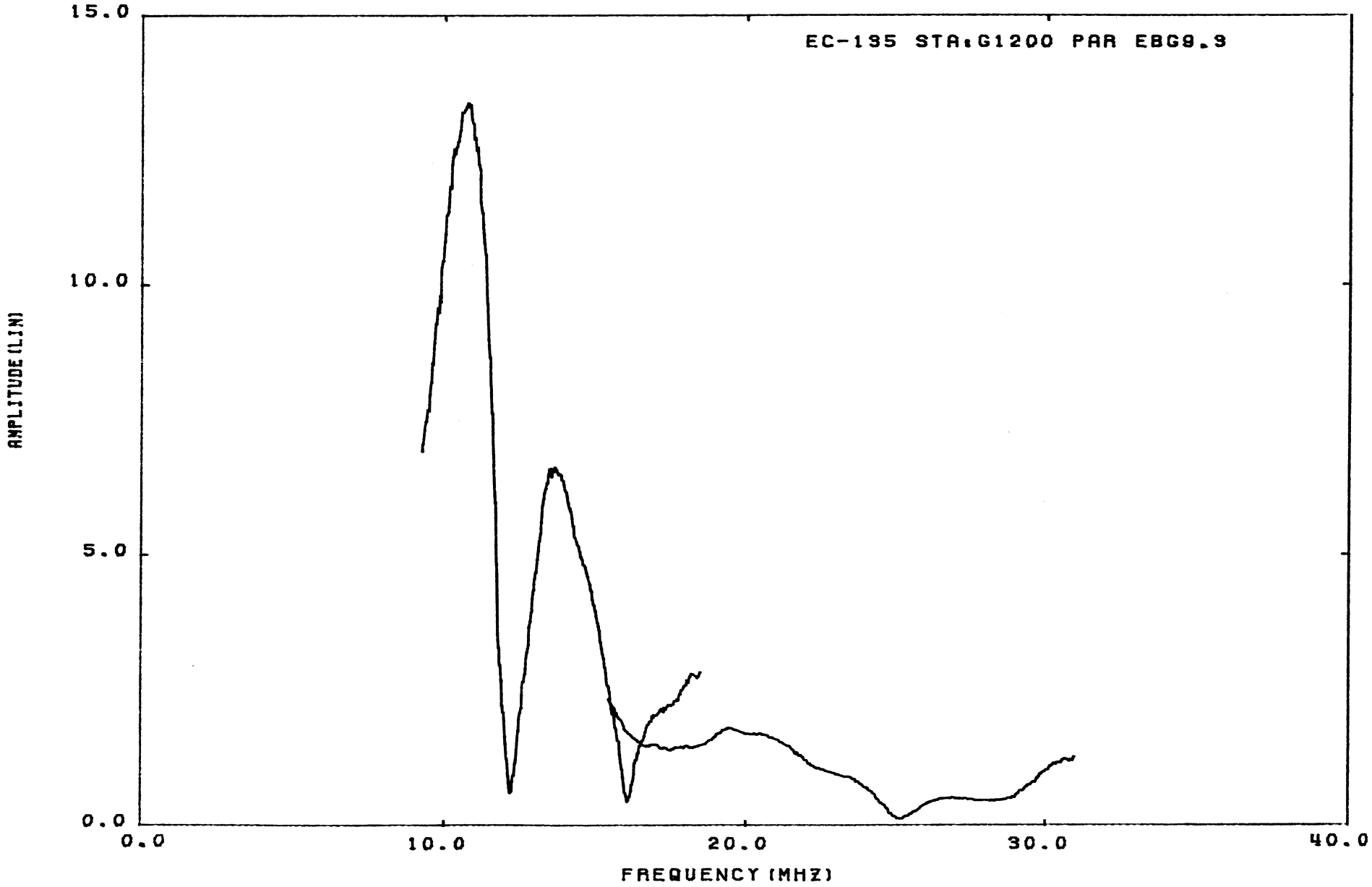

Figure 88a. Current density at STA:F1200G, symmetric excitation without HF wires (0-40 MHz).

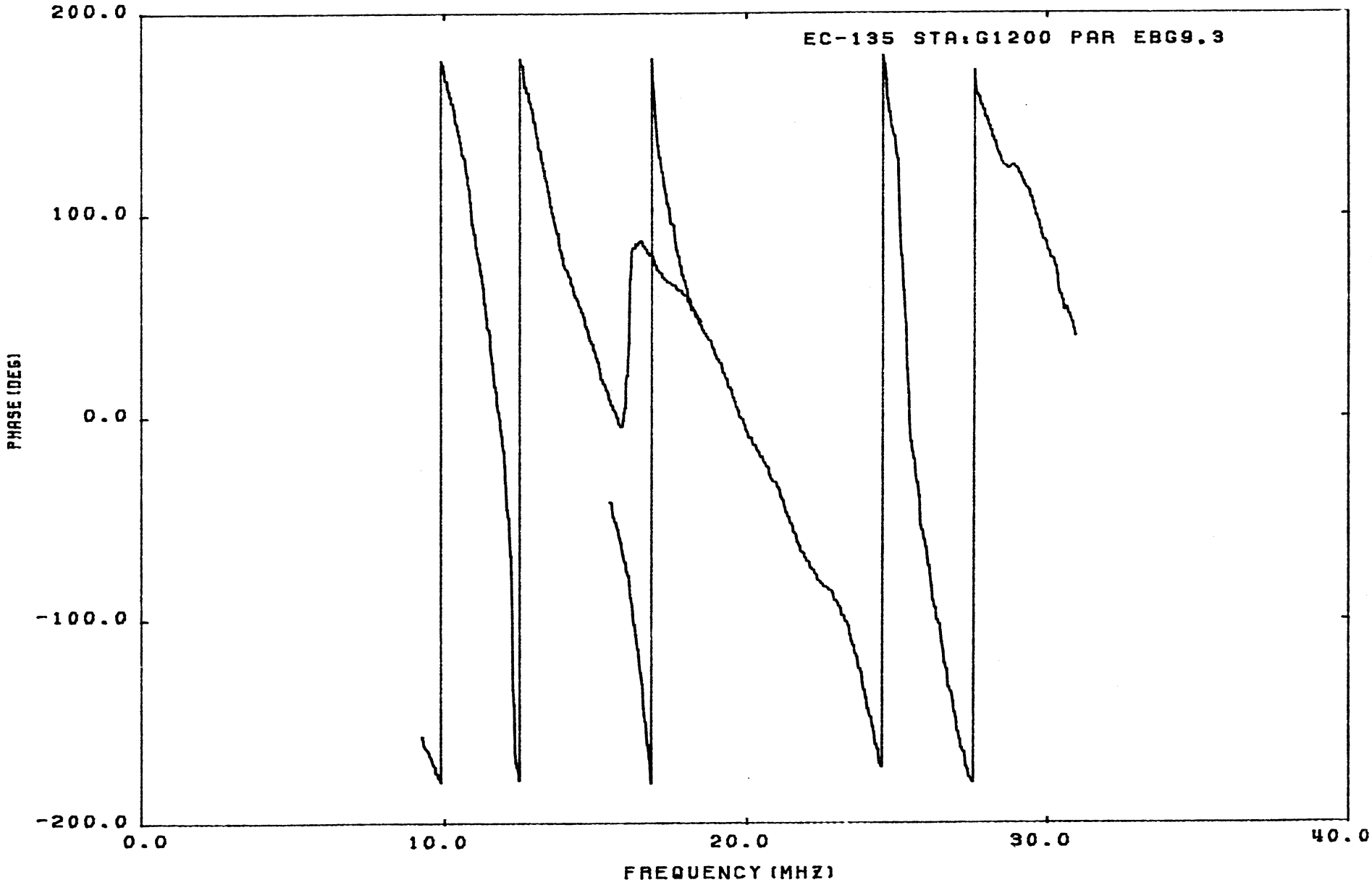

Figure 88b. Current phase at STA:F1200G, symmetric excitation, without HF wires (0-40 MHz).

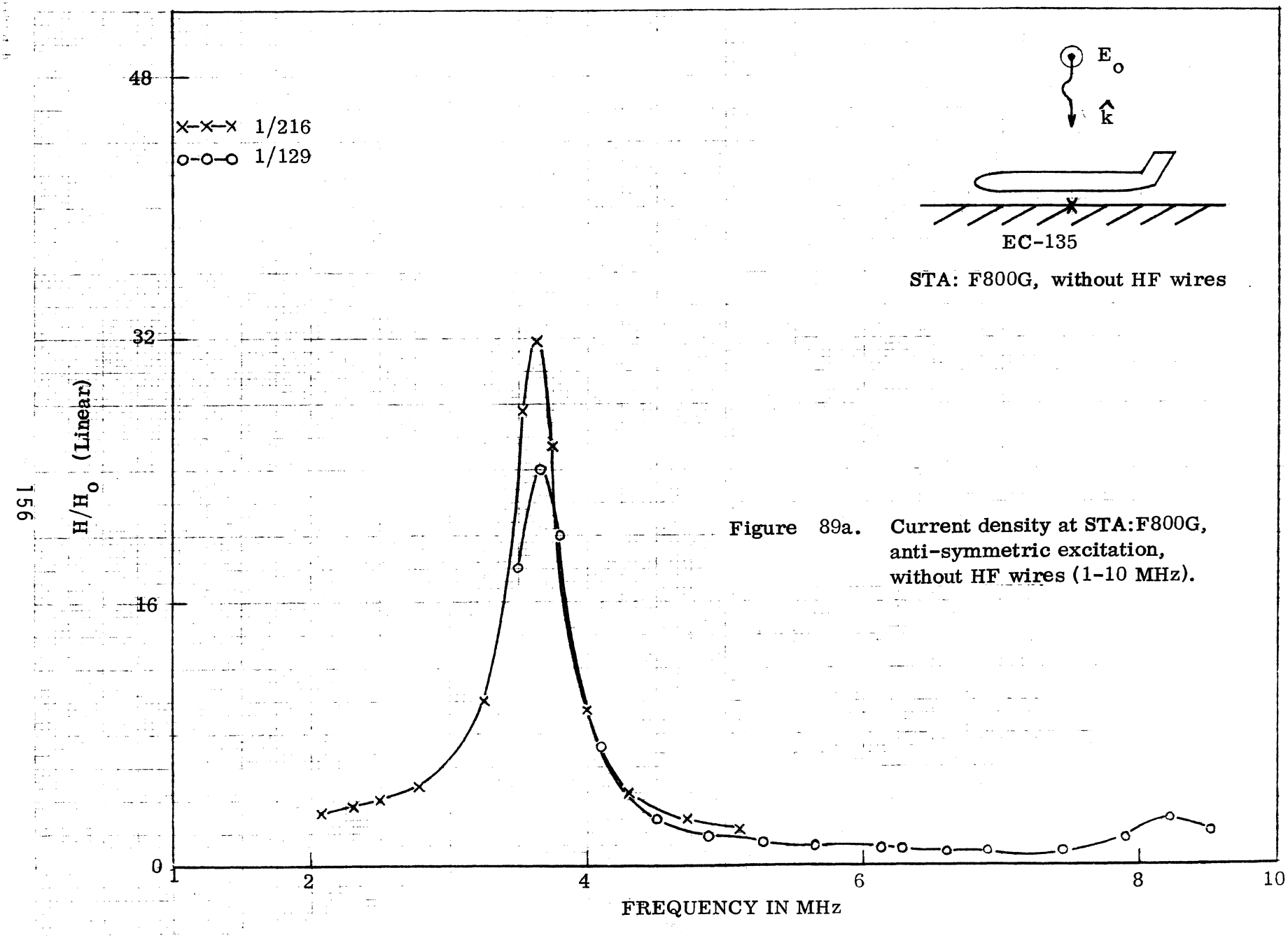

Figure 89a. Current density at STA:F800G, anti-symmetric excitation, without HF wires (1-10 MHz).

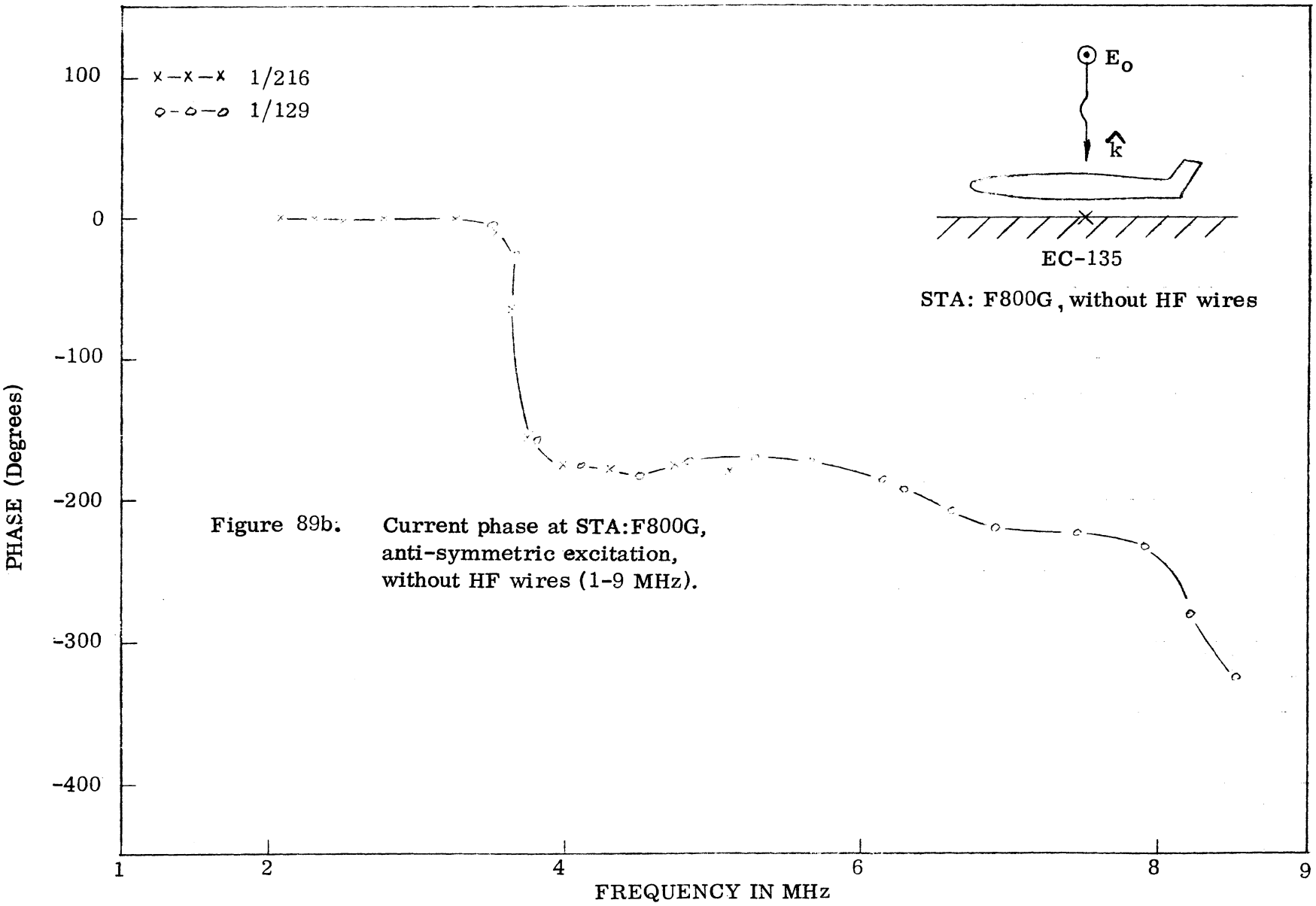

Figure 89b. Current phase at STA:F800G, anti-symmetric excitation, without HF wires (1-9 MHz).

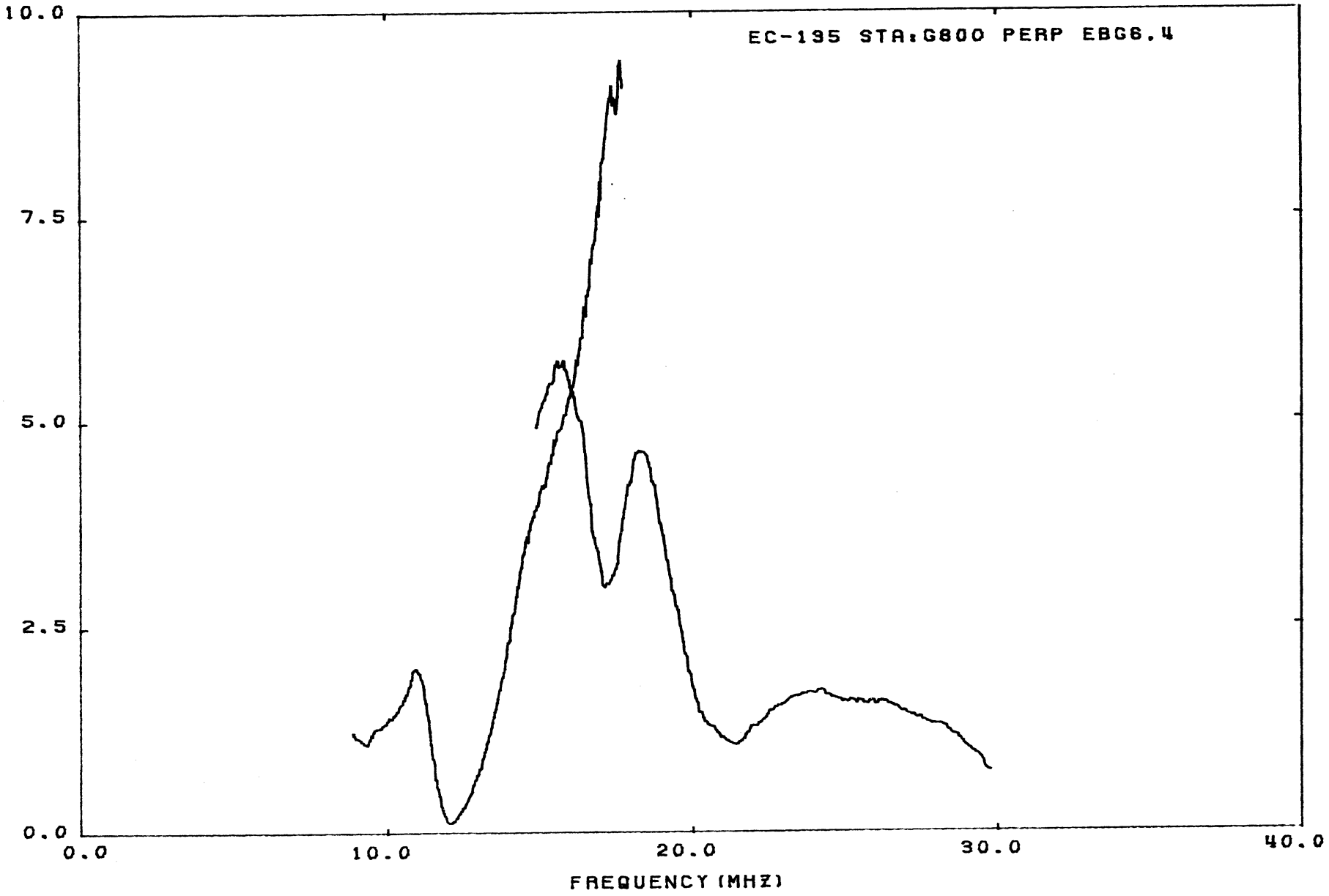

Figure 90a. Current density at STA:F800G, anti-symmetric excitation, without HF wires (0-40 MHz).

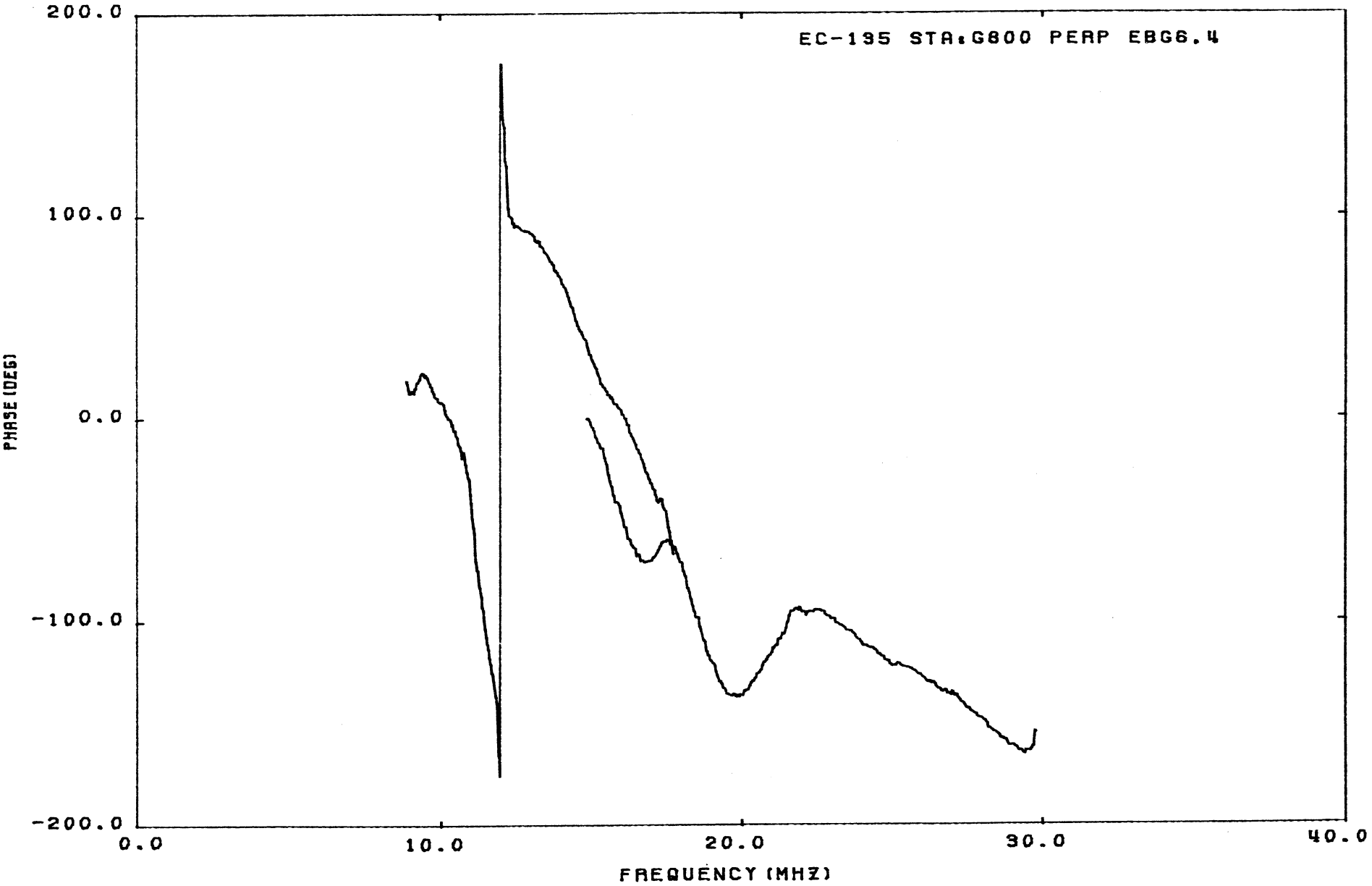

Figure 90b. Current phase at STA:F800G, anti-symmetric excitation, without HF wires (0-40 MHz).

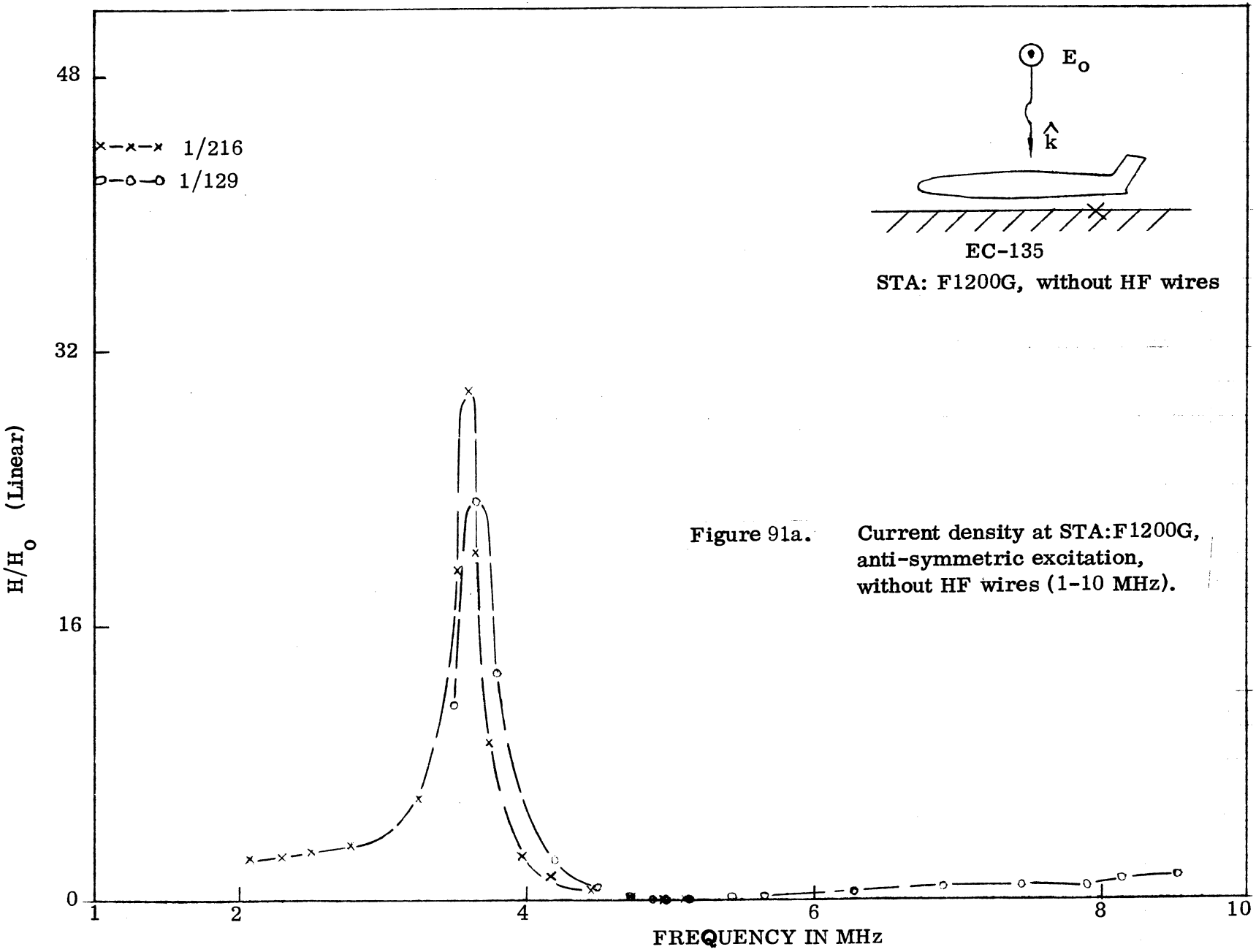

Figure 91a. Current density at STA:F1200G, anti-symmetric excitation, without HF wires (1-10 MHz).

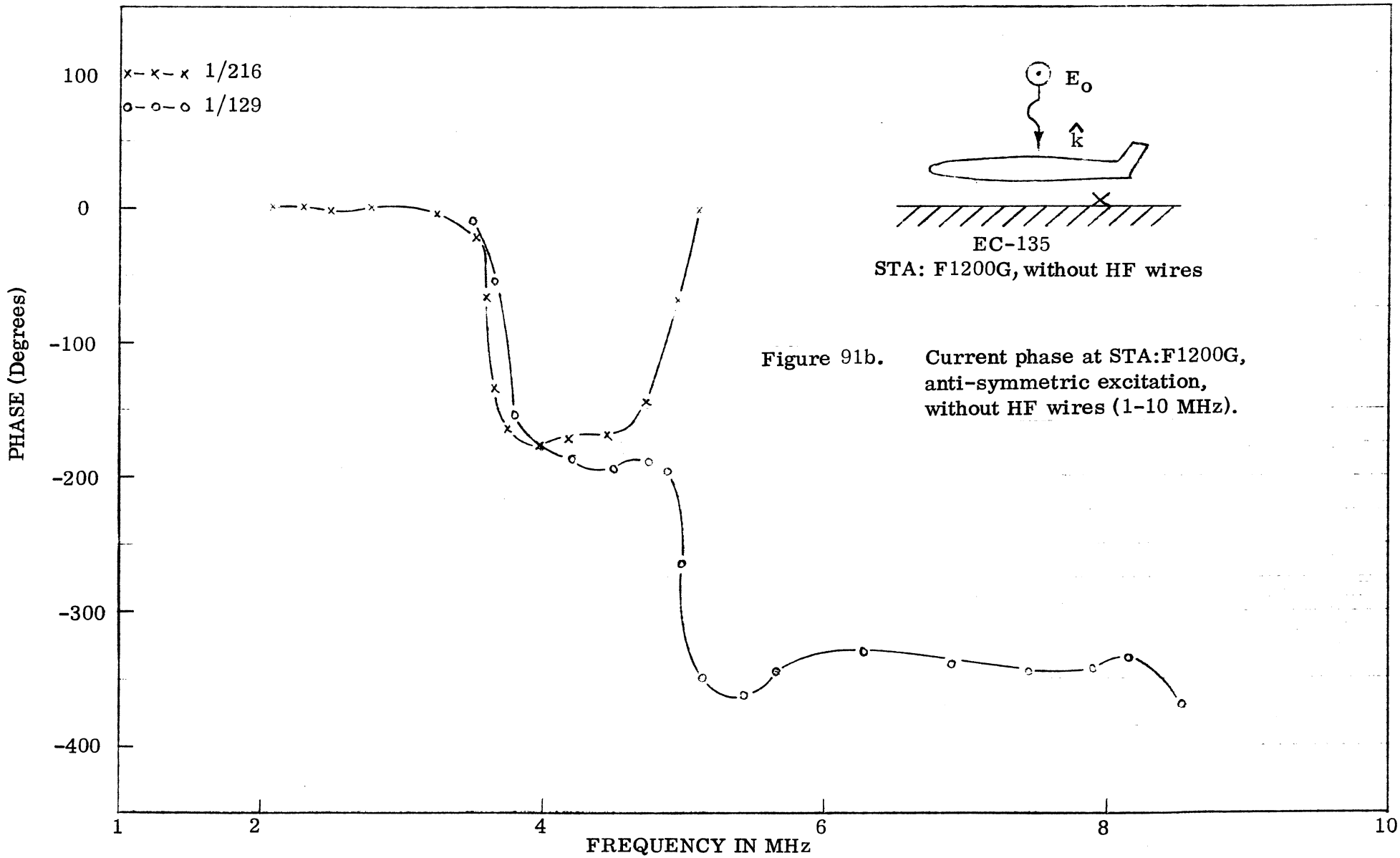

Figure 91b. Current phase at STA:F1200G, anti-symmetric excitation, without HF wires (1-10 MHz).

SECTION IV

GROUND PLANE MEASUREMENTS AT OBLIQUE INCIDENCE

This section presents the measured surface currents on model EC-135 aircraft in the presence of a perfectly conducting ground plane illuminated at 18 degrees from horizontal. The polarization, i.e., incident electric vector, was horizontal and the models were mounted on the metal sheet so that the fuselage was always parallel to the incident electric field. There were no HF wires present on the models. Both amplitude and phase data are presented and cover the full-scale frequency range 1.385 to 35.1 MHz.

1. Facility

A 12x12 foot ground plane inclined at 18 degrees to the horizontal was constructed in our tapered anechoic chamber at the Willow Run facility, and figure 92 shows the geometry as observed from the side. In the area where the models were measured, the plane is a 4x12 foot, 0.030 inch thick aluminum sheet, and this was extended another 8 feet toward the transmitting antenna using plywood covered with 0.005 inch thick aluminum foil. To obtain a uniform ("infinite sheet") field over the measurement area of the ground plane, special attention was given to the front and the rear edges of the structure. To reduce the front edge diffraction, the edge was buried in the chamber absorber and the sheet was partly covered on top with more absorber, whereas for the rear edge a 14 inch diameter cylinder covered with absorber was attached to it.

With this arrangement, the surface current was measured along the ground plane in the direction of propagation to determine the purity of the resultant field. To accommodate the MGL-S8A(R) sensor, holes were drilled 5 cm apart in the ground plane over a span of 80 cm. The surface current was then recorded at each of these positions as the frequency was swept over a 500 - 1000 MHz range. Using the center hole data as a reference, the data were reduced at 500 and 1000 MHz and the results are shown in figure 93. In each case, the variation is ± 0.5 dB, a value considered to be acceptable for the purposes of this program. Due to time

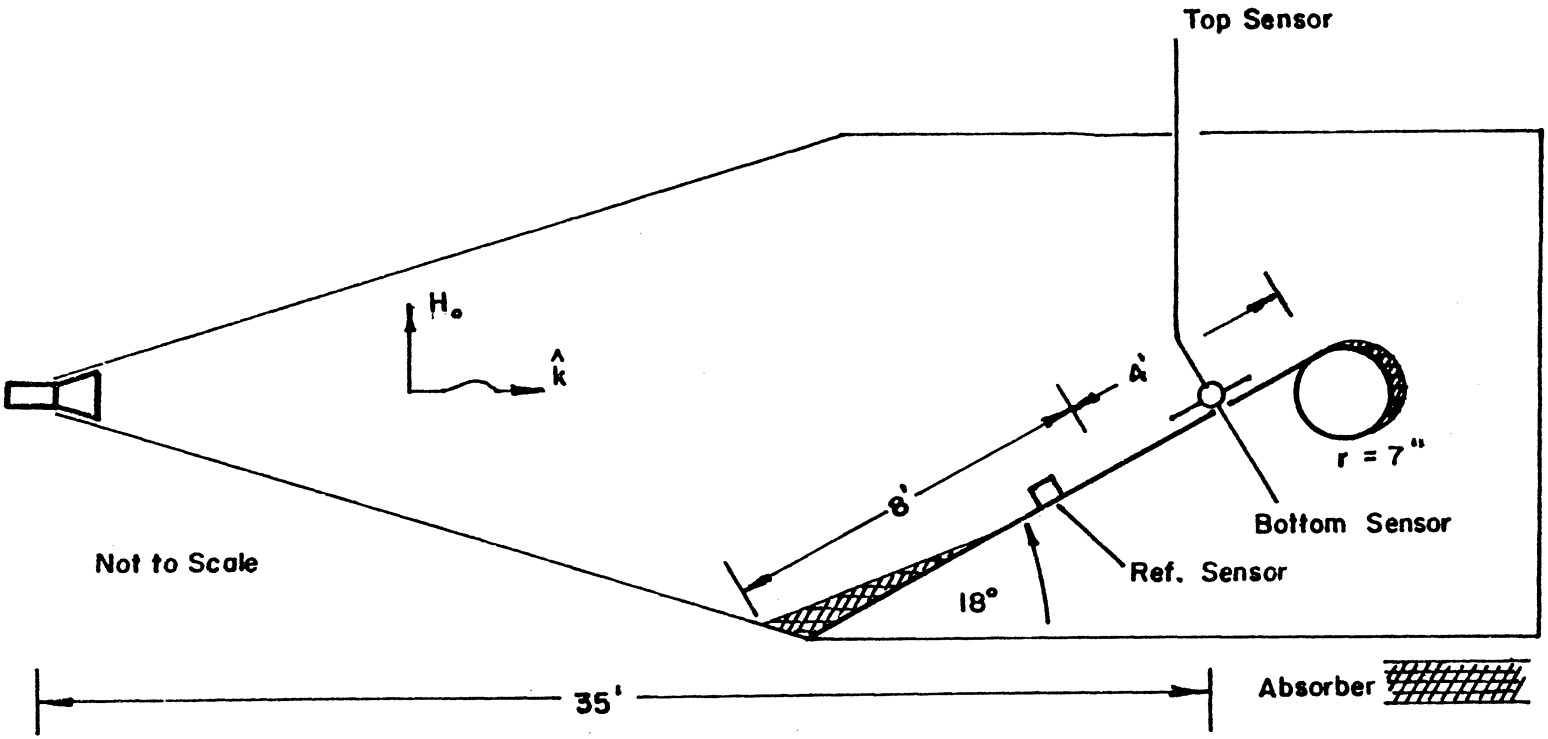

Figure 92. Implementation of the 18 degree ground plane.

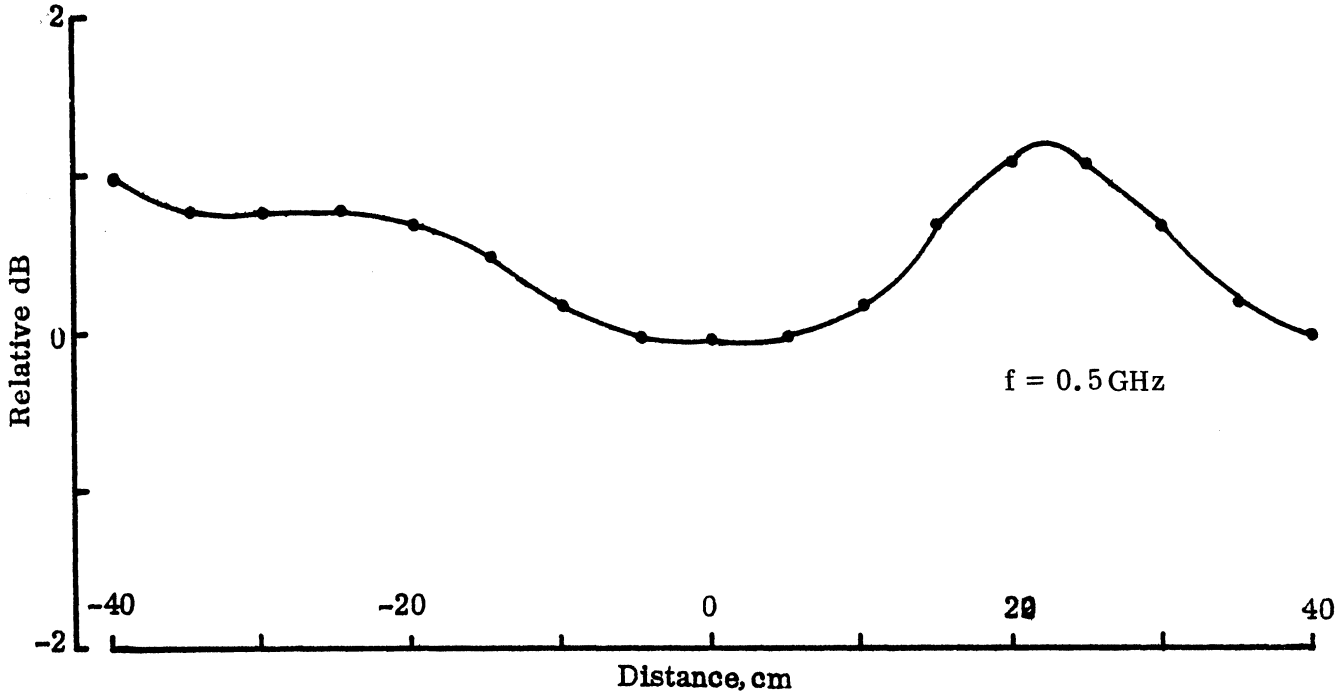

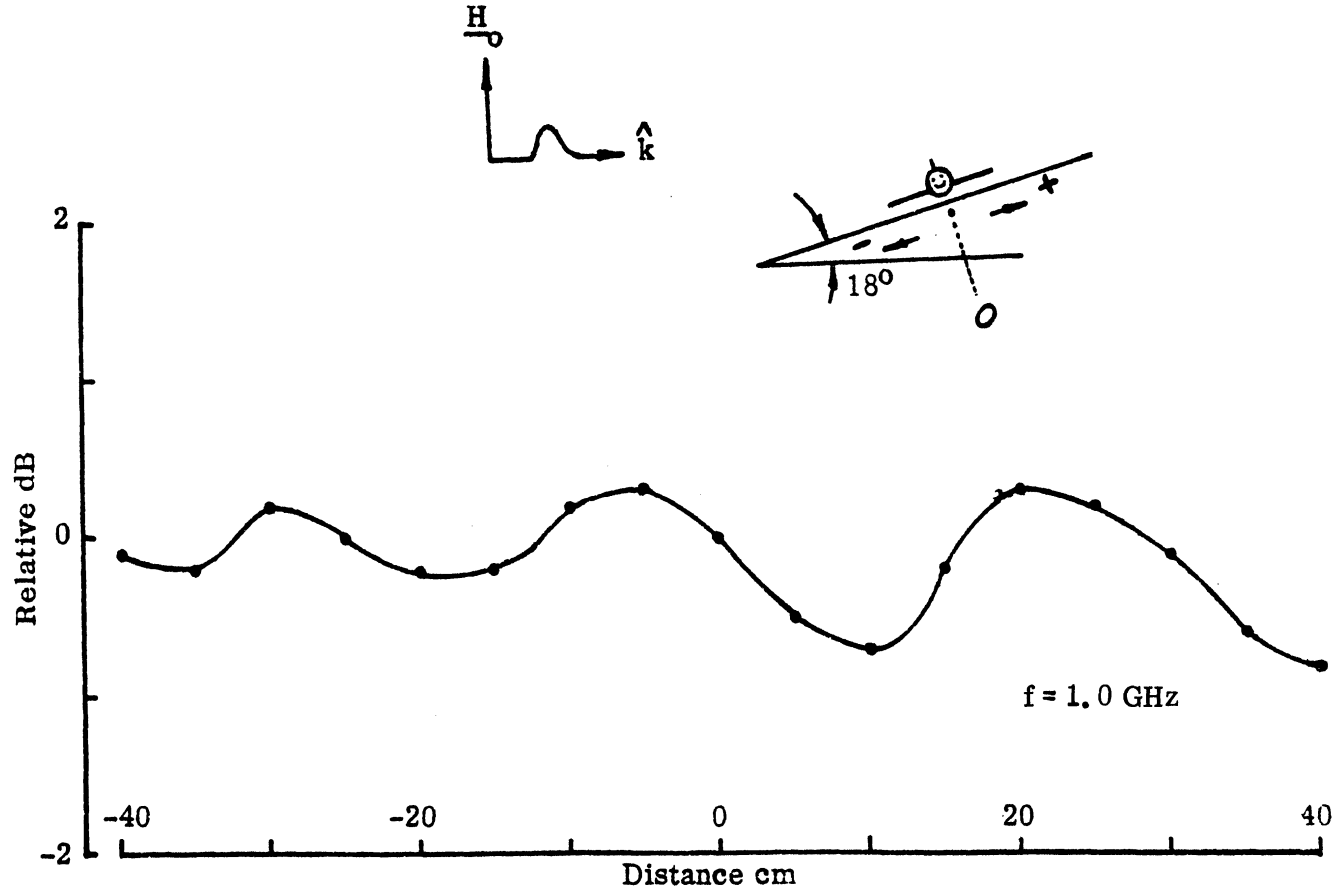

Figure 93. Measured surface current distribution on the ground plane.

limitations and the fact that the connector on the sensor broke and had to be repaired, similar measurements in the 2.0 to 4.0 GHz range were not made. However, past experience (supported by theoretical arguments) shows that as the frequency increases, absorber performance usually improves and, hence, field uniformity of ± 0.5dB or better is expected in the 2.0 to 4.0 GHz range as well.

2. EC-135 Models and Measurements

The measurements were made in two frequency bands using four scale model 707 airplanes modified by adding refueling booms and with styrofoam blocks underneath the wings and fuselage to provide appropriate ground-fuselage clearance. In the 0.45 - 1.10 GHz band 1/325, 1/216, and 1/129 scale models were used, while 1/325, 1/216, and 1/114 models were used in the 2.0 - 4.0 GHz band to get a higher full-scale frequency coverage.

Measurements were made at the following stations on each model:

F400T, F1200T	top of the fuselage
F400B, F1200B	bottom of the fuselage
W600T(A), W600T(B)	top of the right and left wings, respectively
W600B(A), W600B(B)	bottom of the right and left wings, respectively.

The convention for the station designation is the same as before (figure 3), apart from the identification of the right wing (A) and left wing (B) of the model as seen by a passenger sitting in an aircraft facing forward. The model was always placed with the fuselage perpendicular to the direction of the incident wave with the right wing (A) toward the excitation source. For both the top and bottom the measurement procedures were similar. A model was placed on the ground plane with the station to be measured above the "0" position on the ground plane (see insert, figure 93). The sensor was positioned extending either down from the ceiling for the top station measurements or up through the small hole in the ground plane for the bottom station measurements. With the loop just touching the surface of the model, a measurement was made; then, after carefully removing the model without disturbing

the sensor, the measurement was repeated for calibration with respect to the incident field. In measuring the fuselage current for both the top and bottom, the loops were rotated so that the plane of the loop was perpendicular to the ground plane and through the center axis of the fuselage. For the wing current measurements, the loop was still perpendicular to the ground plane, but rotated $\pm$ 56 degrees, the estimated angle between the fuselage and the center of the wings. Such a rotation does alter the loop response to the excitation field, and this is accounted for in the subsequent data reduction process (see equation 11).

3. Theoretical Considerations

Consider the geometry shown in figure 94. A plane electromagnetic wave polarized such that the electric vector is parallel to the z-axis is incident at an angle θ upon the plane y = 0. For convenience, the phase of the incident wave is chosen to be zero at the origin and we can therefore represent the incident electric vector in the form

$$\underline{E}^i = \hat{z} E_o e^{-ik(x \cos\theta + z \sin\theta)} \tag{5}$$

where the time factor $e^{i\omega t}$ has been assumed and suppressed.

If the plane y = 0 is occupied by a perfectly conducting sheet, the field for $y \geq 0$ can be written as a sum of direct and image waves, with the latter having a minus sign to satisfy the boundary condition $E_z = 0$ on the surface. The total field is then

$$\underline{E} = \hat{z} E_o \left\{ e^{-ik(x \cos\theta - y \sin\theta)} - e^{-ik(x \cos\theta + y \sin\theta)} \right\}$$

i.e.
$$\underline{E} = \hat{z} E_o 2i \sin(ky \sin\theta) e^{-ikx\cos\theta} \tag{6}$$

The corresponding magnetic field can be obtained by applying Maxwell's equation $\nabla \times \underline{E} = i\omega\mu \underline{H}$ to (6) or formulated directly from the diagram as was done for the electric field. Either way,

$$\underline{H} = -2 H_o e^{-ik x \cos\theta} \left\{ \hat{x} \sin\theta \cos(ky \sin\theta) + i \hat{y} \cos\theta \sin(ky \sin\theta) \right\} \tag{7}$$

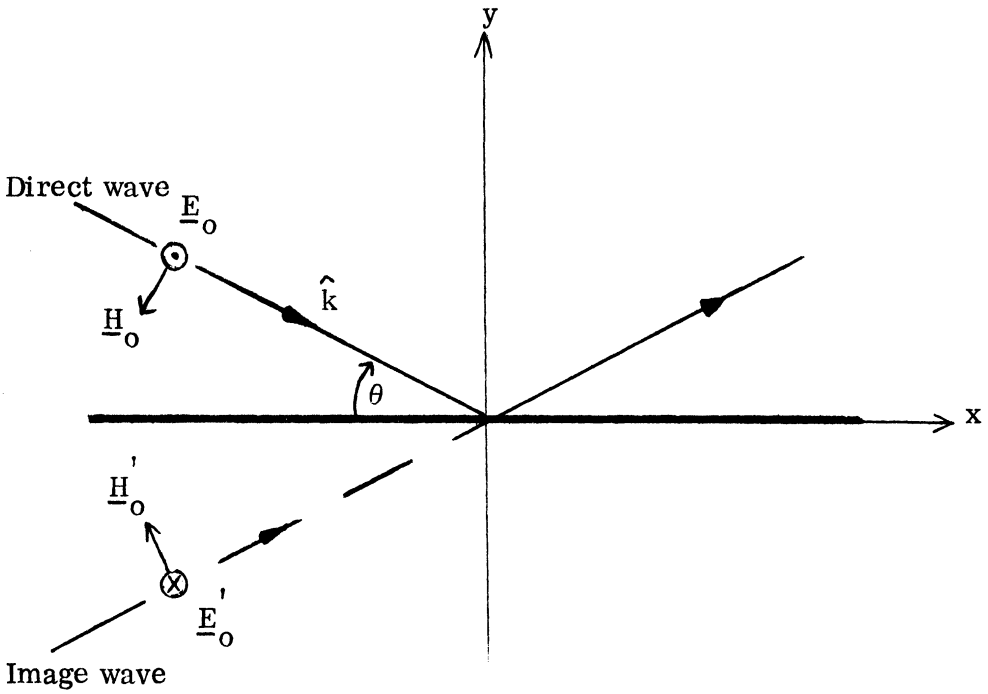

Figure 94. Ground plane geometry.

where $H_o = Z_o E_o$ with $Z_o = \sqrt{\mu_o/\epsilon_o}$.

The case x = 0 is of specific interest since the aircraft model was always positioned so that the station where the measurements were made lay in the plane x = 0. In addition, the loop was oriented vertically and, hence, would not respond to the H_y component of the magnetic field. Thus, from equation (7)

$$\underline{H} = -\hat{x}\, 2 H_o \sin\theta \cos(kh \sin\theta) \quad , \tag{8}$$

where h is the distance from the ground plane to the point of the measurement. This equation now relates the incident field H_o to the calibration measurement H(cal) at the same point in space where the model station is located for the model measurement H(mod). In reducing data, H(mod)/H(cal) is first computed at all sampled frequencies and then renormalized to give

$$H(\text{mod})/H_o = \left[H(\text{mod})/H(\text{cal})\right] 2 \sin\theta \cos(kh \sin\theta) \; . \tag{9}$$

The negative sign that appears in equation (8) can be said to apply to both the H(mod) and H(cal) measurements and, hence, cancels out in (9).

To measure the axial currents on the wings, the sensor loop is rotated $\phi = \pm 56$ degrees, the estimated angle between the fuselage and the center of the wing. H(cal) was also measured with the loop in the rotated position, and to include this effect, equation (9) is multiplied by $\cos\phi$ to become

$$H(\text{mod})/H_o = \left[H(\text{mod})/H(\text{cal})\right] 2 \sin\theta \cos\phi \cos(kh \sin\theta) \; . \tag{10}$$

In the computer code, the equation was expressed in terms of more practical variables. With $\theta = 18$ degrees (the inclination of the ground plane), the frequency in GHz and h in cm,

$$H(\text{mod})/H_o = \left[H(\text{mod})/H(\text{cal})\right] 0.61803 \cos\phi \cos(0.06472\, fh) \; , \tag{11}$$

where the argument of the cosine function is in radians. Equation (11) was used in reducing all of the ground-plane data presented: for the fuselage stations $\phi = 0$

and for the wing measurements $\phi = \pm 56$ degrees was used, respectively. Of course, the sign in the latter has no effect since $\cos(-x) = \cos x$.

4. Data Recording and Reduction

The analog signals representing the amplitude (dB) and phase were first recorded on a dual channel X-Y plotter. A calibration measurement was made for each data measurement, so that for eight stations, two frequency bands and three different scale models the recordings totalled 96.

For reduction of the data the same procedure was used as described in Section III, in which the analog data plots were first digitized and the data subsequently computer-processed and plotted. The reduction codes were based on formulations presented in Section IV, para. 3.

5. Presentation of Plots

The following pages contain 32 plots of amplitude and phase arranged by measurement location, with amplitude data first and then phase data. The amplitude plots are for H/H_o versus frequency where H_o is the incident magnetic field <u>without</u> the ground plane. The phase is shown relative to that of the incident field at the location of the station where the measurement is made. To show the results more clearly, the low frequency (1-9 MHz) and the high frequency (5-35 MHz) data are presented as separate plots. Table 5 summarizes the data and can be used to locate quickly any particular measurement. A pair of figures containing corresponding amplitude and phase data are distinguished by (a) and (b), respectively. Note that on each plot in the upper right hand corner there is a somewhat abbreviated title. The code used is as follows:

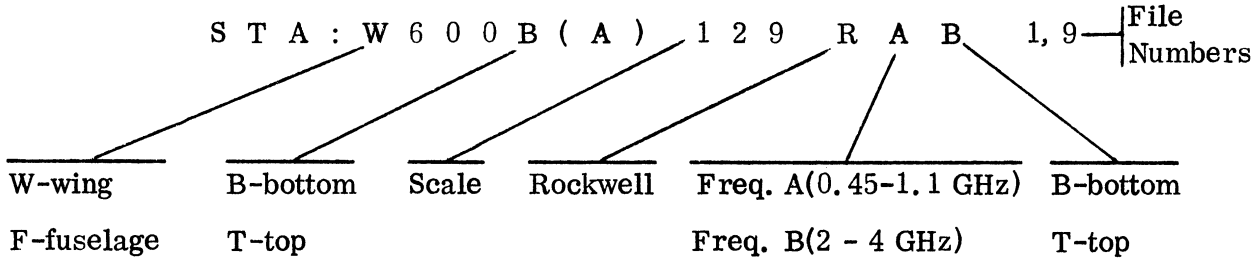

Table 5

DATA SELECTION CHART

Station Number	Low Frequency (1 - 9 MHz)	High Frequency (5 - 35 MHz)
F400T	95a, b	96a, b
F1200T	97a, b	98a, b
F400B	99a, b	100a, b
F1200B	101a, b	102a, b
W600T(A)	103a, b	104a, b
W600T(A)	105a, b	106a, b
W600B(A)	107a, b	108a, b
W600B(B)	109a, b	110a, b

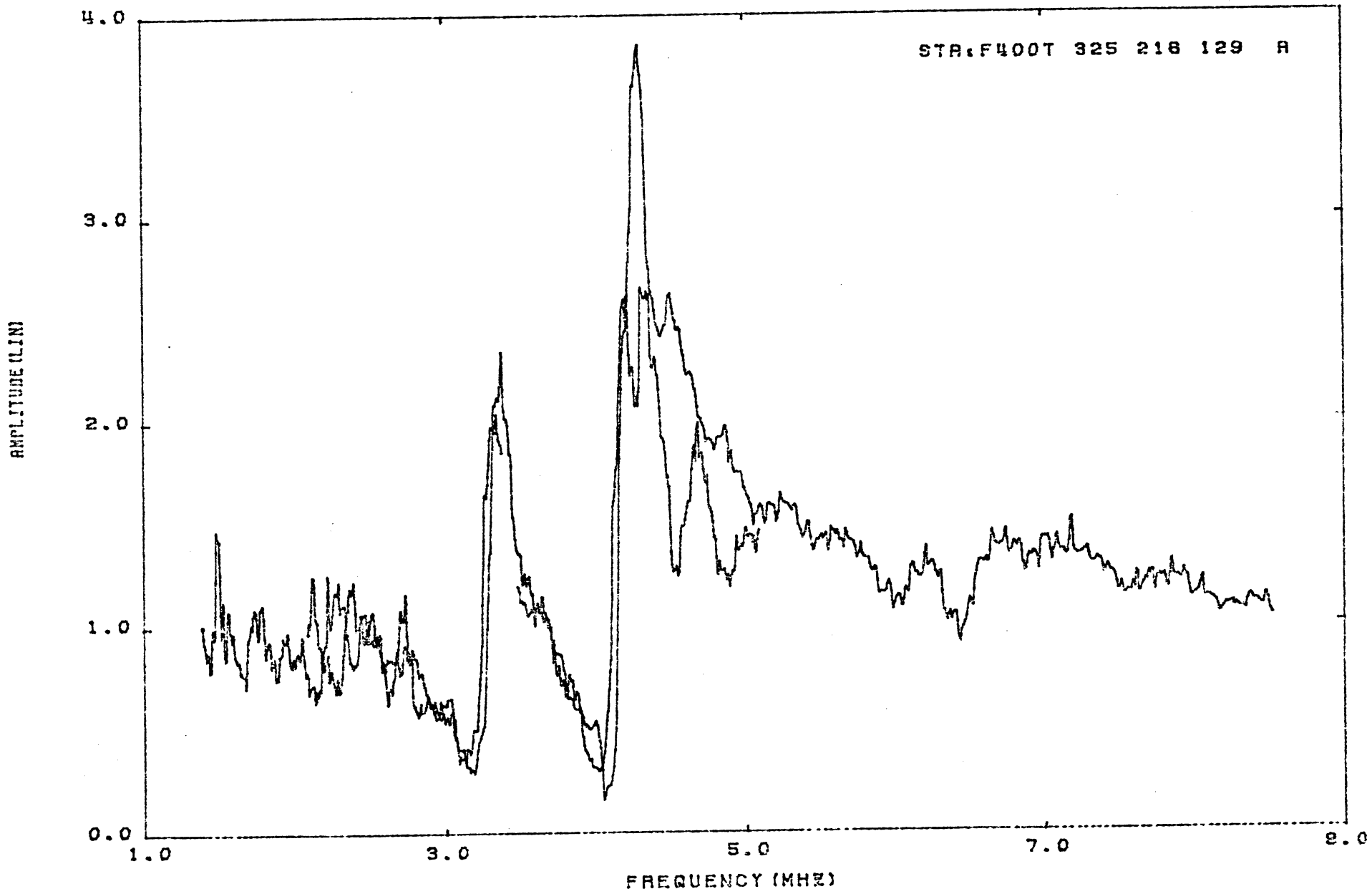

Figure 95a. Current amplitude at STA:F500T (1 - 9 MHz).

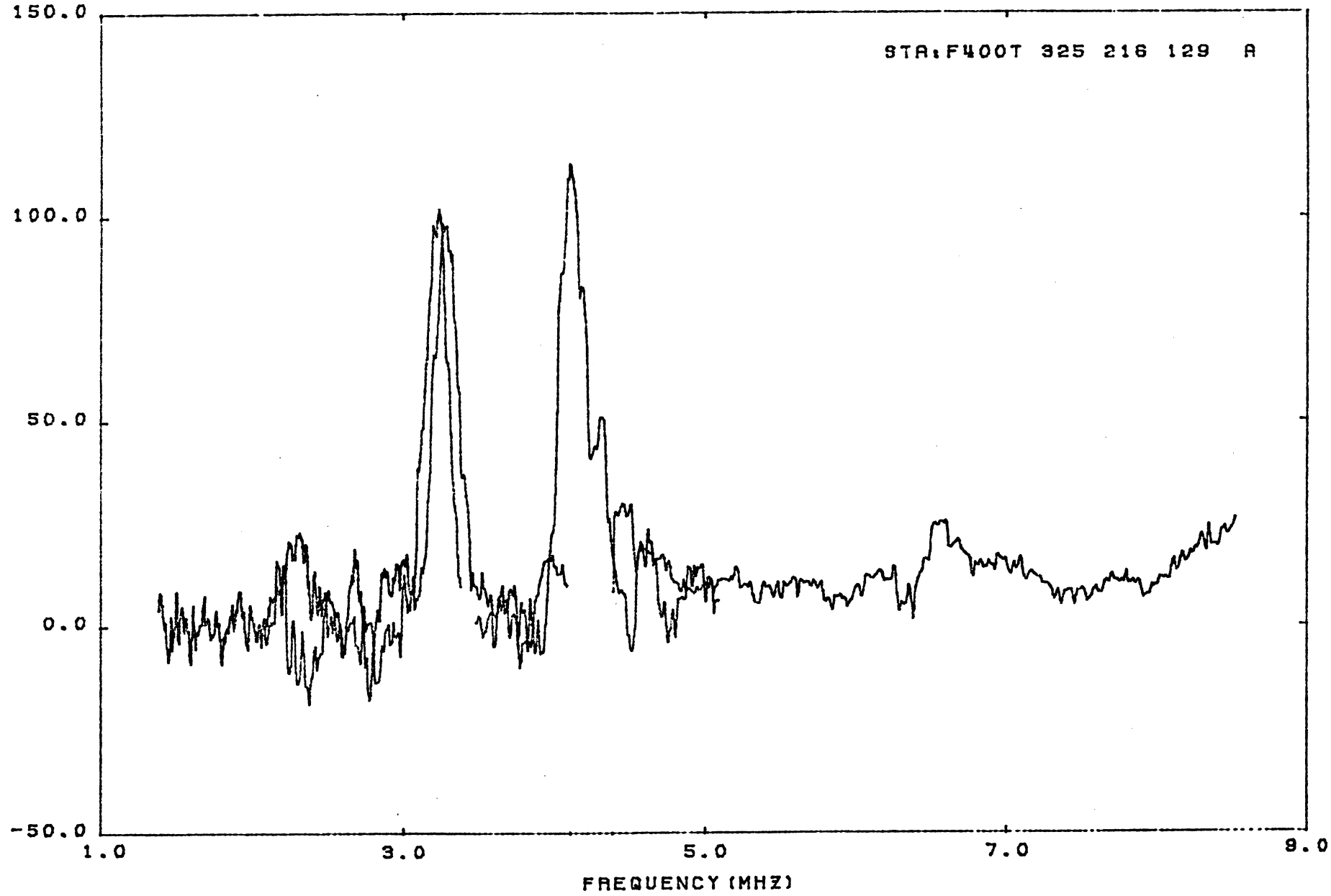

Figure 95b. Current phase at STA:F400T (1 - 9 MHz).

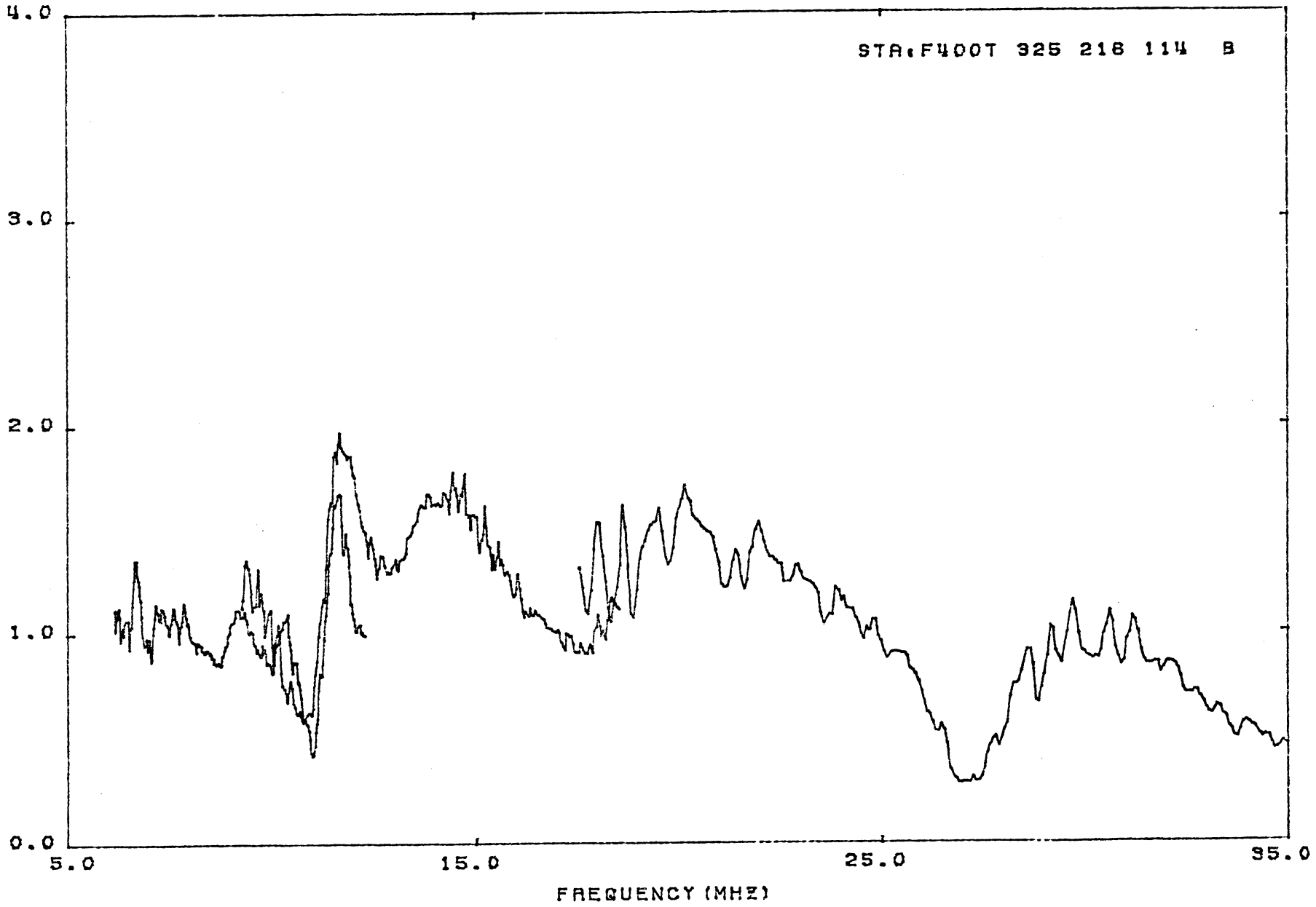

Figure 96a. Current amplitude at STA:F400T (5 -35 MHz).

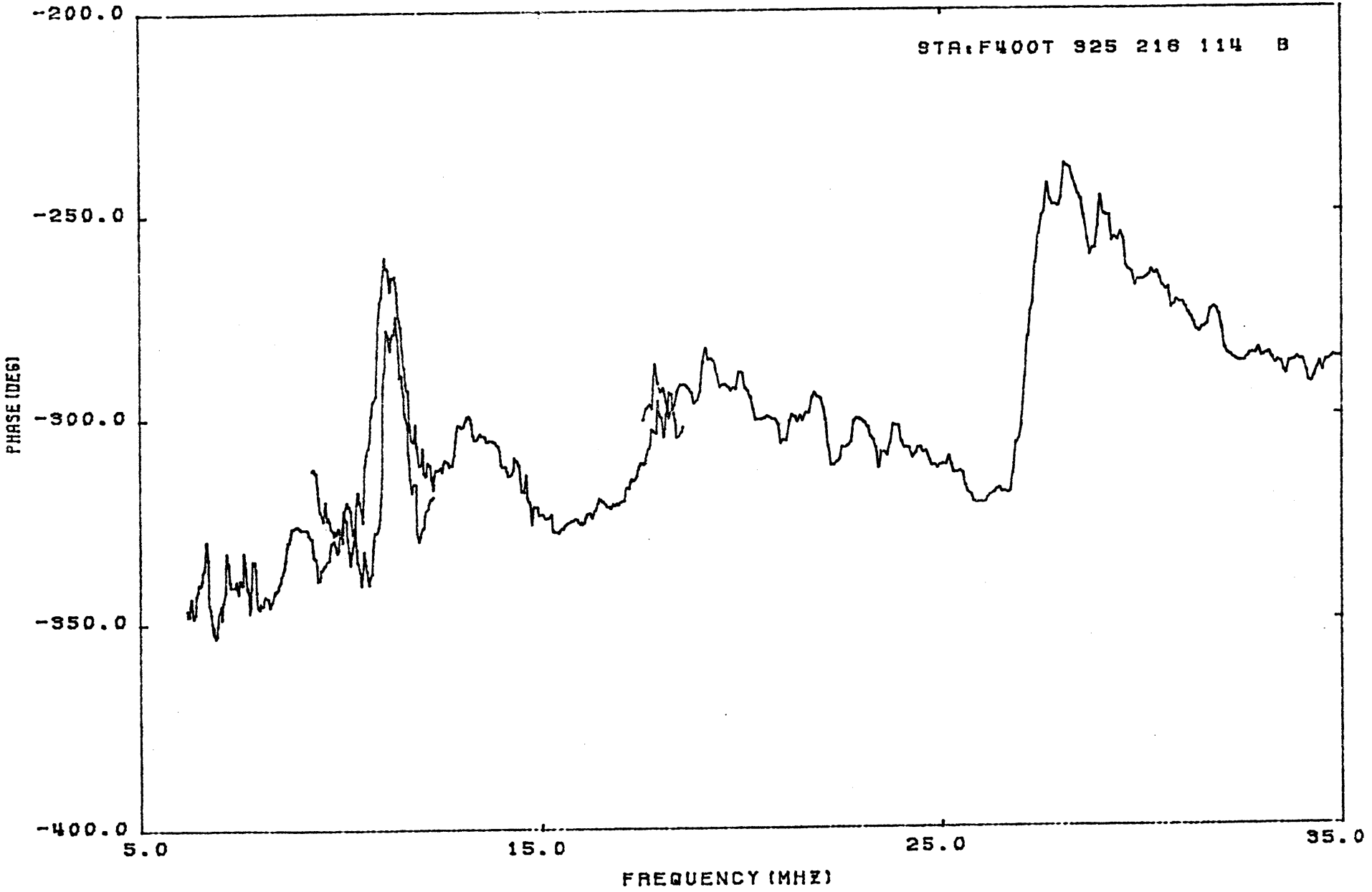

Figure 96b. Current phase at STA:F400T (5 - 35 MHz).

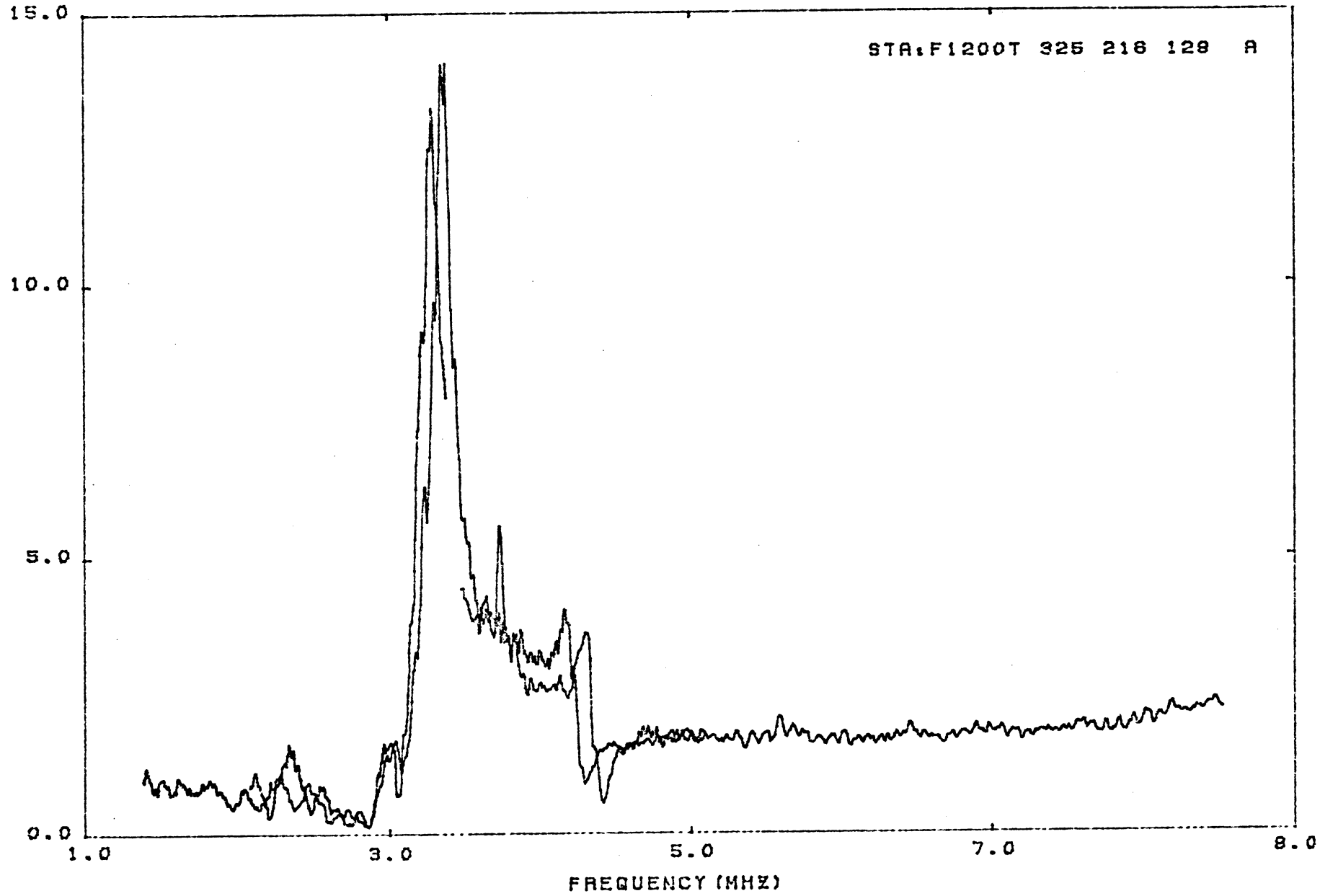

97a. Current amplitude at STA:F1200T (1 - 9 MHz).

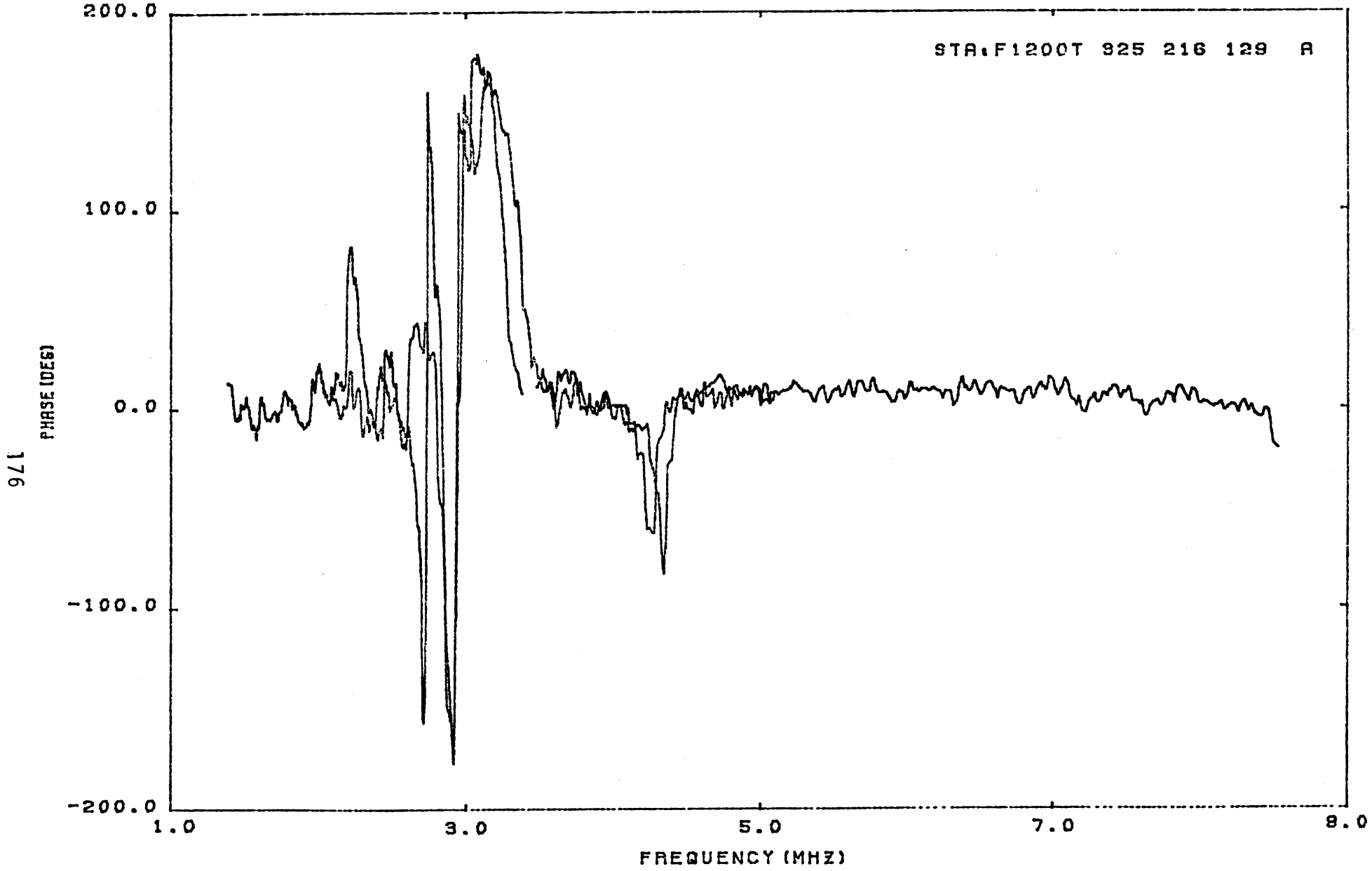

Figure 97b. Current phase at STA:F1200T (1 - 9 MHz).

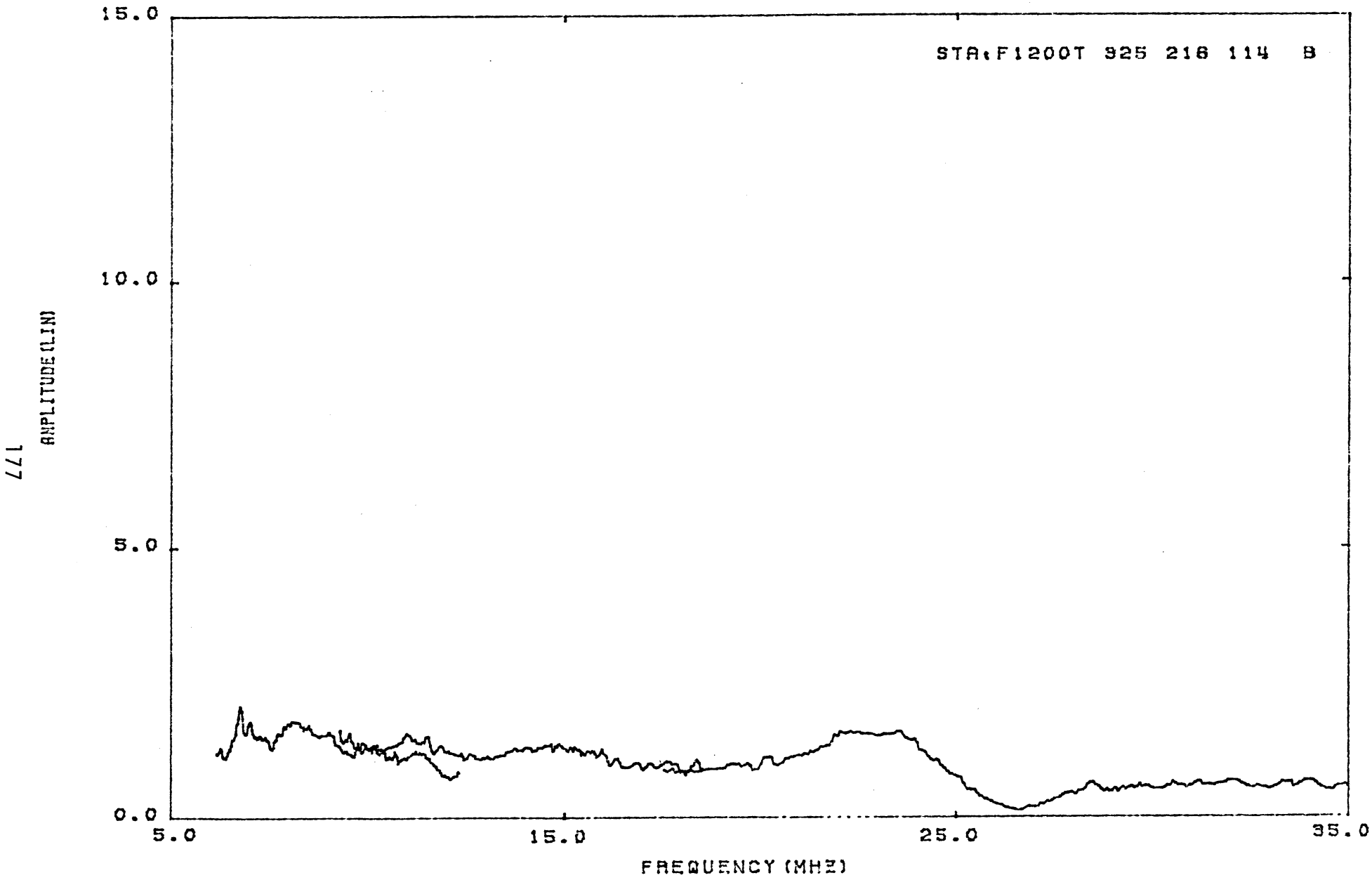

Figure 98a. Current amplitude at STA:F1200T (5 - 35 MHz).

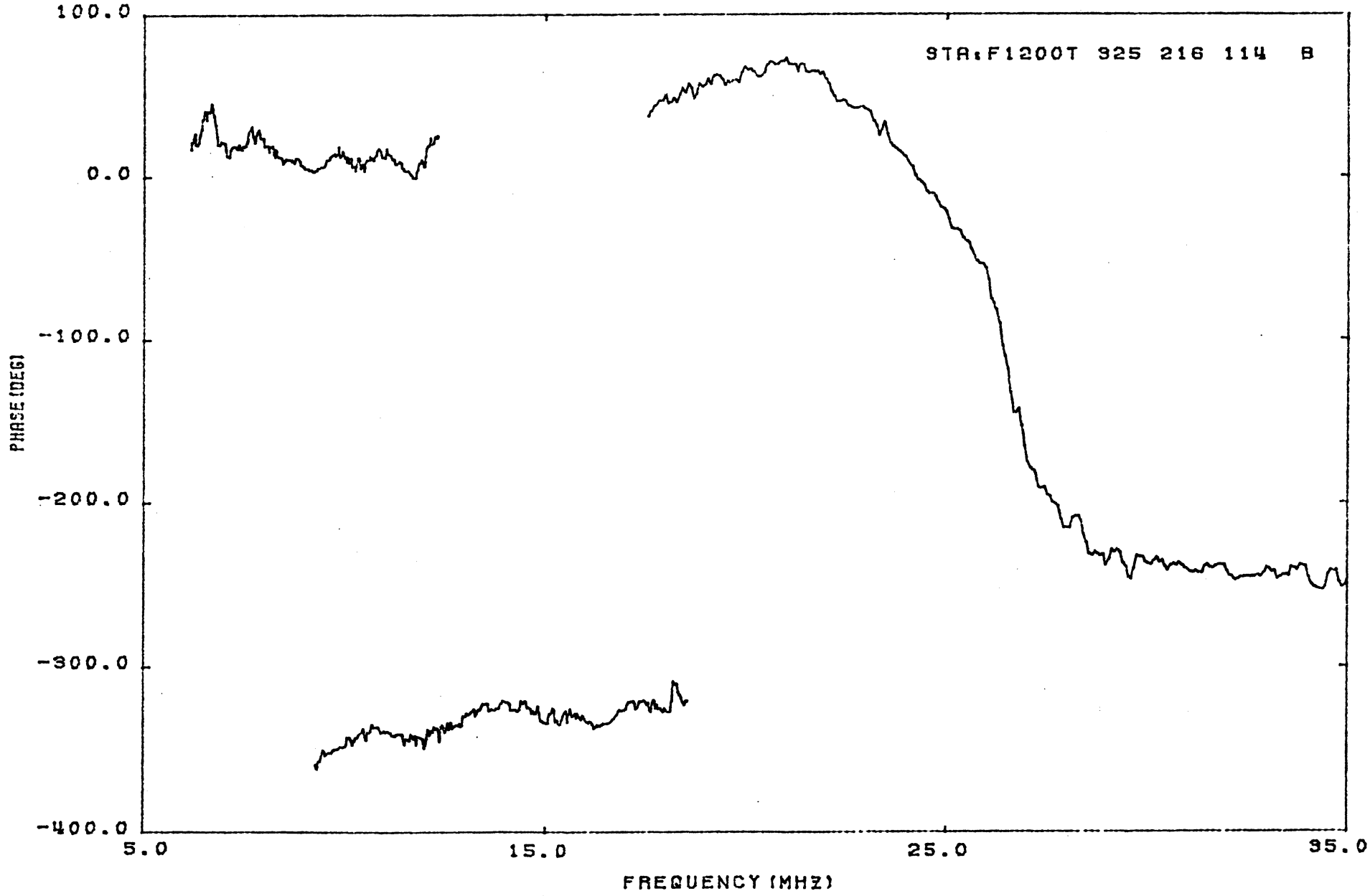

Figure 98b. Current phase at STA:F1200T (5 - 35 MHz).

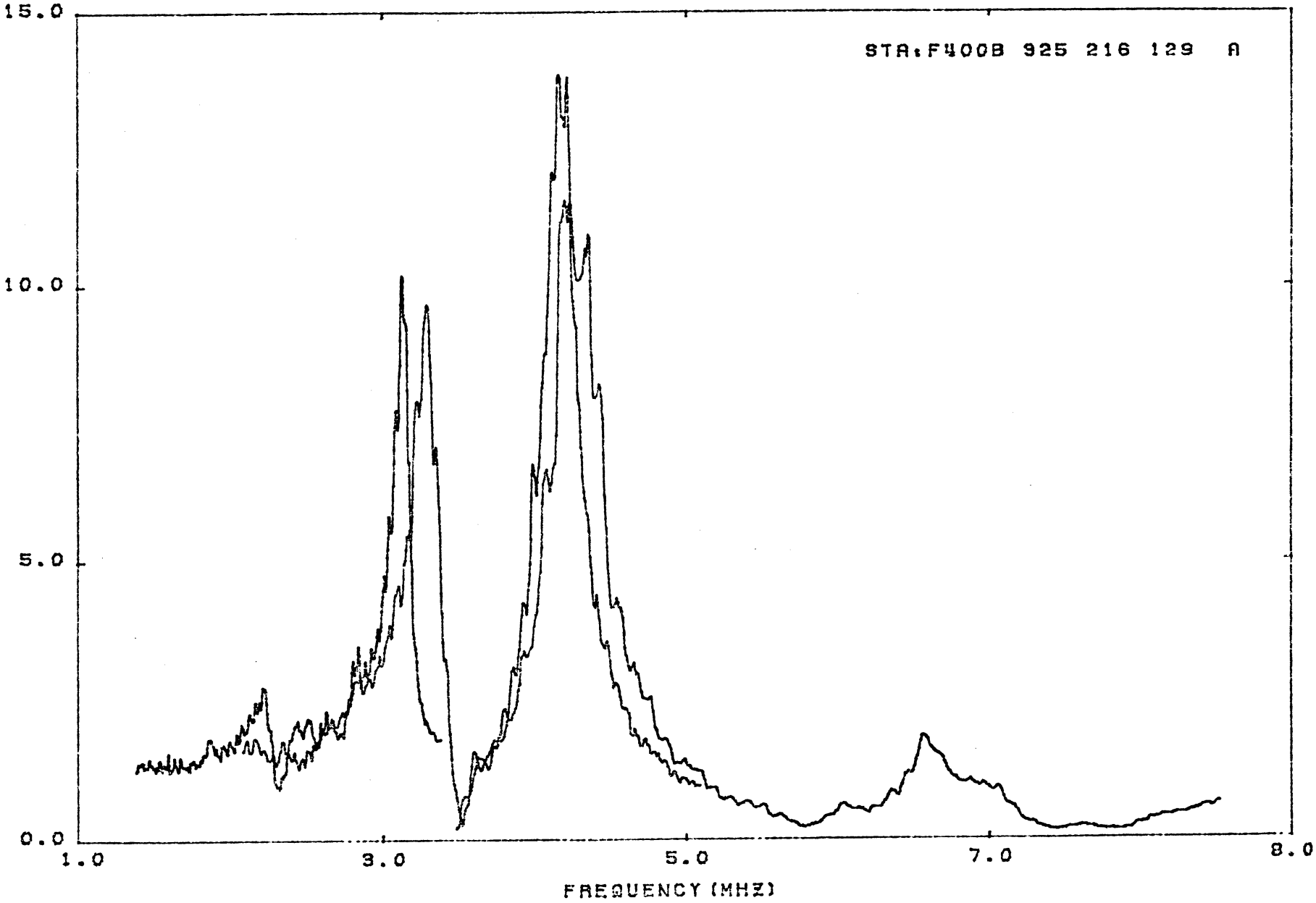

Figure 99a. Current amplitude at STA:F400B (1 - 9 MHz).

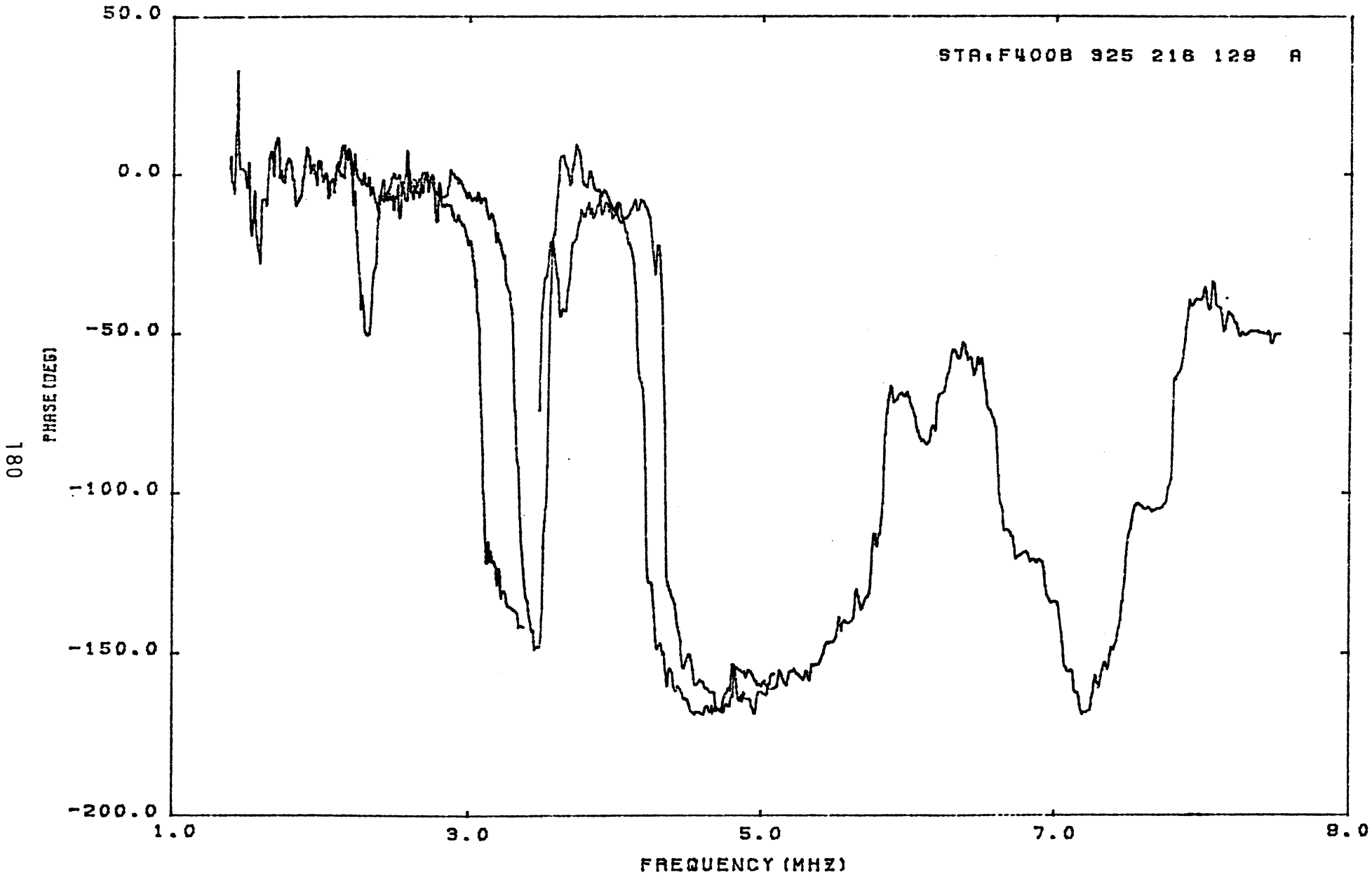

Figure 99b. Current phase at STA:F400B (1 - 9 MHz).

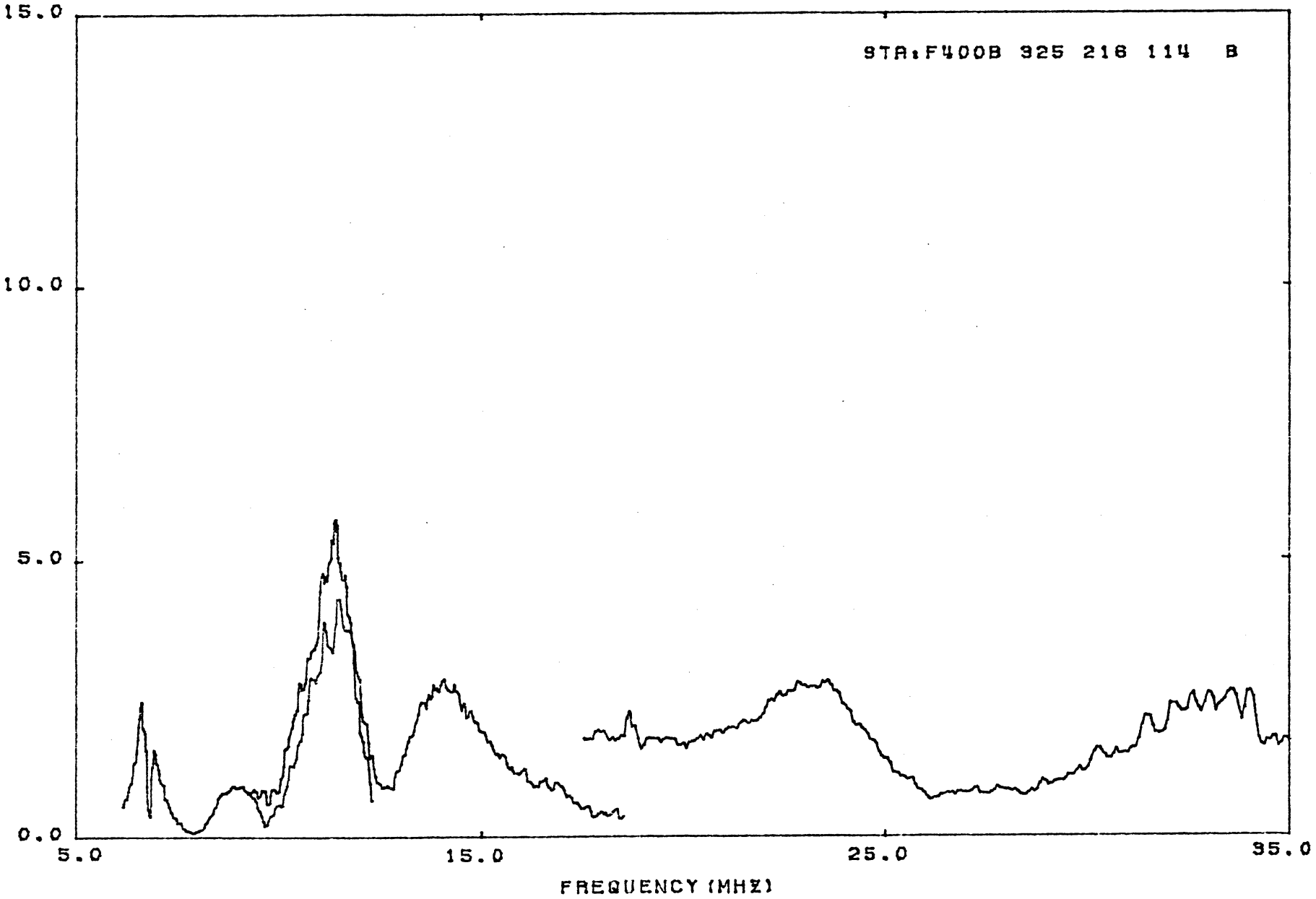

Figure 100a. Current amplitude at STA:F400B (5 - 35 MHz).

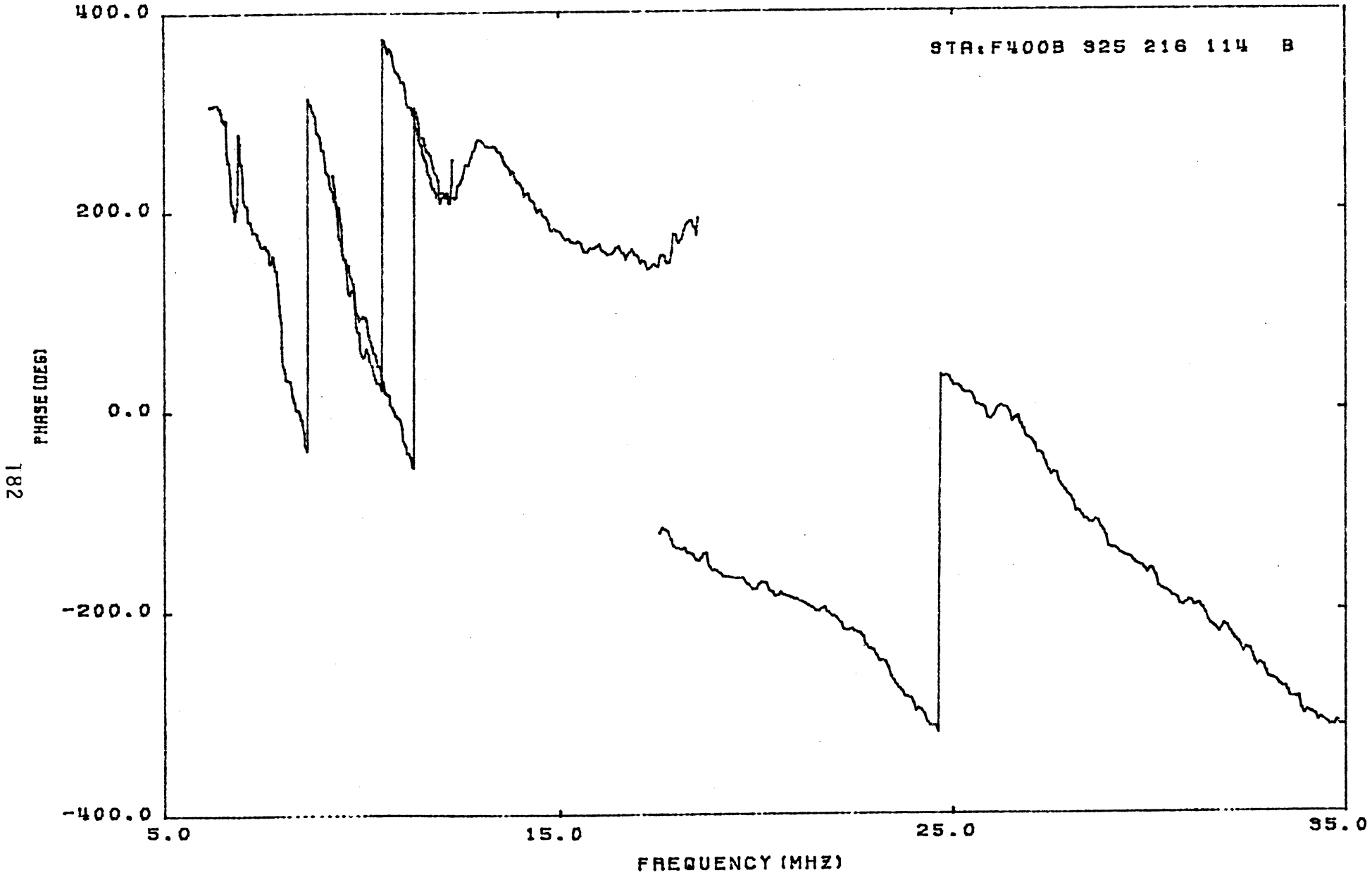

Figure 100b. Current phase at STA:F400B (5-35 MHz).

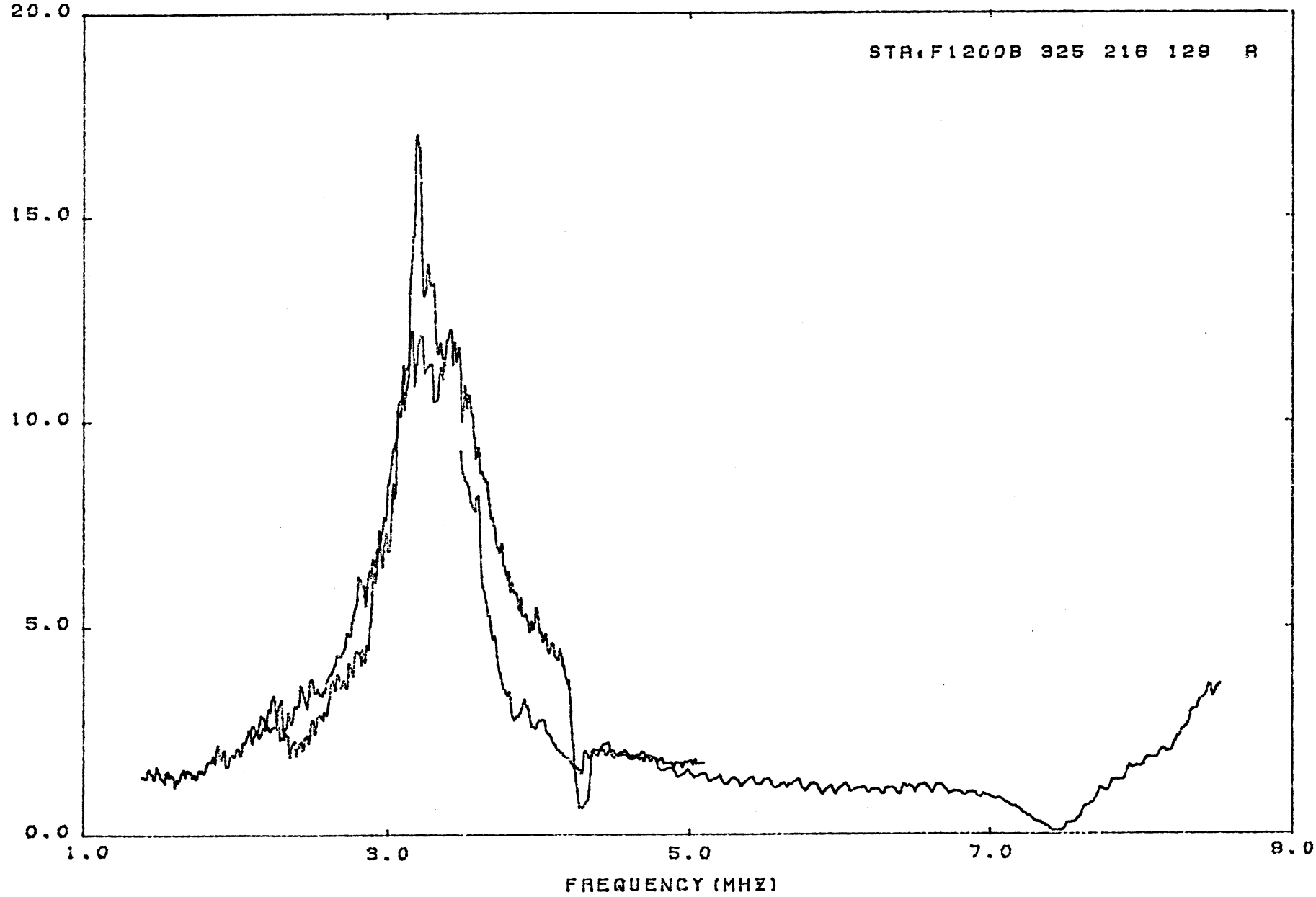

Figure 101a. Current amplitude at STA:F1200B (1 - 9 MHz).

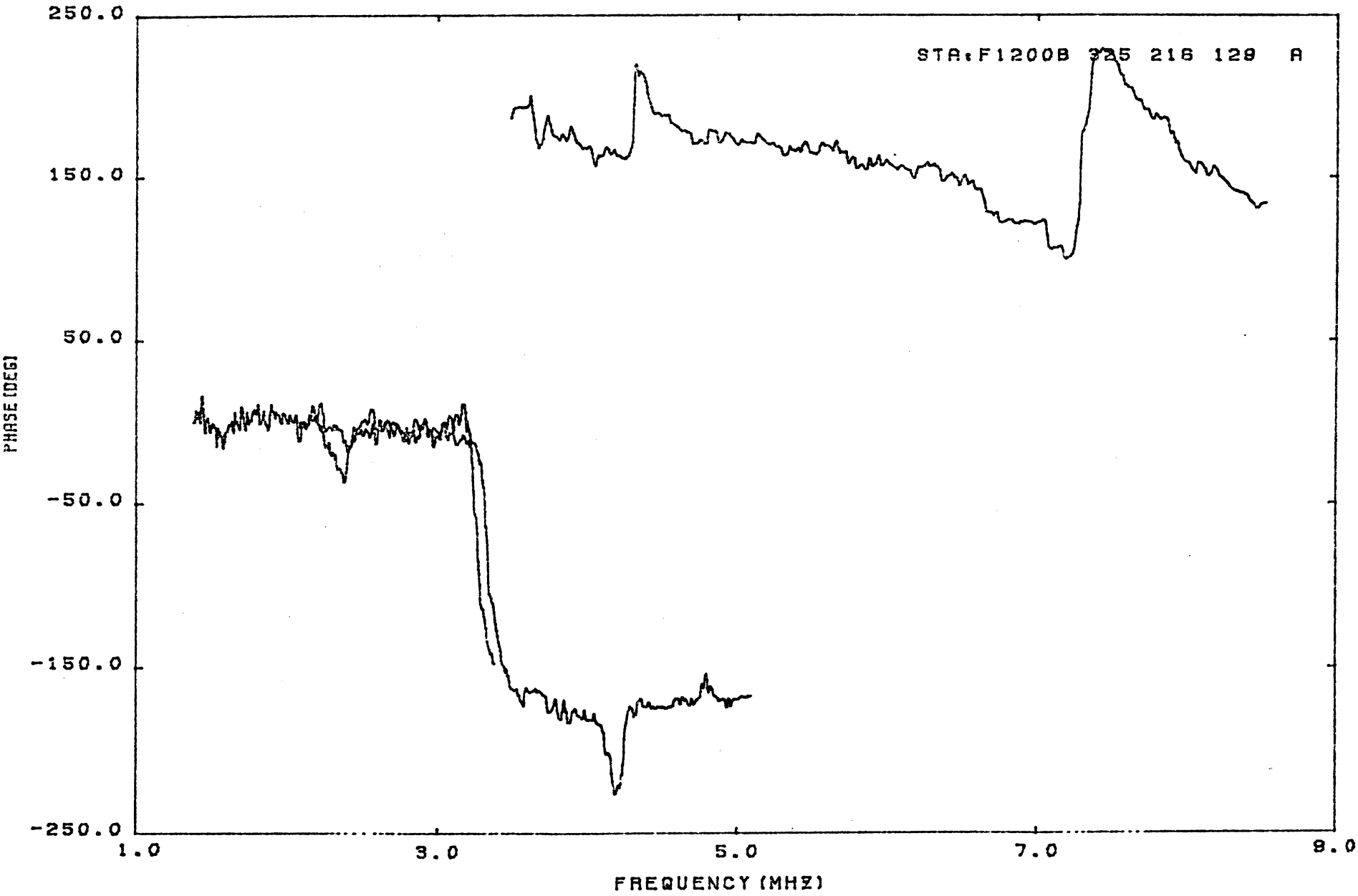

Figure 101b Current phase at STA:F1200B (1 - 9 MHz).

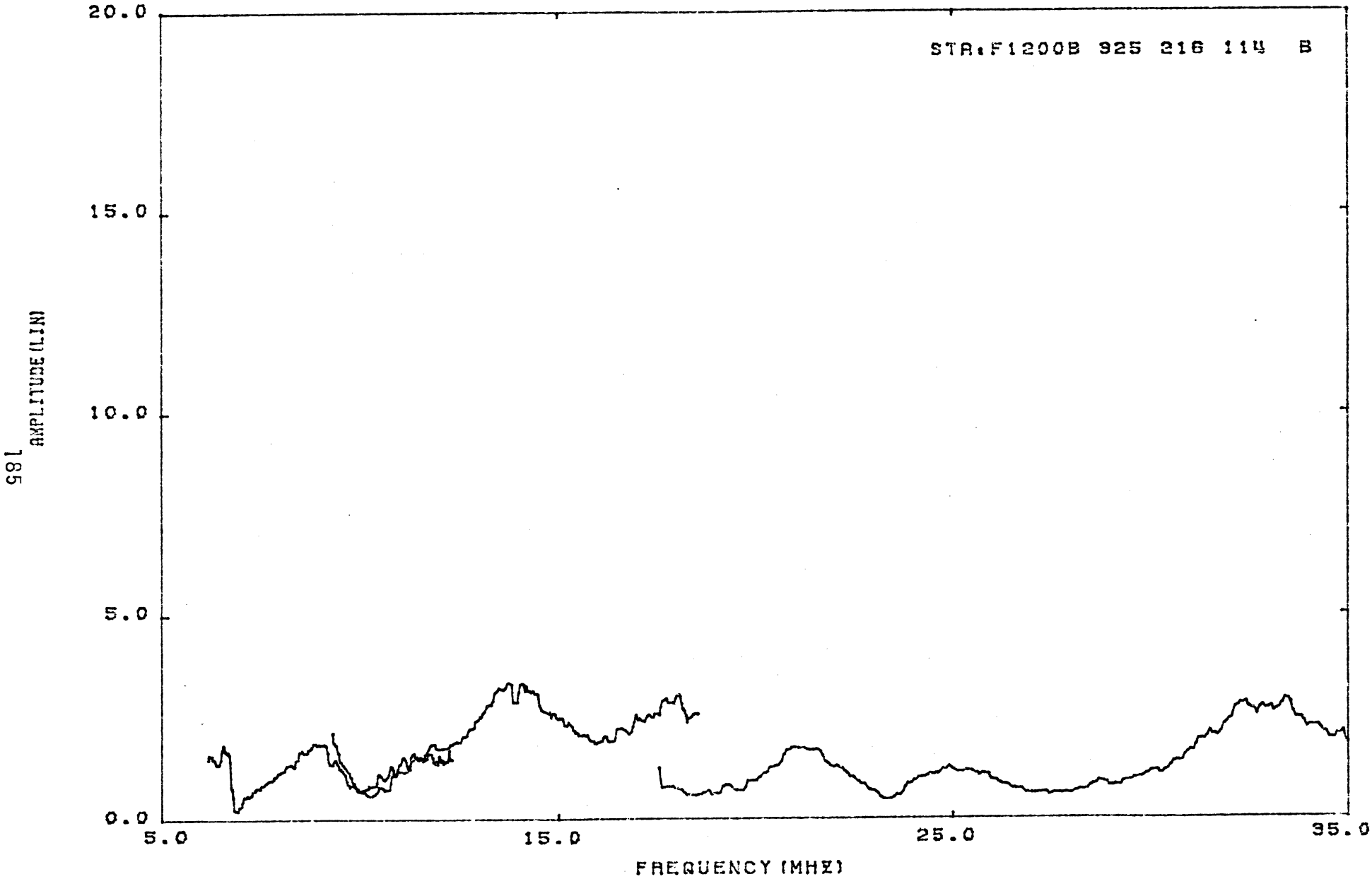

Figure 102a. Current amplitude at STA:F1200B (5 - 35 MHz).

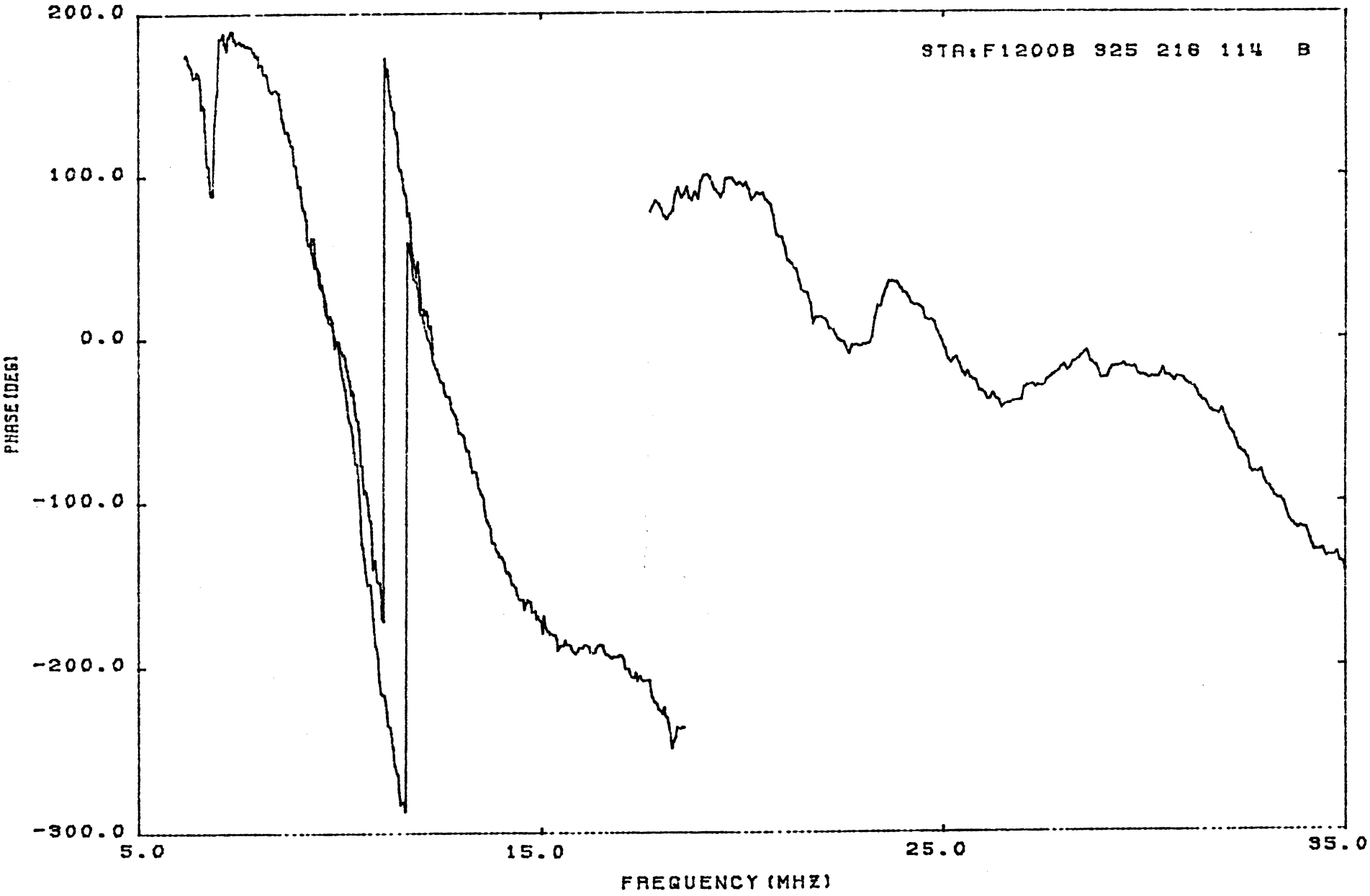

Figure 102b. Current phase at STA:F1200B (5 - 35 MHz).

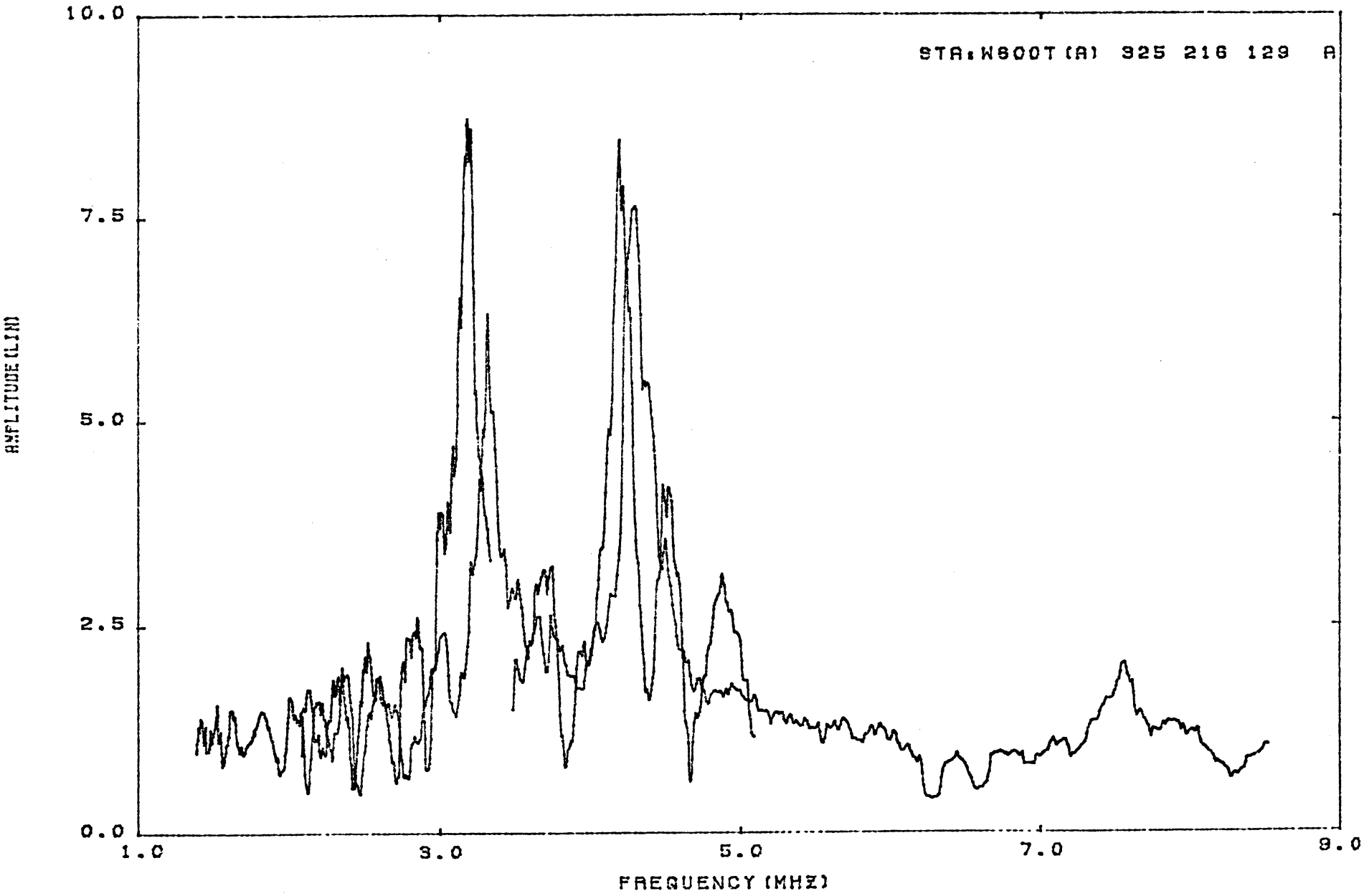

Figure 103a. Current amplitude at STA:W600T(A) (1-9 MHz).

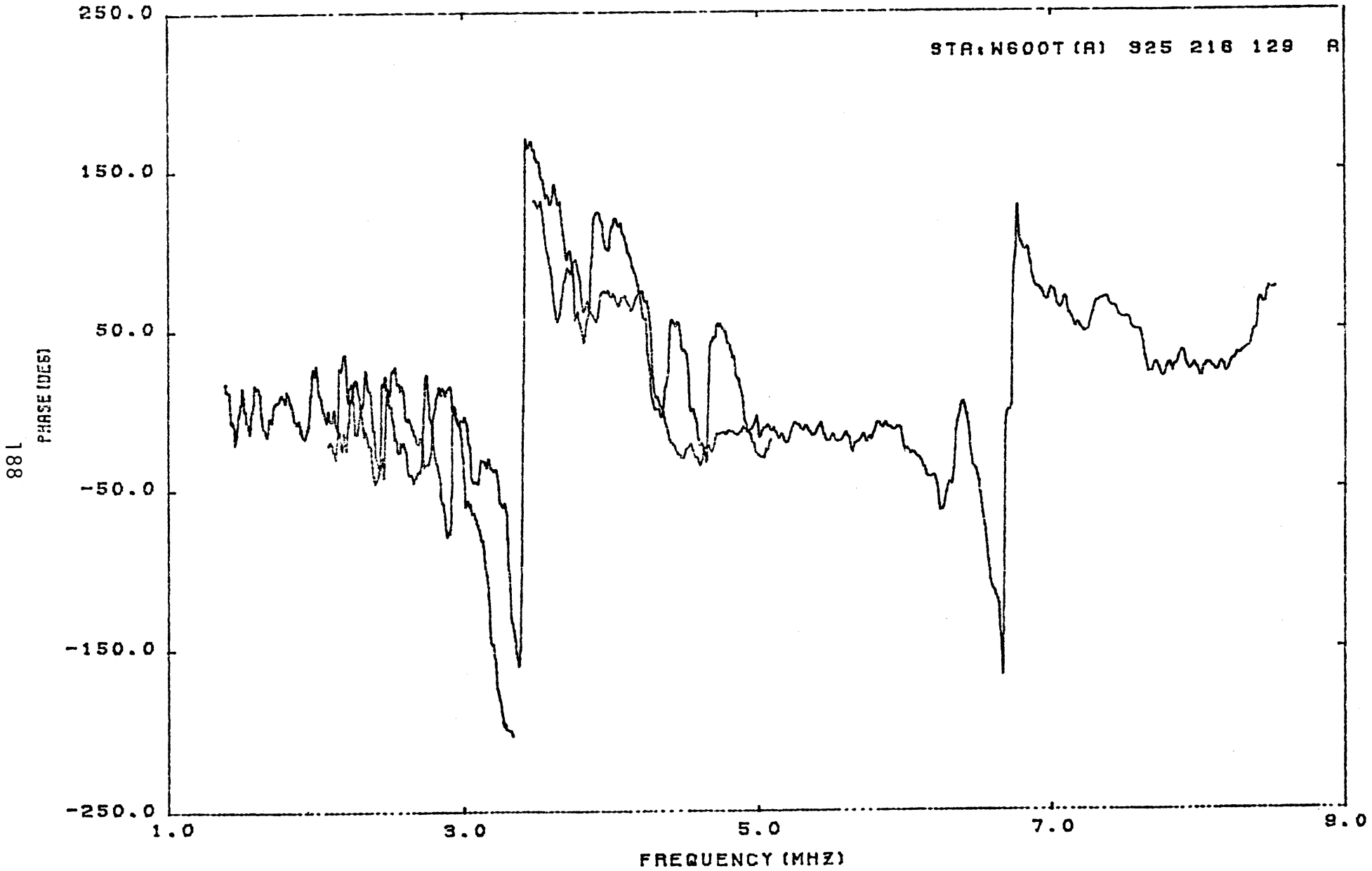

Figure 103b. Current phase at STA:W600T(A) (1-9 MHz).

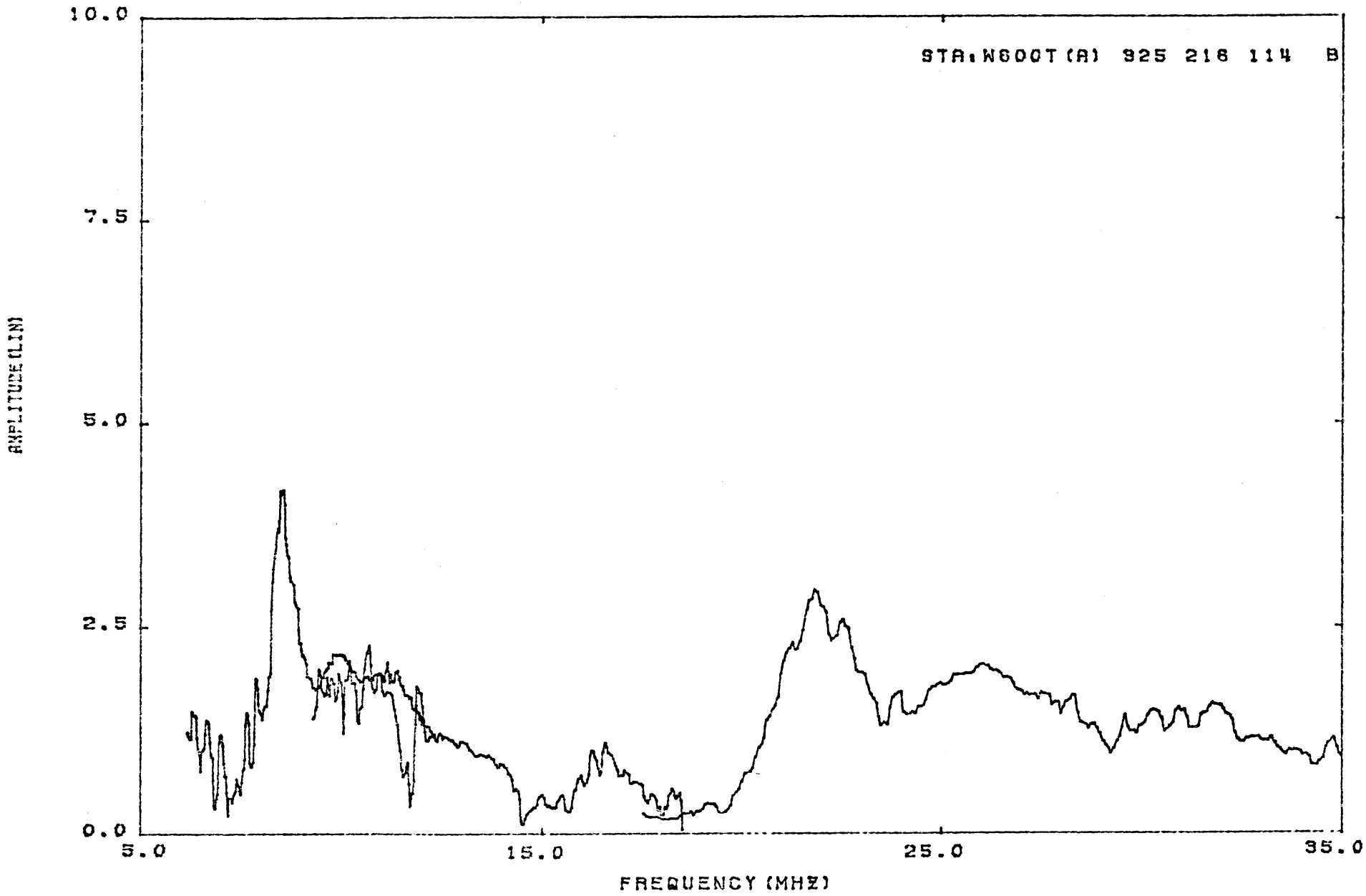

Figure 104a. Current amplitude at STA:W600T(A) (5 - 35 MHz).

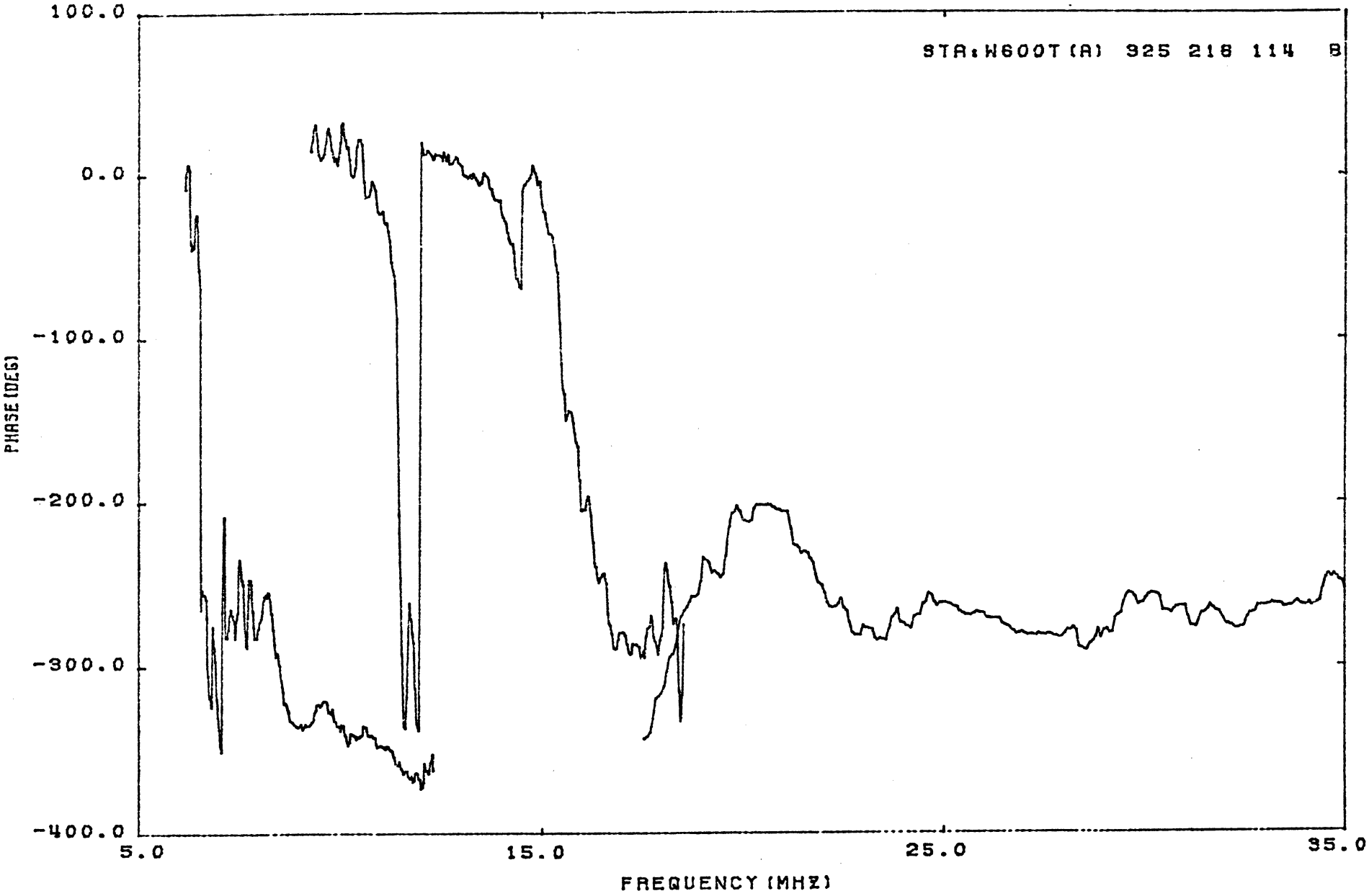

Figure 104b. Current phase at STA:W600T(A) (5 - 35 MHz).

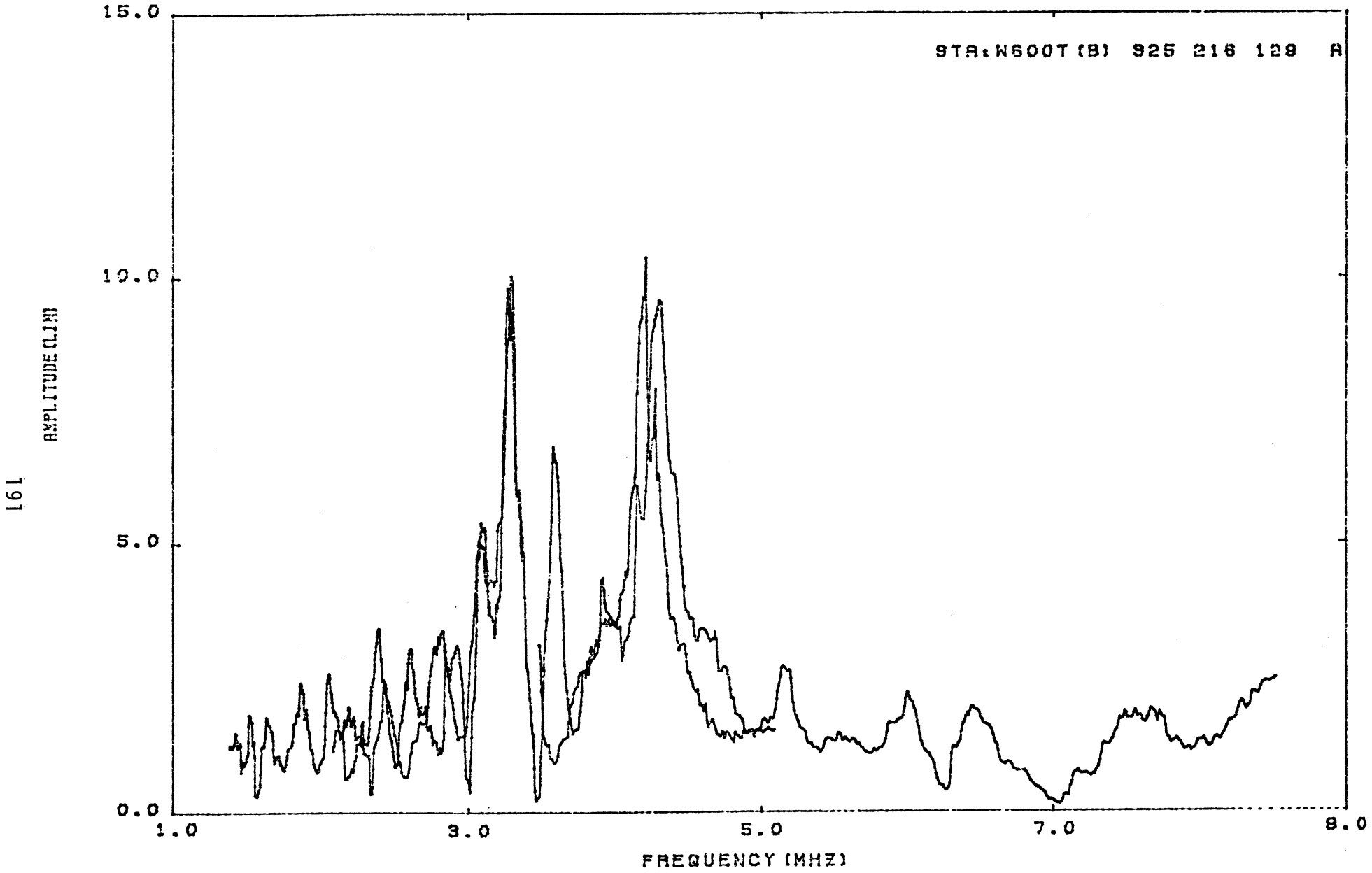

Figure 105a. Current amplitude at STA:W600T(B) (1 - 9 MHz).

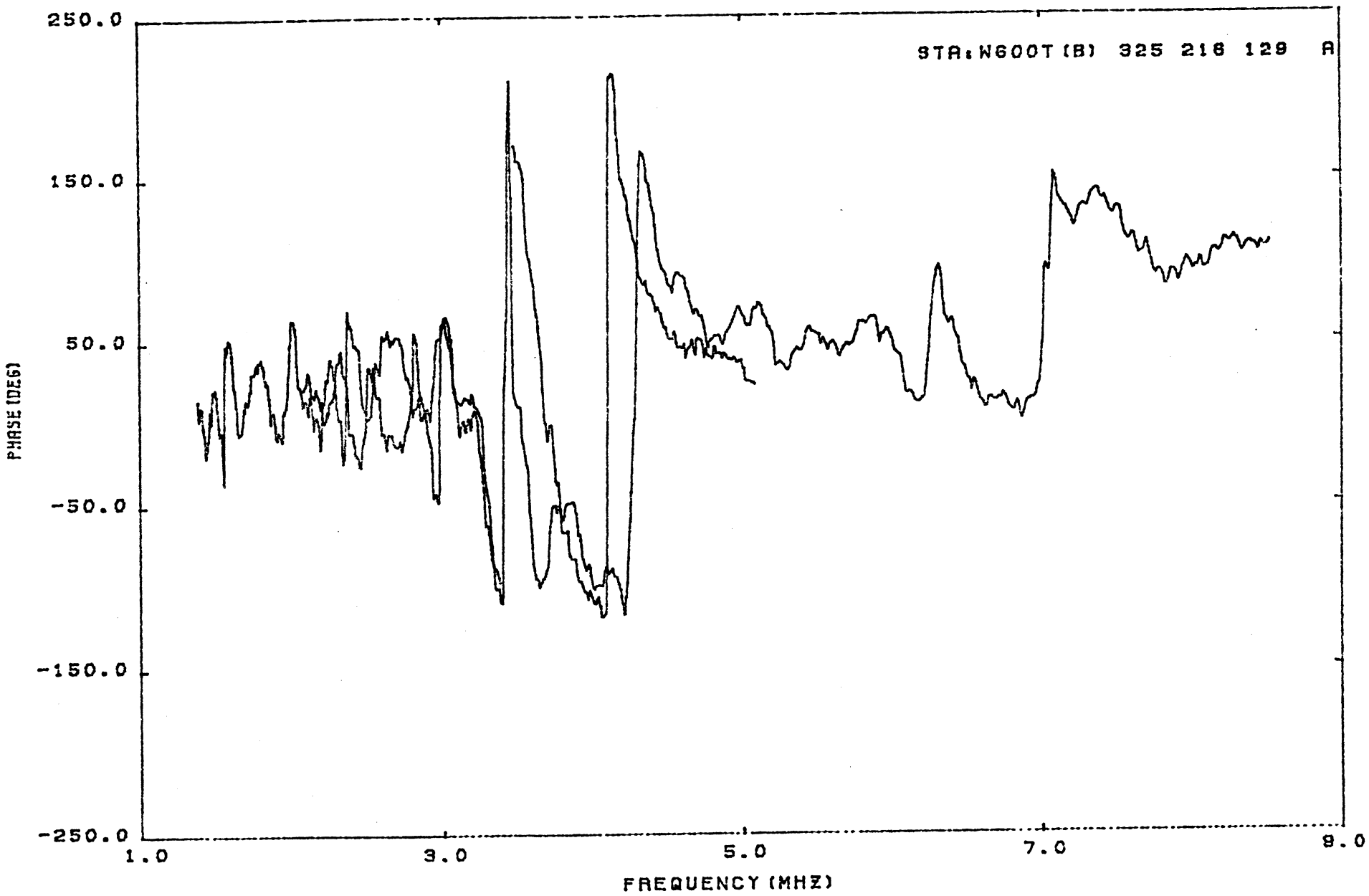

Figure 105b. Current phase at STA:W600T(B) (1 - 9 MHz).

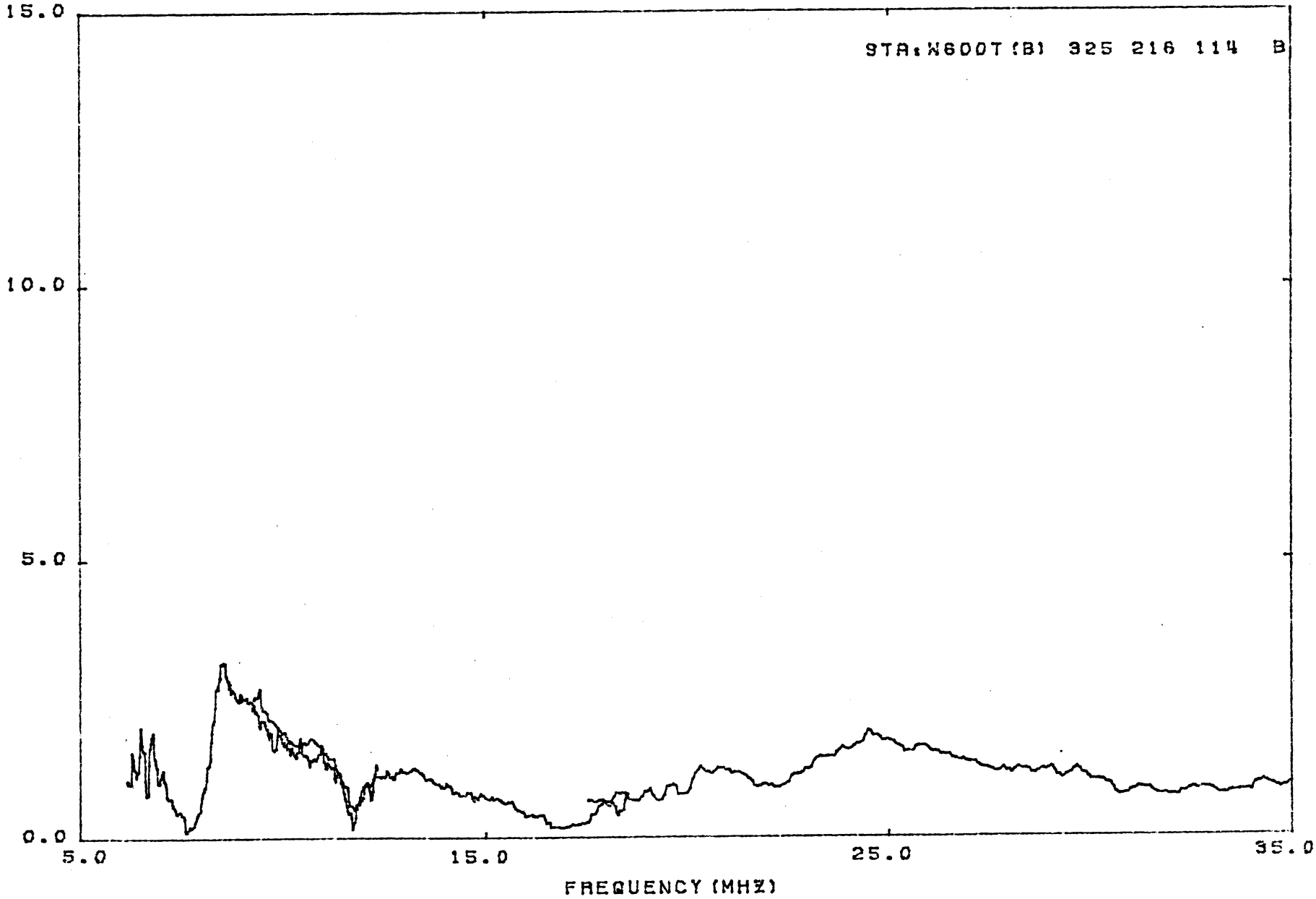

Figure 106a. Current amplitude at STA:W600T(B) (5 - 35 MHz).

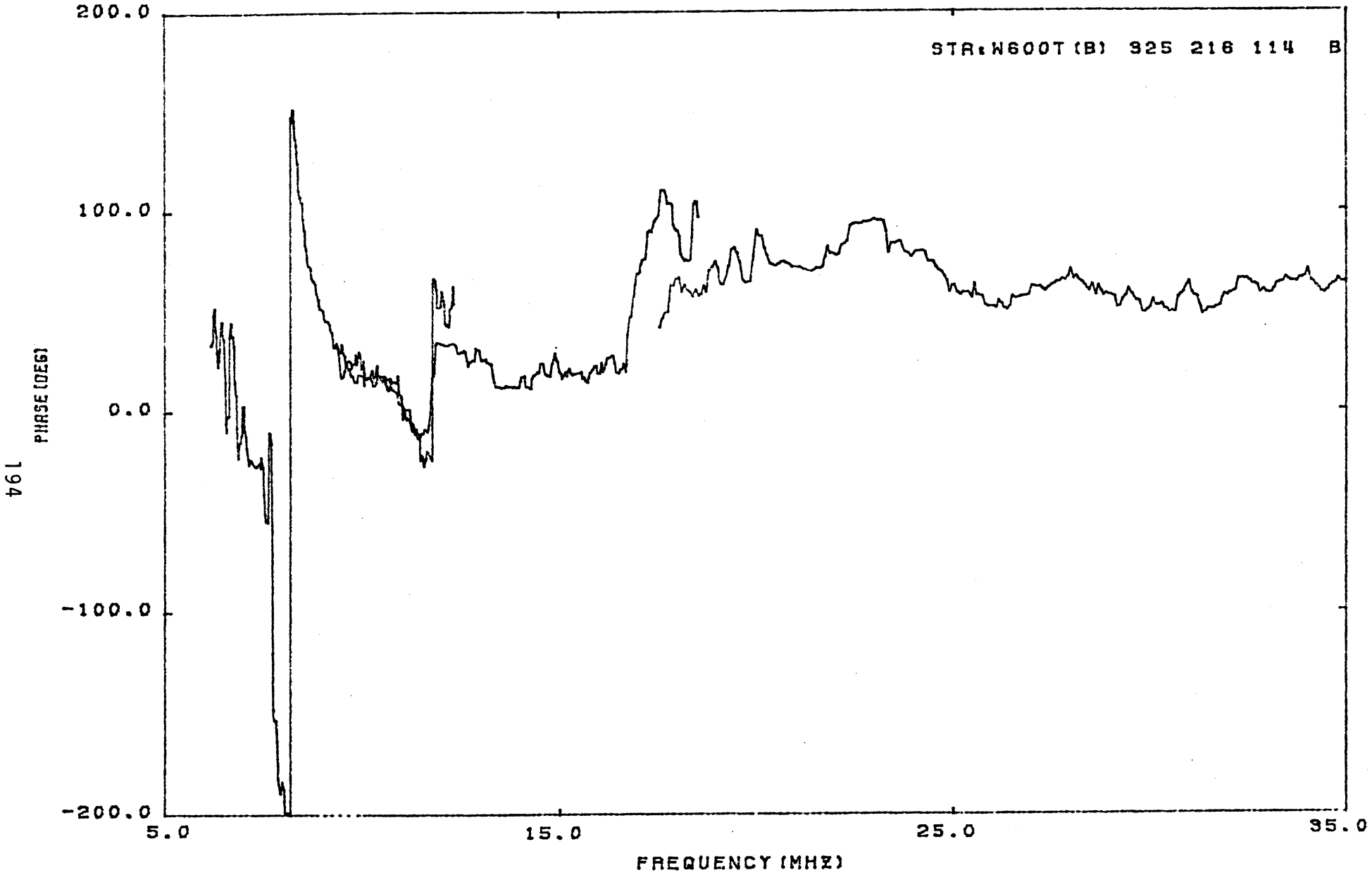

Figure 106b. Current phase at STA:W600T(B) (5 - 35 MHz).

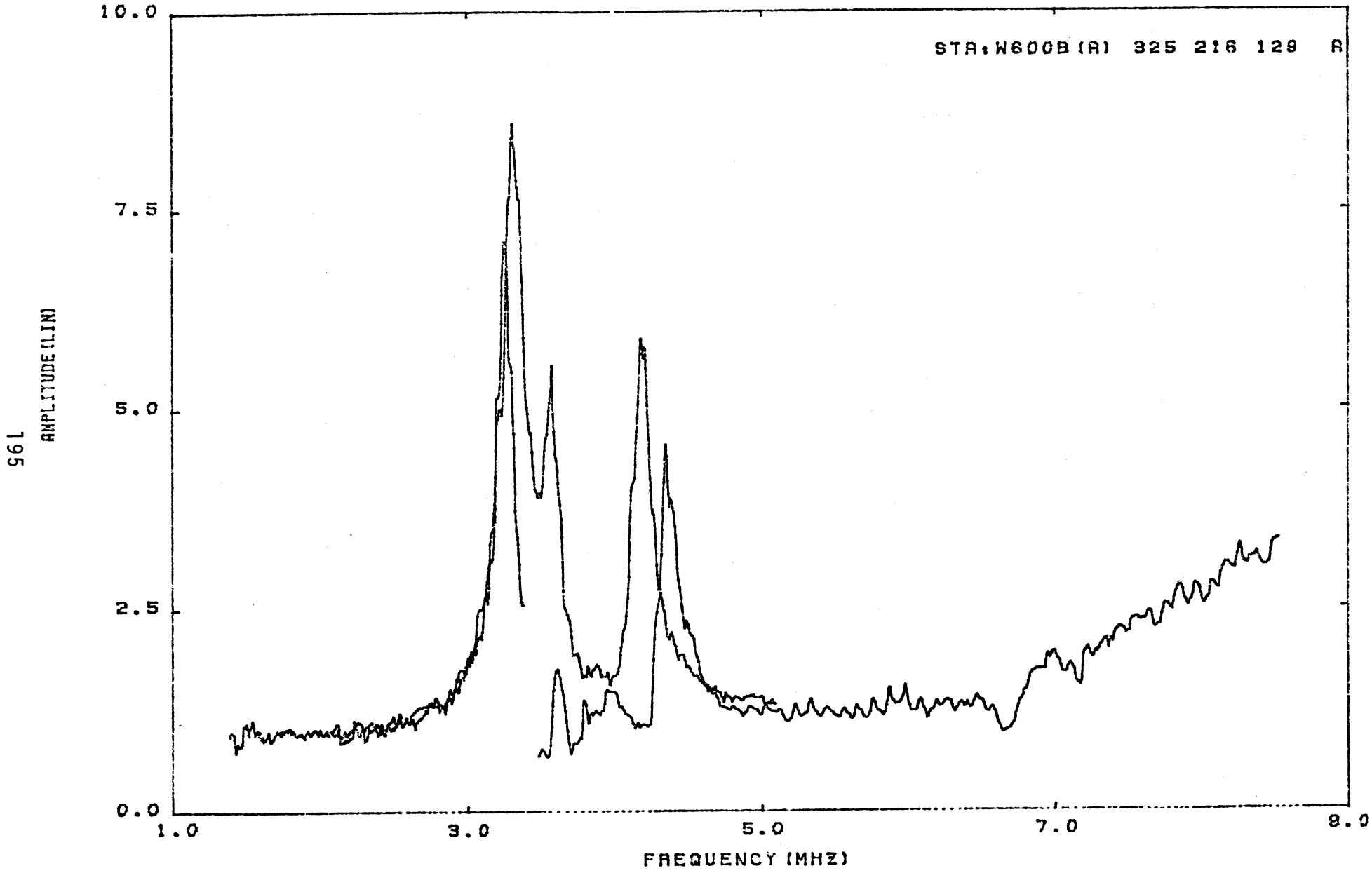

Figure 107a. Current amplitude at STA:W600B(A) (1 - 9 MHz).

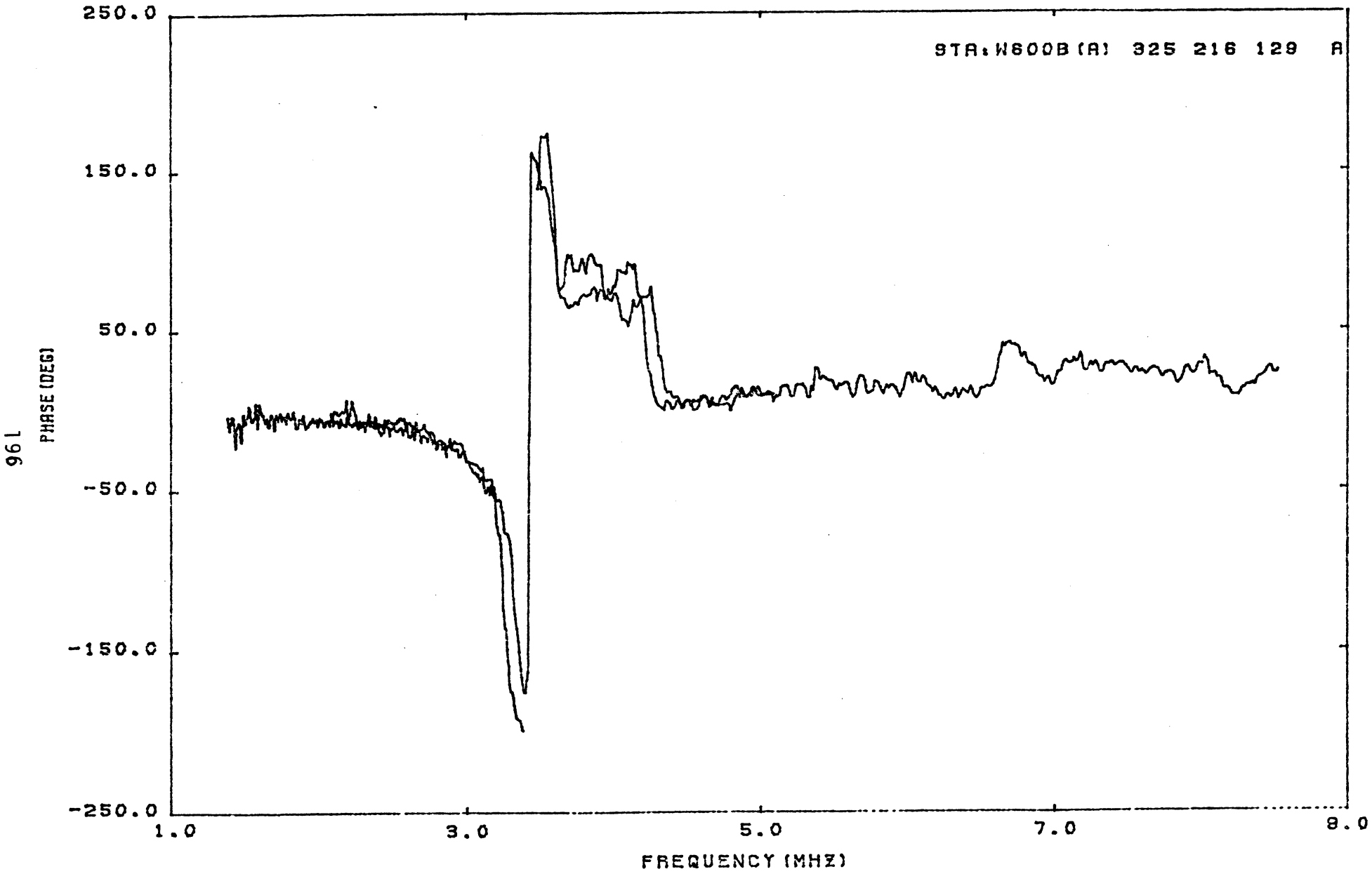

Figure 107b. Current phase at STA:W600B(A) (1 - 9 MHz).

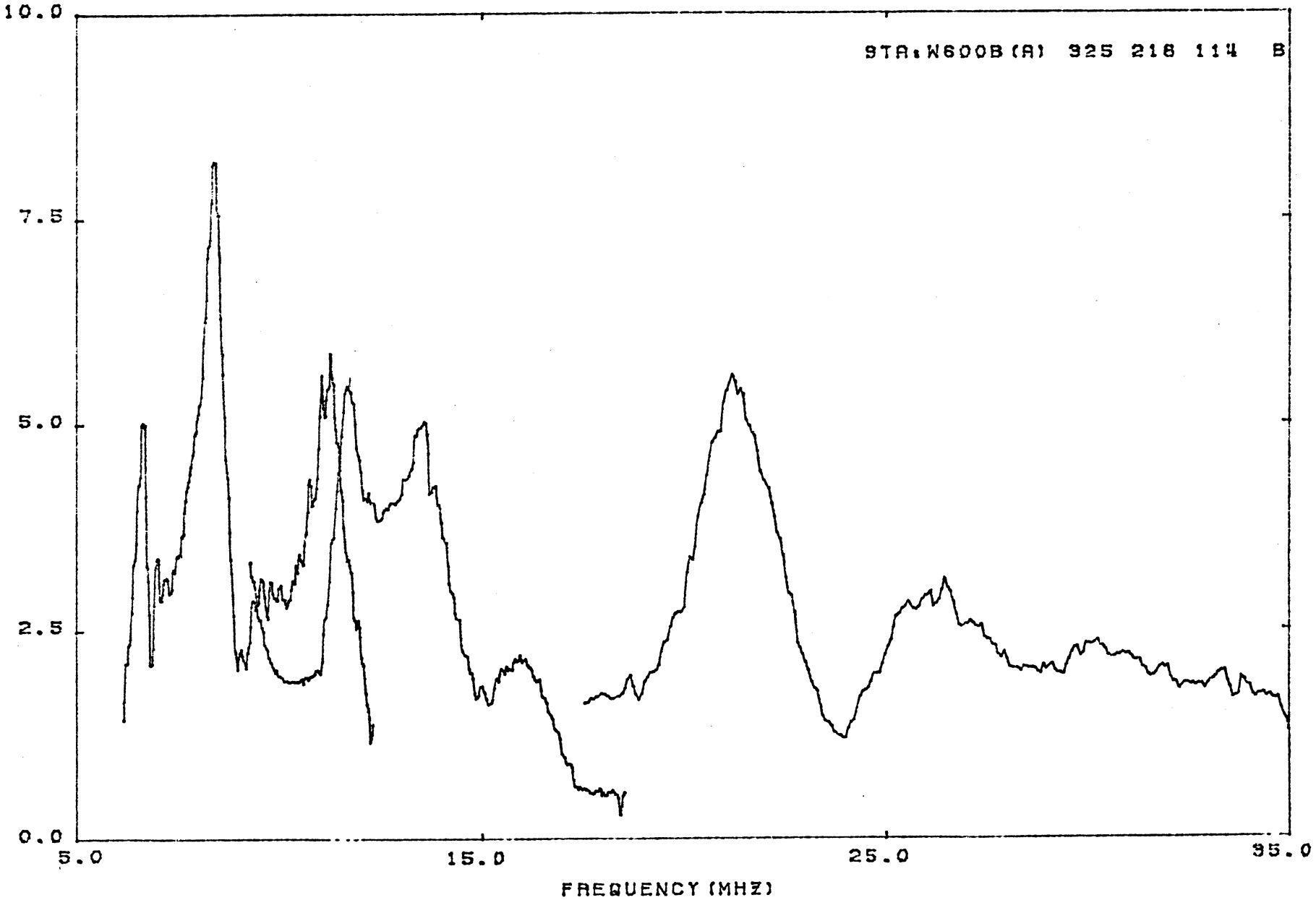

Figure 108a. Current amplitude at STA:W600B(A) (5 - 35 MHz).

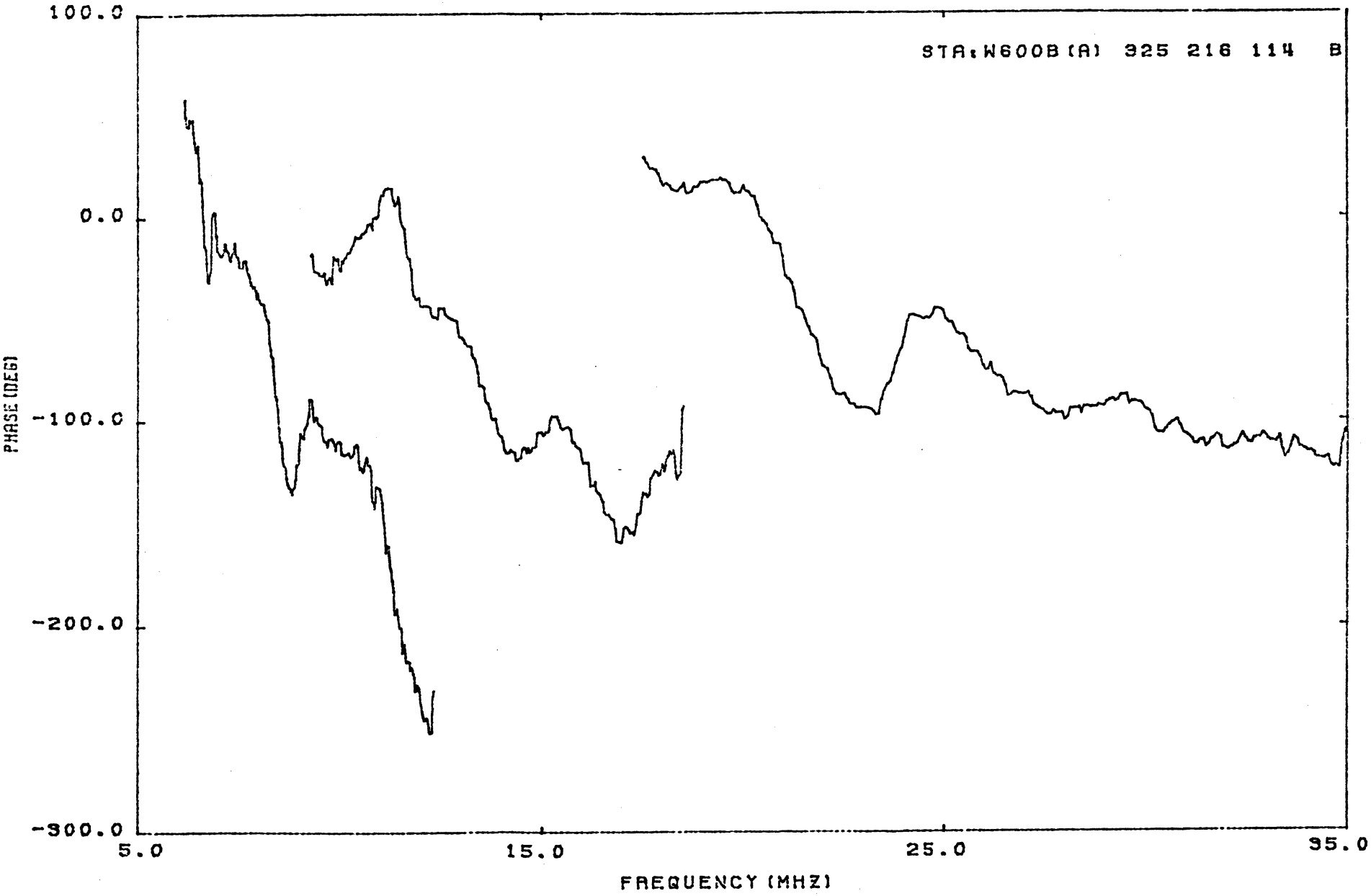

Figure 108b Current phase at STA:W600B(A) (5 - 35 MHz).

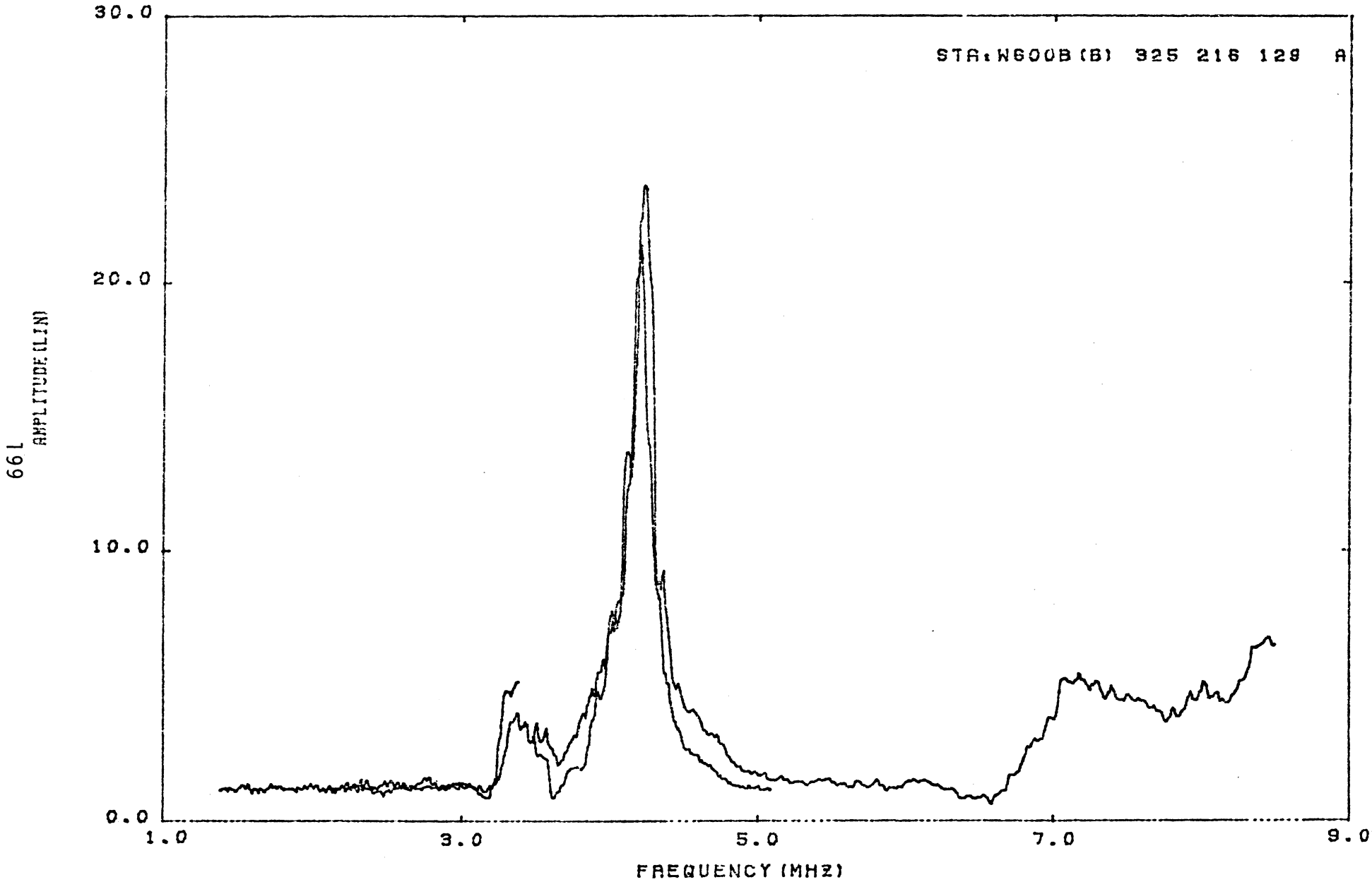

Figure 109a. Current amplitude at STA:W600B(B) (1 - 9 MHz).

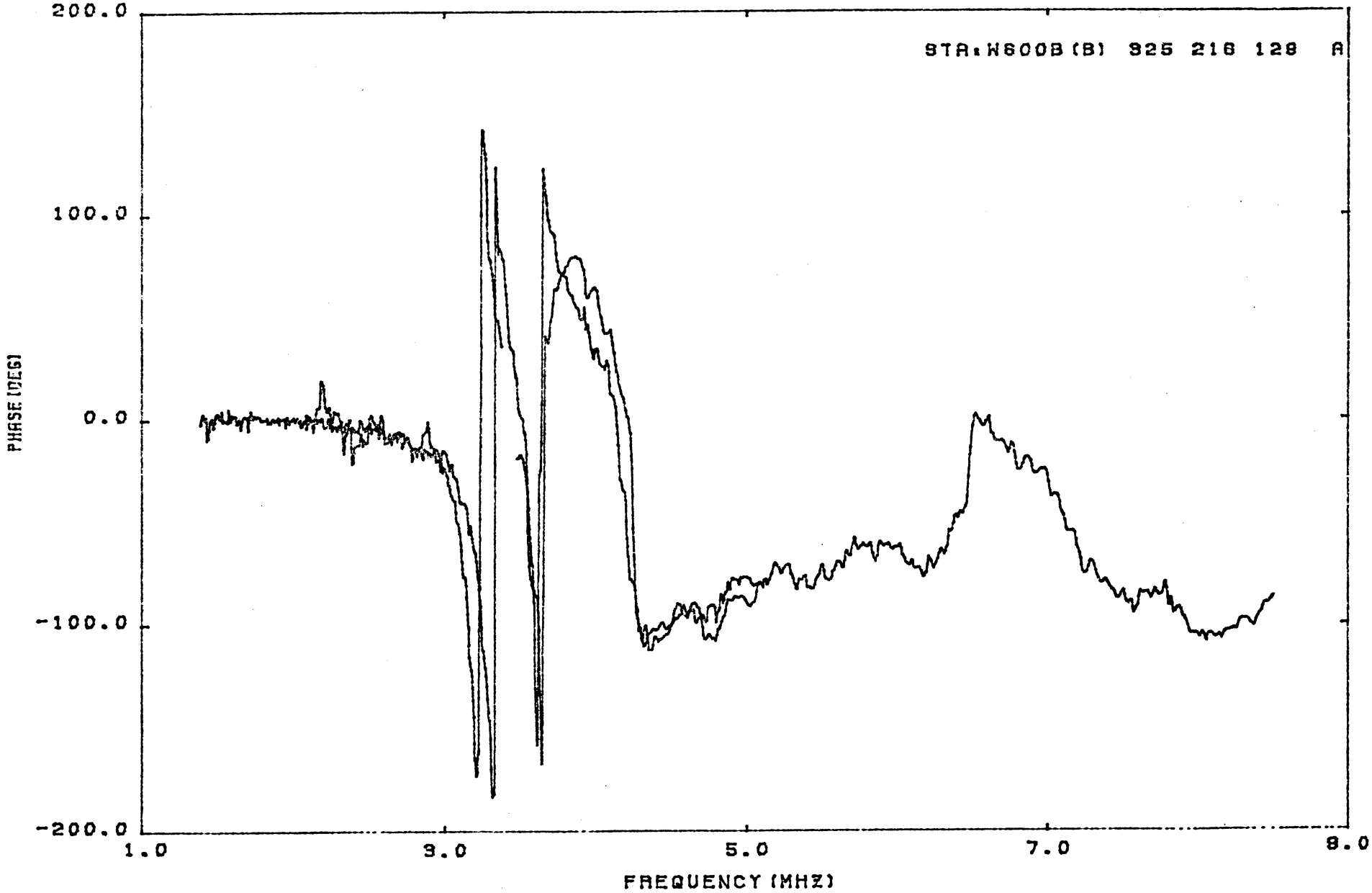

Figure 109b. Current phase at STA:W600B(B) (1 - 9 MHz).

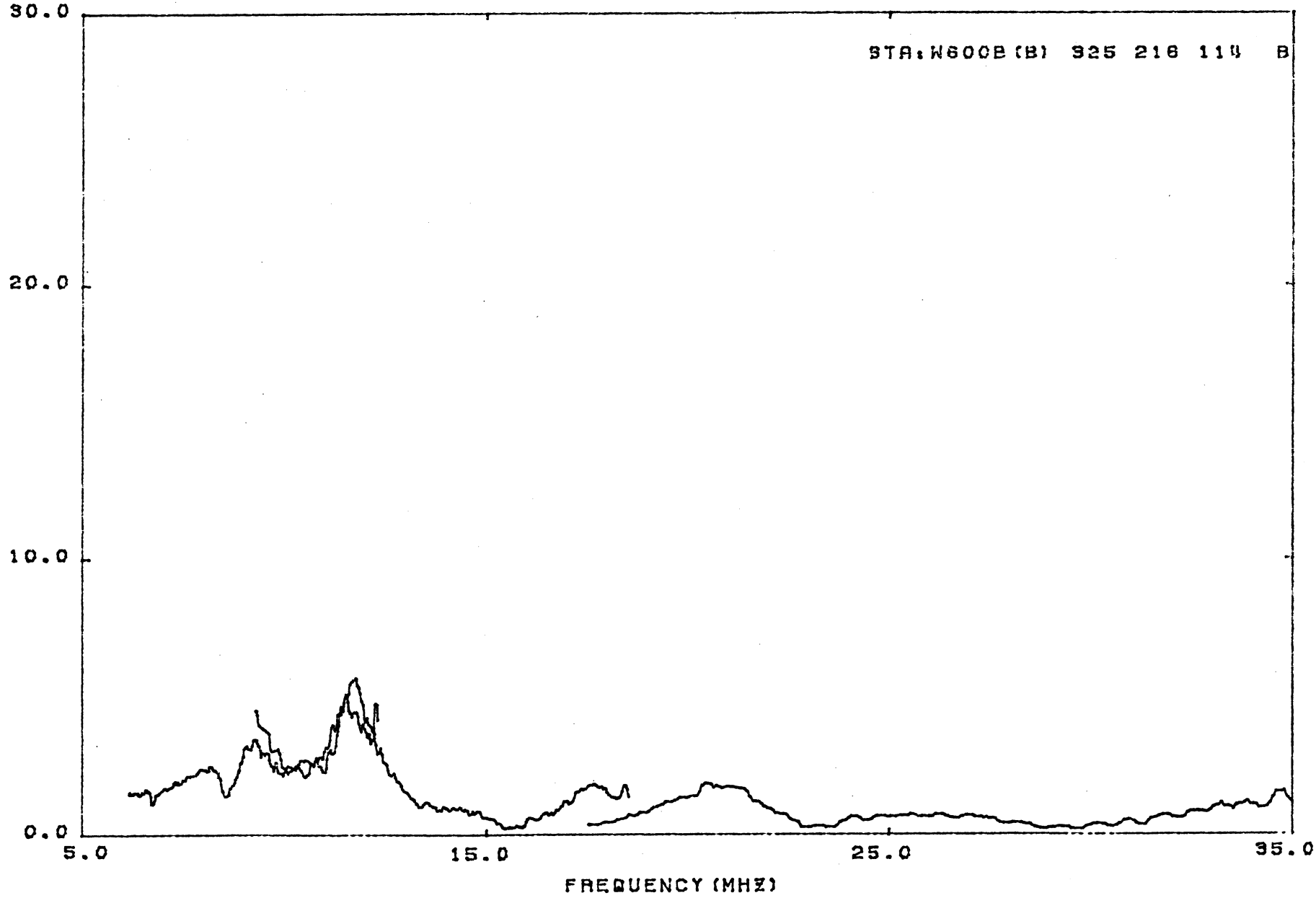

Figure 110a. Current amplitude at STA:W600B(B) (5 - 35 MHz).

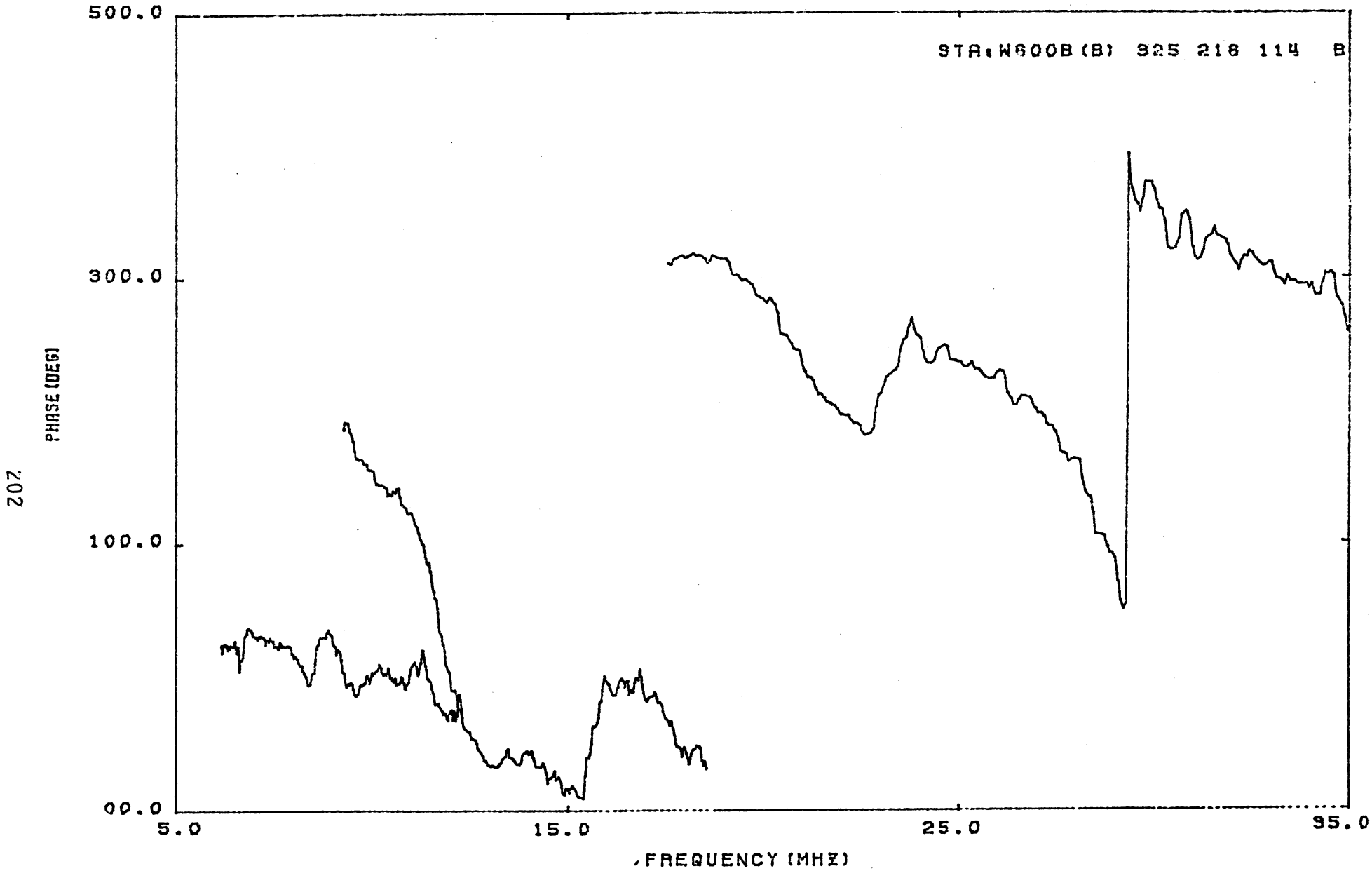

Figure 110l . Current phase at STA:W600B(B) (5 - 35 MHz).

SECTION V
CONCLUSIONS

The results presented here are the fruits of an 18-month investigation during which the measurement facility has undergone a drastic change. At the beginning the facility consisted of a relatively small anechoic chamber in which, for example, the frequency was swept using a motor-driven signal generator, whereas now it has a larger and improved chamber with the latest microwave equipment supplemented by an automatic digital data acquisition and processing system.

Of course, such changes do create their own problems and none of the data in this report were actually obtained with the full system in operation. As each new piece of equipment became available, the measurement capability increased, with a resulting improvement in the coverage and quality of the data. This evolution is apparent in the data of Sections II, III, and IV. When the EC-135 free-space measurements were carried out, a 450 - 1000 MHz capability was not available, and to cover the critical resonance region of the aircraft using the available 1 - 2 GHz band, it was necessary to use models as small as 1/447 scale. Such small models are difficult to handle and the measurements are more prone to error. However, by the time the ground plane measurements were started, the frequency coverage had been extended to 450 MHz and it was possible to use models which were no smaller than 1/325.

The process of data reduction and presentation has also followed a similar evolutionary path. At the start of the investigation, the process was entirely manual, requiring the tedious and time-consuming comparison of measured curves at sampled frequencies, and the subsequent plotting of points adequate to form a graph. The first half of the data in this report was processed in this manner, but during the ground plane measurements a procedure for digitizing the measured curves was developed. All subsequent data were then computer-processed and plotted, leading to a marked improvement in efficiency and accuracy. Although the time taken to digitize the data is by no means insignificant, it would have been almost impossible to present the needed data in the time allotted without this advance.